

The profiling and imaging of sterol molecules in the human brain

Lauren Griffiths

A thesis submitted to Swansea University in fulfilment of the
requirements for the degree of Doctor of Philosophy



Swansea University
Prifysgol Abertawe

Swansea University

2022

Table of Contents

Summary	i
Declaration and Statements.....	ii
Acknowledgements.....	iii
List of Figures.....	iv
List of Tables.....	viii
List of Abbreviations.....	x
Chapter 1 – Introduction.....	1
1.1. Sterol molecules and their biochemistry	2
1.1.1. Cholesterol	2
1.1.2. Oxysterols.....	4
1.2. Oxysterols and their bioactivity	13
1.2.1. Sterols and cholesterol homeostasis	14
1.2.2. Oxysterols and immunology	17
1.3. Sterols in the brain	18
1.3.1. Cholesterol biosynthesis and regulation in the brain	19
1.4. Neurodegeneration and its links to sterols.....	21
1.4.1. Alzheimer’s disease.....	22
1.4.2. Multiple sclerosis	26
1.4.3. Huntington’s disease	30
1.5. Sterolomics	32
1.6. Sterol extraction from biological samples	33
1.7. Solid phase extraction for sterol separation and oxysterol enrichment	34
1.8. Derivatisation of sterol molecules	36
1.9. Chromatographic separation	37
1.10. Mass spectrometry (MS).....	39
1.10.1. Ion Sources	39
1.10.2. Mass Analysers	42
1.10.3. Detectors.....	45
1.10.4. Tandem mass spectrometry (MS ⁿ)	45
1.10.5. Orbitrap Elite and IDX MS	46

1.11. Mass spectrometry imaging (MSI) techniques	48
1.12. Aims of this thesis.....	51
1.13. References	52

Chapter 2 – Methods and materials.....67

2.1. Materials	68
2.1.1. Reagents and solvents	68
2.1.2. Reference internal standards	69
2.2. Methods.....	71
2.2.1. Sterol extraction from human serum.....	71
2.2.2. Sterol extraction from human cerebrospinal fluid (CSF).....	72
2.2.3. Sterol extraction from human brain tissue	73
2.2.4. Separation of oxysterols and cholesterol using solid phase extraction	76
2.2.5. Enzyme-assisted derivatisation of sterol analysis (EADSA).....	77
2.2.6. Purification of oxysterols using solid phase extraction.....	79
2.2.7. On-tissue derivatisation for MALDI analysis	80
2.2.8. Spraying of matrix for MALDI analysis	81
2.2.9. Analysis of biofluid using HPLC and MS ⁿ	81
2.2.10. Analysis of tissue using AP-MALDI.....	84
2.2.11. Orbitrap Elite and Orbitrap ID-X.....	87
2.2.12. Relative quantitation of analytes	88
2.3. References	90

Chapter 3 – The profiling of oxysterols and sterols in cerebrotendinous xanthomatosis (CTX).....91

3.1. Introduction.....	92
3.1.1. Aims	93
3.2. Materials and methods	94
3.2.1. CTX serum and CSF cohort.....	94
3.2.2. CTX brain tissue cohort	94
3.2.3. Serum/ plasma extraction and sample preparation.....	96
3.2.4. CSF extraction and sample preparation	96

3.2.5. Brain tissue homogenisation, extraction, and sample preparation	97
3.2.6. Oxysterol analysis	97
3.3. Results	99
3.3.1. Cholesterol	99
3.3.2. Alternative pathway (26-hydroxylation).....	101
3.3.3. Classical pathway (7 α -hydroxylation)	104
3.3.4. Cerebral pathway (24-hydroxylation)	106
3.3.5. 25-hydroxylation pathway	109
3.3.6. Analysis from regional brain tissue in CTX	112
3.4. Discussion.....	120
3.5. References	122

Chapter 4 – The profiling of sterols in human Alzheimer’s disease brain

tissue.....	123
4.1. Introduction.....	124
4.1.1. Aims	127
4.2. Materials and Methods	128
4.2.1. AD brain tissue cohort	128
4.2.2. Brain tissue homogenisation, extraction, and sample preparation.....	129
4.2.3. Oxysterol analysis	129
4.2.4. Statistical analysis	129
4.3. Results	132
4.3.1. Identification of 25-hydroxycholestenone and (25R)26-hydroxycholestenone	132
4.3.2. Analysis of sterols using brain diagnosis grouping.....	136
4.3.3. Analysis of sterols using <i>APOE</i> status	137
4.4. Discussion.....	148
4.5. References	151

Chapter 5 – The profiling of sterols in multiple sclerosis human brain

tissue.....	153
5.1. Introduction.....	154

5.1.1. Aims	157
5.2. Materials and Methods	158
5.2.1. Multiple sclerosis brain tissue cohort.....	158
5.2.2. Brain tissue homogenisation, extraction, and sample preparation	158
5.2.3. Oxysterol analysis	159
5.2.4. Statistical analysis	162
5.3. Results	163
5.3.1. Confirmation of the presence of 25- and (25R)26-hydroxycholestenone in multiple sclerosis and control human brain tissue.	163
5.3.2. Analysis of 24S-HC, 25-HC and (25R)26-HC	164
5.3.3. Analysis of other monohydroxycholesterols of interest.....	166
5.3.4. The quantification of other sterols, dihydrocholesterols and cholestenic acid metabolites.....	168
5.4. Discussion.....	172
5.5. References	175

Chapter 6 – The optimisation of an imaging method to analyse cholesterol using AP-MALDI mass spectrometry imaging.....179

6.1. Introduction	180
6.2. Methodological differences.....	183
6.2.1. Original published method	184
6.2.2. Cryosectioning and histological staining	185
6.3. Optimisation of an AP-MALDI-MSI method for the visualisation of cholesterol	187
6.3.1. Imaging software for the visualisation and quantification of cholesterol ..	187
6.3.2. Isotope-labelled standard density on tissue.....	188
6.3.3. Potassium phosphate buffer concentration for the enzyme reaction.....	191
6.3.4. Girard-P reagent density on tissue	192
6.3.5. Matrix density on tissue and sprayer system	193
6.3.6. AP-MALDI UHR source and Orbitrap ID-X mass spectrometer parameters	195
6.3.7. Fourier-transform data from Orbitrap ID-X; Reproducibility of the methodology at 50µm spatial resolution	196

6.3.8. Ion-trap fragmentation confirmation of cholesterol and isotope-labelled standard	200
6.3.9. High resolution imaging advantages of AP-MALDI UHR source	201
6.4. Conclusion.....	205
6.5. References	207

Chapter 7 - The analysis of cholesterol in multiple sclerosis and Huntington's disease brain tissue using mass spectrometry imaging.....209

7.1. Introduction.....	210
7.1.1. Aims	211
7.2. Methods and materials	212
7.2.1. Q150 mouse brain tissue	212
7.2.2 Rat brain tissue	212
7.2.3. Multiple sclerosis and control human brain tissue	212
7.2.4. Tissue cutting	213
7.2.5. Tissue histology	214
7.2.6. MALDI sample preparation	215
7.2.7. Matrix application	216
7.2.8. Instrumentation	216
7.2.9. Software analysis of MALDI-MSI data.....	216
7.2.10. Statistical analysis	217
7.3. Results	219
7.3.1. Huntington's disease Q150 mouse model.....	219
7.3.2. Human multiple sclerosis brain tissue	222
7.3.3. The visualisation of other lipids using Metaspace software	230
7.4. Discussion.....	238
7.5. References	242

Chapter 8 - General conclusions.....245

8.1. Concluding findings	246
8.2. Limitations of this work	248
8.3. Future directions	249

8.4. References	251
Appendix	253

Summary

For this project we had a unique opportunity to truly explore sterol molecules within the human brain of healthy and disease individuals. Cholesterol, and its derivative oxysterols, are quickly becoming an important topic within neurodegenerative diseases, with published literature suggesting altered sterol profiles from the peripheral fluid in individuals with these disorders.

The main aims of this work were to analyse oxysterols and cholesterol in neurodegenerative disease human brain tissue and corresponding controls using homogenisation to look whether the sterol profiles differ in Alzheimer's disease, multiple sclerosis and cerebrotendinous xanthomatosis. We also aimed to develop and optimise a method to image cholesterol across intact brain tissue sections and quantify the cholesterol in regions of interest using mass spectrometry imaging.

We successfully achieved the quantification of oxysterols in all neurological disorders named above and identified some significant differences in specific sterol pathways and metabolites in Alzheimer's and multiple sclerosis homogenate tissue samples. Notably, we optimised a method to quantify and visualise cholesterol across intact tissue sections using isotope-labelled standards and matrix-assisted laser desorption/ ionisation (MALDI) - mass spectrometry imaging (MSI) and found significant changes in cholesterol in several regions of interest, including the lesions of human multiple sclerosis brain tissue and the inflammatory edge of white matter lesions using this method. We also observed differences in white matter brain stem regions of Huntington's disease mouse brain tissue. These results highlight the importance of our optimised MALDI-MSI cholesterol method, identifying important changes in tissue that cannot be seen with standard immunohistochemical staining techniques. These changes could be telling of pathologies and mechanisms at play in neurodegenerative diseases and could help target biomarkers for future treatments.

DECLARATION

This work has not previously been accepted in substance for any degree and is not being concurrently submitted in candidature for any degree.

Signed ...

Date07/12/2022.....

STATEMENT 1

This thesis is the result of my own investigations, except where otherwise stated. Where correction services have been used, the extent and nature of the correction is clearly marked in a footnote(s).

Other sources are acknowledged by footnotes giving explicit references. A bibliography is appended.

Signed ..

Date07/12/2022.....

STATEMENT 2

I hereby give consent for my thesis, if accepted, to be available for photocopying and for inter-library loan, and for the title and summary to be made available to outside organisations.

Signed ...

Date07/12/2022.....

Acknowledgements

I would firstly like to thank my supervisory team, Professor Bill Griffiths, Dr Owain Howell and Professor Yuqin Wang for their constant guidance, support and expertise over the last few years. I have learnt so much from each of you individually over the past three years and am incredibly grateful that you gave me the opportunity to pursue this PhD and expand my knowledge into the world of sterol and neurodegenerative research.

I would like to give the biggest thank you to my family and friends for their support throughout this journey. I would like to give a special mention to my parents and brother; you have always encouraged me to be the best I can be and ensured me that I can achieve whatever I put my mind to, and I am eternally grateful for the opportunities you have created for me because of that.

Finally, I would like to acknowledge everyone from the Griffiths-Wang research group and all my colleagues from ILS1 3rd floor for their support, assistance, and kindness. A special thanks goes to Dr Eylan Yutuc for his continual help and guidance throughout my PhD project and thesis writing process.

List of Figures

Figure 1.1. The amphipathic nature of cholesterol.....	2
Figure 1.2. The mevalonate pathway.....	4
Figure 1.3. The Bloch and Kandutsch-Russell pathways for the synthesis of cholesterol.....	5
Figure 1.4. The formation of several oxysterols from cholesterol via reactive oxygen species (ROS) reactions.....	6
Figure 1.5. The classical (7 α -hydroxylation) and alternative/acidic ((25R)26-hydroxylation) oxysterol biosynthesis pathways.....	8
Figure 1.6. The molecular structures of cholic acid and chenodeoxycholic acid.....	10
Figure 1.7. The cerebral, or 24S-hydroxylation, and 25-hydroxylation pathways.....	11
Figure 1.8. The synthesis of 24S,25-epoxycholesterol via a parallel pathway to cholesterol biosynthesis.....	13
Figure 1.9. Schematic of the SREBP2/SCAP mechanism.....	15
Figure 1.10. Cholesterol synthesis, transport and turnover within the brain.....	20
Figure 1.11. The metabolism of APP and subsequent synthesis of amyloid beta (A β) in the brain.....	23
Figure 1.12. The formation of neurofibrillary tangles from hyperphosphorylated tau protein and paired helical filaments (PHFs).....	24
Figure 1.13. Multiple sclerosis subtypes and the pattern of increasing disability over time.....	27
Figure 1.14. The different types of inflammatory lesion present in the multiple sclerosis brain...	28
Figure 1.15. The process of demyelination and remyelination in multiple sclerosis.....	29
Figure 1.16. Effects of the mutant huntingtin (mHtt) on cholesterol metabolism and transport in the CNS.....	31
Figure 1.17. Hydrolysis reaction of cholesteryl ester into cholesterol using potassium hydroxide (KOH).....	34
Figure 1.18. The principle of solid phase extraction to filter analytes of interest.....	35
Figure 1.19. Formation of positively charged cholesterol molecule via an enzyme-assisted derivatisation for sterol analysis (EADSA) incorporating derivatisation with Girard hydrazine.....	37
Figure 1.20. A schematic representation of the Dionex UltiMate 3000 HPLC system.....	38
Figure 1.21. Schematic of the electrospray ionisation process at atmospheric pressure.....	41
Figure 1.22. Schematic of MALDI desorption and the ionisation process.....	42
Figure 1.23. A diagram of a quadrupole mass analyser.....	43
Figure 1.24. A graphic of a linear ion trap (LIT).....	44
Figure 1.25. A schematic of an Orbitrap analyser.....	45
Figure 1.26. Schematic diagram of the Orbitrap Elite hybrid mass spectrometer.....	47
Figure 1.27. Schematic diagram of the Orbitrap ID-X tribrid mass spectrometer.....	48

Figure 1.28. The spatial resolution versus the molecular mass range for different MSI techniques.....	50
Figure 2.1. The separation of oxysterols/sterols using solid phase extraction (SPE1).....	77
Figure 2.2. The derivatisation of oxysterols using the EADSA method.....	78
Figure 2.3. Purification of oxysterols using solid phase extraction (SPE2).....	79
Figure 2.4. Gradient elution for the separation of derivatised sterols using high pressure-liquid chromatography (HPLC).....	82
Figure 2.5. The MS ³ fragmentation and corresponding fragments from several oxysterols.....	84
Figure 2.6. Calculation of the stage velocity (distance/time) based on a 50µm spatial resolution acquisition.....	86
Figure 2.7. Determining the sample area, transition time and calculating the total acquisition time based on parameters from a 50µm spatial resolution acquisition.....	87
Figure 2.8. Schematic of the Orbitrap ID-X tribrid mass spectrometer.....	88
Figure 2.9. A worked example showing the relative quantification of endogenous 24S-HC from control plasma using a deuterated internal standard.....	89
Figure 3.1. Cholesterol metabolism pathways for the synthesis of bile acids.....	93
Figure 3.2. Identification of cholesterol using mass spectra and ion trap fragmentation (ITMS ³) from CTX serum.....	99
Figure 3.3. Analysis comparing CTX and control cholesterol levels in serum and CSF.....	100
Figure 3.4. Reduced levels of several cholesterol metabolites involved in the 26-hydroxylation and 7α-hydroxylation pathways observed in CTX serum, CSF and brain tissue.....	102
Figure 3.5. Spectra of metabolites of the 26-hydroxylation pathway from the serum/plasma data with corresponding ITMS ³ fragmentation.....	103
Figure 3.6. Spectra of metabolites of the 7α-hydroxylation pathway and of 5α-cholestanol from the serum data with the corresponding ITMS ³ fragmentation.....	105
Figure 3.7. The metabolites identified from the cerebral pathway in CTX and control.....	107
Figure 3.8. The conversion of 24S,25-epoxycholesterol (24S,25-EC) to 24-oxocholesterol (24-OC)	108
Figure 3.9. Analysis of metabolites within the 24S-hydroxylation pathway identified within CTX serum and reference plasma, CSF and brain tissue.....	109
Figure 3.10. Spectra of metabolites from the 25-hydroxylation pathway identified in CTX serum and control plasma.....	110
Figure 3.11. Analysis of metabolites within the 25-hydroxylation pathway identified	

within CTX serum, control plasma and CSF.....	111
Figure 3.12. Observations from regional brain tissue samples from an individual with CTX.....	113
Figure 4.1. The role of APOE in cholesterol transport in the brain and the influence of A β and sterols.....	125
Figure 4.2. Position of the dorsolateral prefrontal cortex within the human brain.....	128
Figure 4.3. The structures of 25-hydroxycholestenone (25-HCO) and (25R)26-hydroxycholestenone ((25R)26-HCO) with ITMS ³ fragmentation confirmation.....	133
Figure 4.4. Concentrations of 25-hydroxycholestenone (25-HCO) in the human brain.....	134
Figure 4.5. Concentrations of (25R)26-hydroxycholestenone ((25R)26-HCO) in the human brain.....	135
Figure 4.6. Statistical analysis of sterols identified in AD, MCI and control brain.....	136
Figure 4.7. The statistical analysis of sterols using the <i>APOE</i> status of individuals.....	138
Figure 5.1. The vast number of types of lesions present in a multiple sclerosis brain.....	154
Figure 5.2. Chronic active inflammation and extensive demyelinating pathologies witnessed in the multiple sclerosis disease course.....	160
Figure 5.3. Concentrations of 25- and (25R)26-hydroxycholestenone relatively quantified from human multiple sclerosis and control brain tissue.....	163
Figure 5.4. A chromatogram of monohydroxycholesterols at m/z 539.4363 \pm 5 ppm from multiple sclerosis brain tissue using long gradient LC MS ³	164
Figure 5.5. Analysis of monohydroxycholesterols show significance in (25R)26-HC and 24R-HC.....	165
Figure 5.6. A significant difference in the levels of 7 β -HC and 7 α -HC quantified in multiple sclerosis and control brain tissue.....	167
Figure 5.7. Concentrations of other sterol metabolites showed trends but no significance.....	169
Figure 6.1. A schematic of MALDI imaging.....	181
Figure 6.2. Enzyme-assisted derivatisation of endogenous cholesterol with Girard P.....	183
Figure 6.3. The comparison of several imaging softwares based on software ability, image quality and data handling.....	189
Figure 6.4. An increase in isotope-labelled standard density showed better image quality and removed black pixels.....	190
Figure 6.5. Changing the concentration of buffer from 0.1 mM to 5 mM did not affect image quality but introduced a better pH stability for the enzymatic reaction.....	192
Figure 6.6. The intensity of both endogenous cholesterol and the isotope-labelled standard does not increase as areal density of Girard P reagent increases.....	193

Figure 6.7. A more intense cholesterol signal is obtained at a CHCA areal density of 2.67 $\mu\text{g}/\text{mm}^2$	195
Figure 6.8. A worked example for the calculation of the areal density of endogenous cholesterol on tissue (in ng/mm^2) in a specific region of interest (pons) using internal standard density (120 ng/mm^2)	197
Figure 6.9. The reproducibility of the method proven by staining confirmation and quantification of absolute cholesterol.....	199
Figure 6.10. Ion-trap fragmentation (ITMS ³) data confirms the identity of cholesterol and the isotope-labelled standard in mouse brain tissue sections.....	200
Figure 6.11. The analysis of CYP46A1 overexpressed mouse brain cerebellum at 20 μm higher spatial resolution.....	202
Figure 6.12. The mass spectrometry image created of the striatal/caudate putamen (CP) region of the Q150 ⁺ mouse brain tissue at 10 μm and 5 μm spatial resolution.....	204
Figure 7.1. Cutting of the Q150 mouse and corresponding control.....	214
Figure 7.2. Quantification of regions of interest in Q150 MALDI-MSI images based on LFB staining.....	219
Figure 7.3. The normalised images of cholesterol from the Huntington's and control mouse brain tissue.....	220
Figure 7.4. The quantification of relative cholesterol across HD mouse model brain tissue and corresponding control.....	222
Figure 7.5. The demyelinating and inflammatory pathology seen in the multiple sclerosis cases imaged using the MALDI-MSI method.....	224
Figure 7.6. Pathological regions of interest quantified for relative amounts of cholesterol using MALDI-MSI.....	225
Figure 7.7. MALDI analysis and areas of quantification used for calculating relative cholesterol in multiple sclerosis tissue.....	226
Figure 7.8. MALDI analysis of control brain tissue and areas of quantification for calculating relative cholesterol.....	227
Figure 7.9. Quantifying cholesterol from regions of interest in human multiple sclerosis and control brain tissue.....	229
Figure 7.10. Identification of several masses using Metaspace database software.....	231
Figure 7.11. Dual mapping of two lipids of interest to explore the abundance across tissue.....	232
Figure 9.1. The TIC spectra from 17-minute run for (a) QC plasma, (b) pooled QC CSF, and (c) control brain tissue homogenate from Fraction 1.....	254
Figure 9.2. The TIC spectra from 17-minute run for (a) QC plasma, (b) pooled QC CSF, and (c) control brain tissue homogenate from Fraction 3.....	254

List of Tables

Table 1.1. A table of neurodegenerative diseases and the sterols they are associated with based on the literature	22
Table 2.1. A list of all solvents and reagents used within the project.....	68
Table 2.2. Referenced isotope-labelled standards used for the samples analysed.....	70
Table 2.3. Mass spectrometry methods for ITMS ³ fragmentation.....	83
Table 3.1. Demographics for CTX and control serum and CSF samples.....	95
Table 3.2. Demographics for CTX and control brain tissue.....	96
Table 3.3. Average values of sterols found in CTX and control serum/ plasma and CSF.....	114
Table 3.4. Average values of sterols found in CTX and control cerebrum brain tissue.....	116
Table 3.5. Average values of sterols found in CTX regional brain tissue.....	118
Table 4.1. Demographics of the Alzheimer's/ MCI brain tissue cohort.....	131
Table 4.2. Average values of cholesterol and oxysterols found in AD, MCI and CNTL brain tissue homogenates across total cohort (male and female)	140
Table 4.3. Average values of cholesterol and oxysterols found in AD, MCI and CNTL brain tissue homogenates in males only.....	142
Table 4.4. Average values of cholesterol and oxysterols found in brain homogenate cohort using <i>APOE</i> status grouping <i>APOE2</i> , <i>APOE3</i> and <i>APOE4</i> (male and female)	144
Table 4.5. Average values of cholesterol and oxysterols found in brain homogenate cohort using <i>APOE</i> status grouping <i>APOE2</i> , <i>APOE3</i> and <i>APOE4</i> (male only)	146
Table 5.1. Demographics of the multiple sclerosis and control brain sample cohort.....	161
Table 5.2. Average values of cholesterol and oxysterols found in multiple sclerosis and control brain tissue homogenates in total cohort.....	170
Table 7.1. Demographics of multiple sclerosis and control human brain tissue.....	213
Table 7.2. Full dataset of quantified cholesterol from Q150 ^{-/-} control mouse brain tissue.....	233
Table 7.3. Full dataset of quantified cholesterol from Q150 ⁺ disease mouse brain tissue.....	234
Table 7.4. Full dataset of quantified cholesterol from control human brain tissue.....	235
Table 7.5. Full dataset of quantified cholesterol from human multiple sclerosis brain tissue.....	236

Table 7.6. All masses identified in Metaspace from MALDI-MS data from a coronal rat brain section.....	237
Table 9.1. A table of all oxysterols quantified.....	255
Table 9.2. Full statistical normality test results from Alzheimer’s disease brain diagnosis grouping	267
Table 9.3. Full statistical normality test results from Alzheimer’s disease ApoE status grouping.....	268
Table 9.4. Full statistical normality test results from huma multiple sclerosis and control homogenate cohort.....	269
Table 9.5. Bartlett’s test results from one-way ANOVA test from multiple sclerosis homogenate tissue and corresponding controls.....	270
Table 9.6. Full statistical normality test results from the Q150+ and control mouse brain imaging data.....	270
Table 9.7. Full statistical normality test results from the multiple sclerosis and control human brain imaging data.....	271

List of Abbreviations

Italic font: gene name

Non-italic: enzyme name

Capital letters for gene/ enzyme name: mouse gene

First letter capitalised for gene/ enzyme: human gene

3 β -HCA - 3 β -hydroxycholestenoic acid

3 β ,7 α -diHCA - 3 β ,7 α -dihydroxycholestenoic acid

6 β -HC - 6 β -hydroxycholesterol

7-DHC – 7-dehydrocholesterol

7-OC – 7-oxocholesterol

7 α -HC – 7 α -hydroxycholesterol

7 α -HCO – 7 α -hydroxycholestenone

7 β -HC – 7 β -hydroxycholesterol

7 α H,3O-CA - 7 α -hydroxy-3-oxocholestenoic acid

7 α ,12-diHC – 7 α ,12-dihydroxycholesterol

7 α ,24-diHC – 7 α ,24-dihydroxycholesterol

7 α ,25-diHC - 7 α ,25-dihydroxycholesterol

7 α ,25-diHCO – 7 α ,25-dihydroxycholestenone

7 α ,(25R)26-diHC – 7 α ,(25R)26-dihydroxycholesterol

7 α ,(25R)26-diHCO – 7 α ,(25R)26-dihydroxycholestenone

20S-HC – 20S-hydroxycholesterol

22R-HC – 22R-hydroxycholesterol

24R-HC – 24R-hydroxycholesterol

24S-HC – 24S-hydroxycholesterol

24S,25-EC – 24S,25-epoxycholesterol

25-HC – 25-hydroxycholesterol

25-HCO – 25-hydroxycholestenone

(25R)26-HC/ 26-HC/ 27-HC – (25R)26-hydroxycholesterol

(25R)26-HCO – (25R)26-hydroxycholestenone
 9-AA – 9-aminoacridine
 α – alpha
 β - beta
 μg - micrograms
 ABC – adenosine triphosphase (ATP) -binding cassette
 ACAT – acyl-CoA cholesterol acyltransferase
 AD – Alzheimer’s disease
 AKR – aldo-keto reductase
 ALS – amyotrophic lateral sclerosis
 AP – atmospheric pressure
 APO/ Apo – apolipoprotein
 APP – amyloid precursor protein
 $\text{A}\beta$ – amyloid beta
 BACE1 – beta secretase 1
 BBB – blood-brain barrier
 CAG – cytosine-adenosine-guanine (glutamine amino acid)
 CDCA – chenodeoxycholic acid
 CHCA – α -cyano-4-hydroxycinnamic acid
 CH25H – cholesterol 25-hydroxylase
 ChEI – cholinesterase inhibitors
 CI – chemical ionisation
 CID – collision-induced dissociation
 CLU – clusterin
 CNS – central nervous system
 CO – cholesterol oxidase
 CoA – Coenzyme A
 COPII – coat protein complex II
 CSF – cerebrospinal fluid
 CSF1 – colony-stimulating factor 1

CTF – C terminus fragment
CTX – cerebrotendinous xanthomatosis
CXCR2 – interleukin 8 receptor/ CXC chemokine receptor 2
CYP – cytochrome P450
CYP51A1 – lanosterol 14 α -demethylase
Da - Dalton
DC – direct current
DD – disease duration
DESI – desorption electrospray ionisation
DHB – 2,5-dihydrobenzoic acid
DHCR7 – 7-dehydrocholesterol reductase
DHCR24 – 24-dehydroxycholesterol reductase
DMAPP – 3,3-dimethylallyl pyrophosphate
DMT – disease modifying therapy
DNMT1 – DNA methyltransferase 1
EADSA – enzyme assisted derivatisation for sterol analysis
EAE – experimental autoimmune encephalomyelitis
EASI – easy ambient sonic spray ionisation
EBI2 – Epstein-Barr virus induced receptor 2
EBV – Epstein-Barr virus
EC – epoxycholesterol
EDSS – expanded disability status scale
EI – electron ionisation
EOAD – early onset Alzheimer’s disease
ER – endoplasmic reticulum
ESI – electrospray ionisation
EtOH – ethanol
F - female
FDA – Food and drug administration
FPP – farnesyl pyrophosphate

FT – Fourier transform

GC – gas chromatography

GFAP – glial fibrillary acidic protein

GP – Girard P reagent

GPP – geranyl pyrophosphate

GPPS - geranyl pyrophosphate synthase

GPR183 – G protein coupled receptor 183

HC – hydroxycholesterol

HCA – hydrocholestenoic acid

HD – Huntington’s disease

Hdh – Huntington’s disease gene homolog

HDL – high density lipoprotein

HLA1 – human leukocyte antigen 1

HLB – hydrophilic-lipophilic-balanced

HMG - 3-hydroxy-3-methyl-glutarate

HMGCR – 3-hydroxy-3-methyl-glutaryl CoA reductase

HPLC – high-performance liquid chromatography

HSD3B7 – 3 β -hydroxysteroid dehydrogenase 7

HTT/Htt – huntingtin

ICR – ion cyclotron resonance

IL – interleukin

IMS – methylated industrial spirit

INSIG – insulin-induced gene

IPA – Propan-2-ol

IPP – isopentenyl pyrophosphate

IT – ion trap

ITO – indium tin oxide

KH₂PO₄ – potassium phosphate

KOH – potassium hydroxide

KR – Kandutsch-Russell

LC – liquid chromatography
LCAT – lecithin cholesterol acyl transferase
LDL/R – low-density lipoprotein/ receptor
LESA – liquid extraction for surface analysis
LFB – Luxol Fast Blue
LIT – linear ion trap
LOAD – late onset Alzheimer’s disease
LRP1 – LDLR related protein 1
LSS – lanosterol synthase
LXR – liver X receptor
M - male
 m/z – mass-to-charge ratio
MAG – myelin associated glycoprotein
MALDI – matrix-assisted laser desorption/ionisation
MAP – mitogen-activated protein
MARCH6 – membrane-associated RING finger-6
MCI – mild cognitive impairment
mHTT – mutant huntingtin protein
MeOH – methanol
mg – milligrams
mL - millilitres
MND – motor neuron disease
MOG – myelin oligodendrocyte glycoprotein
MRI – magnetic resonance imaging
mRNA – messenger ribonucleic acid (RNA)
MS – mass spectrometry/ mass spectrometer
MS/MS – tandem mass spectrometry
MSI – mass spectrometry imaging
MSⁿ – tandem mass spectrometry
MVA – mevalonate

MVAPP – mevalonate 3-phospho-5-pyrophosphate
 n – sample number
 NaOH – sodium hydroxide
 NFil – neurofilament protein
 NFTs – neurofibrillary tangles
 ng – nanograms
 Ng:YAG – neodymium-doped yttrium aluminium garnet
 NMDA – N-methyl-D-aspartate
 NP – normal phase
 NPC – Niemann-Pick C1
 NPC1L1 – Niemann-Pick-C1-like-1
 OH – hydroxyl
 PBS – phosphate-buffered saline
 PC – phosphatidylcholine
 PE - phosphatidylethanolamine
 PD – Parkinson’s disease
 PFA – paraformaldehyde
 PHFs – paired helical filaments
 PLP – proteolipid protein
 PMD – post-mortem delay
 PPMS – primary progressive multiple sclerosis
 PPAR – peroxisome proliferator-activated receptor
 PSEN1/2 – presenilin 1/2
 RCT – reverse cholesterol transport
 RF – radio frequency
 ROR – retinoic acid receptor (RAR)-related orphan receptor
 ROS – reactive oxygen species
 RP – reverse phase
 RRMS – relapsing-remitting multiple sclerosis
 RXRs – retinoid X receptors

S1P/S2P – site-1 protease/ site-2 protease
SCAP – SREBP cleavage activating protein
SERM – selective estrogen receptor modulator
SF – SuperFrost slides
SIMS – secondary ion mass spectrometry
SLOS – Smith-Lemli-Opitz syndrome
SM/ SQLE – squalene monooxygenase
SOAT1 – sterol O-acyltransferase 1
SPMS – secondary progressive multiple sclerosis
SPE – solid phase extraction
SPG5 –spastic paraplegia type 5
SQS/FDFT1 – squalene synthetase
SR-B1 – scavenger receptor B1
SRE – sterol regulatory element
SREBP – sterol regulatory element binding protein
TAGs – triacylglycerides
Th – T helper
TMS – trimethylsilyl
ToF – time of flight
ToF/ToF – tandem time of flight
TTP – time to progressive
TTW – time to wheelchair
UGT1A3 – Uridine diphosphate glucose (UDP)-glucuronosyltransferase 1A3
UHPLC – ultra high-performance liquid chromatography
UHR – ultra high resolution
WT – wild type
YAC – yeast artificial chromosome

Chapter 1: Introduction

1.1. Sterol molecules and their biochemistry

Sterols are a type of amphipathic lipid molecule under a subset of steroid molecules that contain a hydroxyl (OH) group on the 3 β position on the A-ring structure (see Figure 1.1), defined structurally around 70 years ago by Woodward and Bloch¹. Sterols are bioactive molecules derived from squalene and are important in several biochemical processes and pathways in both prokaryotes and eukaryotes², involved in many integral processes in the human body including their role in membrane fluidity³, cholesterol homeostasis, immunological regulation, major roles in the central nervous system (CNS) and more⁴⁻⁶. Although there are many sterol molecules known, in this thesis we will focus on cholesterol and its oxygenated derivatives, oxysterols.

1.1.1. Cholesterol

Cholesterol (cholest-5-en-3 β -ol) is the most recognised sterol molecule, and is a vital lipid for cell membrane function, the precursor to bile acid and steroid synthesis, and is involved in other important biological processes especially in the central nervous system (CNS)⁷.

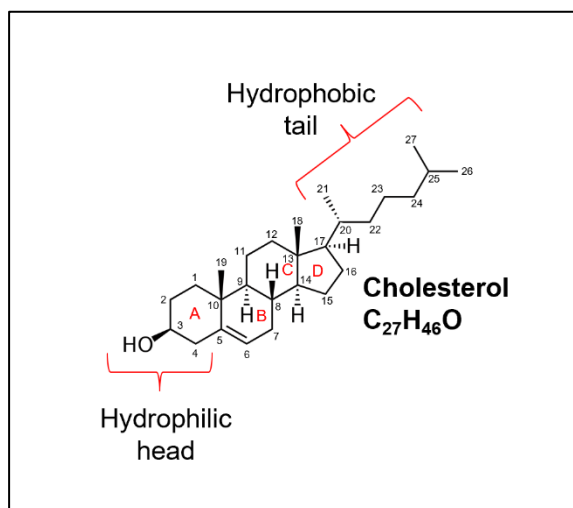


Figure 1.1. The amphipathic nature of cholesterol. This figure details the hydrophobic and hydrophilic properties of sterol molecules, using cholesterol as an example. The figure also details the four-ring core structure within the molecule.

Cholesterol is a stable neutral molecule and comes in two forms within the body; esterified and unesterified with excess free/unesterified cholesterol converted to the

esterified form as storage via the enzyme acyl-CoA cholesterol acyltransferase (ACAT) in the endoplasmic reticulum of the cell, or by lecithin cholesterol acyl transferase (LCAT) found in high density lipoprotein (HDL) particles in plasma. De novo synthesis of cholesterol transpires via a large cascade of reactions known as the mevalonate pathway and, although most cells have the capability to synthesise it, mainly occurs in the liver, intestines, and within the brain⁷.

Cholesterol synthesis begins with acetyl co-enzyme A (CoA) (see the pre-squalene pathway (blue colour) in Figure 1.2). Several acetyl CoA molecules are combined to form 3-hydroxy-3-methylglutarate (HMG)-CoA with the aid of HMG-CoA synthase enzyme. A further Acetyl-CoA is added via HMG-CoA reductase (HMGCR) enzyme to produce mevalonate (MVA). In a multistep reaction, mevalonate is converted into mevalonate 3-phospho-5-pyrophosphate (MVAPP), then converted to isopentenyl pyrophosphate (IPP). The IPP can get converted to 3,3-dimethylallyl pyrophosphate (DMAPP) first before conversion to geranyl pyrophosphate (GPP), or this step can be direct via the GPP synthase enzyme (GPPS). With the addition of IPP, GPP is synthesised to farnesyl pyrophosphate (FPP) by an enzymatic reaction with FPP synthase. For sterol synthesis, the pathway then results in the formation of squalene with an additional FPP molecule and using the enzyme squalene synthetase (SQS), followed by the formation of lanosterol (the post-squalene pathway in red in Figure 1.2).

Cholesterol can be synthesised via two different pathways, the Bloch pathway and the Kandutsch-Russell pathways (KR) (see Figure 1.2), with different cell types using different pathways. The Bloch pathway uses desmosterol as an intermediate before using the 24-dehydroxycholesterol reductase (DHCR24) enzyme to synthesise cholesterol. The KR pathway uses 7-dehydrocholesterol (7-DHC) as an intermediate in a multistep process before the final conversion to cholesterol using the enzyme 7-dehydrocholesterol reductase (DHCR7).

A hybrid pathway has more recently been discovered, named the modified Kandutsch-Russell pathway where synthesis begins with the Bloch pathway before shifting to KR via zymosterol/lathosterol (see Figure 1.3.)⁸⁻¹⁰.

The final step of cholesterol production via the KR pathway (the conversion from 7-dehydrocholesterol via the enzyme DHCR7) has shown to be defective in individuals diagnosed with Smith-Lemli-Opitz syndrome (SLOS), resulting in malformations as a result of decreased cholesterol levels¹¹. Cholesterol can be obtained from the diet or

synthesised within the body, which work in tangent to ensure sufficient levels are available¹². If cholesterol is found to be in excess, there are mechanisms that convert the excess cholesterol to other sterol molecules, known as oxysterols, and subsequently to bile acids.

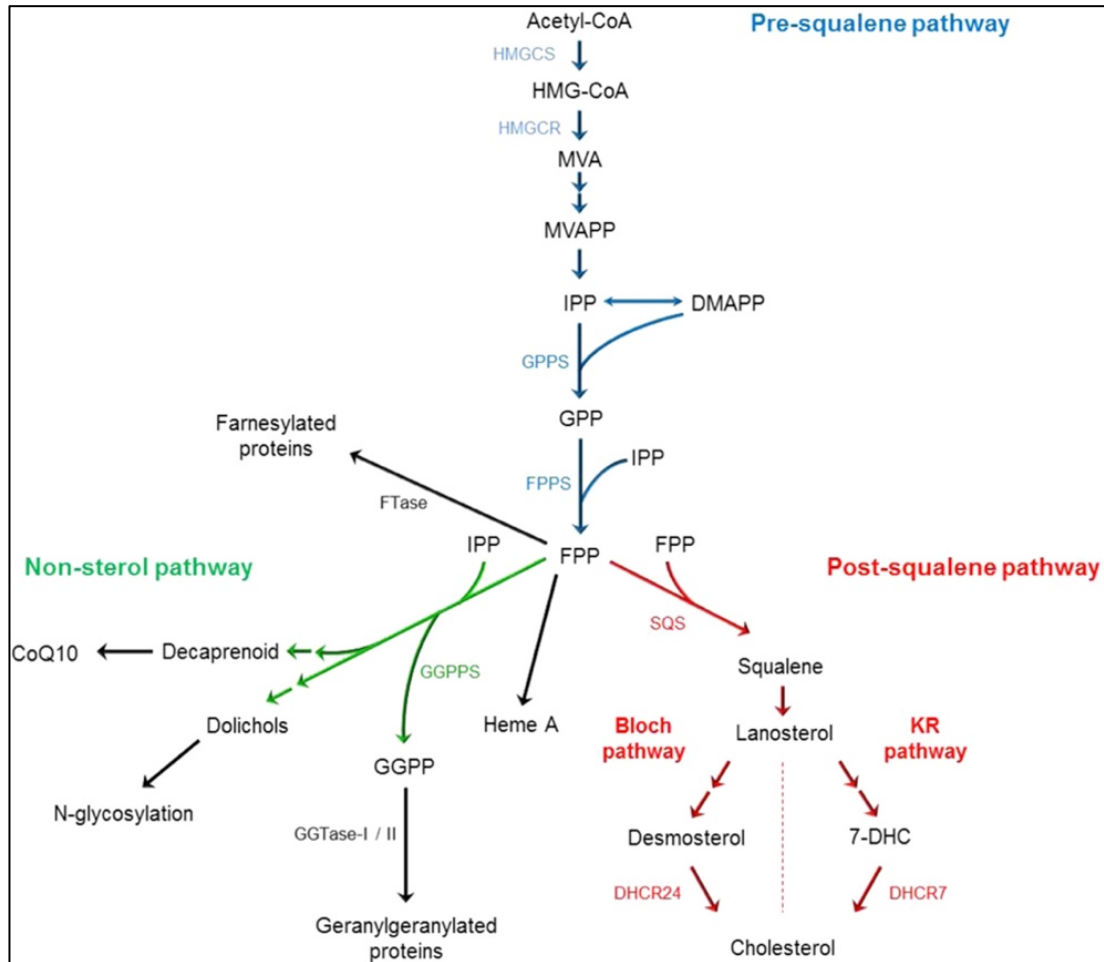


Figure 1.2. The mevalonate pathway. This pathway shows the process of synthesising cholesterol from acetyl Co-A¹³. Obtained with permission from the Experimental Cell Research journal.

1.1.2. Oxysterols

Oxysterols are the oxygenated derivatives of cholesterol, where an additional hydroxyl, ketone or epoxy group is added to either the hydrophobic tail or ring structure, making them more hydrophilic in comparison to cholesterol. Oxysterols are a large subgroup of lipids, used to regulate cholesterol across the body via the flux conversion to several oxysterols. Originally oxysterols were thought to be exclusively intermediates in the bile acid and steroid hormone synthesis pathways.

However, in recent decades there has been overwhelming evidence to support the narrative that many oxysterols are bioactive and influence important factors within the body¹⁴ including in immunology and development^{5,15,16}, and have been associated with numerous diseases including cancer, heart disease and several different neurodegenerative diseases^{17–24}.

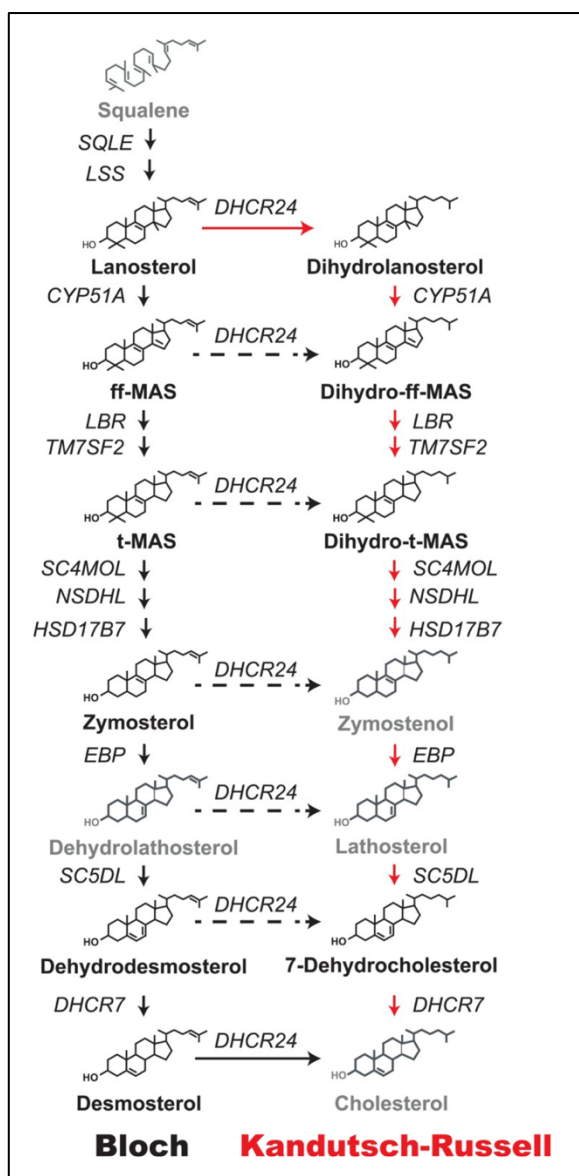


Figure 1.3. The Bloch and Kandutsch-Russell pathways for the synthesis of cholesterol. Image taken with permission from the eLife journal from Mitsche, 2015¹⁰.

There are several different biosynthesis pathways for oxysterols via enzymatic or non-enzymatic reactions, where often hydroxylation on the ring structures are non-enzymatic and hydroxylation of the side chains occur via cytochrome P-450 (CYP) enzyme-catalysed reactions²⁵. Non-enzymatic reactions include auto-oxidation via

reactive oxygen species (ROS), which primarily occurs in the C4, C5, C6 and C7 position of cholesterol resulting in products including 4 α -hydroxycholesterol (4 α -HC; cholest-5-en-3 β ,4 α -diol), 7 α -hydroxycholesterol (7 α -HC; cholest-5-en-3 β ,7 α -diol), 7 β -HC (cholest-5-en-3 β ,7 β -diol) and 7-ketocholesterol, or 7-OC (3 β -hydroxycholest-5-en-7-one)^{25–27} (see Figure 1.4 for structures and exact masses).

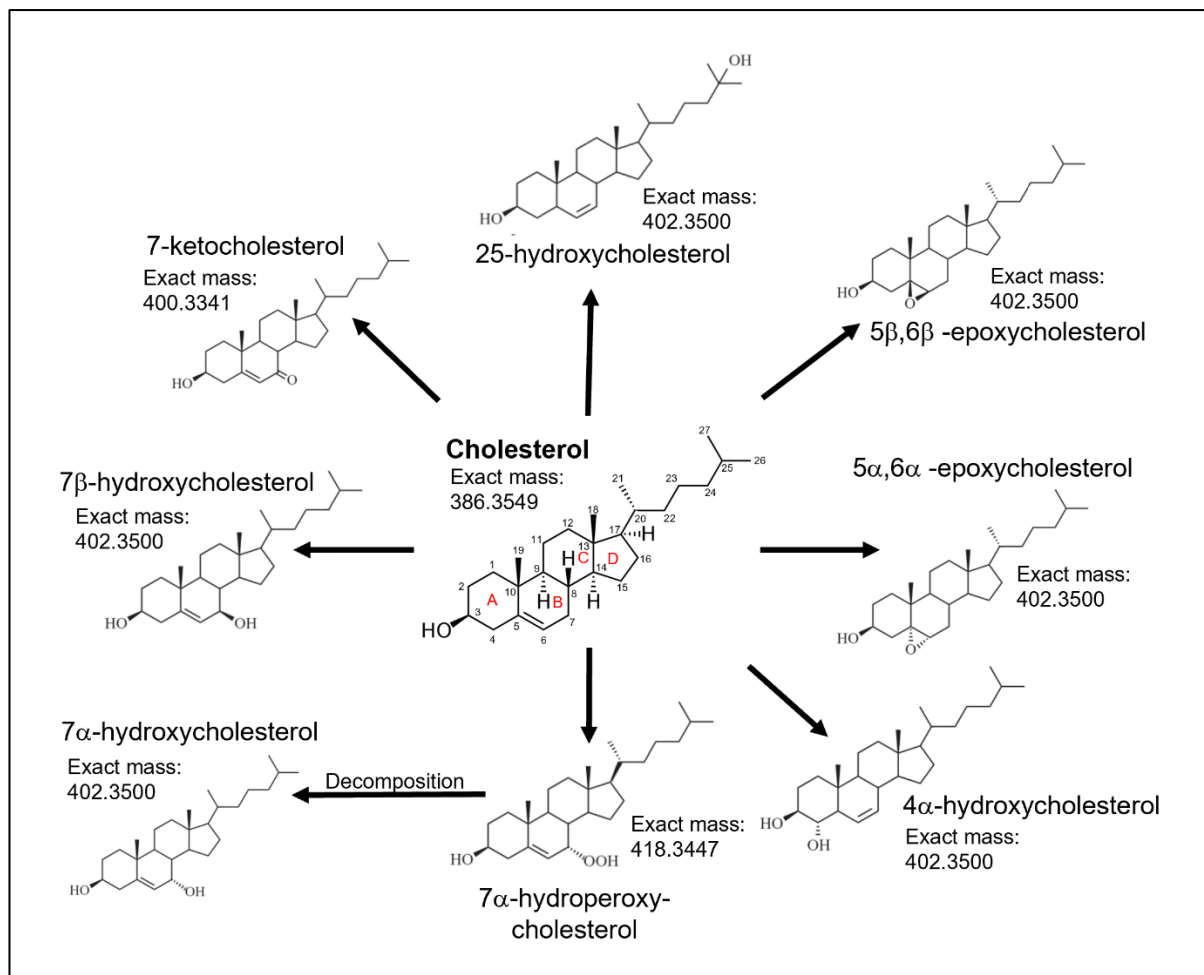


Figure 1.4. The formation of several oxysterols from cholesterol via reactive oxygen species (ROS) reactions. Structural images were taken from Samadi *et al.*, 2020²⁸, with permissions obtained from the Current Medicinal Chemistry journal.

The production of 7 α -HC can also occur from an enzymatic reaction using cholesterol with CYP7A1 which is the first step of the classical, or neutral, pathway (blue coloured pathway in Figure 1.5) of bile acid biosynthesis, catalysing hydroxylation in the C7 position on the B ring. The complete pathway (shown in Figure 1.5) then forms a keto group on the C3 via 3 β -hydroxysteroid dehydrogenase 7 (HSD3B7) enzyme to form 7 α -hydroxycholestenone (7 α -hydroxycholest-4-en-3-one). The next step of the reaction is the addition of a hydroxyl group to the C12 via

enzyme CYP8B1 to form $7\alpha,12\alpha$ -dihydroxycholestenone ($7\alpha,12\alpha$ -dihydroxycholest-4-en-3-one). This is followed by the removal of the double bond and addition of a hydrogen between C4 and C5 using aldo-keto reductase (AKR) 1D1 enzyme to synthesise $7\alpha,12\alpha$ -dihydroxy- 5β -cholestan-3-one. This product can be further converted to 5β -cholestane- $3\alpha,7\alpha,12\alpha$ -triol via AKR1C4 enzyme. All these products can be further converted via enzymatic reactions with CYP27A1 to form products of the acidic pathway (red pathway in Figure 1.5).

The acidic pathway begins via the hydroxylation of cholesterol on the C26 carbon using the CYP27A1 enzyme synthesising (25R)26-HC (cholest-5-en- 3β , (25R)26-diol). This molecule is more commonly referred to as 27-HC in the literature due to the positioning of the hydroxylation however this is not structurally accurate. The hydroxylation occurs on C26 position and induces stereochemistry (25R), resulting in the accurate name of (25R)26-HC^{29,30}. After this initial step, the pathway is split into two; the (25R)26-HC can be converted to 7α , (25R)26-dihydroxycholesterol (7α , (25R)26-diHC) via the addition of a hydroxyl group to the C7 using enzyme CYP7B1, followed by the conversion of the 3β -hydroxyl group to a ketone group via HSD3B7 enzyme to form 7α , (25R)26-dihydroxycholest-4-en-3-one (7α , (25R)26-diHCO).

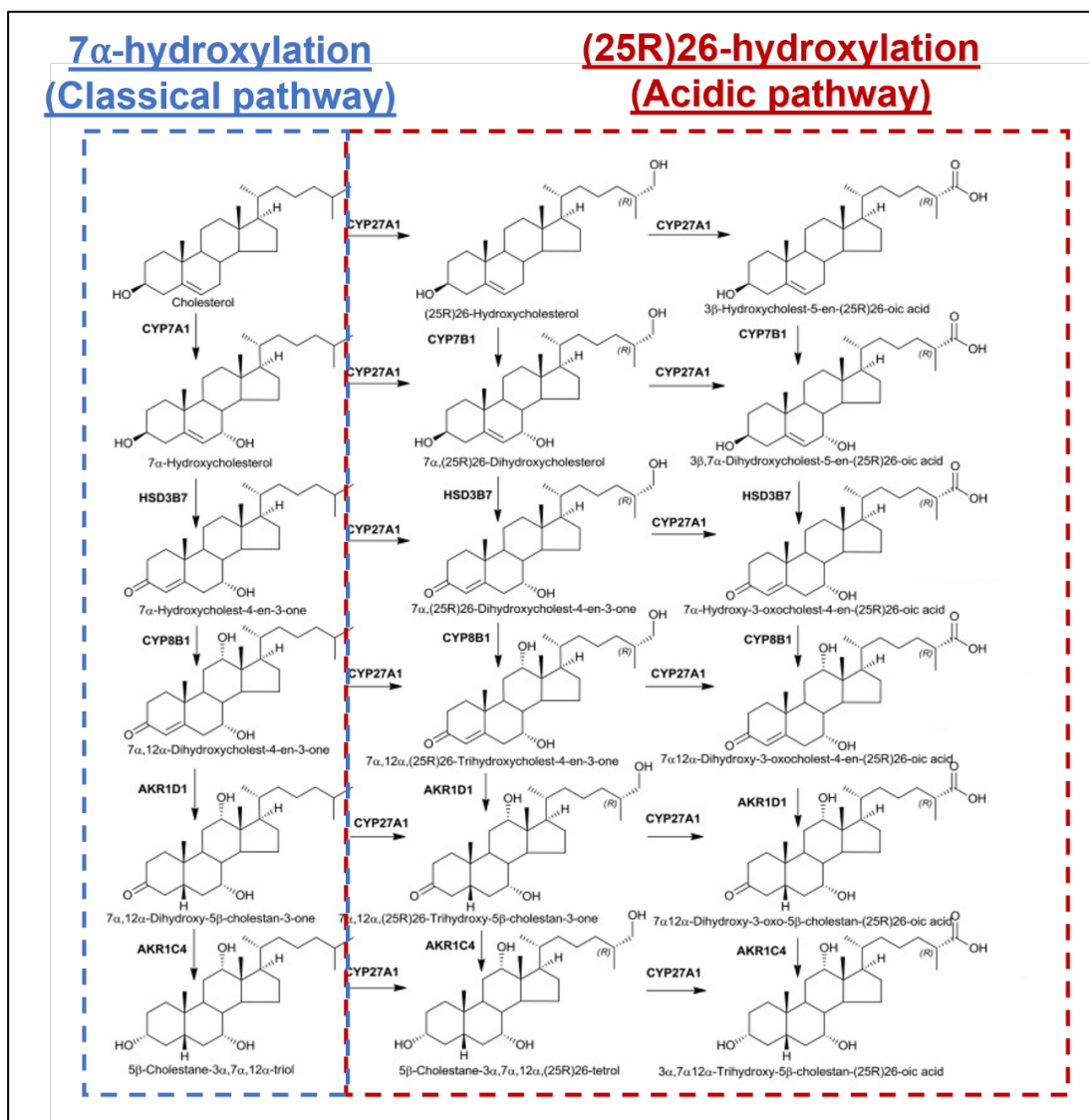


Figure 1.5. The classical (7 α -hydroxylation) and alternative/acidic ((25R)26-hydroxylation) oxysterol biosynthesis pathways³⁰. Taken with permission from the Prostaglandins & Other Lipid Mediators journal.

This can be further converted to 7 α ,12 α , (25R)26-trihydroxycholest-4-en-3-one by the addition of a hydroxyl group on the C12 via enzyme CYP8B1. The removal of the double bond and addition of a hydrogen between C4 and C5 using the AKR1D1 forms 7 α ,12 α , (25R)26-trihydroxy-5 β -cholestan-3-one (see Figure 1.5). The 3-keto group can then be converted back to a 3 β -hydroxyl using AKR1C4 enzyme to form 5 β -cholestane-3 α ,7 α ,12 α , (25R)26-tetrol. All these metabolites from the first part of the acidic pathway can be further converted using CYP27A1 to the metabolites from the second part of the pathway.

The second section is the formation of the carboxylic acids, of which the pathway is named after. The first step is the formation of 3 β -hydroxycholest-5-en-(25R)26-oic acid (3 β -HCA) via the addition of a ketone to C26 using enzyme CYP27A1. An additional hydroxyl group is added to the C7 position using CYP7B1 to form 3 β ,7 α -dihydroxycholest-5-en-(25R)26-oic acid (3 β ,7 α -diHCA). The 3 β -hydroxyl group is converted to a 3-ketone group using HSD3B7 to form 7 α -hydroxy-3-oxocholest-4-en-(25R)26-oic acid (7 α H,3O-CA). The addition of a hydroxyl group to the C12 position using CYP8B1 forms 7 α ,12 α -dihydroxy-3-oxocholest-4-en-(25R)26-oic acid. This is further converted to 7 α ,12 α -dihydroxy-3-oxo-5 β -cholestan-(25R)26-oic acid due to the removal of the double bond and addition of a hydrogen between C4 and C5 from the AKR1D1 enzyme. The formation of 3 α ,7 α ,12 α -trihydroxy-5 β -cholestan-(25R)26-oic acid is the next step, from the conversion of the 3-ketone back to a 3 β -hydroxyl group via the AKR1C4 enzyme. These pathways centre around the use of enzyme CYP27A1 for the addition of either a hydroxyl or ketone group to the 26-carbon, of which (25R)26-HC is the first metabolite.

(25R)26-HC is the most abundant side-chain oxysterol found in human plasma and has been shown to be implicated in human cancer^{18,31}. It was the first naturally occurring selective estrogen receptor modulator (SERM) founded in 2007³², and inhibits the cardiovascular effects of estrogen by inhibiting the production of nitric oxide in vascular cells. From its founded effects in the cardiovascular system, further research showed its importance in cancer, with (25R)26-HC shown to upregulate gene transcription and cell proliferation in cellular models of breast cancer¹⁷ and prostate cancer³³. In addition to its role in cancer, (25R)26-HC, 3 β -HCA and 3 β ,7 α -diHCA have effects on neurons in motor neuron disease (MND), with 3 β -HCA having neurotoxic and 3 β ,7 α -diHCA having neuroprotective effects on motor neurons in mouse models of *SPG5* MND³⁴. Increased (25R)26-HC levels in the CSF is also associated with a defective blood-brain barrier (BBB) due to increased influx from the periphery, which is common in a number of neurological diseases³⁵.

The CYP27A1 enzyme is linked with the genetic disorder cerebrotendinous xanthomatosis (CTX), where a mutation in *CYP27A1* gene causes limited or complete loss of function of the subsequent enzyme, resulting in major reductions in the intermediate and final products of the acidic pathway chenodeoxycholic acid (CDCA) (see Figure 1.6 for structure), with treatment options centring around the

replacement of CDCA. In CTX, the classical pathway side-product cholestanol is shown to be significantly increased due to the downregulation of the acidic pathway³⁶.

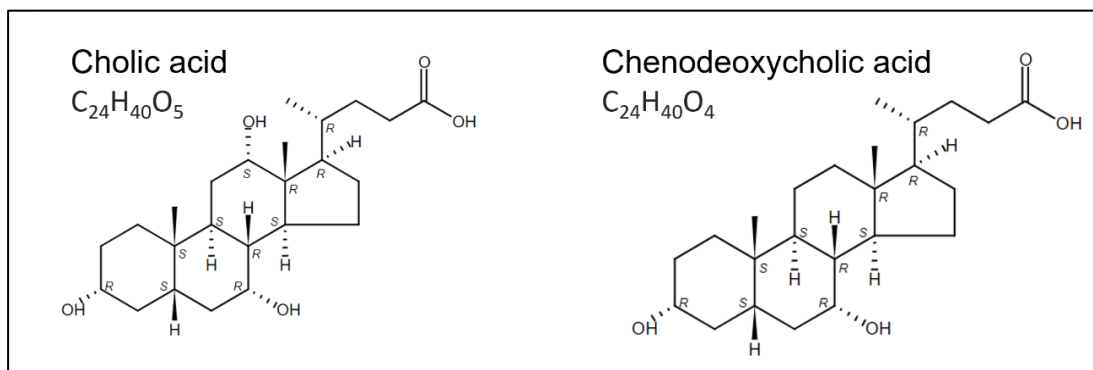


Figure 1.6. The molecular structures of cholic acid and chenodeoxycholic acid.

Other important pathways include the 25-hydroxylation pathway (see purple coloured pathway in Figure 1.7), which relies on the instigation of cholesterol hydroxylation using the CH25H enzyme to convert cholesterol into 25-HC (cholest-5-en-3 β ,25-diol) by the addition of a hydroxyl group to the 25th carbon (C25) but can also be synthesised non-enzymatically via ROS³⁷. The next step of the pathway is the formation of 7 α ,25-dihydroxycholesterol (7 α ,25-diHC) by the addition of a hydroxyl group to the C7 via the CYP7B1 enzyme. 7 α ,25-diHC is then converted to 7 α ,25-dihydroxycholest-4-en-3-one (7 α ,25-diHCO), where the 3 β -hydroxyl group is converted to a 3-ketone group via the HSD3B7 enzyme. This can then be converted either to 7 α ,25-dihydroxy-3-oxocholest-4-en-26-oic acid by the addition of a ketone group to C26 via CYP27A1, or the addition of a hydroxyl group to the C12 position and subsequent conversion to 7 α ,12 α ,25-trihydroxycholest-4-en-3-one using the CYP8B1 enzyme. This metabolite can be further converted to 7 α ,12 α ,24,25-tetrahydroxycholest-4-en-3-one using enzyme CYP3A4 to add a hydroxyl group to C24. The hydroxyl group at C24 is then converted to a ketone group using enzymes AKR1D1 and AKR1C4, synthesising 7 α ,12 α ,25-trihydroxycholest-4-en-3,24-dione. An acetone group (C₃H₆O) is then removed from the structure using the same enzyme combination to form 7 α ,12 α -dihydroxy-3-oxochol-4-en-24-oic acid. The final step of the pathway is the formation of cholic acid (full structure found in

Figure 1.6) via the two enzymes used in the previous steps, AKR1D1 and AKR1C4, which is a primary bile acid³⁸.

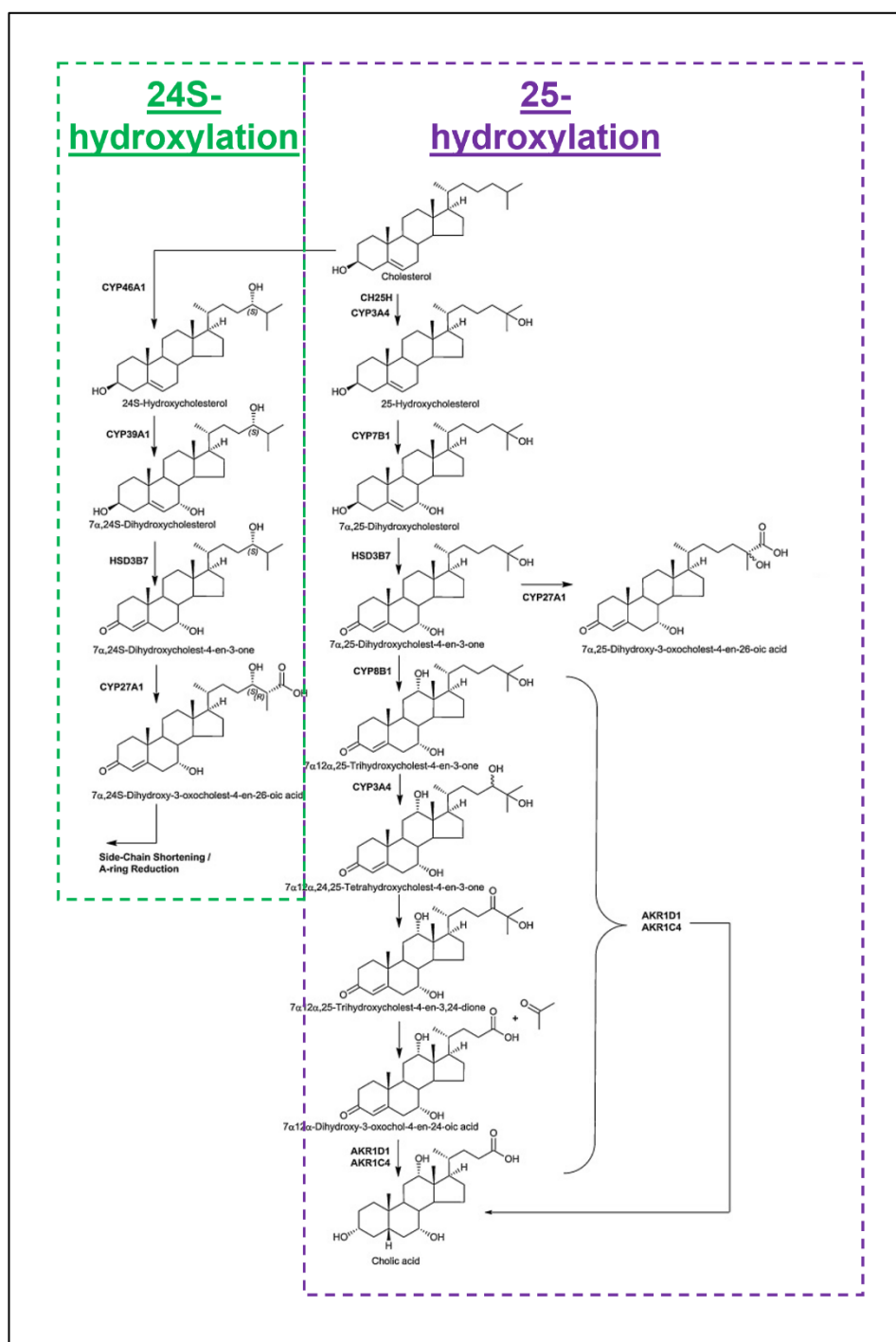


Figure 1.7. The cerebral, or 24S-hydroxylation, and 25-hydroxylation pathways³⁰. Taken with permission from the Prostaglandins & Other Lipid Mediators journal.

Certain metabolites of the 25-hydroxylation pathway are known to be biologically active, with both 25-HC and 7 α ,25-diHC have been shown to play a crucial role in

both the innate and adaptive immune system³⁹. The cholesterol 25 hydroxylase (*CH25H*) gene, which is responsible for hydroxylation at C25, has shown to be upregulated in both macrophage and dendritic cells when exposed to inflammatory mediators⁴⁰, with 25-HC found to regulate immunoglobulin A production⁴¹ and mediate the inhibition of the interleukin-1 family cytokine production pathway⁴², both of which are important in the response to infection. In addition, 7 α ,25-diHC is proven to be a potent ligand of G protein coupled receptor 183 (GPR183), also known as Epstein-Barr virus induced receptor 2 (EBI2)¹⁶, which when activated direct the migration of activated B cells to follicles which can be found in various autoimmune diseases^{43–46}.

The final pathway is the 24-hydroxylation, or cerebral, pathway named from the almost exclusive biosynthesis of the primary pathway intermediates within the brain (see green coloured pathway in Figure 1.7). The first stage is the conversion of cholesterol to 24S-HC (cholest-5-en-3 β ,24S-diol) via the CYP46A1 enzyme which almost exclusively expressed in neuronal cells in the cortical and deep grey matter structures of the brain, and has a major role in cholesterol homeostasis within the brain⁴⁷. 24S-HC is then converted into 7 α ,24S-dihydroxycholesterol (7 α ,24S-diHC) by the addition of a hydroxyl group to the C7 position via the CYP39A1 enzyme (see Figure 1. 7) for excretion⁴⁸. 7 α ,24S-diHC can be further converted to 7 α ,24S-dihydroxycholest-4-en-3-one with the 3 β -hydroxyl group converted to a 3-ketone group via the HSD3B7 enzyme. This metabolite can then undergo the addition of a ketone group onto the C26 position via the CYP27A1 enzyme to form 7 α ,24S-dihydroxy-3-oxocholest-4-en-26-oic acid.

Another oxysterol of note which has not been shown in any of these pathways is 24S,25-epoxycholesterol, or 24S,25-EC (3 β -hydroxycholest-5-en-24S,25-epoxide). It is unique in that it can be formed in parallel to cholesterol via the shunt of the mevalonate pathway (see Figure 1.8). Squalene gets converted to squalene-2,3(S);22(S),23-dioxide via squalene monooxygenase enzyme (SQLE), then further converted to the intermediate 24S,25-epoxylanosterol³⁰ by conversion with the lanosterol synthase (LSS) enzyme. A further multi-step reaction synthesises 24S,25-EC, however it can also be synthesised by the C24 hydroxylation of desmosterol via a CYP46A1 enzymatic reaction. 24S,25-EC has been shown to isomerise to 24-oxocholesterol during sample preparation⁴⁹. 24S,25-EC is a potent ligand for Liver X

receptors (LXRs), which are transcription factors that regulate the transcription of genes crucial for the biosynthesis, metabolism, and excretion of cholesterol⁵⁰.

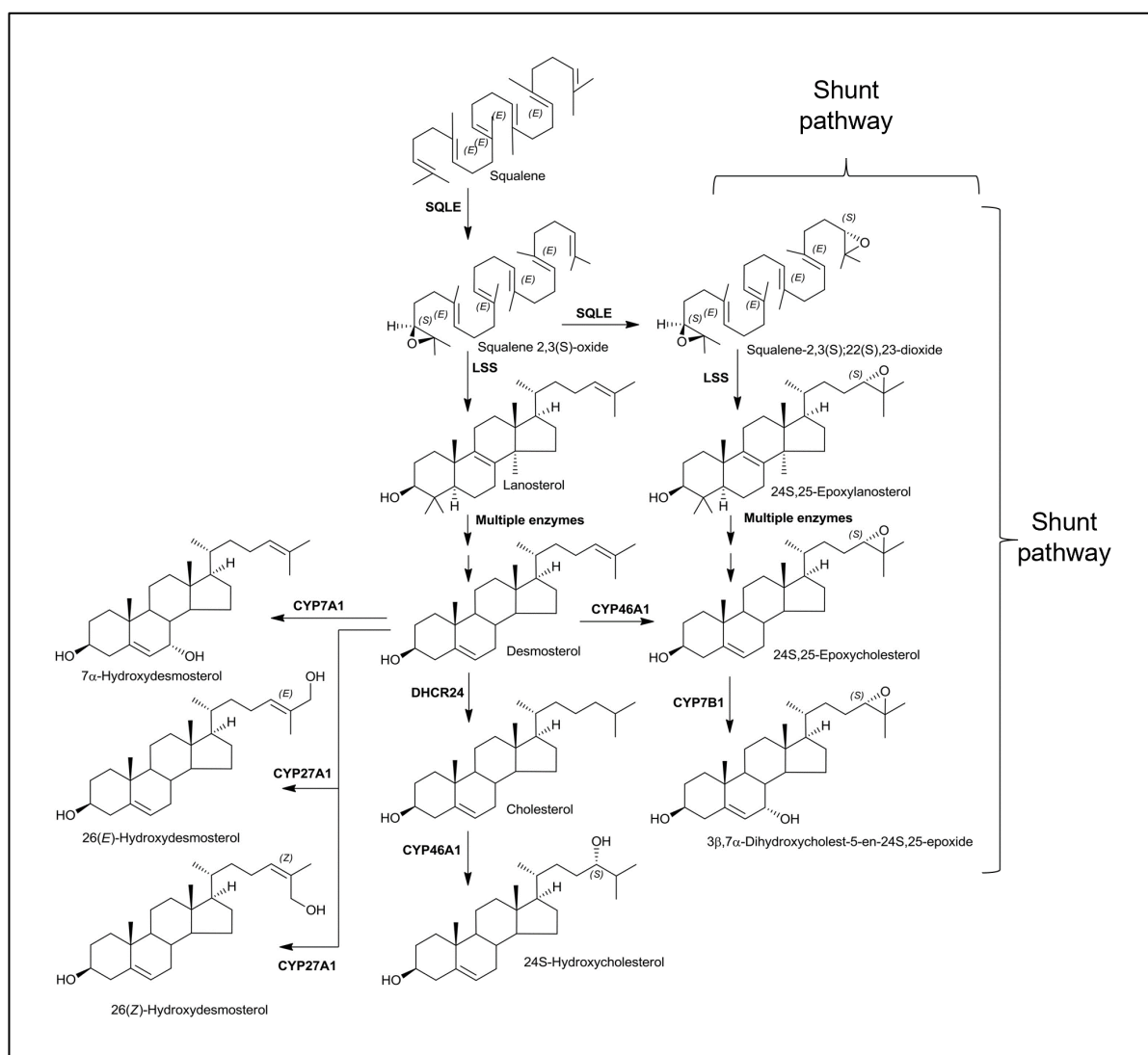


Figure 1.8. The synthesis of 24S,25-epoxycholesterol via a parallel pathway to cholesterol biosynthesis³⁰. Taken with permission from the Prostaglandins & Other Lipid Mediators journal.

1.2. Oxysterols and their bioactivity

Oxysterols are very important molecules throughout the body and are involved in many vital biological processes including cholesterol homeostasis, immunological responses, biological pathways within cancer cells and many crucial pathways in the brain. They act as ligands to several different transcription factors and are

responsible for the up- and down-regulation of important genes linked to cholesterol synthesis, transport and metabolism.

1.2.1. Sterols and cholesterol homeostasis

One of the main roles of oxysterols is their function in regulating cholesterol homeostasis in cells. Cholesterol has a diverse range of functions in the body, including involvement in cell membranes, cell signalling and is the precursor for bile acids and steroid hormones as well as oxysterols themselves. Cholesterol can be absorbed into intestinal cells from the diet via Niemann-Pick-C1-like-1 (NPC1L1) protein⁵¹ or synthesised within the cell itself, but oxysterols play a vital role in making sure excess cholesterol doesn't build up within cells. There are two main processes used for regulation which rely on transcription factors controlling gene expression of lipid biosynthesis genes, using either the sterol regulatory element binding protein (SREBP) or LXRs.

The SREBP route controls the feedback pathway that influences cholesterol biosynthesis and uptake of cholesterol from outside the cell. There are three members of the SREBP family, SREBP1a, SREBP1c and SREBP2, with SREBP2 responsible for cholesterol biosynthesis and homeostasis⁵². SREBP2 is an endoplasmic reticulum (ER) protein consisting of an N-terminal transcription factor domain containing two transmembrane segments separated by a lumen-facing loop, and a C-terminal regulatory domain that interacts with the SREBP cleavage activating protein (SCAP)⁵³.

For activation, SREBP2 must be relocated to the Golgi apparatus. When cholesterol in the ER is depleted, loops 1 and 7 of SCAP interact resulting in a closed formation of SCAP with the dissociation of INSIG via INSIG1 ubiquitination⁵⁴. This allows COPII vesicles to bind to SCAP and transport the SREBP2/SCAP complex to the Golgi (see Figure 1.9 a).

two proteases (S1P and S2P) cleave SREBP2 in the Golgi, releasing the N-terminal fragment (nSREBP2) which enters the nucleus of the cell, binding to sterol regulatory elements (SRE) to activate the transcription of target genes (see Figure 1.9 a) that code for several mevalonate pathway enzymes, including HMGCR, mevalonate kinase, squalene monooxygenase (SM), and additionally regulates the gene for the LDL receptor (LDLR) which controls cholesterol uptake^{4,55,56}.

When cholesterol levels are in excess, some newly synthesised oxysterols such as 25-HC bind to insulin-induced genes (INSIGs) which in turn binds to SCAP, dissociating loops 1 and 7 of SCAP, resulting in an open formation and prevents the binding of coat protein complex II (COPII) vesicles⁵⁷ (see Figure 1.9 b). This results in the SREBP2/SCAP complex being retained within the ER and subsequently the deactivation of cholesterol biosynthesis gene transcription (see Figure 1.9 b). Cholesterol itself can also deactivate this pathway but by binding to SCAP rather than INSIGs, but similarly retaining the SREBP2/SCAP in the endoplasmic reticulum.

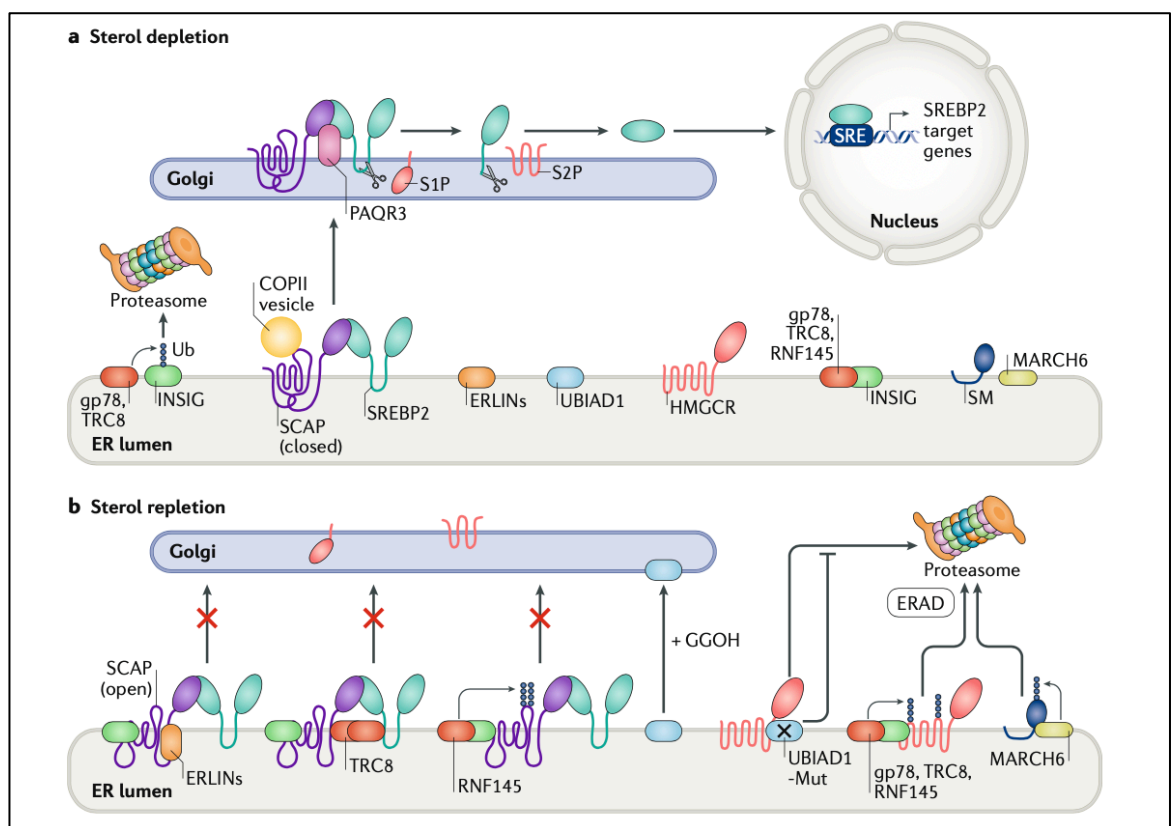


Figure 1.9. Schematic of the SREBP2/SCAP mechanism⁴. The SREBP2/SCAP mechanism shown is responsible for the upregulation of specific cholesterol biosynthesis genes via interactions with INSIG, where a) shows what happens with sterol depletion, and b) shows sterol repletion. Taken with permission from the Nature Reviews Molecular Cell Biology journal.

While SREBP2 is involved in the up-/ down-regulation of cholesterol biosynthesis genes, LXRs are involved in cholesterol elimination including bile acid synthesis,

metabolism, reverse cholesterol transport and cholesterol absorption/excretion, and are generally used to decrease the cellular cholesterol content.

Oxysterols are natural ligands to LXRs, including 24S-HC, 22R-HC, (25R)26-HC, 24S,25-EC and 20S-HC (of which its mechanism of synthesis is currently unknown). 24S,25-EC is a highly potent ligand for LXRs, meaning its binding affinity is far greater compared with other oxysterol ligands. When cellular cholesterol is in excess and subsequently oxysterol levels are increased, their binding to LXRs causes up/downregulation of many key enzymes in cholesterol synthesis and metabolism including CYP7A1 in mouse, UDP-glucuronosyltransferase-1A3 (UGT1A3), NPC1L1, and many of the ATP-binding cassette (ABC) transporters including ABCG5, ABCG8 and ABCA1.

Activated LXR α can stimulate the expression of CYP7A1 in rodents, the enzyme responsible for C7 hydroxylation of cholesterol to synthesise oxysterol 7 α -HC and upregulating the classical pathway to lower the levels of cellular cholesterol present⁵⁸. However, in primary human hepatocytes the activation of LXR α suppresses the expression of CYP7A1⁵⁹. LXR α also upregulates human UGT1A3 which aids bile acid excretion via the urine by glucuronide conjugation⁶⁰. In addition to these two examples, activation of both LXR isoforms also upregulate the transcription of all ABC transporters mentioned above, which work in exporting cholesterol out of the cell and back into the circulation via reverse cholesterol transport (RCT)^{61–63}, which is the process of cholesterol excretion via the liver. LXRs have a key role in regulating ABCA1, ABCG1 and apolipoprotein E (ApoE) proteins to further transport cholesterol from the periphery to the liver for faecal excretion⁵⁰.

Activated LXR α has also shown to have a suppressive effect on two key enzymes in the cholesterol biosynthesis pathway, with both SQS (also referred to as FDFT1) and lanosterol 14 α -demethylase (CYP51A1) genes negatively regulated by LXR α ⁶⁴.

Oxysterols can also influence the transcription of other rate-limiting cholesterol biosynthesis genes such as HMGCR. With high cellular cholesterol concentrations and subsequently increased oxysterol levels, specific molecules including 24S-, 25- and (25R)26-HC can induce the binding of HMGCR to INSIG-1 and as discussed above block the transport of the SREBP-SCAP complex to the Golgi. Oxysterol induced binding of INSIG to HMGCR induces the ubiquitination of the enzyme and results in the degradation of HMGCR, effectively reducing the rate of cholesterol

synthesis⁶⁵. Squalene monooxygenase (SM) is also controlled in a similar way, however uses cholesterol instead of oxysterols to induce ubiquitination and degradation of SM which is mediated by membrane-associated RING finger-6 (MARCH6), an ubiquitin ligase (see Figure 1.9b)⁶⁶.

As well as biosynthesis pathways, cells can uptake cholesterol from the circulation in the form of low-density lipoprotein (LDL) particles when intracellular levels are lacking. The LDL receptors (LDLRs) sit on the surface of cells and bind with high-affinity to their counterparts; the LDLR-LDL complex is endocytosed into the cell with the LDL particle released and degraded to release the cholesteryl ester which is hydrolysed into free cholesterol^{67,68}. The free cholesterol can then be re-esterified via ACAT to form lipid droplets for storage, be used to synthesise steroid hormones or bile acids, or to act as a structural component of membranes⁶⁸. The expression of the LDLR is controlled via a negative feedback mechanism using cholesterol concentration within the cell. If cholesterol is in excess, the transcription of LDLR via SREBP-2 is downregulated; however, if cholesterol levels are depleted, LDLR transcription is induced to aid the restoration of cholesterol content⁵⁶.

To summarise, cholesterol homeostasis within a healthy individual is a culmination of many complex mechanisms, all working in tangent to ensure a satisfactory level of cholesterol is always present. The mechanisms cover synthesis of new cholesterol, uptake from the circulation from dietary cholesterol and the export and eventual excretion from the body. Oxysterols play a crucial role in these pathways, aiding to induce and inhibit the transcription of vital rate-limiting genes within the cholesterol synthesis and metabolism pathways and helping to regulate cholesterol concentration.

1.2.2. Oxysterols and immunology

In addition to being ligands for transcription factors in cholesterol homeostasis, oxysterols are also potent ligands for immunological-related factors including GPR183/ EBI2, CXC chemokine receptor 2 (CXCR2) and DNA methyltransferase 1 (DNMT1).

The GPR183/EBI2 is highly expressed in the spleen by several immune cells, including B cells, dendritic cells, T cells and brain specific glial cells including microglia and astrocytes^{43,69}. Two oxysterols, 7 α ,25-diHC and 7 α , (25R)26-HC, are

ligands for EBI2, with $7\alpha,25$ -diHC being the more potent¹⁶. The binding of $7\alpha,25$ -diHC to EBI2 has shown to have pro-inflammatory effects and stimulates the migration of EBI2-expressing B-, T- and dendritic cells^{43,70,71}. $7\alpha,(25R)26$ -HC has also shown to affect the migration of dendritic cells via EBI2, with CYP27A1 knockout mice experiencing altered dendritic cell migration and maintenance⁷². Another oxysterol involved in immunological responses is 25-HC, which has shown to be a potent antiviral agent by actively inhibiting viral entry, assembly and replication in cells via the effect on cholesterol concentration within the host cells plasma membrane and intracellular components^{15,73,74}. In addition to having anti-viral properties, 25-HC has been shown to have both pro- and anti-inflammatory effects on the immune response. Excess amounts of intracellular cholesterol trigger the activation of the inflammasome (a multiprotein complex responsible for stimulating the production of the pro-inflammatory interleukin (IL)-1 cytokine family) in macrophage cells and IL-1 β secretion⁷⁵. 25-HC works by binding to SREBP and repressing it, subsequently inhibiting cholesterol synthesis and reducing the intracellular levels. On the other hand, it can display pro-inflammatory effects in macrophage cells by stimulating IL-6 and colony-stimulating factor (CSF1) production⁷⁶. Another study showed mice deficient in *CH25H* gene showed less inflammation-induced lung damage after being presented with influenza, suggesting 25-HC is involved in the exacerbation of the immune response and subsequent damage witnessed in the wild-type mice⁷⁶.

1.3. Sterols in the brain

Sterols are highly abundant within the brain, with both oxysterols and cholesterol having major roles in cholesterol homeostasis within the brain and immune function. Cholesterol is important for cell membrane fluidity and is an abundant component of the myelin sheath, which is a lipid-rich substance made from both lipid and protein molecules. It is synthesised by oligodendrocyte cells for the insulation of nerve cells, forming sheaths around the nerve cell axonal tracts to help conduct signal transduction. Myelin sheaths account for around 80% of brain cholesterol in adult mice⁷⁷, and therefore are the major source for brain cholesterol.

In terms of oxysterols present in the brain, the most abundant by far is 24S-HC^{78,79}. The enzyme that synthesises 24S-HC from cholesterol is CYP46A1, which is almost

exclusive expressed in the nuclei of specific neuronal cells found in cortical and other grey matter structures within the brain^{80,81}. Neuron-derived 24S-HC acts almost as a sensor for cholesterol levels in astrocyte cells, and when concentrations are high 24S-HC can bind to INSIG to regulate cholesterol synthesis within the cell by reducing the transcription of cholesterol synthesis genes⁵⁷. Unlike cholesterol, 24S-HC can be exported across the blood-brain barrier (BBB) and into the periphery and this is one of the mechanisms of cholesterol management in the brain. (25R)26-HC can also be synthesised by neurons, astrocytes, and oligodendrocytes^{78,81,82}, although the levels of synthesis are extremely low. (25R)26-HC can be imported and excreted from the brain via the BBB²⁵. Sterols within the central nervous system are also involved in numerous other biosynthesis and signalling pathways and are crucial in cell membrane fluidity.

1.3.1. Cholesterol biosynthesis and regulation in the brain

Cholesterol is imperative in the brain, with an estimated 20% of the body's cholesterol found in the organ^{83,84}. Due to the inability of cholesterol or cholesterol carrying lipoproteins crossing the BBB, the majority of brain cholesterol is a result of *de novo* synthesis. This happens via neuronal cells (fundamental cells of the CNS; initiate action potentials for nerve signal transduction), oligodendrocytes (the key cells responsible for myelin synthesis) and astrocyte cells (fundamental for brain development and structure, and make up the protective blood-brain barrier)⁸⁵. The majority of brain cholesterol is predominantly synthesised by astrocytes and is controlled via regulation of cholesterol biosynthesis and transport genes using SREBP2 (see Figure 1.10).

Neurons are suggested to produce cholesterol via the KR pathway, with astrocytes using the alternative Bloch pathway for biosynthesis^{86,87}, however neurons have a much lower rate of synthesis in comparison to astrocyte cells and subsequently a lower capacity to deal with a lack of cholesterol in comparison to astrocytes⁸⁷, therefore cholesterol synthesis mainly occurs in astrocytes and is then transported to the neuron.

Cholesterol synthesis in astrocytes is controlled using the SREBP2/SCAP pathway within the ER of the cell from acetyl CoA, upregulating the transcription of cholesterol biosynthesis enzymes in the Bloch pathway when required. When being

transported to the neuron, the cholesterol is exported out of the astrocyte from ABCA1 and ABCG1 transporters, forms an HDL-like lipid complex with apolipoprotein E (ApoE) and binds to LDL receptor or LDLR related protein 1 (LRP1) on the neuron cell surface. The lipid complex is internalised, with the cholesterol being released into the cell to be used for membrane repair, myelin formation in oligodendrocytes and synaptogenesis⁸⁸. Excess cholesterol is then converted to 24S-HC via CYP46A1 in the neuron^{80,89}, which can freely cross the BBB unlike cholesterol itself and is excreted into the cerebrospinal fluid (CSF) or the peripheral blood (see Figure 1.10). 24S-HC (and (25R)26-HC) is also an LXR ligand and can upregulate some cholesterol transport genes including ABCA1 and ApoE when levels are high to increase export of cholesterol from the cell.

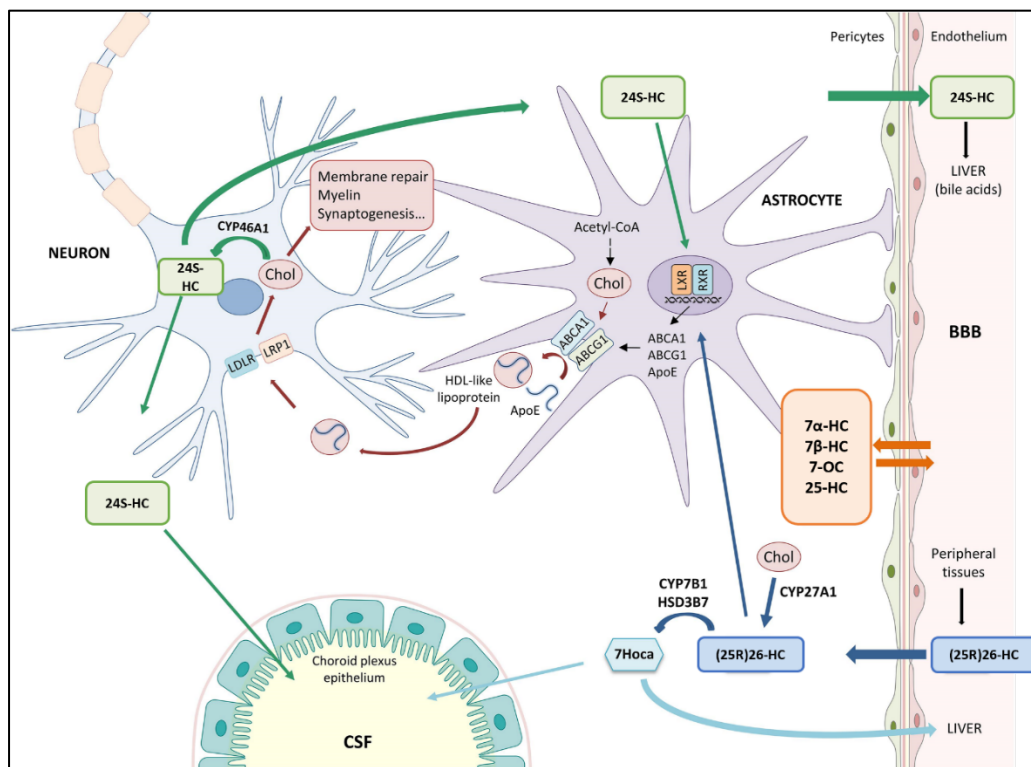


Figure 1.10. Cholesterol synthesis, transport, and turnover within the brain. Figure taken from Gamba et al, 2019⁹⁰. Taken with permission from the Frontiers in Neuroscience journal.

There are other methods of removing excess cholesterol from the neuron, including esterification and direct removal using ApoA1. The majority of synthesised cholesterol in the brain is in the non-esterified form, with only 1% as esterified, or stored, cholesterol in the form of lipid droplets²². This process takes place via the

enzyme sterol O-acyltransferase 1 (SOAT1/ACAT), which is usually activated when cholesterol content in the cells is in excess to prevent a toxic build-up of cholesterol. The next pathway is the excretion of cholesterol via the ABCA1 transporter, where it forms a complex with APOA1 and is suggested to be removed from the brain across the BBB via scavenger receptor B1 (SR-B1)⁹¹.

1.4. Neurodegeneration and its links to sterols

As previously mentioned, cholesterol and oxysterols are a major part of the central nervous system. Their association with neuronal cell bodies and numerous different glial cell types mean an increased likelihood that they are possibly involved or implicated in neurodegeneration and neurodegenerative mechanisms (see Table 1.1 for sterols and associated diseases).

Neurodegenerative diseases are one of the most prevalent disorders globally, covering a wide range of different disorders but generally result in the progressive structural and functional loss of neuronal cell bodies and their processes (dendrites, axons, and synapses), which transpire via several complex pathways, with many of these mechanisms not fully understood. These diseases cause neurological disability over time, including such symptoms as memory and cognitive dysfunction, irreversible decline, impairment, loss of motor functions (resulting in affected movement, speech and breathing, for example), sensory dysfunction (causing pain, loss of hearing, vision, or balance, for example) and changes in mood and personality (loss of inhibitions, anxiety, depression, feelings of euphoria or hopelessness)⁹².

Some of the most common neurodegenerative disorders include dementias such as Alzheimer's disease (AD), Parkinson's disease (PD), Huntington's disease (HD), and MND including amyotrophic lateral sclerosis (ALS). Although not typically viewed as a neurodegenerative disease, multiple sclerosis exhibits a profound and early neuron loss which ultimately determines the severity of disease outcome^{93,94}.

Although many of these diseases are associated with an age-dependent phenotype, there are several neurodegenerative diseases that can display at a much younger age including multiple sclerosis, Batten disease and HD. Within this thesis we have focused on sterol biology in AD, HD and multiple sclerosis and their experimental models.

Table 1.1. A table of neurodegenerative diseases and the sterols they are associated with based on the literature.

Disease	Affected sterols	References
Alzheimer's disease (AD)	24S-HC, (25R)26-HC,	Bretillon <i>et al</i> , 2000 ⁹⁵ Heverin <i>et al</i> , 2004 ⁹⁶ Leoni <i>et al</i> , 2004 ³⁵ Testa <i>et al</i> , 2016 ¹⁹
Parkinson's disease (PD)	Cholesterol, 24S-HC, (25R)26-HC	Bjorkhem <i>et al</i> , 2013 ⁹⁷ Doria <i>et al</i> , 2016 ⁹⁸ Guo <i>et al</i> , 2015 ⁹⁹
Multiple sclerosis	24S-HC, 25-HC, (25R)26-HC	Leoni <i>et al</i> , 2002 ¹⁰⁰ Leoni <i>et al</i> , 2004 ³⁵ Zhornitsky <i>et al</i> , 2016 ¹⁰¹ Crick <i>et al</i> , 2017 ²³
Huntington's disease (HD)	Cholesterol, 24S-HC	Valenza <i>et al</i> , 2007 ¹⁰² Valenza <i>et al</i> , 2010 ¹⁰³ Boussicault <i>et al</i> , 2016 ²⁴ Kacher <i>et al</i> , 2019 ¹⁰⁴
Motor neuron disease (MND)	3 β ,7 α -diHCA, 7 α H,3O-CA	Theofilopoulos <i>et al</i> , 2014 ³⁴

1.4.1. Alzheimer's disease

AD is a progressive neurodegenerative disease characterised by widespread brain atrophy and cognitive dysfunction, manifesting as memory deficit, defective spatial awareness and personality and behavioural changes to name some of the symptoms. Pathologically it is characterised by amyloid beta (A β) plaque deposition and neurofibrillary tangles (NFTs) resulting from phosphorylated tau protein accumulation, both of which cause neurotoxic effects eventually resulting in selective neuronal loss^{105,106}, with more recent research suggesting the interaction between these two pathologies drives downstream neuroinflammation and neurodegeneration in early disease stages¹⁰⁷.

A β is a protein that is normally formed during the natural process of ageing via the breakdown of amyloid precursor protein (APP) (see Figure 1.11), a membrane protein found in many tissue types but mainly in the synapses of neurons. APP is cleaved via one of two enzymes, α -secretase or β -secretase, with β -secretase the more common enzyme in neurons and the brain generally¹⁰⁸. The β -secretase cleaves

the APP at the N terminus resulting in the formation of a C99 β -C terminus fragment (β -CTF) and sAPP β fragment¹⁰⁹ (see Figure 1.11).

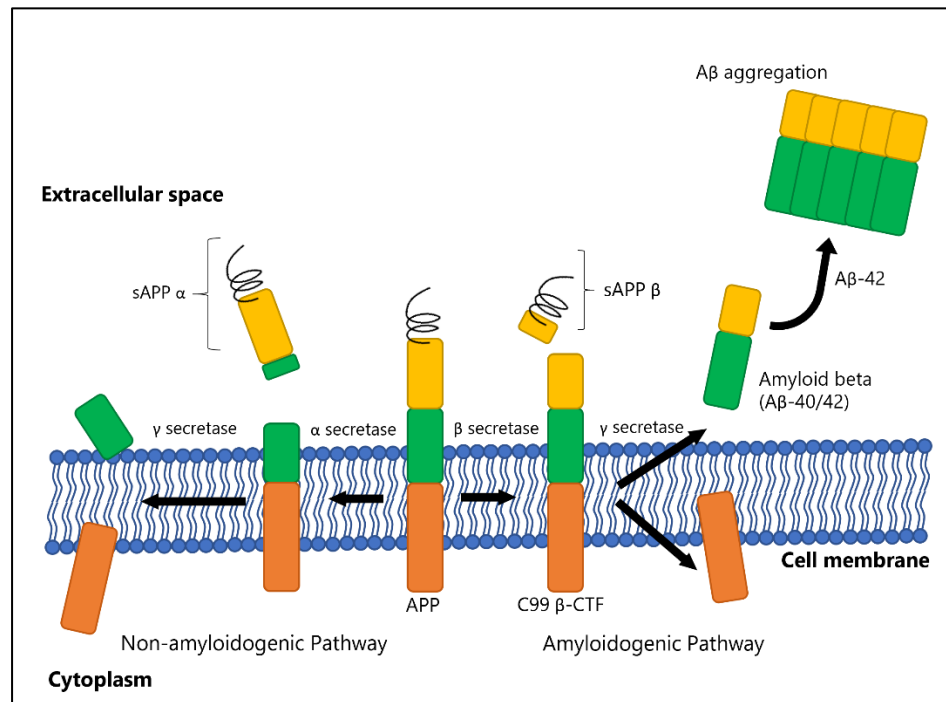


Figure 1.11. The metabolism of APP and subsequent synthesis of amyloid beta (Aβ) in the brain.

The enzyme γ -secretase further cleaves the β -CTF to generate the A β fragment, of which there are two possible isoforms with either 40 amino acids (A β -40), or 42 amino acids (A β -42) at a rate of 90%/10% respectively¹⁰⁸. The A β -42 isoform is more commonly associated to the pathological changes seen in AD, with several studies suggesting the A β -42 is more neurotoxic in comparison to the A β -40¹¹⁰, and is more likely to aggregate and form the neurotoxic plaques that are hallmarks of AD^{111,112}.

In addition to A β pathology, tau protein and NFTs are also a main pathological feature of AD. Tau is a microtubule-associated protein that stimulates the assembly of tubulin into microtubules within the brain¹¹³. In AD, it can become hyperphosphorylated, which aggregates to create NFTs which deposit in projection neurons (see Figure 1.12)^{114–119}. This happens when the phosphorylated tau monomer aggregates, forming a tau oligomer which eventually create paired helical filaments (PHFs) (see Figure 1.12). The accumulation of these PHFs is referred to as NFTs.

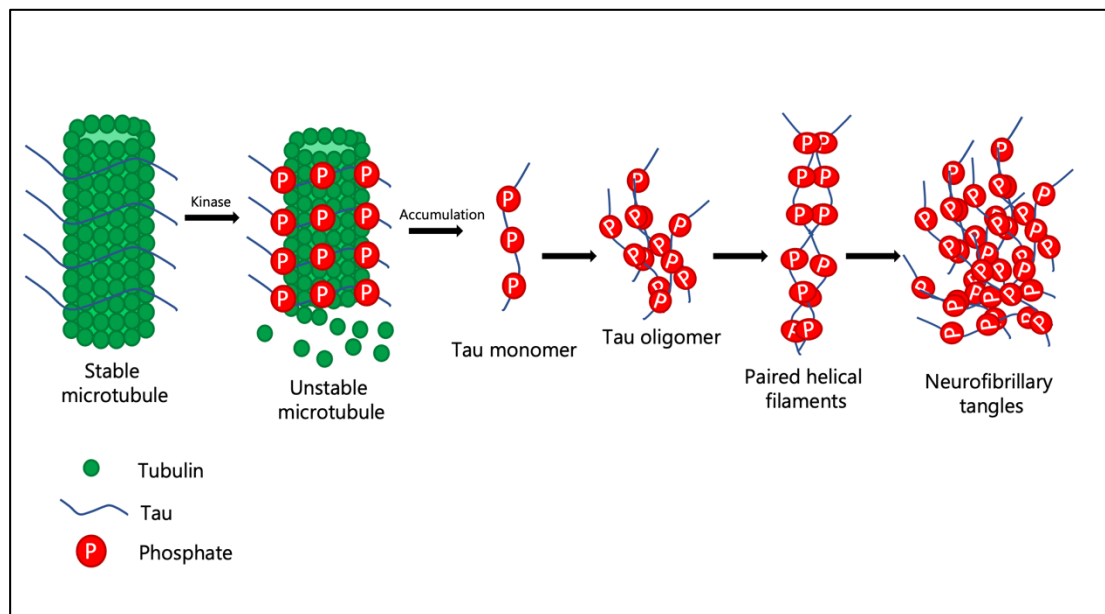


Figure 1.12. The formation of neurofibrillary tangles from hyperphosphorylated tau protein and paired helical filaments (PHFs).

Although NFTs were originally thought to be neurotoxic and one of the contributing factors to the vast neurodegeneration seen in AD due to the correlation with neuronal loss and cognitive decline¹²⁰, contradicting research suggests that NFTs may in fact be neuroprotective, with the phosphorylation of tau a specific cell response to oxidative stress^{121,122} and NFT-bearing neurones found to be functionally intact in transgenic mouse models¹²³. However, they are still widely recognised as a hallmark of disease whether it be a neuroprotective or neurotoxic role.

In addition to these two features of AD, there are several other disease mechanisms and genetic factors that have been reported to show an association with cognitive impairment and dementia in AD patients and contribute to the disease outcome. These pathogenic hypotheses include N-methyl-D-aspartate (NMDA) receptor dysfunction as a result of glutamate and calcium dysregulation, dysfunction of lysosomes resulting in impaired axonal transport and impaired presenilin function resulting in synaptic dysfunction¹²⁴.

Genetic mutations associated with AD include several pathology-associated genes including *PSEN1*, *PSEN2* and *APP*¹²⁵, however other genes related to cholesterol and lipid transport have also been identified in late onset AD (LOAD). LOAD accounts for more than 90% of all cases of AD. Relatively common genetic variation mapped to *APOE*, clusterin (*CLU*) and *ABCA7*, which aid in the transport of cholesterol and

other lipids across cell membranes¹²⁶, have been widely reported and verified as associating with an increased risk of cognitive impairment and AD.

APOE is a key transporter for cholesterol in the brain, produced by astrocytes, and combines with cholesterol, transferring from astrocytes to neurons. In addition to its role in cholesterol transport, APOE also mediates the clearance, metabolism, aggregation and deposition of A β ¹²⁷. *APOE* has three alleles: ϵ 2, ϵ 3 and ϵ 4. Evidence suggests that the ϵ 4 allele is a strong genetic risk factor for AD in comparison to ϵ 3, which is the more common allele¹²⁸. In contrast, the ϵ 2 allele has shown to be protective against LOAD¹²⁹. Previous studies have shown APO ϵ 4 promoted the oligomerisation of A β , more so than the neuroprotective APO ϵ 2 isoform^{130,131}, with AD transgenic mouse models displaying an earlier onset of disease and greater amyloid plaque deposition with the APO ϵ 4 isoform^{132–134}. APO ϵ 4 also showed to be less effective at clearing A β in comparison to APO ϵ 3, resulting in a build-up of A β ¹³⁵, and has also been suggested to be a poor carrier of lipids compared to the other isoforms from conformational changes¹³⁶. A person with two copies of the APO ϵ 4 allele has a greater than 14-fold risk of AD in comparison to those expressing ϵ 2 or ϵ 3¹³⁷.

There have been studies that have shown links between AD and oxysterols, with discrepancies in both 24S-HC and (25R)26-HC identified in plasma, CSF, and brain tissue samples of individuals with AD, as well as differences seen in different ApoE isoforms. In plasma, 24S-HC has been shown to be decreased in late stage AD^{35,95}, with this finding primarily reflecting the loss of neurons in the brain and the subsequent flux across the BBB. In CSF however, both 24S-HC and (25R)26-HC are increased in AD compared with controls^{35,138}. In AD brain tissue, (25R)26-HC is also shown to be increased, with 24S-HC decreased a result of the substantial neuronal loss⁹⁶. The (25R)26-HC data suggests a disturbance in the BBB, meaning increased levels of (25R)26-HC crossing into the brain and CSF.

In regards to ApoE status, a study by Jenner *et al*, 2010 showed increased (25R)26-HC in APO ϵ 4 mice compared to APO ϵ 3¹³⁹, with another study showing ApoE-deficient mice had increased 7 β -HC in plasma¹⁴⁰ suggesting the presence of ApoE or the isoform present can affect the levels of oxysterols, specifically (25R)26-HC and 7 β -HC.

1.4.2. Multiple sclerosis

Multiple sclerosis is a demyelinating, inflammatory and progressive neurodegenerative disease of the CNS, where activated immune cells target myelin sheaths that surround nerve axons. These cells attack and degrade myelin resulting in the active process of demyelination, causing lesions to form within the brain and spinal cord. The disease is more frequently diagnosed in females than in males (at a 2:1 ratio¹⁴¹), with several risk factors identified including smoking, viral infections, vitamin D exposure, geographical location and several genetic associations, including human leukocyte antigen 1 (*HLA1*) and *CYP27B1*^{142–144}.

Multiple sclerosis has three main subtypes: relapsing remitting (RR), secondary progressive (SP) and primary progressive (PP) (see Figure 1.13). The latter is the least common and the most aggressive, with only 10-15% of all multiple sclerosis cases diagnosed with this phenotype and characterised by the lack of relapsing stage and a gradual worsening of disability from onset^{145,146}. RR is the most common, with 85% of individuals with multiple sclerosis diagnosed with RR at some point in their disease course, characterised by the distinct increase in disability, where either partial or full recovery will follow^{145,147}. RR is usually followed over time with SP, which is characterised by a steady increase in disability over time. SP is accompanied by increased cortical pathology including excessive demyelination of the subpia¹⁴⁸, neuronal and axonal loss and widespread inflammation across the brain^{149–151}.

Multiple sclerosis disease centres around the presence and severity of disease processes including demyelinated lesions in the grey and/or white matter, the presence of inflammation, including microglia, macrophages, B and T cells, and neuronal and axonal loss. Mechanisms of repair have been identified also, with remyelination currently at the centre of research efforts for a more natural therapy for lesioned areas^{152–154}.

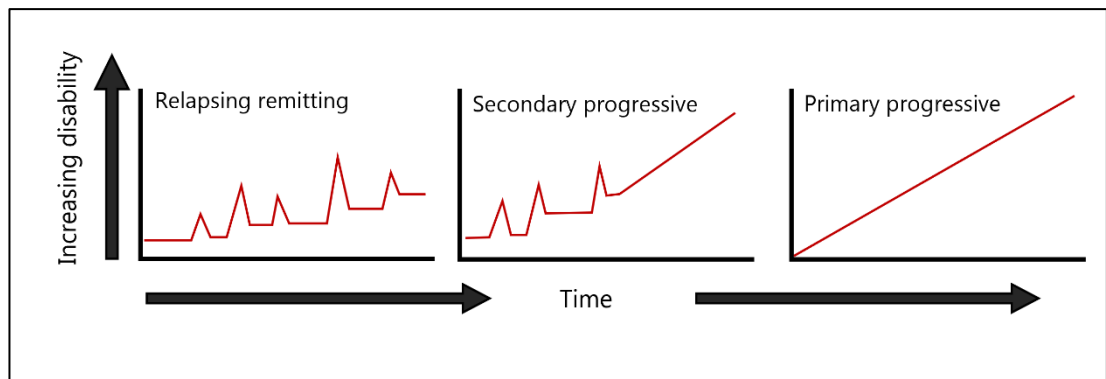


Figure 1.13. Multiple sclerosis subtypes and the pattern of increasing disability over time.

Although the current understanding of initiation is not fully known, in multiple sclerosis myelin is targeted and phagocytosed by immune cells including microglia and macrophage cells. This loss of myelin creates demyelinated lesions to appear in both the grey and white matter of the brain and spinal cord, and results in synapse disruption and impaired signal transduction which manifests as symptoms of disease including spasticity, partial or complete loss of sight and visual disturbances, severe fatigue and incontinence^{155–158}.

For many years, demyelination was thought to be exclusively in the white matter, however grey matter demyelination in cortical layers of the brain had been identified as early as 1916 by James Dawson¹⁵⁹, with other studies confirming via post-mortem, immunohistochemistry and imaging the vast presence of cortical and deep grey matter pathology^{148,160–162}. These lesions can also be accompanied with inflammation in the form of microglia/macrophage cells within the brain (see Figure 1.14), and T/B cell follicle-like structures in the meningeal vessel structure surrounding the brain.

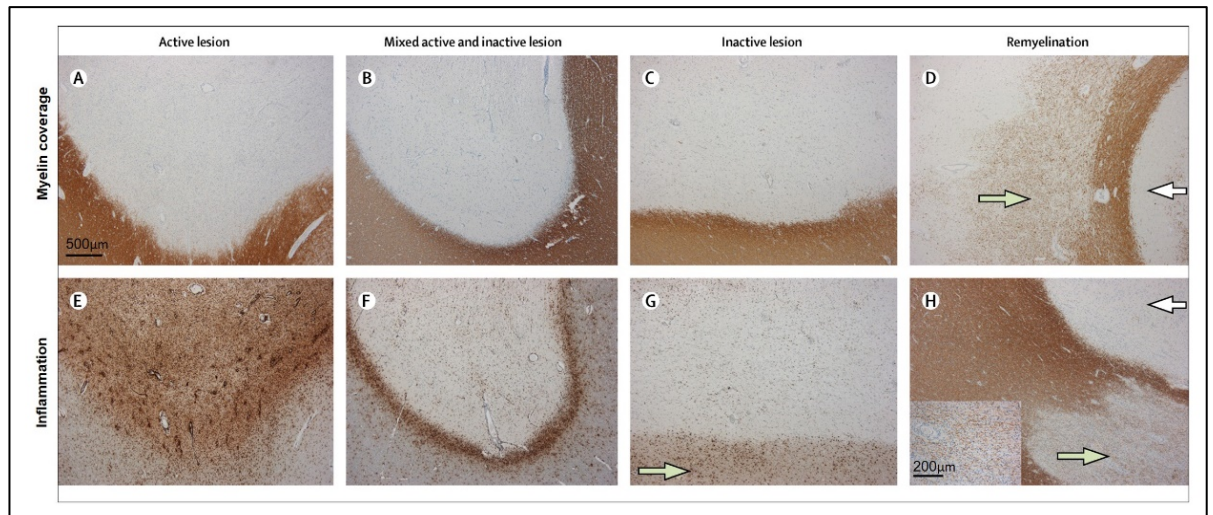


Figure 1.14. The different types of inflammatory lesion present in the multiple sclerosis brain¹⁶³.

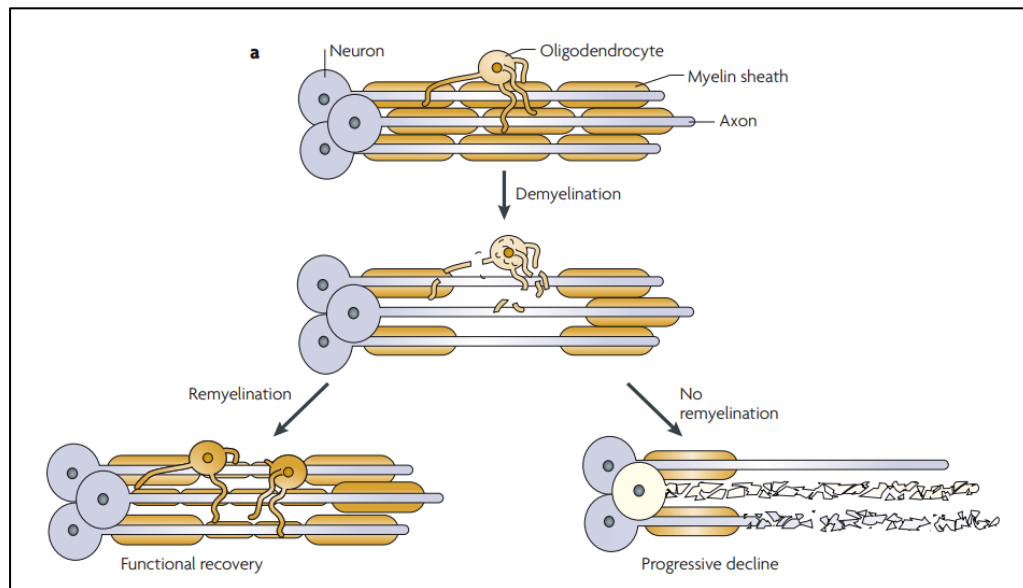
Images A, B, C, D and H shows the myelin (dark brown stain) and its loss in lesions, with images E, F and G showing active microglia/macrophage inflammatory cells (dark brown stain). Images A+E show the characterisation of an active lesion, which is devoid of myelin but saturated with inflammation. Images B and F show the mixed active and inactive lesions, where again the lesion is completely demyelinated and there is an active rim of inflammatory cells around the edge of the lesion. Images C and G show an inactive lesion, where myelin is completely demyelinated, with no inflammatory cells within the lesion or lesion edge. Taken with permission from The Lancet Neurology.

The microglial/ macrophage inflammation can be widespread throughout the brain but can also appear enriched in specific regions and within lesioned areas.

Examples of this include the white matter lesion classification of active, inactive and active/ inactive lesions as noted by Kuhlmann *et al* in 2017^{163,164} (see Figure 1.14) .

Lesions have also been noted in both the cortical and deep grey matter, and are thought to be more extensive than white matter lesions in the brain, with up to 60% of the cortex demyelinated in some cases^{148,161,165–168}.

With the huge levels of demyelination present in disease, repair mechanisms are available for the damaged nerve cells by aiding to regenerate the phagocytosed myelin, which is a process known as remyelination¹⁶⁹. Remyelination is the body's process of repair for demyelinated axons, which produces new myelin membranes from new mature oligodendrocyte cells derived from adult CNS progenitor cells^{170,171} (see Figure 1.15). The newly synthesised myelin appears thinner than the original from developmental stages¹⁷², producing patchy-looking myelin on stained sections (refer to Figure 1.14 D & H) but is enough to regain saltatory conduction within the axon¹⁷³.



1.15. The process of demyelination and remyelination in multiple sclerosis¹⁷¹. The degeneration of the myelin sheath and damage to oligodendrocyte cells results in the formation of demyelinated lesions in the CNS. There are two pathways following; either recovery via the remyelination mechanism, where oligodendrocytes produced new myelin for partial or complete axonal recovery, or a lack of remyelination which results in a progressive decline in disease and disability. Taken with permission from Nature Reviews Neuroscience.

The vast demyelination will be accompanied by significant neuronal loss in later stages of disease. The subsequent loss of axons, synapses and neurones within the cortex is the outcome from several disease mechanisms including oxidative damage via ROS, inflammatory stress and neuronal stress¹⁷⁴.

In terms of biomarkers, many of the markers of disease are related to the pathophysiology associated with multiple sclerosis for example markers of immune activation (oligoclonal bands), BBB dysfunction (albumin), demyelination (proteolipid protein (PLP)/myelin oligodendrocyte glycoprotein (MOG)/myelin associated glycoprotein (MAG)), neurodegeneration (neurofilament protein (NFil)), and glial cell activation (GFAP). Recently, specific lipids have been suggested as markers of disease, including the presence of altered sterol profiles and apolipoprotein^{23,101,175}.

Disrupted serum and oxysterol/ cholesterol levels have been associated with adverse clinical outcomes in multiple sclerosis¹⁰¹, and in conjunction with ApoB levels, a cholesterol transporter important for transporting LDLs in plasma^{176,177}, could indicate disease progression¹⁷⁸. Other literature showed that increased levels of LDL

in serum correlated positively with disease activity with new magnetic resonance imaging (MRI) lesions in both progressive and relapsing-remitting disease^{179,180}, with increased LDL, total cholesterol and ApoB levels independently associated with a higher expanded disability status scale (EDSS) score^{181,182}.

In terms of oxysterols, profiles differ based on the disease stage^{183,184}. In relation to 24S-HC, higher circulating levels in younger patients reflect higher brain cholesterol metabolism and ongoing neurodegeneration^{100,101}. In older patients and PP disease, 24S serum levels were lower, suggesting increased brain atrophy and significant neuronal loss^{185,186}. Other oxysterols, including 25-HC and (25R)26-HC have also been reported. In multiple sclerosis patients with gadolinium-enhancing lesions, (25R)26-HC levels in the CSF were significantly increased compared with controls³⁵. For (25R)26-HC and 25-HC, plasma levels were found to be significantly decreased in patients with RR disease compared with neurological control patients however, in the CSF levels of (25R)26-HC were significantly increased in comparison to the control grouping²³. In addition to multiple sclerosis, Huntington's disease (HD) has also shown altered cholesterol and oxysterol profiles in human and animal models of disease.

1.4.3. Huntington's disease

HD is an autosomal-dominant progressive neurodegenerative disease, where a mutation in the huntingtin (HTT) gene results in an expansion of 36 or more cytosine-adenosine-guanine (CAG) trinucleotide repeats¹⁸⁷, which codes for the amino acid glutamine, with the most common HD alleles having between 40 to 50 repeats¹⁸⁸, with longer expansion resulting in earlier onset¹⁸⁹. This polyglutamine repeat can result in a dysfunctional phenotype and misfolding of the huntingtin protein which can lead to aggregation and a gain of toxic function as a result. Individuals with the polyglutamine expansion can become symptomatic at any point between 2 and 85 years, but most commonly between 30 and 50 years old¹⁹⁰. When symptoms are displayed, the disease will progress with time, with on average between 15 to 20 years from onset of symptoms to death²⁴.

The neuropathological changes witnessed in HD are found in several brain regions, with prominent atrophy and striatal medium spiny neuronal cell loss in the caudate and putamen. Other regions affected include the substantia nigra, hippocampus,

selective deeper layers of the cerebral cortex and Purkinjee cells in the cerebellum to name a few^{191–194}. These pathological mechanisms result in complex symptomatic presentation including chorea (sporadic involuntary movement), incoordination and slow saccadic eye movements.

Sterols, and cholesterol in particular, have been a popular topic in HD with several studies highlighting cholesterol differences in HD cell models, various mouse models and human tissue in comparison to control^{24,103,195,196} (see Figure 1.16). Although many published articles have reported differences, there are several conflicting findings in terms of cholesterol content within the plasma and brain tissue itself.

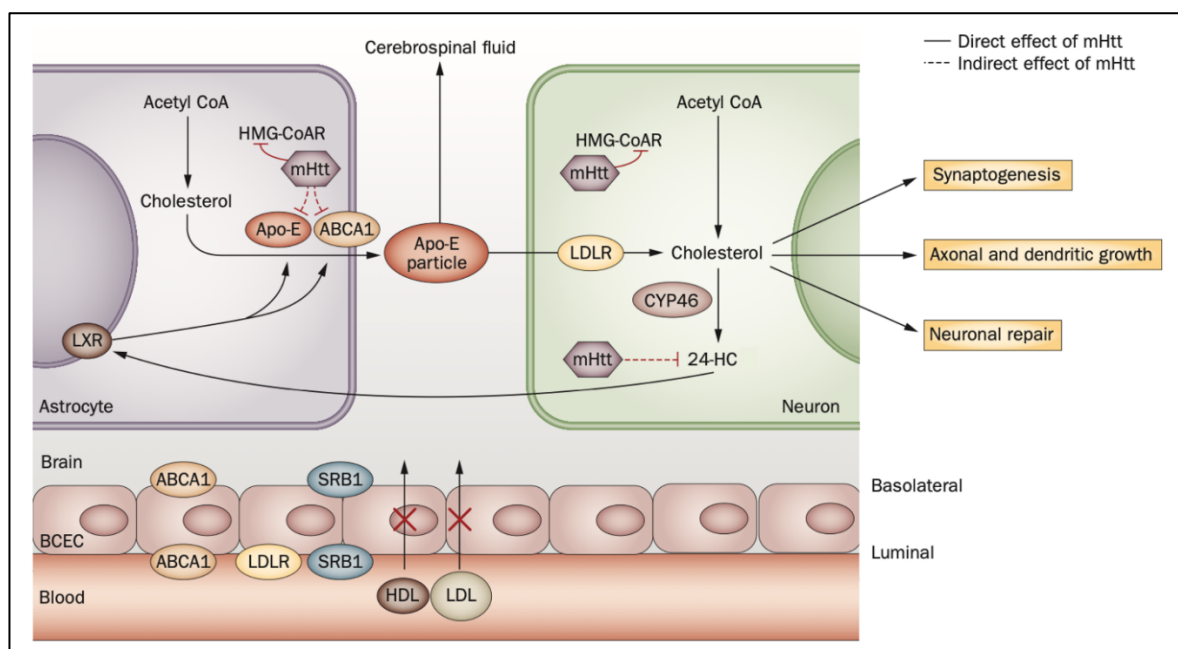


Figure 1.16. Effects of the mutant huntingtin (mHtt) on cholesterol metabolism and transport in the CNS¹⁹⁷. The mHtt has shown to inhibit HMG CoA reductase, an enzyme essential for cholesterol biosynthesis in astrocytes and neurons. The inhibition of this enzyme results in the general decrease of brain cholesterol and subsequently 24S-HC production, which is a ligand for LXRs. Without LXR binding, important transcripts including ApoE and ABCA1 for cholesterol transport cannot be translated meaning cholesterol cannot be transferred from the astrocyte to the neuron. Taken with permission from Nature Reviews Neurology.

Data has been published showing a decrease in total cholesterol in HD patient plasma and relatives compared with control¹⁹⁸, with another paper showing no change in cholesterol between pre-diagnosis and established HD but did see reduced

24S-HC in HD compared with pre diagnosed¹⁹⁹. In the brain tissue, research in 2016 showed significantly increased cholesterol in the striatum of R6/2 mouse models²⁴, and another showing increases in the yeast artificial chromosome 72 (YAC72) model¹⁹⁶. Others show contrasting data with decreased cholesterol in striatum of *Hdh* knock-in mice¹⁰⁴, and in R6/2 mice¹⁰² and both cholesterol and 24S-HC reduced in whole brain *Hdh*^{Q111}, YAC72 and YAC128, with R6/2 mouse models showing significant decreases in 24S-HC¹⁰³.

Other contrasting data reports a downregulation of cholesterol biosynthesis genes in HD striatal cells, mouse models and human cortical tissue including *HMGCR*, *CYP51* and *7DHCR*^{102,200,201}, which would in turn lower cholesterol and oxysterol concentrations across the brain (see Figure 1.16). The theorised mechanisms underpinning the decrease of cholesterol and 24S-HC in HD centre around the mHTT inhibition of HMG CoA reductase enzyme, a key enzyme for cholesterol synthesis (shown in Figure 1.16). Not only does a lack of cholesterol synthesis create issues with synaptogenesis, axonal/ dendritic growth and neuronal repair, it also indirectly affects the production of 24S-HC and the activation of LXRs which have an important role in the regulation of lipid transporters including ApoE and ABCA1. In regards to APOE, a cholesterol transporter between astrocytes and neurons, astrocyte cells expressing mHTT have shown to produce and secrete lower amounts of APOE^{103,202}. The mHTT been shown to have an active effect on the translocation and maturation of SREBP, and with the decreased levels of 24S-HC, therefore cannot upregulate the LXR transcripts including ApoE and ABCA1 (see Figure 1.16), both integral for the transport of cholesterol to neurons^{203,204} and generally decreases SREBP levels in astrocytes^{205,206}.

Generally, there is strong evidence to suggest the 24S-HC and cholesterol profiles in HD are compromised due to mutant huntingtin, affecting several important mechanisms in the brain responsible for cholesterol synthesis and transport resulting in widespread cholesterol deficiency across the brain, and potential in the periphery.

1.5. Sterolomics

The definition of sterolomics is the quantitative, or semi-quantitative analysis of all metabolites derived from cholesterol and its cyclic precursors²⁰⁷ and includes the analysis of oxysterols, hormonal steroids, bile acids and all precursors and

metabolites²⁰⁸, and becomes extremely important in diseases like CTX, SPG5 and SLOS where enzyme mutations or depletions result in alterations in sterol profiles²⁰⁷. Sterols are one of the eight lipid categories classified by LipidMaps²⁰⁹, however certain challenges with the analysis of sterols means there is a general under-representation in un-targeted lipidomics. Some of these challenges include a difference in amounts of different sterols compounds present within a sample, the difficulty of charging a neutral molecule, and detecting multiple compounds with a similar structural makeup.

These issues can be overcome using multiple separation methods throughout sample preparation and analysis, which include solid phase extraction (SPE) for the enrichment of the lower abundant compounds such as oxysterols, derivatisation to ensure ionisation, and chromatographic separation paired with mass spectrometry to separate and analyse multiple compounds with a related structure based on the polarity, mass-to-charge ratio (m/z) and unique fragmentation patterns of the ions.

1.6. Sterol extraction from biological samples

Sterols are found in almost all living organisms²¹⁰, and are present intracellularly and within the cell membranes of many cell types. This means sterols can be extracted from biological materials including cells, biological fluids and tissues including plasma, cerebrospinal fluid (CSF) and brain tissue. Generally, sterol extraction involves a solvent mix of at least two different solvents, for example chloroform/methanol or dichloromethane/methanol, to disrupt lipoproteins but also solubilise the lipids.

The classical methods for sterol extraction were developed in the 1950s, where there are two highlighted methodologies; the Bligh-Dyer method and the Folch method^{211,212}, both liquid-liquid extraction methods that centre around the use of chloroform/method extraction to solubilize the lipids for the analysis of the extracted sterols using gas chromatography mass spectrometry (GC-MS) however it was reported that this method resulted in an incomplete lipid extraction²¹³. In 1961, Getz reported that an ethanol/ ether mix obtained more lipids in comparison to the Folch method²¹⁴, and was also used in 1970 by Lucas, adding pure ethanol to extract lipids, including cholesterol, from rat liver tissue²¹⁵. In more recent years, extraction methods have been developed for analyse using liquid chromatography mass

spectrometry (LC-MS), which offers higher sensitivity in comparison with GC-MS. This technique was utilised by Liu in 2003 using rat brain tissue²¹⁶ and by McDonald in 2007²¹⁷. The method of Liu was further developed by Griffiths in 2008 for plasma extraction with additional steps to further separate oxysterols, and included derivatisation to determine further oxysterols²¹⁸. If the aim is to quantify total sterol levels, one of the additional steps would include saponification, where an alkaline solution such as potassium hydroxide is used to hydrolyse the ester bond of the sterol ester^{219,220} (see Figure 1.17).

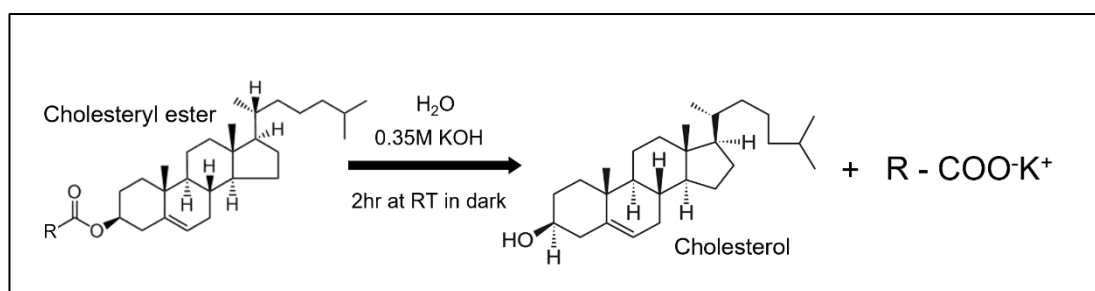


Figure 1.17. Hydrolysis reaction of cholesteryl ester into cholesterol using potassium hydroxide (KOH).

1.7. Solid phase extraction for sterol separation and oxysterol enrichment

Cholesterol is far more abundant in biological material in comparison to oxysterols. For true analysis of the oxysterols present in any given sample, separation from cholesterol would be key. SPE is a sample preparation technique that uses a solid and liquid phase to selectively isolate a specific type of analyte from a sample for a number of purposes including purification, derivatisation and enrichment of compounds present in the sample being analysed²²¹. It was introduced in the early 1970s due to the disadvantages that liquid-liquid extraction had, including the time taken to process the sample and the large sample volume required^{222,223}. This preparation is paramount for oxysterol analysis due to the overwhelming abundance of not just cholesterol, but other lipid species present in biological samples, including triacylglycerides (TAGs) and phospholipids.

In SPE, the aqueous based sample (mobile phase) is passed through a solid cartridge (stationary phase), usually in the form of a column (see Figure 1.18) but can also come in the form of SPE plates and solid phase microextractions which uses a fibre

coated with an extracting phase to extract different analytes from the sample²²⁴. The stationary phase will usually adopt one of three methods for adsorption; normal phase/ polar, reversed phase/ non-polar, or ion exchange chromatography to retain the analyte of interest onto the stationary phase, with the most common materials including silica and polymer-based sorbents²²⁵. The analyte must have a greater affinity for the solid phase than the matrix²²¹, which will retain the analyte of interest and will then be eluted by a suitable solvent to leave an eluent enriched with the analyte. They can be used to separate lipid classes, or lipids within the same class dependent on the sample and the analytes of interest²²⁶, for example sterol molecules. For sterol analysis, most SPE methods use a reversed-phase column.

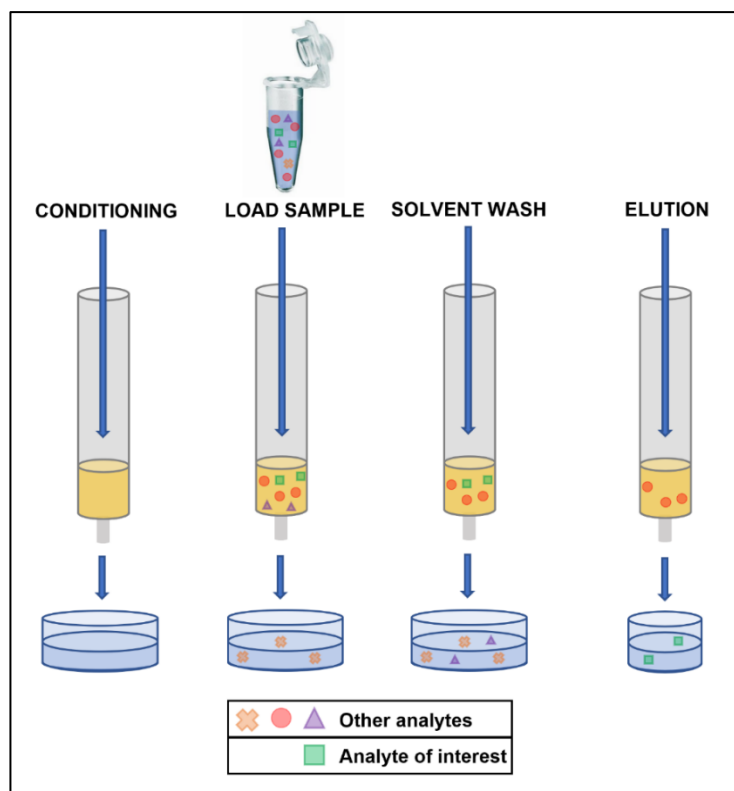


Figure 1.18. The principle of solid phase extraction to filter analytes of interest.

The SPE process usually consists of four stages, with the first step being a pre-wash to condition the column, followed by sample loading. The column is then washed (column post-wash) to remove unwanted analytes, finishing with elution (see Figure 1.18). The elution will contain the analyte of interest, which other background analytes either eluted during the solvent wash, or still stuck within the sorbent.

Research into oxysterols commonly uses solid phase extraction techniques, first seen in 1995 with Dzeletovic et al, who swapped to solid phase extraction having previously used laborious methodology with off-line liquid chromatography separation of oxysterols from cholesterol, using an Isolute silica cartridge conditioned with hexane. The SPE made for a quicker separation, but also determine two additional oxysterols not seen previously²¹⁹.

Since then, SPE of oxysterols has become the gold standard separation technique, with one of the more recent and robust methods utilising silica-based reversed phase SepPak C18 200mg cartridges for the separation of oxysterols from cholesterol, with ethanol based solvent as the mobile phase⁴⁹. A second SPE following after a derivatisation step is typically applied to remove excess derivatisation reagent, using a polymeric reversed-phase hydrophilic-lipophilic-balanced (HLB) Oasis 60mg cartridge with aqueous methanol as the mobile phase, which retains all oxysterols and cholestenoic acids to the stationary phase for final elution in absolute methanol to ensure an eluent enriched with oxysterols²²⁷.

Derivatisation steps are often included in sample preparation to attach a charge to the molecule of interest.

1.8. Derivatisation of sterol molecules

The analysis of sterol molecules centres around the utilisation of mass spectrometry techniques, coupling with both GC and LC. More recent techniques have optimised LC approaches for sterol analysis, however for these techniques to be satisfactory, the molecules of interest need to be charged. Sterols are neither acidic or basic, and do not readily ionise into $[M+H]^+$ or $[M-H]^-$. To improve their visibility in the mass spectrometer (MS), derivatisation methods have been optimised to add a charge tag to the molecule before injection into the MS. Derivatisation not only adds a charge to the analyte but can also help with the solubility. These include the formation of picolinyl esters via picolinic acid²²⁸, nicotinyl esters via nicotinic acid²²⁹ and oximes via carbonyl-hydroxylamine reactions^{216,230}, all of which result in positively charged ions. In recent years the use of derivatisation methods using hydrazine/ hydrazone molecules have become commonly used^{231–235}, including the addition of a Girard P hydrazine via an enzymatic assisted reaction to create a positive charged sterol hydrazone molecule (see Figure 1.19). The method, founded by the Griffiths-Wang

group in 2007²³⁶, utilises the cholesterol oxidase enzyme originally described by Brooks et al²³⁷, which first converts the 3 β hydroxyl group into a C3 ketone, or oxo, group which allows for the Girard P hydrazine to bind to the 3 position and adding a positive charge-tag²³⁸ (Figure 1.19).

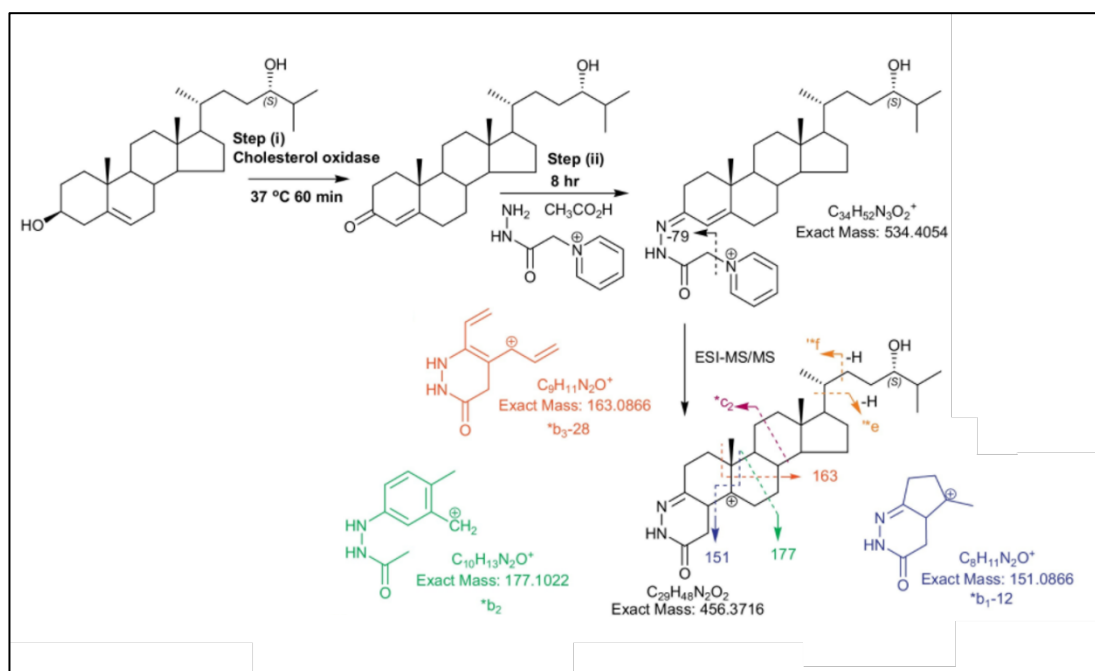


Figure 1.19. Formation of positively charged cholesterol molecule via an enzyme-assisted derivatisation for sterol analysis (EADSA) incorporating derivatisation with Girard hydrazine²³⁹. The formation of the Girard hydrazone allows for several fragments ions to be created from electrospray ionisation ion trap fragmentation (ESI-MS/MS). Taken with permission from the Journal of Steroid Biochemistry and Molecular Biology.

1.9. Chromatographic separation

The structural similarities of oxysterols do require further separation in addition to SPE, with several oxysterols having the same mass. A chromatographic application is therefore needed to separate the sterol molecules based on their individual properties, such as polarity or volatility.

In classical methodology, GC was used for sterol separation²¹⁹, which requires the ions to be in gaseous form, separating based on both the volatility of the ion and its interactions with the GC column. The ‘gold standard’ method described by Dzelotovic in 1995²¹⁹ derivatised sterols to trimethylsilyl (TMS) ethers to enhance volatility, with the method being cited hundreds of times²⁴⁰ with a number of monohydroxycholesterols being detected including 24S-HC, 25-HC, (25R)26-C,

7 α -HC, 7 β -HC and 7-oxo to name a few, all of which were detected with GC-MS within a 19-minute run.

Although the classical analysis method for oxysterols is using GC-MS due to its stable analysis of sterols and relatively short analysis time, high-performance LC (HPLC) has now become the more common method for analysis due to its increased sensitivity²⁴¹.

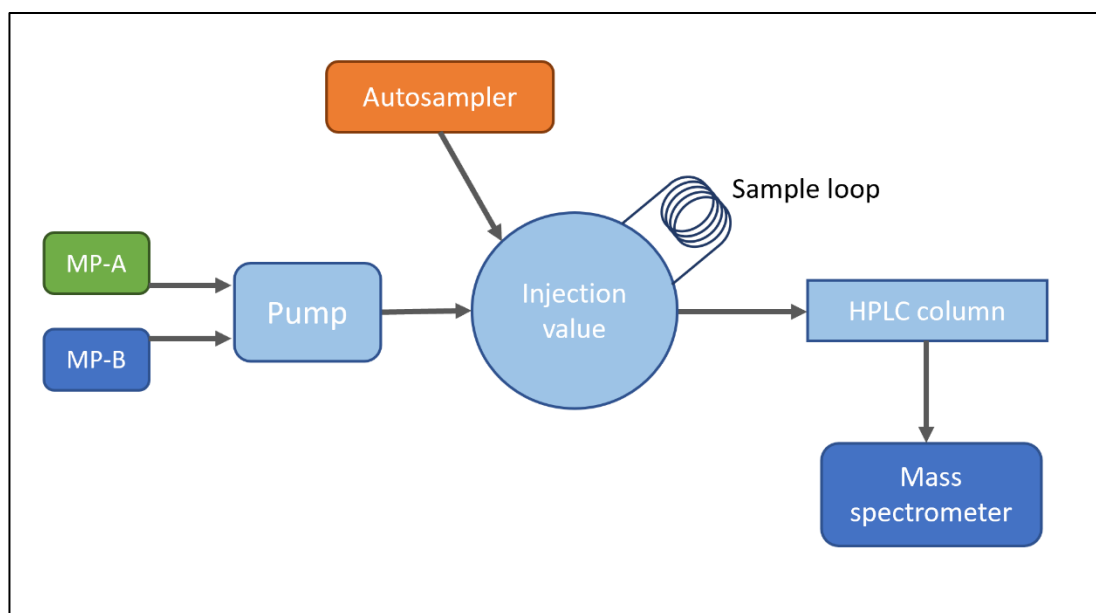


Figure 1.20. A schematic representation of the Dionex UltiMate 3000 HPLC system. MP = mobile phase; mobile phase A contains 33.3% MeOH, 16.7% ACN, 0.1% formic acid; mobile phase B contains 63.3% MeOH, 31.7% ACN, 0.1% formic acid).

Liquid chromatography uses a liquid mobile phase, with a stationary phase bound to a solid support, usually in a column form. The mobile phases and stationary phases are the most important parts of the method as it can alter the separation of the molecules of interest based on the polarity of the mobile phase solvents, and the length, carbon load percentage or internal diameter of the column used for separation.

There are two main types of stationary phase in LC; normal phase (NP) and reversed phase (RP). In NP, analytes are adsorbed to polar silica particles and elute with non-polar solvents. NP is perceived as have a lower reproducibility than RP, and was shown to have lower sensitivity in comparison to RP in a study from 1998²⁴². In comparison, RP has a non-polar stationary phase and polar mobile phase, which is usually aqueous based mixed with one or more solvents such as acetonitrile or

methanol. With RP, analytes are expected to separate based on their hydrophobicity, with more hydrophobic molecules eluting later.

HPLC techniques utilise the different polarities of analytes using the solid-phase analytical column and liquid mobile phases to separate the compounds based on their structural differences.

The sample is collected from the allocated vial in the autosampler, with the autosampler needle drawing the specified volume and injecting into the sample loop (see Figure 1.20). The two mobile phases are used create a solvent gradient, which flows through the HPLC column using the solvent pump and allow the sample to travel down the column (see Figure 1.20). After the analytes have eluted from the column, they are then eluted into the mass spectrometer.

1.10. Mass spectrometry (MS)

Sterols are quite complex lipids, with few ways of being able to analyse them. One method for analysis is by mass spectrometry. Mass spectrometry is an analytical technique that measures the mass-to-charge ratio (m/z), and there by molecular weight, of ions producing a mass spectrum which shows the abundance of ions against their m/z ²⁴³. It is used extensively in both academia and industry for the analysis of proteins, pharmaceuticals, lipids and carbon dating²⁴⁴. A mass spectrometer contains three different components, including an ion source which ionises the sample into gaseous ions, the mass analyser which separates the ions under vacuum based on their m/z , and finally the detector which measures their abundance.

1.10.1. Ion Sources

The ion source is the first component of the mass spectrometer, with the aim of ionising the analytes that are injected into the instrument, creating charged molecules in the gaseous phase. The ionisation of neutral molecules can be achieved in various ways, including electron or proton transfer, ion pair formation or charge transfer²⁴³.

Several different methods have been developed for the ionisation of an analyte, dating back to 1918²⁴⁵ with electron ionisation (EI), chemical ionisation (CI), and more robust techniques including electrospray ionisation (ESI) in 1988²⁴⁶ and matrix-assisted laser desorption/ionisation (MALDI) in 1987²⁴⁷. The earlier

techniques, including EI, and to a lesser extent CI, tend to show ion source fragmentation, resulting in a difficulty in assigning molecular masses^{248,249}. The softer ionisation techniques, including both ESI and MALDI have much lower fragmentation rates and allows for the efficient analysis of non-volatile compounds. ESI is the most widely used ionisation technique in lipidomic mass spectrometry, with several advantages over other ionisation techniques which include its compatibility with LC, and comparatively high ionisation efficiency. The technique utilises an electrical potential difference to transfer ions from solution into a gaseous form via a series of stages. The first is the generation of a charged droplet containing analytes emitted from the high voltage-charged electrospray capillary. The solvent then evaporates, leaving very small but highly charged droplets, finally the droplets “explode” with the generation of an aerosol of ions (see Figure 1.21)²⁵⁰. A theory of how this occurs is Coulomb explosion. This uses the thinking of Coulomb force of repulsion between like charges, which when the ESI droplet diminishes in size from high temperatures and voltages, it forces the ions closer which results in a Coulomb explosion^{251,252}.

Although ESI is the dominant methodology of ionisation in lipidomics, there are some molecules that are difficult to analyse, including sterols. A derivatisation step can improve the sensitivity of sterol analysis with ESI, as shown by several groups^{34,220,227,234,238} (mentioned in detail in section 1.8).

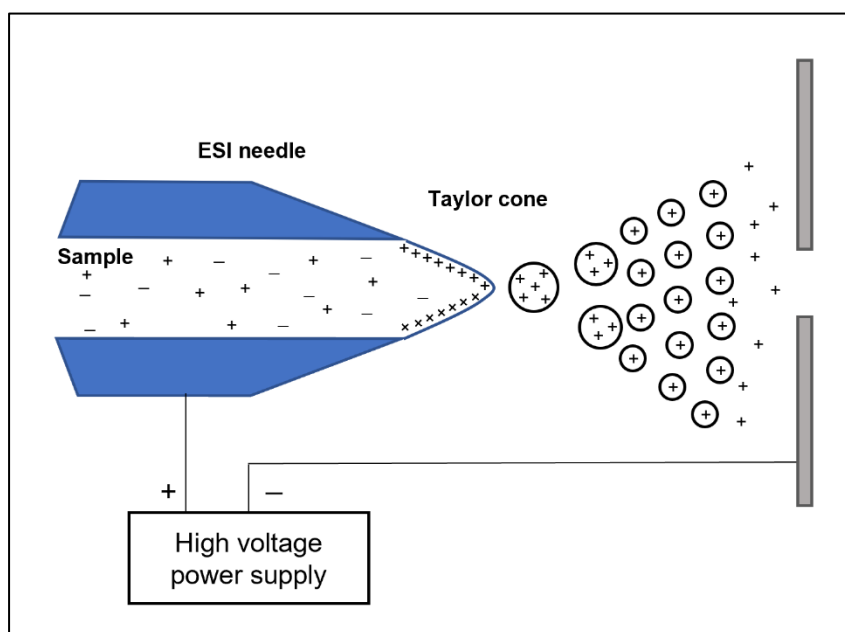


Figure 1.21. Schematic of the electrospray ionisation process at atmospheric pressure.

MALDI is another soft ionisation technique, however, utilises a completely different mechanism for the ionisation of biomolecules by a laser beam, typically a neodymium-doped yttrium aluminium garnet (Nd:YAG) laser either at atmospheric pressure (AP) or under vacuum, shot at the sample-matrix mix which absorbs energy leading to desorption of sample ions from the surface and into the mass spectrometer. One of the most important factors in MALDI is the matrix choice used for analysis. The role of the matrix is both to aid desorption and ionisation of the analytes within the sample²⁵³ (see Figure 1.22). They are usually weak acids due to their ability to be sufficient proton donors to the sample molecules and aiding ionisation, with common properties including a low mass, good solubility in solvent, low-volatility, and high absorptivity. There are many different matrices available, with the optimum matrix choice dependent upon sample type and whether analysis is in a positive or negative ion mode. Both α -cyano-4-hydroxycinnamic acid (CHCA) and 2,5-dihydrobenzoic acid (DHB) are common matrices for positive ion mode, giving adequate ionisation for lipid and peptide analysis, with 9-aminoacridine (9-AA) found to be better for negative ion mode analysis^{254–257}. After the analytes are ionised, the ions then enter the mass analyser for separation and detection.

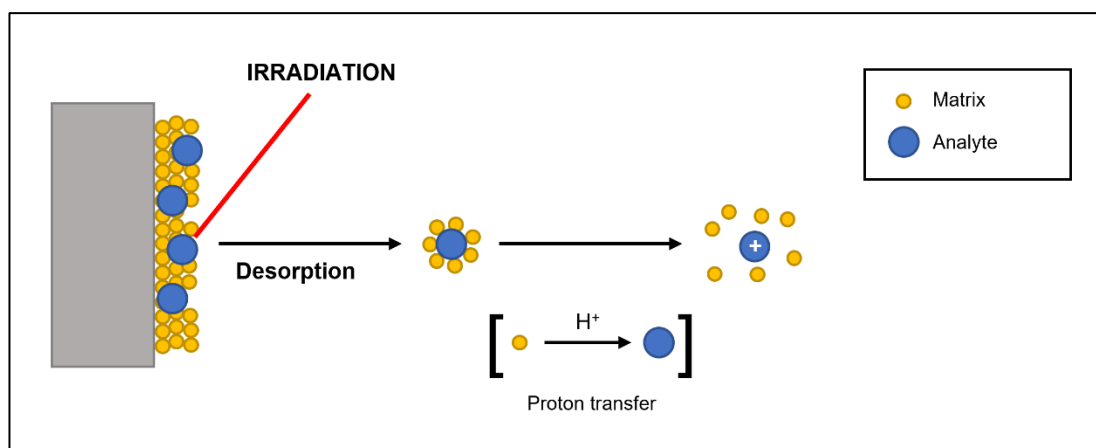


Figure 1.22. Schematic of MALDI desorption and the ionisation process.

1.10.2. Mass Analysers

Unlike ESI and AP-MALDI which happens at atmospheric pressure, the rest of the mass spectrometric analysis is done under vacuum conditions. The ions travel through the mass analyser, whose function is to separate the ions according to their

m/z . There are several different types of mass analyser, which each use a different property to separate m/z , and include time of flight (ToF), quadrupole, ion-trap, and orbitrap analysers. Generally mass analysers are divided into two categories: trapping-type (ion trap and orbitrap) or beam-type (quadrupole and ToF). ToF analysers use the time taken for an ion to pass from the ion source to the detector to calculate the m/z ²⁴³. ToF is commonly paired with MALDI ion sources, mainly due to ToF analysers needing a pulse of ions which MALDI can supply. Quadrupoles are a popular type of mass analyser and are often used in conjunction with other mass analysers in a hybrid/tri-brid system. A quadrupole consists of four cylindrical rods, where opposite rods are electrically connected. A radio frequency (RF) and direct current (DC) potential are applied to the paired rods which in combination cause the oscillation of ions as they travel through the quadrupole (see Figure 1.23). Only ions of a particular m/z will have a stable trajectory with a given RF and DC, meaning that a quadrupole can be used as a mass filter with other unstable ions outside of the m/z range being filtered out. In addition to its mass filter properties, it can also be used as an ion transmission guide, or as a collision cell for collision-induced dissociation (CID)²⁵⁸.

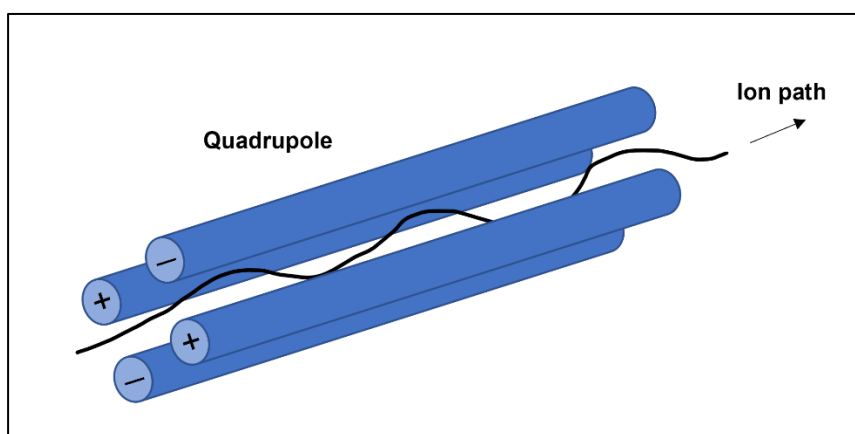


Figure 1.23. A diagram of a quadrupole mass analyser. A quadrupole contains four cylindrical rods, with opposite rods each having a RF and DC potential, which when combined result in the ions oscillating through the quadrupole analyser.

Ion-traps are another type of analyser and come in two forms: a 3D (or Paul) trap, and a 2D (linear) trap. The linear ion trap (LIT) has several advantages over the 3D and therefore is the more popular trap. The LIT is comparable to the quadrupole, where there are four hyperbolic poles, with the difference of a potential field being

applied to either end of the poles. This results in the ions being ‘trapped’ within the quadrupole and can then be selectively ejected either axially or radially, and detected by the two electron multiplier detectors either side of the ion trap²⁵⁹ (see Figure 1.24). Mass spectrometers with simple ion-traps have good sensitivity and are compact and affordable but do have a relatively low resolving power which means they are commonly using in conjunction with other mass analysers in hybrid or tribrid systems.

The low resolving power means the ion trap cannot resolve two peaks with a very similar m/z , which may need to be achieved by using a different trapping method, such as an Orbitrap.

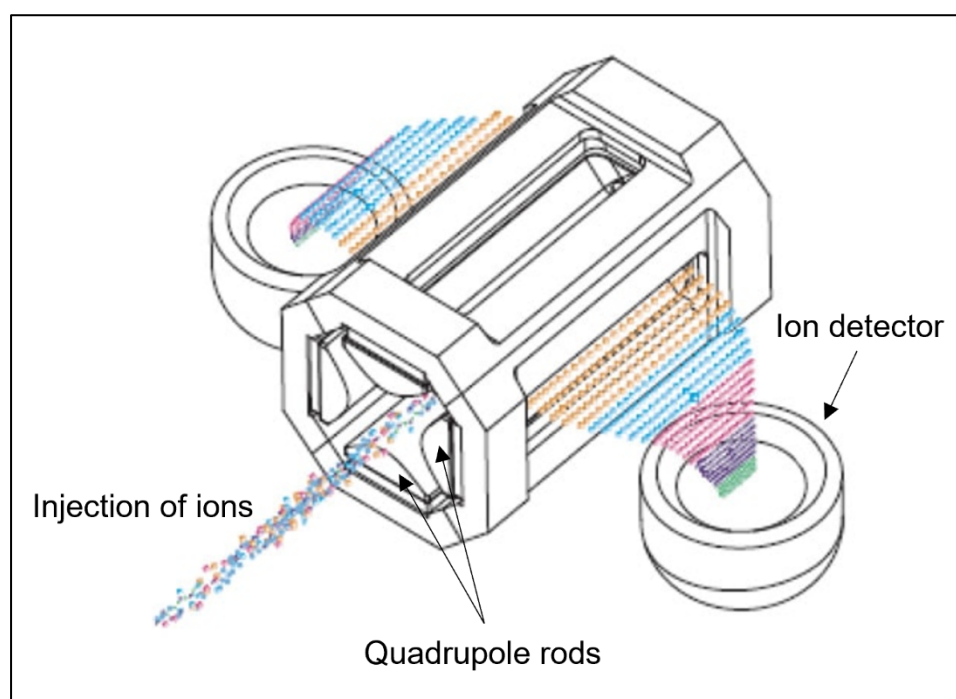


Figure 1.24. A graphic of a linear ion trap (LIT)²⁶⁰. The LIT consists of four rods (quadrupole-like), with two detectors each side to detect the ions escaping the LIT. The ions are detected based on their mass-to-charge ratio. Taken with permission from Thermo-Fisher.

The orbitrap analyser was first invented by Makarov and commercialised in 2000^{261,262}, and is made up of three primary components; one inner spindle-shaped electrode and two concave-shaped outer electrodes (see Figure 1.25). A voltage is applied to both the inner and outer electrodes to create a linear electric field, which induces the axial oscillation of ions when they enter the orbitrap analyser²⁵⁸. The outer electrodes detect the axial harmonic motion of the ions, and uses Fourier transform (FT) to convert the signal from the oscillating ions from a time domain

into a frequency domain, with the axial frequencies proportional to the m/z of the ions²⁶². Not only does this mean a high resolving power to distinguish between m/z values with a small difference, it can also achieve high mass accuracy meaning it is capable of calculating the m/z of an ion to up to four decimal places²⁶³.

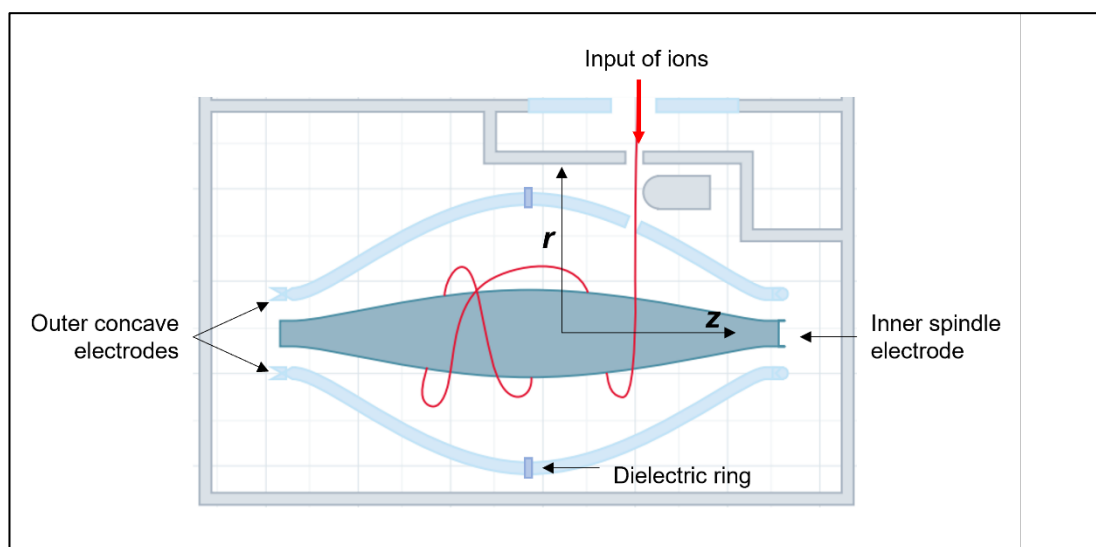


Figure 1.25. A schematic of an Orbitrap analyser²⁶⁴. Taken with permission from the Bioanalysis journal.

1.10.3. Detectors

The detector of the mass spectrometer has numerous desirable properties which include fast time response, low noise, high collection efficiency and long term stability²⁶⁵. There are several different types of detectors such as electron multipliers and Faraday cups, the former of which was spoken about in section 1.10.2 as the detector used in the linear ion trap. The Faraday cup is a simple electrode that intercepts the ion beam directly to provide an absolute measure of ion current. In contrast, the electron multiplier is the most widely used detector type in mass spectrometry, with three main types available including discrete dynode multipliers, continuous dynode multipliers and microchannel plate multipliers. Although the types differ, the mechanism of action is the same where ions strike the first dynode/electron-generating surface which results in the ejection of one or more electrons and accelerate towards the secondary dynode/electron-generating surface. When the electrons hit the second electron-generating surface there is an ejection of additional electrons, with this process repeats through a series of dynodes²⁶⁶.

1.10.4. Tandem mass spectrometry (MSⁿ)

Tandem MS, also known as product ion analysis, is a multi-step process of fragmenting ions of interest based on their m/z . This process can be repeated multiple times to extract further structural information from an ion of interest. This is important in sterolomics as many oxysterols have the same mass and chemical formula, therefore fragmentation of an ion can help to distinguish it from another ion with a very similar structure. There are many instruments capable of fragmenting an ion, which can be done either by tandem-in-space or tandem-in-time, however in this thesis only tandem-in-time is utilised. Tandem-in-time analysis is done using a single instrument, but separate stages are carried out at different times^{243,267}, with an example being a linear ion-trap (ITMS).

In ITMS, fragmentation occurs in a sequence, beginning with the selection of ions of a specific m/z with others expelled from the trap completely. The selected ions are then fragmented via CID using a neutral gas such as helium. Analysis of the fragment ions is then carried out either using the stability limit or resonant ejection of the fragments. This can then be repeated by selecting a fragment from the trap and further fragmenting it (MSⁿ)²⁶⁸.

There are also hybrid and tribrid mass spectrometer systems, defined by their multiple mass analysers, with examples including linear ion trap and Orbitrap systems (hybrid) and systems with an additional quadrupole (tribrid). The multiple mass analysers allow for the separation of masses independent of their fragmentation. Examples of these systems include both the Orbitrap Elite (hybrid) and Orbitrap ID-X (tribrid) systems which were used in this thesis.

1.10.5. Orbitrap Elite and IDX MS

For this thesis, Orbitrap systems were used for both the analysis of extracts from both biofluid samples and brain tissue samples. The Orbitrap Elite system (shown in Figure 1.26) used for our analysis begins with an ESI ion source, followed by the S-lens to focus the ions into a tight beam before propelling them towards the neutral blocker which removes neutral or uncharged molecules from the ion beam. The octopole works to focus the ion beam further before it is introduced into the ion trap (high-pressure and low-pressure cells). The ion trap ‘packets’ the ions, which can be

sent for FT scanning in the Orbitrap or fragmented multiple times for tandem MS. If fragmented during tandem MS, the fragmented ions are detected using the electron multiplier detectors. Alternatively, the ion ‘packet’ can be propelled through the quadrupole, which can also be used as a mass filter or ion guide, and into the C-trap which focuses the ions before injection into the orbitrap. The ions move around the orbitrap by oscillating axially, where individual ion frequencies get converted into m/z using FT at a very high resolution.

For tandem mass spectrometry (MS^n), the ions of a specific m/z are isolated in the ion trap and fragmented using helium gas. The daughter ions are filtered out, with a single fragment isolated again for further fragmentation in the trap for MS^3 analysis.

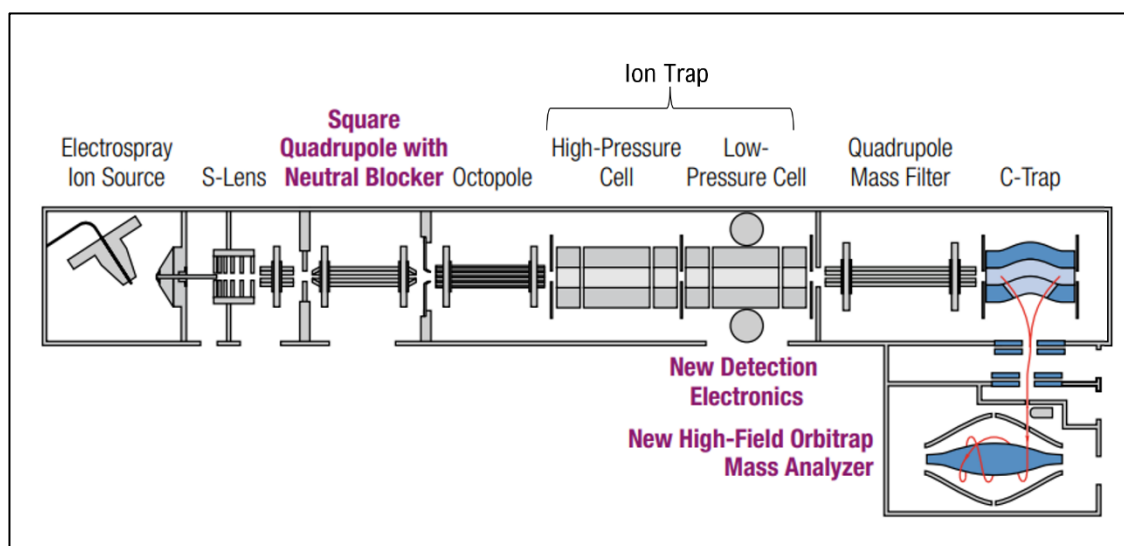


Figure 1.26. Schematic diagram of the Orbitrap Elite hybrid mass spectrometer. The individual components of the Orbitrap Elite mass spectrometer system, including the dual mass analyser system of a quadrupole/ ion trap. Taken with permission from Thermo Scientific.

The Orbitrap ID-X (shown in Figure 1.26) again begins with ionisation through the ESI source, followed by the S-lens to focus the ion ‘packet’ into a tight beam before the active beam guide removes neutral or negative ions (when looking in positive ion mode). The quadrupole filters the ion beam to retain the mass of interest via the application of a set voltage to the four cylindrical rods (see Figure 1.23 for reference). The ions of a selected mass then either move to the Orbitrap via the C-trap for FT scanning, or to the dual-pressure linear ion trap for fragmentation (high-pressure and low-pressure cells). For FT-MS, the ions move around the orbitrap by

oscillating axially, where individual ion frequencies get converted into m/z using FT at a very high resolution.

For ion trap fragmentation, or tandem mass spectrometry (MS^n), the ions of a specific m/z are isolated in the ion trap and fragmented using helium gas. The daughter ions are filtered out, with a single fragment isolated again for further fragmentation in the trap for MS^3 analysis.

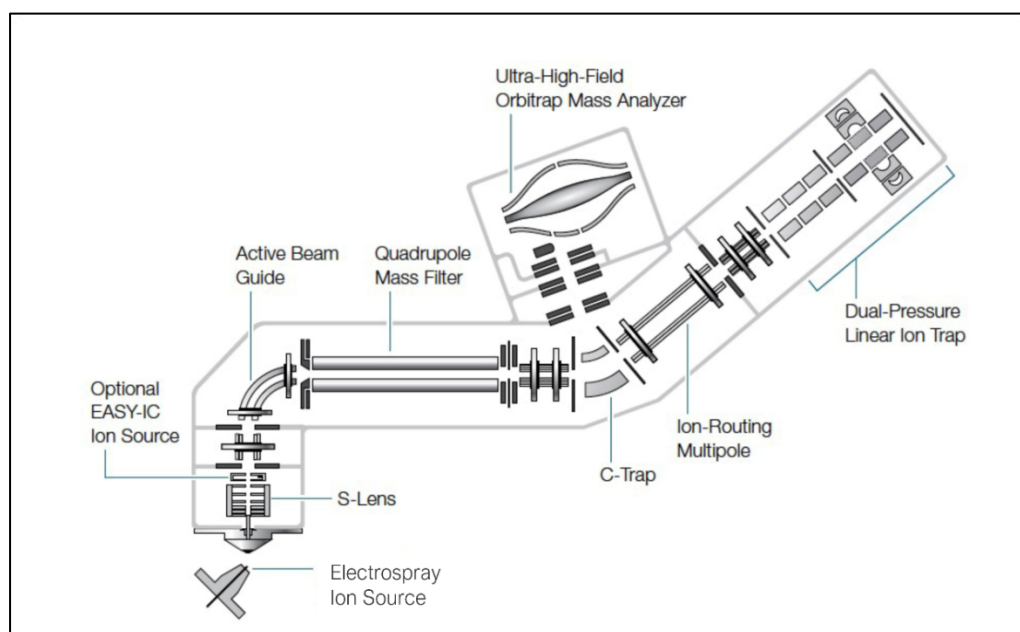


Figure 1.27. Schematic diagram of the Orbitrap ID-X tribrid mass spectrometer. The individual components of the Orbitrap ID-X mass spectrometer system. Taken with permission from Thermo Scientific.

1.11. Mass spectrometry imaging (MSI) techniques

The more conventional methods for the analysis of sterols from tissue samples is through homogenisation techniques. However, this process loses the structural integrity and information from the tissue sample, which is important and relevant when analysing certain diseases including multiple sclerosis, AD and HD, all of whom display neuropathological hallmarks of disease which can be seen within the tissue. These regions of interest could be of huge importance when analysing specific biomolecules and could change significantly between regions. However, current protocols to isolate these regions rely on methods such as micro-punctures or dissection of tissue which carry a risk of oversampling outside of the regions of interest resulting in inaccurate results.

Within the last few decades, exciting new techniques surrounding mass spectrometry imaging have been discovered, allowing for the precise analysis of proteins, lipids and many other biomolecules across intact tissue sections. These techniques can provide exact analysis of pathological and anatomical regions of interest.

There are many imaging techniques that utilise several ion sources for MSI including desorption electrospray ionisation (DESI), easy ambient sonic spray ionisation (EASI) and secondary ion mass spectrometry (SIMS), however, the most popular ionisation technique is matrix assisted laser desorption/ ionisation (MALDI)²⁶⁹ due to its capability of analysing a broad range of molecules including many lipid species. However, each imaging technique has its advantages depending on the analysis required.

SIMS is a hard ionisation technique that can be achieved at very high spatial resolution (up to 100 nm) with high sensitivity²⁷⁰, and is known for its analysis of inorganic compounds and biomolecules with low molecular weights²⁷¹ (see Figure 1.28). SIMS works by using a primary ion beam under vacuum which interacts with the sample surface. The secondary ions generated are ejected from this process called ‘spluttering’, which are then accelerated, focused, and taken into the mass spectrometer (usually coupled with a ToF)²⁷². However, like with most hard ionisation techniques there is a disadvantage of excess fragmentation when ‘spluttering’ occurs, and has a limited mass range²⁷³. They also cannot simultaneously do both full scan and MS/MS analyses²⁷⁴.

DESI is a spray-based soft ionisation technique, which is used to analyse different types of molecules at a wider mass range (see Figure 1.28)^{271,275}. However, it does have a much lower maximum spatial resolution in comparison to other imaging methods like SIMS due to the minimum laser spot size being larger (generally around 200µm²⁷⁶). This can be increased (up to 10-20µm spatial resolution²⁷⁷), however with increased spatial resolution you get a decrease in sensitivity and signal so balancing these factors is key to DESI analysis. DESI works by using charged droplets, which are a result of solvent ESI. These charged droplets impact the sample surface to desorb analytes in the secondary droplets formed²⁷⁸.

Like DESI, EASI is another desorption spray technique, however, has a much softer ionisation. It uses sonic spray rather than electrospray for ionisation making it a voltage-free process and has been successfully applied to rat brain tissue for lipid analysis²⁷⁹.

MALDI-MSI utilises the laser ionisation by shooting directly onto the matrix-sprayed tissue surface, effectively exciting and desorbing ions from the sample surface, and gaining a spatial resolution of $10\mu\text{m}$ ^{280,281} but again, with an increased spatial resolution you get a decrease in sensitivity and signal. It has the quickest acquisition rate of the MSI techniques, with the development of lasers with high repetition rates and the use of continuous raster sampling meaning a with instruments like the atmospheric pressure (AP)-MALDI, a $1\text{cm} \times 1\text{cm}$ area at $50\mu\text{m}$ can be acquired within 2.5hrs²⁸². However, the time of acquisition is dependent on several parameters (for example a higher spatial resolution would take a longer time to acquire), so a balance is needed to obtain a high-resolution image with good sensitivity without taking extensive periods of time.

Applying these techniques to sterol analysis has been difficult, primarily due to the difficulty with ionising these molecules and that most sterols are isobaric. Some groups have tried to overcome this by using methods to improve ionisation including silver nanoparticles²⁸³ and MALDI-2 (a post-ionisation laser technique to improve ion yield)²⁸⁴. More recently derivatisation of sterols with Girard-P hydrazine has been applied to MSI to improve ionisation from MALDI²⁵⁶. The coupling of mass spectrometry imaging methods with gas phase ion mobility has been increasingly explored to help with separation of isobaric molecular species, and also improve detection of low abundant ions (for example oxysterols) using drift gas and an electric field prior to analysis by the mass spectrometry²⁸⁵.

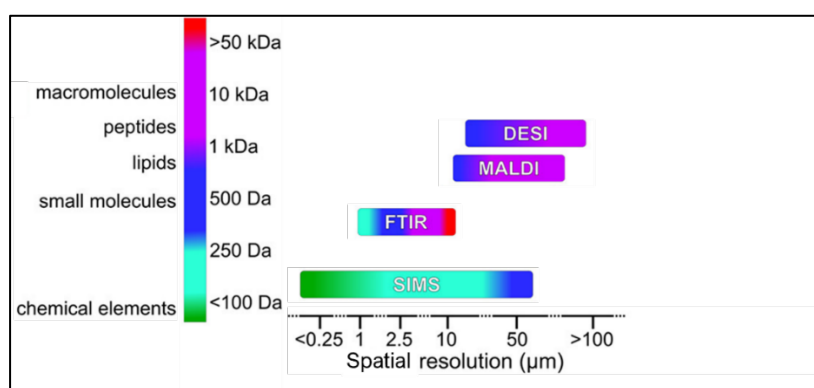


Figure 1.28. The spatial resolution versus the molecular mass range for different MSI techniques²⁷⁶. 1 Dalton (Da) is equivalent to 0.9999 atomic mass units. Taken with permission from the American Chemical Society.

These novel techniques open a possibility to explore the visualisation of these molecules across tissue to record the distribution across a sample rather than the total profile, which could be important in exploring sterols in diseases including neurodegenerative conditions and cancer where region specificity is vital.

1.12. Aims of this thesis

This thesis and the work included was focused on the understanding of sterol profiles in the human brain in both control and neurodegenerative samples. The analysis was broad, and completed using various biomaterials, utilising different methods of analysis including HPLC-MS/MS/MS and MALDI imaging techniques.

The main objectives of this work included:

1. The analysis of sterols from plasma/serum and brain tissue from individuals with cerebrotendinous xanthomatosis (CTX) to understand the sterol profiles of an individual with a depleted enzyme (CYP27A1) important for sterol regulation and the differences between the biological materials.
2. The analysis and understanding of sterol profiles surrounding various neurodegenerative diseases using homogenisation of human brain tissue.
3. The optimisation of a reproducible sample preparation method for the imaging of cholesterol using MALDI-MS for the visualisation and quantification of cholesterol in animal brain tissue.
4. The application of a robust and reproducible mass spectrometry imaging method to human and mouse neurodegenerative brain tissue for the visualisation and accurate quantification of cholesterol across whole brain and within specific neuropathological regions of interest.

1.13. References

1. Woodward, R. B. & Bloch, K. The cyclization of squalene in cholesterol synthesis. *J. Am. Chem. Soc.* **75**, 2023–2024 (1953).
2. Chen, L.-L., Wang, G.-Z. & Zhang, H.-Y. Sterol biosynthesis and prokaryotes-to-eukaryotes evolution. *Biochem. Biophys. Res. Commun.* **363**, 885–888 (2007).
3. Summons, R. E., Bradley, A. S., Jahnke, L. L. & Waldbauer, J. R. Steroids, triterpenoids and molecular oxygen. *Philos. Trans. R. Soc. B Biol. Sci.* **361**, 951–968 (2006).
4. Luo, J., Yang, H. & Song, B.-L. Mechanisms and regulation of cholesterol homeostasis. *Nat. Rev. Mol. Cell Biol.* **21**, 225–245 (2020).
5. Wielkoszyński, T. *et al.* Oxysterols increase inflammation, lipid marker levels and reflect accelerated endothelial dysfunction in experimental animals. *Mediators Inflamm.* **2018**, (2018).
6. Dai, L. *et al.* Cholesterol Metabolism in Neurodegenerative Diseases: Molecular Mechanisms and Therapeutic Targets. *Mol. Neurobiol.* **58**, 2183–2201 (2021).
7. Craig, M., Yarrarapu, S. N. S. & Dimri, M. Biochemistry, Cholesterol. *StatPearls* (2021).
8. Bloch, K. The Biological Synthesis of Cholesterol. *Science (80-.)*. **150**, 19–28 (1965).
9. KANDUTSCH, A. A. & RUSSELL, A. E. Preputial gland tumor sterols. 3. A metabolic pathway from lanosterol to cholesterol. *J. Biol. Chem.* **235**, 2256–61 (1960).
10. Mitsche, M. A., McDonald, J. G., Hobbs, H. H. & Cohen, J. C. Flux analysis of cholesterol biosynthesis in vivo reveals multiple tissue and cell-type specific pathways. *Elife* **4**, (2015).
11. Porter, F. D. Smith–Lemli–Opitz syndrome: pathogenesis, diagnosis and management. *Eur. J. Hum. Genet.* **16**, 535–541 (2008).
12. Nestel, P. J. & Poyser, A. Changes in cholesterol synthesis and excretion when cholesterol intake is increased. *Metabolism* **25**, 1591–1599 (1976).
13. Moutinho, M., Nunes, M. J. & Rodrigues, E. The mevalonate pathway in neurons: It's not just about cholesterol. *Exp. Cell Res.* **360**, 55–60 (2017).
14. Griffiths, W. J. & Wang, Y. Oxysterol research: a brief review. *Biochem. Soc. Trans.* **47**, 517–526 (2019).
15. Willinger, T. Oxysterols in intestinal immunity and inflammation. *J. Intern. Med.* **285**, 367–380 (2019).
16. Hannedouche, S. *et al.* Oxysterols direct immune cell migration via EBI2. *Nature* **475**, 524–527 (2011).
17. DuSell, C. D., Umetani, M., Shaul, P. W., Mangelsdorf, D. J. & McDonnell, D. P. 27-Hydroxycholesterol Is an Endogenous Selective Estrogen Receptor Modulator. *Mol. Endocrinol.* **22**, 65–77 (2008).

18. Kloudova, A., Guengerich, F. P. & Soucek, P. The Role of Oxysterols in Human Cancer. *Trends Endocrinol. Metab.* **28**, 485–496 (2017).
19. Testa, G. *et al.* Changes in brain oxysterols at different stages of Alzheimer's disease: Their involvement in neuroinflammation. *Redox Biol.* **10**, 24–33 (2016).
20. Zmysłowski, A. & Szterk, A. Oxysterols as a biomarker in diseases. *Clin. Chim. Acta* **491**, 103–113 (2019).
21. Björkhem, I. *et al.* Oxysterols and Parkinson's disease: Evidence that levels of 24S-hydroxycholesterol in cerebrospinal fluid correlates with the duration of the disease. *Neurosci. Lett.* **555**, 102–105 (2013).
22. Petrov, A. M., Kasimov, M. R. & Zefirov, A. L. Brain Cholesterol Metabolism and Its Defects: Linkage to Neurodegenerative Diseases and Synaptic Dysfunction. *Acta Naturae* **8**, 58–73 (2016).
23. Crick, P. J. *et al.* Reduced Plasma Levels of 25-Hydroxycholesterol and Increased Cerebrospinal Fluid Levels of Bile Acid Precursors in Multiple Sclerosis Patients. *Mol. Neurobiol.* **54**, 8009–8020 (2017).
24. Boussicault, L. *et al.* CYP46A1, the rate-limiting enzyme for cholesterol degradation, is neuroprotective in Huntington's disease. *Brain* **139**, 953–970 (2016).
25. Brown, A. J. & Jessup, W. Oxysterols: Sources, cellular storage and metabolism, and new insights into their roles in cholesterol homeostasis. *Mol. Aspects Med.* **30**, 111–122 (2009).
26. Russell, D. Oxysterol biosynthetic enzymes. *Biochim. Biophys. Acta - Mol. Cell Biol. Lipids* **1529**, 126–135 (2000).
27. Choi, C. & Finlay, D. K. Diverse Immunoregulatory Roles of Oxysterols—The Oxidized Cholesterol Metabolites. *Metabolites* **10**, 384 (2020).
28. Samadi, A. *et al.* A Comprehensive Review on Oxysterols and Related Diseases. *Curr. Med. Chem.* **28**, 110–136 (2020).
29. Javitt, N. 26-Hydroxycholesterol: synthesis, metabolism, and biologic activities. *J. Lipid Res.* **31**, 1527–1533 (1990).
30. Griffiths, W. J. & Wang, Y. Oxysterols as lipid mediators: Their biosynthetic genes, enzymes and metabolites. *Prostaglandins Other Lipid Mediat.* **147**, 106381 (2020).
31. Björkhem, I., Meaney, S. & Diczfalusy, U. Oxysterols in human circulation: which role do they have? *Curr. Opin. Lipidol.* **13**, 247–253 (2002).
32. Umetani, M. *et al.* 27-Hydroxycholesterol is an endogenous SERM that inhibits the cardiovascular effects of estrogen. *Nat. Med.* **13**, 1185–1192 (2007).
33. Raza, S. *et al.* The cholesterol metabolite 27-hydroxycholesterol stimulates cell proliferation via ER β in prostate cancer cells. *Cancer Cell Int.* **17**, 52 (2017).
34. Theofilopoulos, S. *et al.* Cholestenoic acids regulate motor neuron survival via liver X receptors. *J. Clin. Invest.* **124**, 4829–4842 (2014).
35. Leoni, V. *et al.* Diagnostic use of cerebral and extracerebral oxysterols. *Clin. Chem. Lab. Med.* **42**, (2004).
36. Pilo de la Fuente, B. *et al.* Usefulness of cholestanol levels in the diagnosis and follow-up of patients with cerebrotendinous xanthomatosis. *Neurol. (English Ed.)* **26**, 397–404 (2011).
37. Gill, S., Chow, R. & Brown, A. J. Sterol regulators of cholesterol homeostasis and beyond: The oxysterol hypothesis revisited and revised. *Prog. Lipid Res.*

- 47, 391–404 (2008).
38. Fan, L., Joseph, J. F., Durairaj, P., Parr, M. K. & Bureik, M. Conversion of chenodeoxycholic acid to cholic acid by human CYP8B1. *Biol. Chem.* **400**, 625–628 (2019).
39. Cyster, J. G., Dang, E. V., Reboldi, A. & Yi, T. 25-Hydroxycholesterols in innate and adaptive immunity. *Nat. Rev. Immunol.* **14**, 731–743 (2014).
40. Park, K. & Scott, A. L. Cholesterol 25-hydroxylase production by dendritic cells and macrophages is regulated by type I interferons. *J. Leukoc. Biol.* **88**, 1081–1087 (2010).
41. Bauman, D. R. *et al.* 25-Hydroxycholesterol secreted by macrophages in response to Toll-like receptor activation suppresses immunoglobulin A production. *Proc. Natl. Acad. Sci.* **106**, 16764–16769 (2009).
42. Reboldi, A. *et al.* 25-Hydroxycholesterol suppresses interleukin-1–driven inflammation downstream of type I interferon. *Science (80-.).* **345**, 679–684 (2014).
43. Pereira, J. P., Kelly, L. M., Xu, Y. & Cyster, J. G. EBI2 mediates B cell segregation between the outer and centre follicle. *Nature* **460**, 1122–1126 (2009).
44. Howell, O. W. *et al.* Meningeal inflammation is widespread and linked to cortical pathology in multiple sclerosis. *Brain* **134**, 2755–2771 (2011).
45. Magliozzi, R. *et al.* Meningeal B-cell follicles in secondary progressive multiple sclerosis associate with early onset of disease and severe cortical pathology. *Brain* **130**, 1089–1104 (2007).
46. Nashi, E., Wang, Y. & Diamond, B. The role of B cells in lupus pathogenesis. *Int. J. Biochem. Cell Biol.* **42**, 543–550 (2010).
47. Dai, L. *et al.* Cholesterol Metabolism in Neurodegenerative Diseases: Molecular Mechanisms and Therapeutic Targets. *Mol. Neurobiol.* **58**, 2183–2201 (2021).
48. Björkhem, I. *et al.* From Brain to Bile. *J. Biol. Chem.* **276**, 37004–37010 (2001).
49. Griffiths, W. J. *et al.* Analytical strategies for characterization of oxysterol lipidomes: Liver X receptor ligands in plasma. *Free Radic. Biol. Med.* **59**, 69–84 (2013).
50. Zhao, C. & Dahlman-Wright, K. Liver X receptor in cholesterol metabolism. *J. Endocrinol.* **204**, 233–240 (2010).
51. Altmann, S. W. *et al.* Niemann-Pick C1 Like 1 Protein Is Critical for Intestinal Cholesterol Absorption. *Science (80-.).* **303**, 1201–1204 (2004).
52. Horton, J. D., Goldstein, J. L. & Brown, M. S. SREBPs: activators of the complete program of cholesterol and fatty acid synthesis in the liver. *J. Clin. Invest.* **109**, 1125–1131 (2002).
53. Sakai, J. *et al.* Identification of Complexes between the COOH-terminal Domains of Sterol Regulatory Element-binding Proteins (SREBPs) and SREBP Cleavage-Activating Protein. *J. Biol. Chem.* **272**, 20213–20221 (1997).
54. Lee, J. N., Song, B., DeBose-Boyd, R. A. & Ye, J. Sterol-regulated Degradation of Insig-1 Mediated by the Membrane-bound Ubiquitin Ligase gp78. *J. Biol. Chem.* **281**, 39308–39315 (2006).
55. Xue, L. *et al.* Targeting SREBP-2-Regulated Mevalonate Metabolism for Cancer Therapy. *Front. Oncol.* **10**, (2020).
56. Brown, M. S., Radhakrishnan, A. & Goldstein, J. L. Retrospective on

- Cholesterol Homeostasis: The Central Role of Scap. *Annu. Rev. Biochem.* **87**, 783–807 (2018).
57. Radhakrishnan, A., Ikeda, Y., Kwon, H. J., Brown, M. S. & Goldstein, J. L. Sterol-regulated transport of SREBPs from endoplasmic reticulum to Golgi: Oxysterols block transport by binding to Insig. *Proc. Natl. Acad. Sci.* **104**, 6511–6518 (2007).
 58. Peet, D. J. *et al.* Cholesterol and Bile Acid Metabolism Are Impaired in Mice Lacking the Nuclear Oxysterol Receptor LXR α . *Cell* **93**, 693–704 (1998).
 59. Goodwin, B. *et al.* Differential Regulation of Rat and Human CYP7A1 by the Nuclear Oxysterol Receptor Liver X Receptor- α . *Mol. Endocrinol.* **17**, 386–394 (2003).
 60. Barbier, O., Trottier, J., Kaeding, J., Caron, P. & Verreault, M. Lipid-activated transcription factors control bile acid glucuronidation. *Mol. Cell. Biochem.* **326**, 3–8 (2009).
 61. Yu, L. *et al.* Disruption of Abcg5 and Abcg8 in mice reveals their crucial role in biliary cholesterol secretion. *Proc. Natl. Acad. Sci.* **99**, 16237–16242 (2002).
 62. Hu, X. *et al.* LXR β activation increases intestinal cholesterol absorption, leading to an atherogenic lipoprotein profile. *J. Intern. Med.* **272**, 452–464 (2012).
 63. Afonso, M. S. *et al.* Molecular Pathways Underlying Cholesterol Homeostasis. *Nutrients* **10**, 760 (2018).
 64. Wang, Y. *et al.* Regulation of Cholesterologenesis by the Oxysterol Receptor, LXR α . *J. Biol. Chem.* **283**, 26332–26339 (2008).
 65. DeBose-Boyd, R. A. Feedback regulation of cholesterol synthesis: sterol-accelerated ubiquitination and degradation of HMG CoA reductase. *Cell Res.* **18**, 609–621 (2008).
 66. Gill, S., Stevenson, J., Kristiana, I. & Brown, A. J. Cholesterol-Dependent Degradation of Squalene Monooxygenase, a Control Point in Cholesterol Synthesis beyond HMG-CoA Reductase. *Cell Metab.* **13**, 260–273 (2011).
 67. Goldstein, J. L. & Brown, M. S. The LDL Pathway in Human Fibroblasts: A Receptor-Mediated Mechanism for the Regulation of Cholesterol Metabolism. in 147–181 (1976). doi:10.1016/B978-0-12-152811-9.50011-0.
 68. Goldstein, J. L. & Brown, M. S. The LDL Receptor. *Arterioscler. Thromb. Vasc. Biol.* **29**, 431–438 (2009).
 69. Gatto, D., Paus, D., Basten, A., Mackay, C. R. & Brink, R. Guidance of B Cells by the Orphan G Protein-Coupled Receptor EBI2 Shapes Humoral Immune Responses. *Immunity* **31**, 259–269 (2009).
 70. Liu, C. *et al.* Oxysterols direct B-cell migration through EBI2. *Nature* **475**, 519–523 (2011).
 71. Gatto, D. *et al.* The chemotactic receptor EBI2 regulates the homeostasis, localization and immunological function of splenic dendritic cells. *Nat. Immunol.* **14**, 446–453 (2013).
 72. Lu, E., Dang, E. V., McDonald, J. G. & Cyster, J. G. Distinct oxysterol requirements for positioning naïve and activated dendritic cells in the spleen. *Sci. Immunol.* **2**, (2017).
 73. Liu, S.-Y. *et al.* Interferon-Inducible Cholesterol-25-Hydroxylase Broadly Inhibits Viral Entry by Production of 25-Hydroxycholesterol. *Immunity* **38**, 92–105 (2013).
 74. Li, C. *et al.* 25-Hydroxycholesterol Protects Host against Zika Virus Infection

- and Its Associated Microcephaly in a Mouse Model. *Immunity* **46**, 446–456 (2017).
75. Dang, E. V., McDonald, J. G., Russell, D. W. & Cyster, J. G. Oxysterol Restraint of Cholesterol Synthesis Prevents AIM2 Inflammasome Activation. *Cell* **171**, 1057–1071.e11 (2017).
 76. Gold, E. S. *et al.* 25-Hydroxycholesterol acts as an amplifier of inflammatory signaling. *Proc. Natl. Acad. Sci.* **111**, 10666–10671 (2014).
 77. Dietschy, J. M. Central nervous system: cholesterol turnover, brain development and neurodegeneration. *Biol. Chem.* **390**, (2009).
 78. Björkhem, I. Crossing the barrier: Oxysterols as cholesterol transporters and metabolic modulators in the brain. *J. Intern. Med.* **260**, 493–508 (2006).
 79. Iuliano, L. *et al.* Cholesterol metabolites exported from human brain. *Steroids* **99**, 189–193 (2015).
 80. Lund, E. G. *et al.* Knockout of the Cholesterol 24-Hydroxylase Gene in Mice Reveals a Brain-specific Mechanism of Cholesterol Turnover. *J. Biol. Chem.* **278**, 22980–22988 (2003).
 81. Björkhem, I., Cedazo-Minguez, A., Leoni, V. & Meaney, S. Oxysterols and neurodegenerative diseases. *Mol. Aspects Med.* **30**, 171–179 (2009).
 82. Meaney, S. *et al.* Novel route for elimination of brain oxysterols across the blood-brain barrier: conversion into 7 α -hydroxy-3-oxo-4-cholestenoic acid. *J. Lipid Res.* **48**, 944–951 (2007).
 83. Mahley, R. W. Central Nervous System Lipoproteins. *Arterioscler. Thromb. Vasc. Biol.* **36**, 1305–1315 (2016).
 84. Björkhem, I. & Meaney, S. Brain Cholesterol: Long Secret Life Behind a Barrier. *Arterioscler. Thromb. Vasc. Biol.* **24**, 806–815 (2004).
 85. Quan, G., Xie, C., Dietschy, J. M. & Turley, S. D. Ontogenesis and regulation of cholesterol metabolism in the central nervous system of the mouse. *Dev. Brain Res.* **146**, 87–98 (2003).
 86. Nieweg, K., Schaller, H. & Pfrieger, F. W. Marked differences in cholesterol synthesis between neurons and glial cells from postnatal rats. *J. Neurochem.* **109**, 125–134 (2009).
 87. Zhang, J. & Liu, Q. Cholesterol metabolism and homeostasis in the brain. *Protein Cell* **6**, 254–264 (2015).
 88. Kim, W. S., Weickert, C. S. & Garner, B. Role of ATP-binding cassette transporters in brain lipid transport and neurological disease. *J. Neurochem.* **104**, 1145–1166 (2008).
 89. Ramirez, D. M. O., Andersson, S. & Russell, D. W. Neuronal expression and subcellular localization of cholesterol 24-hydroxylase in the mouse brain. *J. Comp. Neurol.* **507**, 1676–1693 (2008).
 90. Gamba, P. *et al.* A Crosstalk Between Brain Cholesterol Oxidation and Glucose Metabolism in Alzheimer’s Disease. *Front. Neurosci.* **13**, (2019).
 91. Panzenboeck, U. *et al.* ABCA1 and Scavenger Receptor Class B, Type I, Are Modulators of Reverse Sterol Transport at an in Vitro Blood-Brain Barrier Constituted of Porcine Brain Capillary Endothelial Cells. *J. Biol. Chem.* **277**, 42781–42789 (2002).
 92. Cummings, J. The Role of Neuropsychiatric Symptoms in Research Diagnostic Criteria for Neurodegenerative Diseases. *Am. J. Geriatr. Psychiatry* **29**, 375–383 (2021).
 93. Reich, D. S., Lucchinetti, C. F. & Calabresi, P. A. Multiple Sclerosis. *N. Engl. J. Med.* **378**, 169–180 (2018).

94. Lassmann, H. Multiple Sclerosis Pathology. *Cold Spring Harb. Perspect. Med.* **8**, a028936 (2018).
95. Bretillon, L. *et al.* Plasma levels of 24S-hydroxycholesterol in patients with neurological diseases. *Neurosci. Lett.* **293**, 87–90 (2000).
96. Heverin, M. *et al.* Changes in the levels of cerebral and extracerebral sterols in the brain of patients with Alzheimer's disease. *J. Lipid Res.* **45**, 186–193 (2004).
97. Björkhem, I. *et al.* Oxysterols and Parkinson's disease: Evidence that levels of 24S-hydroxycholesterol in cerebrospinal fluid correlates with the duration of the disease. *Neurosci. Lett.* **555**, 102–105 (2013).
98. Doria, M., Maugest, L., Moreau, T., Lizard, G. & Vejux, A. Contribution of cholesterol and oxysterols to the pathophysiology of Parkinson's disease. *Free Radic. Biol. Med.* **101**, 393–400 (2016).
99. Guo, X. *et al.* The serum lipid profile of Parkinson's disease patients: a study from China. *Int. J. Neurosci.* **125**, 838–844 (2015).
100. Leoni, V. *et al.* Changes in human plasma levels of the brain specific oxysterol 24S-hydroxycholesterol during progression of multiple sclerosis. *Neurosci. Lett.* **331**, 163–166 (2002).
101. Zhornitsky, S., McKay, K. A., Metz, L. M., Teunissen, C. E. & Rangachari, M. Cholesterol and markers of cholesterol turnover in multiple sclerosis: relationship with disease outcomes. *Mult. Scler. Relat. Disord.* **5**, 53–65 (2016).
102. Valenza, M. *et al.* Progressive dysfunction of the cholesterol biosynthesis pathway in the R6/2 mouse model of Huntington's disease. *Neurobiol. Dis.* **28**, 133–142 (2007).
103. Valenza, M. *et al.* Cholesterol Defect Is Marked across Multiple Rodent Models of Huntington's Disease and Is Manifest in Astrocytes. *J. Neurosci.* **30**, 10844–10850 (2010).
104. Kacher, R. *et al.* CYP46A1 gene therapy deciphers the role of brain cholesterol metabolism in Huntington's disease. *Brain* **142**, 2432–2450 (2019).
105. Hardy, J. & Selkoe, D. J. The Amyloid Hypothesis of Alzheimer's Disease: Progress and Problems on the Road to Therapeutics. *Science (80-.).* **297**, 353–356 (2002).
106. Holtzman, D. M., Morris, J. C. & Goate, A. M. Alzheimer's Disease: The Challenge of the Second Century. *Sci. Transl. Med.* **3**, (2011).
107. Pascoal, T. A. *et al.* Amyloid- β and hyperphosphorylated tau synergy drives metabolic decline in preclinical Alzheimer's disease. *Mol. Psychiatry* **22**, 306–311 (2017).
108. Sinha, S. & Lieberburg, I. Cellular mechanisms of β -amyloid production and secretion. *Proc. Natl. Acad. Sci.* **96**, 11049–11053 (1999).
109. Flammang, B. *et al.* Evidence that the Amyloid- β Protein Precursor Intracellular Domain, AICD, Derives From β -Secretase-Generated C-Terminal Fragment. *J. Alzheimer's Dis.* **30**, 145–153 (2012).
110. Lesné, S. *et al.* A specific amyloid- β protein assembly in the brain impairs memory. *Nature* **440**, 352–357 (2006).
111. Jarrett, J. T., Berger, E. P. & Lansbury, P. T. The carboxy terminus of the .beta. amyloid protein is critical for the seeding of amyloid formation: Implications for the pathogenesis of Alzheimer's disease. *Biochemistry* **32**, 4693–4697 (1993).

112. Teplov, D. B. Structural and kinetic features of amyloid β -protein fibrillogenesis. *Amyloid* **5**, 121–142 (1998).
113. Weingarten, M. D., Lockwood, A. H., Hwo, S. Y. & Kirschner, M. W. A protein factor essential for microtubule assembly. *Proc. Natl. Acad. Sci.* **72**, 1858–1862 (1975).
114. Khatoon, S., Grundke-Iqbal, I. & Iqbal, K. Levels of normal and abnormally phosphorylated tau in different cellular and regional compartments of Alzheimer disease and control brains. *FEBS Lett.* **351**, 80–84 (1994).
115. Wang, Y. & Mandelkow, E. Tau in physiology and pathology. *Nat. Rev. Neurosci.* **17**, 22–35 (2016).
116. Chu, D. & Liu, F. Pathological Changes of Tau Related to Alzheimer's Disease. *ACS Chem. Neurosci.* **10**, 931–944 (2019).
117. Lin, Y.-T. *et al.* The binding and phosphorylation of Thr231 is critical for Tau's hyperphosphorylation and functional regulation by glycogen synthase kinase 3 β . *J. Neurochem.* **103**, 802–813 (2007).
118. Arnold, S. E., Hyman, B. T., Flory, J., Damasio, A. R. & Van Hoesen, G. W. The Topographical and Neuroanatomical Distribution of Neurofibrillary Tangles and Neuritic Plaques in the Cerebral Cortex of Patients with Alzheimer's Disease. *Cereb. Cortex* **1**, 103–116 (1991).
119. Arriagada, P. V., Growdon, J. H., Hedley-Whyte, E. T. & Hyman, B. T. Neurofibrillary tangles but not senile plaques parallel duration and severity of Alzheimer's disease. *Neurology* **42**, 631–631 (1992).
120. Markesbery, W. R. *et al.* Neuropathologic Substrate of Mild Cognitive Impairment. *Arch. Neurol.* **63**, 38 (2006).
121. Castellani, R. *et al.* Sublethal RNA Oxidation as a Mechanism for Neurodegenerative Disease. *Int. J. Mol. Sci.* **9**, 789–806 (2008).
122. Li, H.-L. *et al.* Phosphorylation of tau antagonizes apoptosis by stabilizing β -catenin, a mechanism involved in Alzheimer's neurodegeneration. *Proc. Natl. Acad. Sci.* **104**, 3591–3596 (2007).
123. Kuchibhotla, K. V. *et al.* Neurofibrillary tangle-bearing neurons are functionally integrated in cortical circuits in vivo. *Proc. Natl. Acad. Sci.* **111**, 510–514 (2014).
124. Kocahan, S. & Doğan, Z. Mechanisms of Alzheimer's Disease Pathogenesis and Prevention: The Brain, Neural Pathology, N-methyl-D-aspartate Receptors, Tau Protein and Other Risk Factors. *Clin. Psychopharmacol. Neurosci.* **15**, 1–8 (2017).
125. Thies, W. & Bleiler, L. 2013 Alzheimer's disease facts and figures. *Alzheimer's Dement.* **9**, 208–245 (2013).
126. Karch, C. M. & Goate, A. M. Alzheimer's Disease Risk Genes and Mechanisms of Disease Pathogenesis. *Biol. Psychiatry* **77**, 43–51 (2015).
127. Kanekiyo, T., Xu, H. & Bu, G. ApoE and A β in Alzheimer's Disease: Accidental Encounters or Partners? *Neuron* **81**, 740–754 (2014).
128. Harold, D. *et al.* Genome-wide association study identifies variants at CLU and PICALM associated with Alzheimer's disease. *Nat. Genet.* **41**, 1088–1093 (2009).
129. Corder, E. H. *et al.* Protective effect of apolipoprotein E type 2 allele for late onset Alzheimer disease. *Nat. Genet.* **7**, 180–184 (1994).
130. Wisniewski, T., Golabek, A., Matsubara, E., Ghiso, J. & Frangione, B. Apolipoprotein E: Binding to Soluble Alzheimer's β -Amyloid. *Biochem. Biophys. Res. Commun.* **192**, 359–365 (1993).

131. Wisniewski, T., Lalowski, M., Golabek, A., Frangione, B. & Vogel, T. Is Alzheimer's disease an apolipoprotein E amyloidosis? *Lancet* **345**, 956–958 (1995).
132. Morris, J. C. *et al.* APOE predicts amyloid-beta but not tau Alzheimer pathology in cognitively normal aging. *Ann. Neurol.* **67**, 122–131 (2010).
133. Lim, Y. Y. & Mormino, E. C. APOE genotype and early β -amyloid accumulation in older adults without dementia. *Neurology* **89**, 1028–1034 (2017).
134. Fryer, J. D. *et al.* Apolipoprotein E Markedly Facilitates Age-Dependent Cerebral Amyloid Angiopathy and Spontaneous Hemorrhage in Amyloid Precursor Protein Transgenic Mice. *J. Neurosci.* **23**, 7889–7896 (2003).
135. Castellano, J. M. *et al.* Human apoE Isoforms Differentially Regulate Brain Amyloid- β Peptide Clearance. *Sci. Transl. Med.* **3**, (2011).
136. Hatters, D. M., Peters-Libeu, C. A. & Weisgraber, K. H. Apolipoprotein E structure: insights into function. *Trends Biochem. Sci.* **31**, 445–454 (2006).
137. Boche, D. & Nicoll, J. A. R. Hypothesis: Entrapment of lipoprotein particles in the brain causes Alzheimer's disease. *Free Neuropathol.* **2**, 30 (2021).
138. Leoni, V. *et al.* Side chain oxidized oxysterols in cerebrospinal fluid and the integrity of blood-brain and blood-cerebrospinal fluid barriers. *J. Lipid Res.* **44**, 793–799 (2003).
139. Jenner, A. M. *et al.* The effect of APOE genotype on brain levels of oxysterols in young and old human APOE ϵ 2, ϵ 3 and ϵ 4 knock-in mice. *Neuroscience* **169**, 109–115 (2010).
140. Weingärtner, O. *et al.* Vascular effects of oxysterols and oxyphytosterols in apoE $-/-$ mice. *Atherosclerosis* **240**, 73–79 (2015).
141. Confavreux, C. & Vukusic, S. Natural history of multiple sclerosis: A unifying concept. *Brain* **129**, 606–616 (2006).
142. Correale, J. & Gaitán, M. I. Multiple sclerosis and environmental factors: The role of vitamin D, parasites, and Epstein-Barr virus infection. *Acta Neurol. Scand.* **132**, 46–55 (2015).
143. Oksenberg, J. R., Baranzini, S. E., Sawcer, S. & Hauser, S. L. The genetics of multiple sclerosis: SNPs to pathways to pathogenesis. *Nat. Rev. Genet.* **9**, 516–26 (2008).
144. Trojano, M. & Avolio, C. *Translational Neuroimmunology in Multiple Sclerosis: From Disease Mechanisms to Clinical Applications*. (2016).
145. Lublin, F. D. & Reingold, S. C. Defining the clinical course of multiple sclerosis results of an international survey. *Neurology* **46**, 907–911 (1996).
146. Andersson, P. B., Waubant, E., Gee, L., Goodkin, D. E. & WI, M. Multiple Sclerosis That Is Progressive From the Time of Onset. *Arch. Neurol.* **56**, 1138 (1999).
147. Noseworthy, J. H., Lucchinetti, C., Rodriguez, M. & Weinshenker, B. G. Multiple sclerosis. *N. Engl. J. Med.* **343**, 938–952 (2000).
148. Griffiths, L. *et al.* Substantial subpial cortical demyelination in progressive multiple sclerosis: have we underestimated the extent of cortical pathology? *Neuroimmunol. Neuroinflammation* (2020) doi:10.20517/2347-8659.2019.21.
149. Pitteri, M., Romualdi, C., Magliozzi, R., Monaco, S. & Calabrese, M. Cognitive impairment predicts disability progression and cortical thinning in MS: An 8-year study. *Mult. Scler.* **23**, 848–854 (2017).
150. Frischer, J. M. *et al.* Clinical and pathological insights into the dynamic nature of the white matter multiple sclerosis plaque. *Ann. Neurol.* **78**, 710–721

- (2015).
151. Curti, E., Graziuso, S., Tsantes, E., Crisi, G. & Granella, F. Correlation between cortical lesions and cognitive impairment in multiple sclerosis. 1–8 (2018) doi:10.1002/brb3.955.
 152. Harlow, D. E., Honce, J. M. & Miravalle, A. A. Remyelination Therapy in Multiple Sclerosis. *Front. Neurol.* **6**, (2015).
 153. Lubetzki, C., Zalc, B., Williams, A., Stadelmann, C. & Stankoff, B. Remyelination in multiple sclerosis: from basic science to clinical translation. *Lancet Neurol.* **19**, 678–688 (2020).
 154. Neumann, B. *et al.* Metformin Restores CNS Remyelination Capacity by Rejuvenating Aged Stem Cells. *Cell Stem Cell* **25**, 473–485.e8 (2019).
 155. Giannantoni, A. *et al.* Lower urinary tract dysfunction and disability status in patients with multiple sclerosis. *Arch. Phys. Med. Rehabil.* **80**, 437–441 (1999).
 156. Fisk, J. D., Pontefract, A., Ritvo, P. G., Archibald, C. J. & Murray, T. J. The impact of fatigue on patients with multiple sclerosis. *Can. J. Neurol. Sci.* **21**, 9–14 (1994).
 157. Schapiro, R. T. Managing symptoms of multiple sclerosis. *Neurol. Clin.* **23**, 177–187 (2005).
 158. Ziemssen, T. Symptom management in patients with multiple sclerosis. *J. Neurol. Sci.* **311**, S48–S52 (2011).
 159. Dawson, J. W. XVIII.—The Histology of Disseminated Sclerosis. *Trans. R. Soc. Edinburgh* **50**, 517–740 (1916).
 160. Brownell, B. & Hughes, J. T. The distribution of plaques in the cerebrum in multiple sclerosis. *Cortex* **265**, (1962).
 161. Calabrese, M. & Castellaro, M. Cortical Gray Matter MR Imaging in Multiple Sclerosis. *Neuroimaging Clin. N. Am.* **27**, 301–312 (2017).
 162. Calabrese, M., Filippi, M. & Gallo, P. Cortical lesions in multiple sclerosis. *Nat. Rev. Neurol.* **6**, 438–444 (2010).
 163. Filippi, M. *et al.* Association between pathological and MRI findings in multiple sclerosis. *Lancet Neurol.* **18**, 198–210 (2019).
 164. Kuhlmann, T. *et al.* An updated histological classification system for multiple sclerosis lesions. *Acta Neuropathol.* **133**, 13–24 (2017).
 165. Kutzelnigg, A. *et al.* Cortical demyelination and diffuse white matter injury in multiple sclerosis. *Brain* **128**, 2705–2712 (2005).
 166. Kutzelnigg, A. & Lassmann, H. Cortical demyelination in multiple sclerosis: A substrate for cognitive deficits? *J. Neurol. Sci.* **245**, 123–126 (2006).
 167. Rinaldi, F. *et al.* Cortical lesions and cognitive impairment in multiple sclerosis. *Neurol. Sci.* **31**, (2010).
 168. Gh Popescu, B. F. & Lucchinetti, C. F. Meningeal and cortical grey matter pathology in multiple sclerosis. *BMC Neurol.* **12**, 11 (2012).
 169. Campbell, G. R. & Mahad, D. J. Metabolic support of axons by oligodendrocytes: Implications for multiple sclerosis. *Mult. Scler. Relat. Disord.* **3**, 28–30 (2014).
 170. Ffrench-Constant, C. & Raff, M. C. Proliferating bipotential glial progenitor cells in adult rat optic nerve. *Nature* **319**, 499–502 (1986).
 171. Franklin, R. J. M. & Ffrench-Constant, C. Remyelination in the CNS: From biology to therapy. *Nature Reviews Neuroscience* vol. 9 839–855 (2008).
 172. Blakemore, W. F. Pattern of remyelination in the CNS. *Nature* **249**, 577–578 (1974).

173. Smith, K. J., Blakemore, W. F. & McDonald, W. I. Central remyelination restores secure conduction [12]. *Nature* **280**, 395–396 (1979).
174. Haider, L. *et al.* Multiple sclerosis deep grey matter: The relation between demyelination, neurodegeneration, inflammation and iron. *J. Neurol. Neurosurg. Psychiatry* **85**, 1386–1395 (2014).
175. Leoni, V. & Caccia, C. 24S-hydroxycholesterol in plasma: A marker of cholesterol turnover in neurodegenerative diseases. *Biochimie* **95**, 595–612 (2013).
176. Dominiczak, M. H. & Caslake, M. J. Apolipoproteins: metabolic role and clinical biochemistry applications. *Ann. Clin. Biochem. Int. J. Lab. Med.* **48**, 498–515 (2011).
177. Shireman, R. B. & Fisher, W. R. Apolipoprotein B: its role in the control of fibroblast cholesterol biosynthesis and in the regulation of its own binding to cellular receptors. *J. Lipid Res.* **20**, 594–8 (1979).
178. Browne, R. W. *et al.* Apolipoproteins are associated with new MRI lesions and deep grey matter atrophy in clinically isolated syndromes. *J. Neurol. Neurosurg. Psychiatry* **85**, 859–864 (2014).
179. Uher, T. *et al.* Serum lipid profile changes predict neurodegeneration in interferon- β 1a-treated multiple sclerosis patients. *J. Lipid Res.* **58**, 403–411 (2017).
180. Weinstock-Guttman, B. *et al.* Lipid profiles are associated with lesion formation over 24 months in interferon- β treated patients following the first demyelinating event. *J. Neurol. Neurosurg. Psychiatry* **84**, 1186–1191 (2013).
181. Ďurfinová, M. *et al.* Cholesterol level correlate with disability score in patients with relapsing-remitting form of multiple sclerosis. *Neurosci. Lett.* **687**, 304–307 (2018).
182. Tettey, P. *et al.* An adverse lipid profile is associated with disability and progression in disability, in people with MS. *Mult. Scler. J.* **20**, 1737–1744 (2014).
183. Mukhopadhyay, S. *et al.* Interdependence of oxysterols with cholesterol profiles in multiple sclerosis. *Mult. Scler. J.* **23**, 792–801 (2017).
184. Sodero, A. O. 24S-hydroxycholesterol: Cellular effects and variations in brain diseases. *J. Neurochem.* **157**, 899–918 (2021).
185. van de Kraats, C. *et al.* Oxysterols and cholesterol precursors correlate to magnetic resonance imaging measures of neurodegeneration in multiple sclerosis. *Mult. Scler. J.* **20**, 412–417 (2014).
186. Teunissen, C. . *et al.* Decreased levels of the brain specific 24S-hydroxycholesterol and cholesterol precursors in serum of multiple sclerosis patients. *Neurosci. Lett.* **347**, 159–162 (2003).
187. Aylward, E. H. *et al.* Rate of caudate atrophy in presymptomatic and symptomatic stages of Huntington’s disease. *Mov. Disord.* **15**, 552–560 (2000).
188. Finkbeiner, S. Huntington’s Disease. *Cold Spring Harb. Perspect. Biol.* **3**, a007476–a007476 (2011).
189. Ross, C. A. & Poirier, M. A. Protein aggregation and neurodegenerative disease. *Nat. Med.* **10**, S10–S17 (2004).
190. Roos, R. A. Huntington’s disease: a clinical review. *Orphanet J. Rare Dis.* **5**, 40 (2010).
191. Walker, F. O. Huntington’s disease. *Lancet* **369**, 218–228 (2007).
192. Jeste, D. V., Barban, L. & Parisi, J. Reduced Purkinje cell density in

- Huntington's disease. *Exp. Neurol.* **85**, 78–86 (1984).
193. Rubinsztein, D. C. Molecular Biology of Huntington's Disease (HD) and HD-Like Disorders. in *Genetics of Movement Disorders* 365–383 (Elsevier, 2003). doi:10.1016/B978-012566652-7/50035-6.
 194. Spargo, E., Everall, I. P. & Lantos, P. L. Neuronal loss in the hippocampus in Huntington's disease: a comparison with HIV infection. *J. Neurol. Neurosurg. Psychiatry* **56**, 487–491 (1993).
 195. Del Toro, D. *et al.* Altered cholesterol homeostasis contributes to enhanced excitotoxicity in Huntington's disease. *J. Neurochem.* **115**, 153–167 (2010).
 196. Trushina, E. *et al.* Mutant huntingtin inhibits clathrin-independent endocytosis and causes accumulation of cholesterol in vitro and in vivo. *Hum. Mol. Genet.* **15**, 3578–3591 (2006).
 197. Karasinska, J. M. & Hayden, M. R. Cholesterol metabolism in Huntington disease. *Nat. Rev. Neurol.* **7**, 561–572 (2011).
 198. Markianos, M., Panas, M., Kalfakis, N. & Vassilopoulos, D. Low plasma total cholesterol in patients with Huntington's disease and first-degree relatives. *Mol. Genet. Metab.* **93**, 341–346 (2008).
 199. Leoni, V. *et al.* Plasma 24S-hydroxycholesterol and caudate MRI in pre-manifest and early Huntington's disease. *Brain* **131**, 2851–2859 (2008).
 200. Sipione, S. *et al.* Early transcriptional profiles in huntingtin-induced striatal cells by microarray analyses. *Hum. Mol. Genet.* **11**, 1953–1965 (2002).
 201. Kreilaus, F., Spiro, A. S., McLean, C. A., Garner, B. & Jenner, A. M. Evidence for altered cholesterol metabolism in Huntington's disease post mortem brain tissue. *Neuropathol. Appl. Neurobiol.* **42**, 535–546 (2016).
 202. Leoni, V. & Caccia, C. The impairment of cholesterol metabolism in Huntington disease. *Biochim. Biophys. Acta - Mol. Cell Biol. Lipids* **1851**, 1095–1105 (2015).
 203. Abildayeva, K. *et al.* 24(S)-Hydroxycholesterol Participates in a Liver X Receptor-controlled Pathway in Astrocytes That Regulates Apolipoprotein E-mediated Cholesterol Efflux. *J. Biol. Chem.* **281**, 12799–12808 (2006).
 204. Wang, N. *et al.* ATP-binding cassette transporters G1 and G4 mediate cholesterol and desmosterol efflux to HDL and regulate sterol accumulation in the brain. *FASEB J.* **22**, 1073–1082 (2008).
 205. Valenza, M. Dysfunction of the Cholesterol Biosynthetic Pathway in Huntington's Disease. *J. Neurosci.* **25**, 9932–9939 (2005).
 206. Valenza, M. *et al.* Cholesterol-loaded nanoparticles ameliorate synaptic and cognitive function in Huntington's disease mice. *EMBO Mol. Med.* **7**, 1547–1564 (2015).
 207. Griffiths, W. J. & Wang, Y. Sterolomics in biology, biochemistry, medicine. *TrAC Trends Anal. Chem.* **120**, 115280 (2019).
 208. Griffiths, W. J. & Wang, Y. Sterolomics: State of the art, developments, limitations and challenges. *Biochim. Biophys. Acta - Mol. Cell Biol. Lipids* **1862**, 771–773 (2017).
 209. Fahy, E. *et al.* A comprehensive classification system for lipids. *J. Lipid Res.* **46**, 839–861 (2005).
 210. Myant, N. B. The Distribution of Sterols and Related Steroids in Nature. in *The Biology of Cholesterol and Related Steroids* 123–159 (Elsevier, 1981). doi:10.1016/B978-0-433-22880-6.50010-2.
 211. BLIGH, E. G. & DYER, W. J. A rapid method of total lipid extraction and purification. *Can. J. Biochem. Physiol.* **37**, 911–917 (1959).

212. Folch, J., Lees, M. & Sloane Stanley, G. H. A simple method for the isolation and purification of total lipides from animal tissues. *J. Biol. Chem.* **226**, 497–509 (1957).
213. Doemin, N. N. & Blokhina, V. D. *The initial effects of ionizing radiations on cells*. (Academic Press, 1961).
214. Getz, G. S. & Bartley, W. The intracellular distribution of fatty acids in rat liver. The fatty acids of intracellular compartments. *Biochem. J.* **78**, 307–312 (1961).
215. Lucas, C. C. & Ridout, J. H. Fatty livers and lipotropic phenomena. *Prog. Chem. Fats Other Lipids* **10**, 5–150 (1970).
216. Liu, S., Sjövall, J. & Griffiths, W. J. Neurosteroids in Rat Brain: Extraction, Isolation, and Analysis by Nanoscale Liquid Chromatography–Electrospray Mass Spectrometry. *Anal. Chem.* **75**, 5835–5846 (2003).
217. McDonald, J. G., Thompson, B. M., McCrum, E. C. & Russell, D. W. Extraction and Analysis of Sterols in Biological Matrices by High Performance Liquid Chromatography Electrospray Ionization Mass Spectrometry. in 145–170 (2007). doi:10.1016/S0076-6879(07)32006-5.
218. Griffiths, W. J. *et al.* Discovering oxysterols in plasma: A window on the metabolome. *J. Proteome Res.* **7**, 3602–3612 (2008).
219. Dzeletovic, S., Breuer, O., Lund, E. & Diczfalusy, U. Determination of cholesterol oxidation products in human plasma by isotope dilution-mass spectrometry. *Anal. Biochem.* **225**, 73–80 (1995).
220. Yutuc, E. *et al.* Deep mining of oxysterols and cholestenoic acids in human plasma and cerebrospinal fluid: Quantification using isotope dilution mass spectrometry. *Anal. Chim. Acta* **1154**, (2021).
221. Buszewski, B. & Szultka, M. Past, Present, and Future of Solid Phase Extraction: A Review. *Crit. Rev. Anal. Chem.* **42**, 198–213 (2012).
222. Berrueta, L. A., Gallo, B. & Vicente, F. A review of solid phase extraction: Basic principles and new developments. *Chromatographia* **40**, 474–483 (1995).
223. Breuer, O. & Björkhem, I. Simultaneous quantification of several cholesterol autoxidation and monohydroxylation products by isotope-dilution mass spectrometry. *Steroids* **55**, 185–192 (1990).
224. Wells, M. J. M. Principles of extraction and the extraction of semivolatile organics from liquids. in *Sample Preparation Techniques in Analytical Chemistry* (ed. Mitra, S.) 113 (2003).
225. Poole, C. F. New trends in solid-phase extraction. *TrAC Trends Anal. Chem.* **22**, 362–373 (2003).
226. Kim, H. Y. & Salem, N. Separation of lipid classes by solid phase extraction. *J. Lipid Res.* **31**, 2285–9 (1990).
227. Crick, P. J., Bentley, T. W., Wang, Y. & Griffiths, W. J. Revised sample preparation for the analysis of oxysterols by enzyme-assisted derivatisation for sterol analysis (EADSA). *Anal. Bioanal. Chem.* **407**, 5235–5239 (2015).
228. Honda, A. *et al.* Highly sensitive quantification of key regulatory oxysterols in biological samples by LC-ESI-MS/MS. *J. Lipid Res.* **50**, 350–357 (2009).
229. Sidhu, R. *et al.* A validated LC-MS/MS assay for quantification of 24(S)-hydroxycholesterol in plasma and cerebrospinal fluid. *J. Lipid Res.* **56**, 1222–1233 (2015).
230. DeBarber, A. E. *et al.* A blood test for cerebrotendinous xanthomatosis with potential for disease detection in newborns. *J. Lipid Res.* **55**, 146–154 (2014).

231. Griffiths, W. J., Liu, S., Alvelius, G. & Sjövall, J. Derivatisation for the characterisation of neutral oxosteroids by electrospray and matrix-assisted laser desorption/ionisation tandem mass spectrometry: The Girard P derivative. *Rapid Commun. Mass Spectrom.* **17**, 924–935 (2003).
232. Crick, P. J. *et al.* Quantitative charge-tags for sterol and oxysterol analysis. *Clin. Chem.* **61**, 400–11 (2015).
233. DeBarber, A. E. *et al.* Profiling sterols in cerebrotendinous xanthomatosis: Utility of Girard derivatization and high resolution exact mass LC-ESI-MSn analysis. *J. Chromatogr. B Anal. Technol. Biomed. Life Sci.* **879**, 1384–1392 (2011).
234. Soroosh, P. *et al.* Oxysterols are agonist ligands of ROR t and drive Th17 cell differentiation. *Proc. Natl. Acad. Sci.* **111**, 12163–12168 (2014).
235. Girard, A. & Sandulesco, G. Sur une nouvelle série de réactifs du groupe carbonyle, leur utilisation à l'extraction des substances cétoniques et à la caractérisation microchimique des aldéhydes et cétones. *Helv. Chim. Acta* **19**, 1095–1107 (1936).
236. Karu, K. *et al.* Liquid chromatography-mass spectrometry utilizing multi-stage fragmentation for the identification of oxysterols. *J. Lipid Res.* **48**, 976–987 (2007).
237. Brooks, C. J. W. *et al.* Selective reactions in the analytical characterisation of steroids by gas chromatography—Mass spectrometry. *J. Steroid Biochem.* **19**, 189–201 (1983).
238. Griffiths, W. J. *et al.* Analysis of oxysterols by electrospray tandem mass spectrometry. *J. Am. Soc. Mass Spectrom.* **17**, 341–362 (2006).
239. Griffiths, W. J., Abdel-Khalik, J., Crick, P. J., Yutuc, E. & Wang, Y. New methods for analysis of oxysterols and related compounds by LC–MS. *J. Steroid Biochem. Mol. Biol.* **162**, 4–26 (2016).
240. Dias, I. H. K., Wilson, S. R. & Roberg-Larsen, H. Chromatography of oxysterols. *Biochimie* **153**, 3–12 (2018).
241. McDonald, J. G., Smith, D. D., Stiles, A. R. & Russell, D. W. A comprehensive method for extraction and quantitative analysis of sterols and secosteroids from human plasma. *J. Lipid Res.* **53**, 1399–1409 (2012).
242. Careri, M., Ferretti, D., Manini, P. & Musci, M. Evaluation of particle beam high-performance liquid chromatography–mass spectrometry for analysis of cholesterol oxides. *J. Chromatogr. A* **794**, 253–262 (1998).
243. Hossain, M. The Mass Spectrometer and Its Components. in *Selected Reaction Monitoring Mass Spectrometry (SRM-MS) in Proteomics* 17–52 (Springer International Publishing, 2020). doi:10.1007/978-3-030-53433-2_2.
244. Rasool Hassan, B. A. Mass Spectrometry Importance and Uses. *Pharm. Anal. Acta* **03**, (2012).
245. Dempster, A. J. A new method of positive ray analysis. *Phys. Rev.* **11**, 316–325 (1918).
246. Dole, M. *et al.* Molecular Beams of Macroions. *J. Chem. Phys.* **49**, 2240–2249 (1968).
247. Karas, M., Bachmann, D., Bahr, U. & Hillenkamp, F. Matrix-assisted ultraviolet laser desorption of non-volatile compounds. *Int. J. Mass Spectrom. Ion Process.* **78**, 53–68 (1987).
248. Downard, K. M. *Mass Spectrometry*. (Royal Society of Chemistry, 2004). doi:10.1039/9781847551306.
249. Munson, B. Chemical Ionization Mass Spectrometry: Theory and

- Applications. in *Encyclopedia of Analytical Chemistry* (John Wiley & Sons, Ltd, 2006). doi:10.1002/9780470027318.a6004.
250. Kebarle, P. & Verkerk, U. H. Electrospray: From ions in solution to ions in the gas phase, what we know now. *Mass Spectrom. Rev.* **28**, 898–917 (2009).
 251. Kebarle, P. & Tang, L. From ions in solution to ions in the gas phase - the mechanism of electrospray mass spectrometry. *Anal. Chem.* **65**, 972A-986A (1993).
 252. Banerjee, S. & Mazumdar, S. Electrospray Ionization Mass Spectrometry: A Technique to Access the Information beyond the Molecular Weight of the Analyte. *Int. J. Anal. Chem.* **2012**, 1–40 (2012).
 253. Fitzgerald, M. C., Parr, G. R. & Smith, L. M. Basic matrixes for the matrix-assisted laser desorption/ionization mass spectrometry of proteins and oligonucleotides. *Anal. Chem.* **65**, 3204–3211 (1993).
 254. Cerruti, C. D. *et al.* MALDI imaging mass spectrometry of lipids by adding lithium salts to the matrix solution. *Anal. Bioanal. Chem.* **401**, 75–87 (2011).
 255. Brunelle, A. MALDI Mass Spectrometry Imaging of lipids in positive and negative ion mode. *HTX Imaging* (2015).
 256. Angelini, R. *et al.* Visualizing Cholesterol in the Brain by On-Tissue Derivatization and Quantitative Mass Spectrometry Imaging. *Anal. Chem.* **93**, 4932–4943 (2021).
 257. Shiea, J. *et al.* Use of a Water-Soluble Fullerene Derivative as Precipitating Reagent and Matrix-Assisted Laser Desorption/Ionization Matrix To Selectively Detect Charged Species in Aqueous Solutions. *Anal. Chem.* **75**, 3587–3595 (2003).
 258. Haag, A. M. Mass Analyzers and Mass Spectrometers. in 157–169 (2016). doi:10.1007/978-3-319-41448-5_7.
 259. Blackler, A. R., Klammer, A. A., MacCoss, M. J. & Wu, C. C. Quantitative Comparison of Proteomic Data Quality between a 2D and 3D Quadrupole Ion Trap. *Anal. Chem.* **78**, 1337–1344 (2006).
 260. Thermo-Fisher. Ion Trap LC-MS. <https://www.thermofisher.com/uk/en/home/industrial/mass-spectrometry/liquid-chromatography-mass-spectrometry-lc-ms/lc-ms-systems/ion-trap-lc-ms.html#how-does-ion-trap-work>.
 261. Makarov, A. Mass spectrometer. (1999).
 262. Makarov, A. Electrostatic Axially Harmonic Orbital Trapping: A High-Performance Technique of Mass Analysis. *Anal. Chem.* **72**, 1156–1162 (2000).
 263. Zubarev, R. A. & Makarov, A. Orbitrap Mass Spectrometry. *Anal. Chem.* **85**, 5288–5296 (2013).
 264. Scigelova, M. & Makarov, A. Advances in bioanalytical LC–MS using the Orbitrap™ mass analyzer. *Bioanalysis* **1**, 741–754 (2009).
 265. Medhe, S. Mass Spectrometry: Detectors Review. [Http://www.sciencepublishinggroup.com](http://www.sciencepublishinggroup.com) **3**, 51 (2018).
 266. Rockwood, A. L., Kushnir, M. M. & Clarke, N. J. Mass Spectrometry. in *Principles and Applications of Clinical Mass Spectrometry* 33–65 (Elsevier, 2018). doi:10.1016/B978-0-12-816063-3.00002-5.
 267. Johnson, J. V., Yost, R. A., Kelley, P. E. & Bradford, D. C. Tandem-in-space and tandem-in-time mass spectrometry: triple quadrupoles and quadrupole ion traps. *Anal. Chem.* **62**, 2162–2172 (1990).
 268. de Hoffman, E. & Stroobant, V. *Mass Spectrometry: Principles and*

- Applications*. (Wiley & Sons, 2007).
269. Rosas-Román, I. & Winkler, R. Contrast optimization of mass spectrometry imaging (MSI) data visualization by threshold intensity quantization (TriQ). *PeerJ Comput. Sci.* **7**, e585 (2021).
 270. Wucher, A., Cheng, J. & Winograd, N. Protocols for Three-Dimensional Molecular Imaging Using Mass Spectrometry. *Anal. Chem.* **79**, 5529–5539 (2007).
 271. Wu, C., Dill, A. L., Eberlin, L. S., Cooks, R. G. & Ifa, D. R. Mass spectrometry imaging under ambient conditions. *Mass Spectrom. Rev.* **32**, 218–243 (2013).
 272. Agüi-Gonzalez, P., Jähne, S. & Phan, N. T. N. SIMS imaging in neurobiology and cell biology. *J. Anal. At. Spectrom.* **34**, 1355–1368 (2019).
 273. Yoon, S. & Lee, T. G. Biological tissue sample preparation for time-of-flight secondary ion mass spectrometry (ToF–SIMS) imaging. *Nano Conver.* **5**, 24 (2018).
 274. Ali, A. *et al.* Single-cell metabolomics by mass spectrometry: Advances, challenges, and future applications. *TrAC Trends Anal. Chem.* **120**, 115436 (2019).
 275. Ferguson, C. N., Benchaar, S. A., Miao, Z., Loo, J. A. & Chen, H. Direct Ionization of Large Proteins and Protein Complexes by Desorption Electrospray Ionization-Mass Spectrometry. *Anal. Chem.* **83**, 6468–6473 (2011).
 276. Iakab, S. A., Ràfols, P., Correig-Blanchar, X. & García-Altares, M. Perspective on Multimodal Imaging Techniques Coupling Mass Spectrometry and Vibrational Spectroscopy: Picturing the Best of Both Worlds. *Anal. Chem.* **93**, 6301–6310 (2021).
 277. He, M. J. *et al.* Comparing DESI-MSI and MALDI-MSI Mediated Spatial Metabolomics and Their Applications in Cancer Studies. *Front. Oncol.* **12**, 891018 (2022).
 278. Margulis, K. *et al.* Distinguishing malignant from benign microscopic skin lesions using desorption electrospray ionization mass spectrometry imaging. *Proc. Natl. Acad. Sci.* **115**, 6347–6352 (2018).
 279. Alberici, R. M., Vendramini, P. H. & Eberlin, M. N. Easy ambient sonic-spray ionization mass spectrometry for tissue imaging. *Anal. Methods* **9**, 5029–5036 (2017).
 280. Good, C. J. *et al.* High Spatial Resolution MALDI Imaging Mass Spectrometry of Fresh-Frozen Bone. *Anal. Chem.* **94**, 3165–3172 (2022).
 281. Smith, A. *et al.* High Spatial Resolution MALDI-MS Imaging in the Study of Membranous Nephropathy. *PROTEOMICS – Clin. Appl.* **13**, 1800016 (2019).
 282. KRAnalytics. MALDI Atmospheric Pressure Mass Spectrometry. <https://www.kranalytical.co.uk/products/ap-maldi.php> (2018).
 283. Muller, L. *et al.* Laser Desorption/Ionization Mass Spectrometric Imaging of Endogenous Lipids from Rat Brain Tissue Implanted with Silver Nanoparticles. *J. Am. Soc. Mass Spectrom.* **28**, 1716–1728 (2017).
 284. Bowman, A. P. *et al.* Evaluation of lipid coverage and high spatial resolution MALDI-imaging capabilities of oversampling combined with laser post-ionisation. *Anal. Bioanal. Chem.* **412**, 2277–2289 (2020).
 285. Sans, M., Feider, C. L. & Eberlin, L. S. Advances in mass spectrometry imaging coupled to ion mobility spectrometry for enhanced imaging of biological tissues. *Curr. Opin. Chem. Biol.* **42**, 138–146 (2018).

Chapter 2: General materials and methods

2.1. Materials

2.1.1. Reagents and solvents

All solvents and reagents used during this project for sterol extraction, solid phase extraction, histochemical staining and tissue preparations for mass spectrometry imaging are detailed in Table 2.1.

Table 2.1. A list of all solvents and reagents used within the project.

Reagent	Product number	Manufacturer	Additional information
Methanol	M/4056/17	Fisher Scientific (Loughborough, UK)	HPLC grade
Ethanol	E/0650DF/17	Fisher Scientific (Loughborough, UK)	Analytical grade
Propan-2-ol (IPA)	P/7507/17	Fisher Scientific (Loughborough, UK)	HPLC grade
Acetonitrile	A/0626/17	Fisher Scientific (Loughborough, UK)	HPLC grade
Methylated industrial spirit (IMS)	M/4400/17	Fisher Scientific (Loughborough, UK)	
Xylene	X/0200/17	Fisher Scientific (Loughborough, UK)	> = 97%
Water	W/0106/17	Fisher Scientific (Loughborough, UK)	HPLC grade
Formic acid	F/1900/PB15	Fisher Scientific (Loughborough, UK)	
Glacial acetic acid	20104.334	VWR Chemicals (Bedfordshire, UK)	
Potassium phosphate (KH ₂ PO ₄) crystals	P9791-500G	Sigma-Aldrich (Gillingham, UK)	
Sodium hydroxide (NaOH) pellets	S5881-500G	Sigma-Aldrich (Gillingham, UK)	
Cholesterol oxidase (CO) from <i>Streptomyces sp.</i>	C8649-100UN	Sigma-Aldrich (Gillingham, UK)	
Girard P reagent (GP)	G0030	Tokyo Chemical Industrial (Tokyo, Japan)	
Sep-Pak tC18	WAT054925	Waters (Elstree, UK)	
Oasis HLB	WAT094226	Waters (Elstree, UK)	
Borosilicate mini homogeniser	FB56679	Fisher Scientific (Loughborough, UK)	
Precellys soft tissue homogenising CK14 2mL tubes	P000912-LYSK0-A	Bertin Instruments (Montigny-le-Bretonneux, France)	
1.5mL centrifuge tubes	S1615-5550	StarLab (Milton Keynes, UK)	
Eppendorf™ 2mL polypropylene microtubes	10038760	Fisher Scientific (Loughborough, UK)	

12mL tubes	163270	Greiner BioOne (Stroud, UK)	
15mL tubes	430052	Corning (Flintshire, UK)	
50mL Falcon tubes	430921	Corning (Flintshire, UK)	
10mL FinnTip™ pipette tips	9402151	Thermo Scientific (Paisley, UK)	
200µL FinnTip Flex™ pipette tips	94060320	Thermo Scientific (Paisley, UK)	
200µL Ultrapoint® yellow graduated tips, loose	S1113-1006	StarLab (Milton Keynes, UK)	
1000µL TipOne® graduated tips, loose	S1111-6001	StarLab (Milton Keynes, UK)	
10µL TipOne® graduated tips, loose	S1111-3000	StarLab (Milton Keynes, UK)	
Plastipak™ Centric Luer-lock Syringe	309649	Fisher Scientific (Loughborough, UK)	
Polypropylene Screw Neck Vial with Cap, 300 µL volume	186002639	Waters (Elstree, UK)	
Indium tin oxide (ITO) coated glass slides	-	Diamond Coatings (Halesowen, UK)	25x75x0.7 mm Resistance: 8-12 Ohms/Sq
Glass microscope slides	BPB019	Rogo-Sampaic (RS) France (Wissous, France)	
Superfrost Plus glass slides	J1800AMNZ	Thermo Scientific (Paisley, UK)	
Menzel-Gläser coverslips	11911998	Thermo Scientific (Paisley, UK)	24x50mm
Paraformaldehyde (PFA)	158127-500G	Sigma-Aldrich (Gillingham, UK)	
Luxol Fast Blue MBS powder	115711/5	TCS Biosciences (London, UK)	
Cresyl Violet acetate powder	229630250	Acros Organics/ Fisher Scientific (Geel, Belgium)	
Lithium carbonate powder	413265000	Acros Organics/ Fisher Scientific (Geel, Belgium)	99%+, ACS reagent
DPX mounting media	LAMB/DPX	Thermo Scientific (Paisley, UK)	

2.1.2. Reference internal standards

For each experiment undertaken within this project, a specific mixture of isotope-labelled standards was used to allow for relative quantification. Each biological fluid or brain tissue analysis had stock solutions containing several deuterated standard compounds supplied by Avanti. The list of all deuterated reference standards is shown in Table 2.2.

Table 2.2. Referenced isotope-labelled standards used for the samples analysed. ** - sprayed onto tissue, not spiked into the sample.

Steroid/ Sterol/ Oxysterol		Standard used per sample type	Conc. (ng/μL)	Volume (μL)	Supplier	Product number
Common name	Systematic name					
$[^2\text{H}_7]$ 22R-hydroxycholest-4-en-3-one	$[^2\text{H}_7]$ Cholest-5-ene-3 β ,22R-diol	Plasma (100μL)	5	4	Avanti Polar Lipids (Alabaster, AL, USA)	700052P-1MG
		CSF (250μL)	5	0.4		
		Brain tissue (20-200mg)	5	40		
$[^2\text{H}_7]$ 24R/S-hydroxycholesterol	$[^2\text{H}_7]$ Cholest-5-ene-3 β ,24R/S-diol	Brain tissue (20-100mg)	4	50		700018P
		Brain tissue (>100mg)	4	100		
$[^2\text{H}_6]$ 24R/S-hydroxycholesterol	$[^2\text{H}_6]$ Cholest-5-ene-3 β ,24R/S-diol	Plasma	4	5		LM4110
		CSF	4	0.5		
$[^2\text{H}_7]$ 7 α -hydroxycholesterol	$[^2\text{H}_7]$ Cholest-5-ene-3 β ,7 α -diol	Plasma	4	5		LM-4113
		CSF	4	0.5		
		Brain tissue	4	5		
$[^2\text{H}_6]$ 7 α ,25-dihydroxycholesterol	$[^2\text{H}_6]$ Cholest-5-ene-3 β ,7 α ,25-triol	Plasma	4	0.5		700078P
		CSF	0.4	1		
		Brain tissue	4	5		
25 $[^2\text{H}_6]$ -hydroxyvitamin-D ₃	$[^2\text{H}_6]$ 9,10-secocholesta-5,7,10(19)-triene-3,25-diol	Plasma	4	5	Medical Isotopes (Pelham, NH, USA)	D2831
		CSF	4	1		
		Brain tissue	4	5		
$[^2\text{H}_7]$ 7-ketocholesterol	$[^2\text{H}_7]$ 7-Oxocholest-5-en-3 β -ol	Plasma	4	5	Avanti Polar Lipids (Alabaster, AL, USA)	700046P
$[^2\text{H}_7]$ Cholesterol	$[^2\text{H}_7]$ Cholest-5-en-3 β -ol	Plasma	1000	20		LM4100-1EA
		CSF	1000	0.8		
		Brain	1000	200		
		MALDI-MSI**	200	1500		

2.2. Methods

2.2.1. Sterol extraction from human serum and plasma

Control

The control plasma (CRF093) was from a 61-year-old female with no known conditions (n=1), which was used as a reference plasma sample with approval from the Health Research Authority Research Ethics Committee (11/WA/0040 and 13/WA/019). The plasma was aliquoted and stored at -80°C until required for sample preparation, where it was removed from the freezer and kept at room temperature for 30 minutes to thaw. Each 100 µL plasma sample was sonicated in 1.05 mL 99% EtOH spiked with an isotope-labelled standard mix including [²H₆] 20 ng of 24R/S-hydroxycholesterol (see section 2.1.2 – Reference internal standards table 2.2 for full internal standard information). An additional 350 µL of water was added dropwise under sonication to the plasma/ethanol mixture to give a final concentration of 70% EtOH.

Cerebrotendinous xanthomatosis (CTX)

The CTX serum samples (n=4) were provided by Prof. Ludger Schöls, German Centre of Neurodegenerative Diseases, University of Tübingen, Germany and corresponded to the same patients as CSF samples processed described below (see section 2.2.2 – CTX). Details of ethical permissions can be found in Höflinger et al¹. The samples were transported using dry ice in polypropylene tubes, with the samples still frozen on arrival. The samples were stored at -80°C until required for sample preparation, where it was removed from the freezer and kept at room temperature for 30 minutes to thaw. Each 100 µL serum sample was sonicated in 1.05 mL 99% EtOH spiked with 20 ng of [²H₆] 24R/S-hydroxycholesterol isotope-labelled standard (see section 2.1.2 – Reference internal standards table 2.2 for full internal standard information). An additional 350µL of water was added dropwise under sonication to the plasma/ethanol mixture to give a final solution of 70% EtOH.

2.2.2. Sterol extraction from human cerebrospinal fluid (CSF)

Quality control

The quality control CSF used within this project was pooled CSF generated by combining individual CSF samples from multiple donors (n=67) obtained from the University Hospital of Umeå, Sweden and elsewhere (n=4 technical replicates). Details of ethical permissions can be found in Yutuc et al². All 67 CSF samples were transported to Swansea using dry ice in polypropylene tubes, with the samples still frozen on arrival, with the CSF pooled within Swansea University. The aliquoted pooled CSF were stored at -80°C until required for sample preparation, where it was removed from the freezer and kept at room temperature for 30 minutes to thaw. Each 250 µL CSF sample was sonicated in 2.10 mL 99% EtOH containing 2 ng of [²H₆] 24R/S-hydroxycholesterol isotope-labelled standard (see section 2.1.2 – Reference internal standards table 2.2 for full internal standard information) and diluted to 70% EtOH by adding 650 µL of HPLC grade water drop-wise to ensure full incorporation. There was a lower amount of [²H₆] 24R/S-hydroxycholesterol isotope-labelled standard used for CSF compared to both plasma and brain homogenate due to endogenous oxysterols being 100-fold lower in CSF.

CTX

The CTX CSF samples (n=4) were provided by Prof. Ludger Schöls from the German Centre of Neurodegenerative Diseases, University of Tübingen, Germany and corresponded to the same patients as serum samples processed described above (see section 2.2.1 – CTX). The samples were transported using dry ice in polypropylene tubes, with the samples still frozen on arrival. The samples were stored at -80°C until required for sample preparation, where it was removed from the freezer and kept at room temperature for 30 minutes to thaw. Each 250 µL CSF sample was sonicated in 2.10 mL 99% EtOH containing with 2 ng of [²H₆]24R/S-hydroxycholesterol isotope-labelled standard (see section 2.1.2 – Reference internal standards table 2.2 for full internal standard information) and diluted to 70% EtOH by adding 650 µL of HPLC grade water drop-wise.

2.2.3. Sterol extraction from human brain tissue

Throughout this thesis, the brain tissue samples and amount available for homogenisation varied largely and as a result, the exact method of sterol extraction varied as the project progressed. For example, for the initial stages a glass homogeniser was used with ~200 mg of CTX tissue, then after developing the method over time using the Precellys ceramic bead homogenisation tubes for both the AD and multiple sclerosis tissue which used less tissue (between 20-90 mg given the limited availability of the tissue) and were one-time use. All homogenates were comparable and quantifiable from the isotope-labelled standards used.

Control tissue

The control human brain tissue (n=1 for Chapter 3; n=5 for Chapter 5) was sent from the Thomas Willis Oxford Brain Bank, with the appropriate research ethics approval (REC 13/WA/0292). The brain was transported to Swansea using dry ice in polypropylene bags and was still frozen on arrival. The samples were stored at -80°C until required for cryostat cutting/ sample preparation. The brain tissue was obtained from cryostat cuttings, placed into an Eppendorf tube and weighed to obtain the total tissue weight. The Eppendorf tubes were weighed after the tissue had been removed to give a more accurate weight of tissue used. Brain tissue (between 9.6 and 29.3 mg depending on the availability per case) was homogenised in 99% EtOH containing 200 ng of [²H₇]24R/S-hydroxycholesterol isotope-labelled standard using a hand-held glass homogeniser (see section 2.1.2 – Reference internal standards table 2.2 for full internal standard information). A total volume of 4.2 mL was used to extract the sterols via two 2.1 mL extractions. The 4.2 mL of 99% EtOH containing extracted sterols was placed into a 15mL Corning tube, then attenuated to 70% EtOH with the addition of 1.8 mL of HPLC-grade water, which was added dropwise whilst sonicating to get a total of 6mL of sterol extract at 70% EtOH. The Corning tube containing the homogenised brain was centrifuged at 2,400 g at 4°C for one hour to obtain the brain tissue pellet, and the sterol extract was separated from the pellet. The sterol-rich brain extract supernatant corresponding to 10% of the brain weight used (600 µL of sterol extract) was added to 980 µL of 99% EtOH dropwise under sonication for 5 minutes. An additional 420 µL of HPLC-grade water was added

dropwise whilst under sonication to give a final volume of 2 mL and a final concentration of 70% EtOH.

CTX

The CTX human brain tissue samples were gifted from Dr Andrea DeBarber from Oregon Health and Science University (OHSU), Portland, Oregon, USA. The samples were autopsy samples from a single 26-year-old male with CTX (see Chapter 3 for demographics), with multiple regions taken from the one individual. The brain regions analysed were cerebrum (identified as a block of grey matter accompanied with adjacent white matter tissue), cerebellum which included a CTX lesion, basal ganglia, substantia nigra and medulla oblongata. Details of ethical permission can be found in Höflinger et al¹. All CTX brain tissue was transported to Swansea using dry ice sealed in plastic packaging, with the tissue still frozen on arrival. However, the condition of the brain tissue was not optimal ('sponge' like) as the tissue was stored for 7 years in a -80°C freezer before arrival in Swansea.

On arrival the samples were stored at -80°C in a sealed plastic bag until required for sample preparation. Brain tissue (between 90 – 250 mg depending on the availability per region) was homogenised in 99% EtOH containing 200 ng of [²H₇] 24R/S-hydroxycholesterol isotope-labelled standard per 4.2 mL using a hand-held glass homogeniser (see section 2.1.2 – Reference internal standards table 2.2 for full internal standard information). A total volume of 4.2 mL was used to extract the sterols in replicate 2.1 mL extractions. The 4.2 mL of 99% EtOH with the extracted sterols was then attenuated to 70% EtOH with the addition of 1.8 mL of HPLC-grade water, which was added dropwise whilst sonicating to get 6 mL of sterol extract at 70% EtOH. The extract was centrifuged as above to obtain the brain tissue pellet, and sterol extract was decanted from the pellet.

For tissue that was above 100 mg in mass, the pellet was homogenised for a second time in an additional 4.2 mL of 99% EtOH with contained standards (again, see section 2.1.2 – Reference internal standards table 2.2 for full internal standard information), and attenuated to 6 mL of 70% EtOH, bringing the total volume to 12 mL of sterol extract at 70% EtOH with a total of 400 ng of [²H₇] 24R/S-hydroxycholesterol isotope-labelled standard.

The sterol extract supernatant corresponding to 10% of the brain weight used (600 μ L for tissue under 100 mg and 1200 μ L for tissue over 100 mg) was added to 99% EtOH dropwise under sonication for 5 minutes (980 μ L for tissue under 100 mg and 210 μ L for tissue over 100 mg), followed by HPLC-grade water added dropwise whilst under sonication (for tissue under 100 mg, 420 μ L of water was added to give a final volume of 2 mL; for tissue over 100 mg, 90 μ L of water was added to give a final volume of 1.5 mL) for a final concentration of 70% EtOH.

Alzheimer's disease (AD)

The AD brain tissue samples (n=48) were provided by the Rush Alzheimer's Disease Centre located in Rush University in Chicago, Illinois, USA. The forty-eight samples provided were post-mortem brain tissue supplied from the dorsolateral prefrontal cortex (see Chapter 4 for the case list). Ethical permission was approved by Institutional Review Board #1 at Rush University Medical Center (ORA Number: L91020181-CR14 Principal Investigator: David Bennett). The brain tissue was pre-weighed (all samples between 50 – 100 mg of tissue) and placed into Precellys soft tissue homogenisation 2 mL tubes with ceramic beads then shipped on dry ice, with the tissue still frozen on arrival to Swansea. The samples were stored at -80°C until required for sample preparation. Brain tissue was homogenised in a total of 4.2 mL of 99% EtOH containing 200 ng [2 H $_7$] 24R/S-hydroxycholesterol which was performed in four 1.05 mL intervals (see section 2.1.2 – Reference internal standards table 2.2 for full internal standard information). Each interval run on the homogeniser consisted of two 20 second runs at a speed of 4 metres/second (m/s) with a 5 second break between the two runs. The 4.2 mL of 99% EtOH extract was attenuated with 1.8 mL of HPLC-grade water under sonication for a total of 6 mL of 70% EtOH sterol extract. Sterol extract corresponding to 10% of the brain weight used (600 μ L of sterol extract) was added dropwise into 1.4 mL of 70% EtOH, giving a final volume of 2 mL.

Multiple sclerosis

The multiple sclerosis brain tissue samples (n=16) were sent from the UK Multiple Sclerosis Society Tissue Bank, Imperial College London, UK (see Chapter 5 for case list). The brain tissue was transported to Swansea using dry ice in a plastic

polypropylene bag, with the samples still frozen on arrival. The samples were stored at -80°C until required for cryostat cutting/ sample preparation.

The brain tissue was obtained from cryostat cuttings, which were weighed and placed into Precellys soft tissue homogenisation 2mL tubes with ceramic beads (see above for specifications). Brain tissue was homogenised in 4.2 mL of 99% EtOH containing 200 ng [$^2\text{H}_7$] 24R/S-hydroxycholesterol in four 1.05 mL intervals (see section 2.1.2 – Reference internal standards table 2.2 for full internal standard information) and attenuated in 1.8 mL of HPLC-grade water under sonication to give a total of 6 mL of 70% EtOH sterol extract. Sterol extract corresponding to 10% of the brain weight used (600 μL of sterol extract) was added to 1.4 mL of 70% EtOH, giving a final volume of 2 mL.

2.2.4. Separation of oxysterols and cholesterol using solid phase extraction

For this project, we analysed the free (non-esterified) oxysterols in the biological samples rather than the esterified forms (fatty acyls), which are used for intracellular storage or transport in lipoproteins. The necessary saponification reaction in strong base required to hydrolyse the esters bonds for that process can sometimes result in altered structures e.g., dehydration of labile hydroxyl groups at C-7.

Sep-Pak C₁₈ 200 mg cartridges, which are silica cartridges which retain more polar sterols, were washed with 4 mL of 99% EtOH and conditioned with 6 mL of 70% EtOH.

Fraction 1, (SPE1-Fr1) which elutes the oxysterols, was collected by loading the sample (1.5 mL or 2 mL) at 70% EtOH onto the conditioned column (see Figure 2.1), followed by an additional 5.5 mL of 70% EtOH (or 5 mL depending on the sample volume), giving Fraction 1 a total volume of 7 mL at 70% EtOH. The 7 mL was vortexed, briefly centrifuged and split into two equal volumes in two Greiner tubes labelled A and B (3.5 mL in each tube) (SPE1-Fr1a, Fr1b). For Fr2, 4 mL of 70% EtOH was added to the column and collected to ensure sufficient removal of oxysterols from the SepPak cartridge.

For Fr3, 2 mL of 99% EtOH was added to the column, eluting the cholesterol. This fraction was vortexed, centrifuged and split equally into two volumes labelled A and B (1 mL each) (SPE1-Fr3a, Fr3b). For Fr4, an additional 2 mL of 99% EtOH was added to wash through the column to ensure sufficient removal of all other sterols

from the SepPak cartridge. Fractions 1a, 1b, 3a and 3b were lyophilised using a scan speed vacuum concentrator overnight to remove solvent.

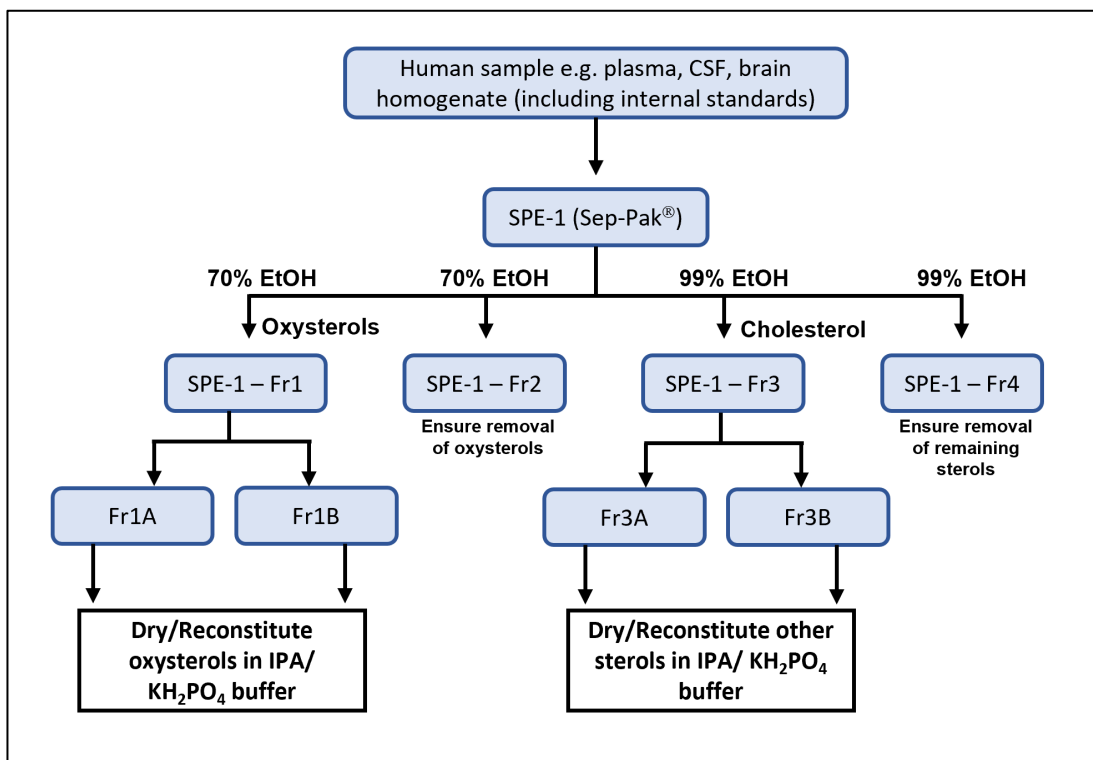


Figure 2.1. The separation of oxysterols/sterols using solid phase extraction (SPE1). Due to the very high abundance of cholesterol, oxysterols need to be separated from cholesterol on the Sep-Pak C₁₈ 200 mg cartridge prior to mass spectrometry analysis.

2.2.5. Enzyme-assisted derivatisation of sterol analysis (EADSA)

Sterols have poor ionisation properties so for an accurate analysis of all oxysterols within the samples we prefer to charge-tag the sterol molecule before analysing with mass spectrometry. Using the EADSA method²⁻⁴, the 3 β -hydroxyl group converts to a 3-oxo group to allow for a pre-charged Girard-P hydrazine to be added to the structure (Figure 2.2; B).

For this to occur, oxidation of the sterols in the 3 β -position was performed using cholesterol oxidase enzyme. The dried samples were reconstituted in 100 μ L of propan-2-ol (IPA), followed by the addition of 1mL of 50 mM potassium phosphate buffer at pH 7.0. The 3.0 μ L (0.264 units) of bacterial cholesterol oxidase from *Streptomyces spec.* was added to Fraction 1a and 3a but not to 1b and 3b, which allows for the analysis of compounds with an endogenous oxo group within the (b)

fraction (Figure 2.2; A). All fractions were incubated in a water bath at 37°C for one hour to allow the oxidation reaction to occur.

After a one-hour incubation, 2 mL of 99% MeOH was added to stop the cholesterol oxidase reaction, with 150 µL of glacial acetic acid to catalyse reaction with Girard P (190 mg bromide salt) and the formation of the hydrazone. The two separate Girard-P hydrazine's were added to the samples as followed:

To Fr1a and 3a, 190 mg of [²H₅] Girard-P reagent (bromide salt), and to Fr1b and 3b, 150 mg of [²H₀] Girard-P reagent (chloride salt). Samples were incubated at room temperature overnight in the dark.

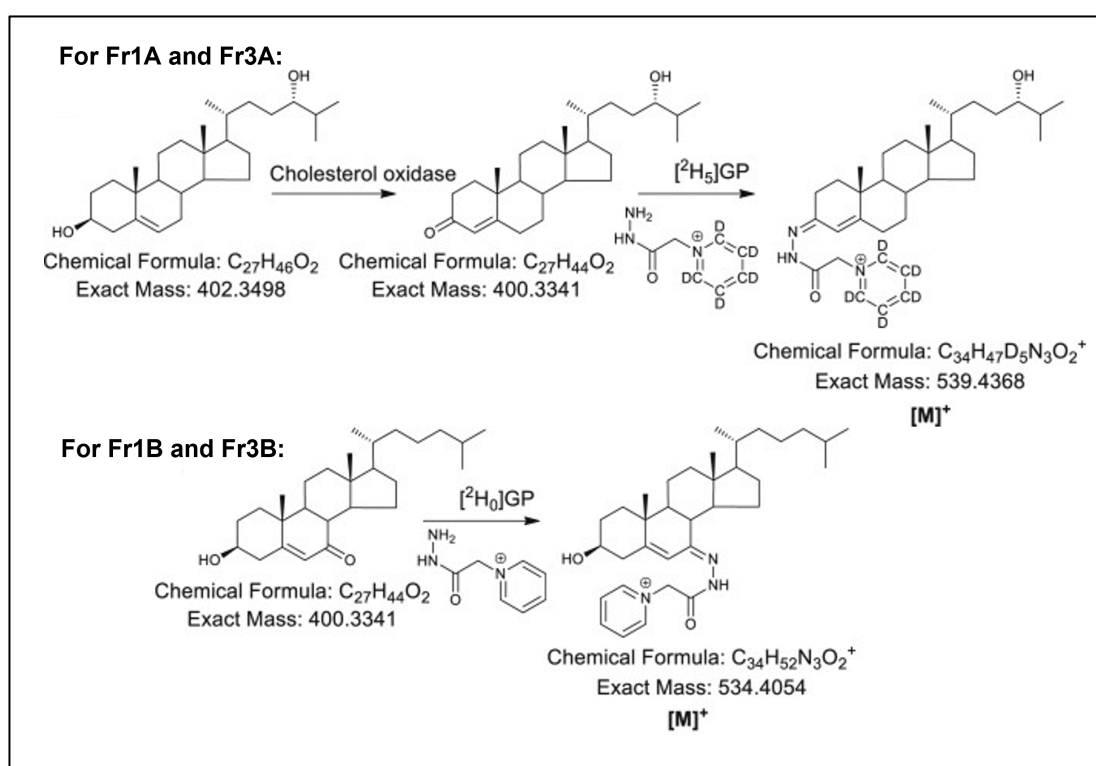


Figure 2.2. The derivatisation of oxysterols using the EADSA method. (A) The addition of the pre-ionised [²H₀] Girard-P hydrazine molecule to the naturally occurring 7-oxocholesterol, resulting in a charged hydrazone molecule with m/z 534.4054. (B) The enzymatic conversion of the 3β-hydroxyl group on 24S-HC to a 3-oxo using cholesterol oxidase. The [²H₅] Girard-P hydrazine reacts with the 3-oxo group, resulting in a charged hydrazone molecule with m/z 539.4368. (Image from Yutuc et al, 2020⁵).

2.2.6. Purification of oxysterols using solid phase extraction

The derivatised oxysterols were separated from excess Girard-P via a second solid phase extraction, and to ensure all oxysterols of interest were recovered a recycling method was performed.

The samples were loaded onto a conditioned Oasis HLB 60 mg cartridge, with 3 mL of sample at 70% MeOH. An additional 1 mL of 70% MeOH was used to remove any remaining sample from the tube and added to the respective column (a total of 4 mL of sample). The sample was allowed to drip through, with the monohydroxycholesterols (e.g. 24S-HC) being held in the Oasis HLB cartridge and the eluent collected in a Greiner tube.

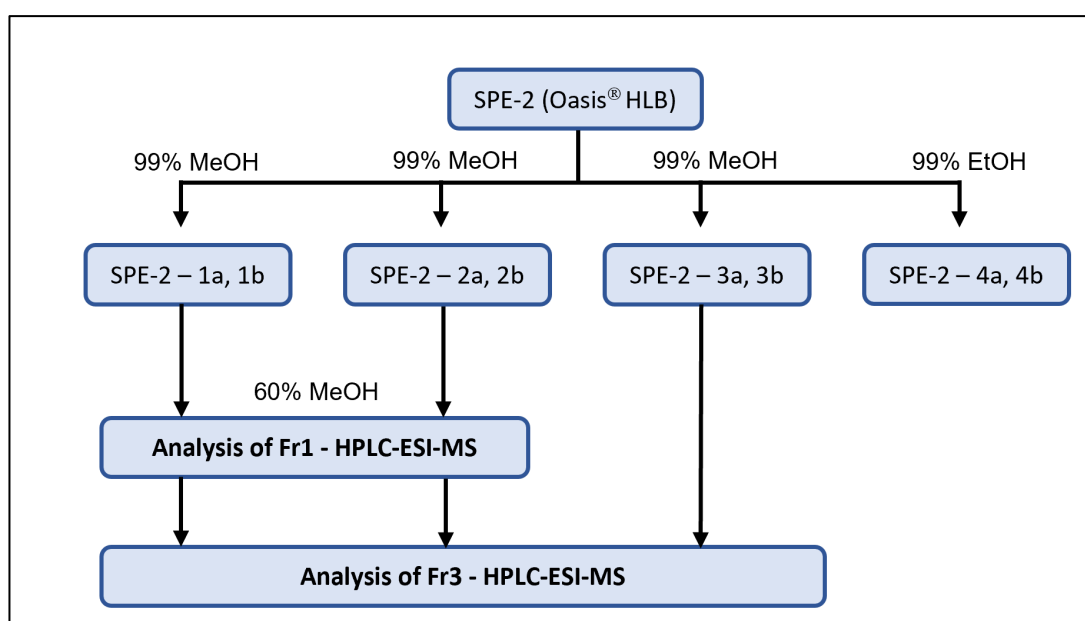


Figure 2.3. Purification of oxysterols/sterols using solid phase extraction (SPE2). The oxysterols of interest in Fr1 need separation from excess Girard-P reagent and eluted in four separate stages, with the first two eluents being used for LCMS analysis For Fr3, the first three eluents are used.

The column was washed with 1 mL of 35% MeOH and combined with the collected eluent which was diluted to 35% MeOH using 4 mL of HPLC-grade H₂O, vortexed and reapplied to the Oasis cartridge and allowed to drip through under vacuum at a flow rate of roughly 0.25 mL/minute to retain the dihydroxycholesterols in the cartridge, for example 7 α ,25-diHC. The collected eluent was diluted to 17.5% MeOH, the column was re-conditioned with 1 mL of 17.5% MeOH. The eluents were combined and re-applied to the column to retain the cholestenoic acids in the

cartridge, for example 3 β -HCA. A subsequent 6 mL wash with 10% MeOH ensured the removal of acetic acid from the column and was immediately followed by eluting the derivatised oxysterols of interest into Eppendorf tubes in three separate 1 mL stages using 99% MeOH (SPE2-1, 2, 3) (see Figure 2.3), followed by 1 mL of 99% EtOH (SPE2-4). Oxysterols mostly elute in the first two 1 mL volumes; cholesterol elutes in the first three 1 mL volumes. In total, each sample has eight Eppendorf tubes (SPE2-1a, 1b, 2a, 2b, 3a, 3b, 4a, 4b).

2.2.7. On-tissue derivatisation for MALDI analysis

The enzyme-assisted derivatisation process can also be applied to intact tissue sections.

The 10 μ m thick tissue section for analysis was removed from -80°C storage and immediately placed into a vacuum desiccator with silica gel beads to prevent condensation on the tissue section.

After the tissue was free of surface moisture, the tissue sections were placed into a SunCollect pneumatic sprayer system and sprayed with 200 ng/ μ L [2 H $_7$] cholesterol isotope-labelled standard in 99% EtOH (54 layers; 20 μ L/min flowrate; 900 mm/min velocity; final density of 120 ng/mm 2). Following the isotope-labelled standard, cholesterol oxidase enzyme was sprayed in 5 mM potassium phosphate buffer at pH 7.0 at a final concentration of 0.264 units/mL (18 layers; 1st layer 10 μ L/min, 2nd layer 15 μ L/min, all other layers 20 μ L/min flowrate; 900 mm/min velocity; final density of 52.8 μ U/mm 2).

The slides were incubated in a water bath chamber for one hour set at 37°C above 30 mL of pre-warmed HPLC-grade water to create humid conditions for the oxidation reaction to occur, then placed into a desiccator under vacuum to remove excess moisture on the slide. Once dry, the slide was again placed into the sprayer system and sprayed with a [2 H $_0$] Girard-P solution in delivery solvent (70% MeOH, 5% glacial acetic acid), at a final concentration of 0.5 mg/mL (18 layers; 1st layer 10 μ L/min, 2nd layer 15 μ L/min, all other layers 20 μ L/min flowrate; 900 mm/min velocity; final density of 0.1 μ g/mm 2). The slides were again incubated within a chamber above 10 mL of pre-warmed GP incubation solvent (50% MeOH, 5% glacial acetic acid) at 37°C for one hour. After incubation, the slides were removed from the chamber and placed in the desiccator under vacuum to remove excess

moisture. The slide was sprayed with matrix and analysed immediately after this step or stored in a vacuum desiccator at 4°C in a dark environment.

2.2.8. Spraying of matrix for MALDI analysis

The matrix used for analysis was α -cyano-4-hydroxycinnamic acid (CHCA), sprayed at a concentration of 5 mg/mL in a matrix delivery solvent solution comprised of 40% IPA, 30% ACN and 30% HPLC-grade H₂O. A separate SunCollect pneumatic sprayer system was used to spray on the matrix (16 layers; 80 μ L/min flowrate; 1200 mm/min velocity; final density of 2.67 μ g/mm²).

2.2.9. Analysis of biofluid using HPLC and MSⁿ

All samples were analysed using a Dionex HPLC system coupled with an Orbitrap Elite mass spectrometer. For the analysis of oxysterols (Fr1 from SPE-1) the first two eluents from SPE-2 were combined (1a, 1b, 2a, 2b) and diluted to 60% MeOH immediately before injection (see Figure 2.3). Plasma and CSF samples were run without further dilution, and brain homogenate supernatant were either run without further dilution or at a 10x dilution in 60% MeOH.

For analysis of cholesterol (Fr3 from SPE-1), the first three eluents from SPE-2 were combined (1a, 1b, 2a, 2b, 3a, 3b) and diluted to 60% MeOH. Due to the high abundance of cholesterol within the samples, this fraction was run with a dilution of at least 1 in 1000 in 60% MeOH.

After the samples were prepared, they were placed within the temperature-controlled tray at 4°C located in the autosampler of the HPLC system. When instructed, 35 μ L of the sample was drawn up via the sampling needle and loaded into the sample loop awaiting injection into the mobile phase within the HPLC system that runs through the column, which is kept at ambient temperature (25°C).

Separation of the derivatised sterols/ oxysterols was performed using a Hypersil Gold C₁₈ column (50 x 2.1 mm, 1.9 μ m particle size), at a flow rate of 200 μ L per minute. The duration of the runs used within this study include a 17-minute gradient and a 37-minute gradient (see Figure 2.4), with the longer of the two permitting the separation of closely eluting compounds, for example monohydroxycholesterols at *m/z* 539.4346, for more accurate quantification of each oxysterol.

For the 17-minute gradient, the mobile phase ratio begins at 20% B: 80% A and remains for 1 minute, gradually increasing to 80% B at 8 minutes. At 12 minutes, the percentage drops back to 20% B for the remainder of the run time.

For the 37-minute gradient, the mobile phase ratio again begins at 20% B: 80% A for the initial 10 minutes, before gradually increasing to 50% B at 20 minutes. The mobile phase B remains at 50% B for 6 minutes before gradually increasing to 80% B at 29 minutes. At 32 minutes, mobile phase B decreases to 20% where it continues for the remainder of the run (see Figure 2.4).

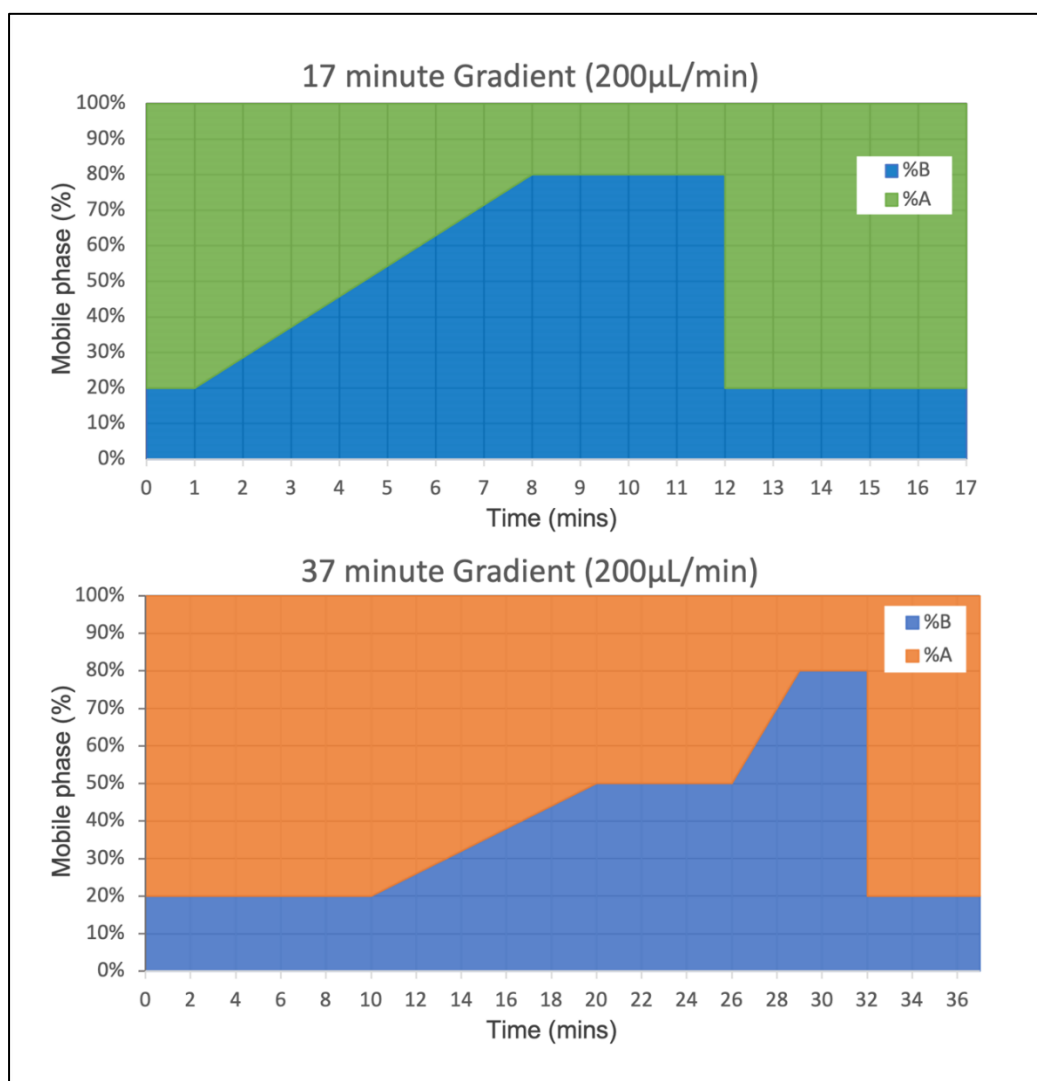


Figure 2.4. Gradient elution for the separation of derivatised sterols using high performance-liquid chromatography (HPLC). The two gradients used for all samples analysed, showing the transition of the mobile phase percentage across the shorter 17-minute and longer 37-minute run. Mobile phase A contains 33.3% MeOH 16.7% can, 49.9% H₂O and 0.1% formic acid. Mobile phase B contains 63.3% MeOH, 31.7% ACN, 4.9% H₂O and 0.1% formic acid.

Several m/z values were selected for fragmentation, with a maximum of 12 methods being run per sample, each method with several MS³ fragmentation masses (see Table 2.3 for methods for each sample type, length of run and the corresponding fragmentation m/z). The specific MS³ fragmentation using the ion trap is shown in Figure 2.5 (all ITMS³ spectra for all oxysterols quantified in this thesis are shown in Appendix Table 9.1).

Table 2.3. Mass spectrometry methods for ITMS³ fragmentation. Table showing the MS methods used, fragmenting specific masses to allow for the identification of sterols, with a second fragmentation (MS³) after the loss of pyridine (m/z 79.0422^b for [²H₀] GP and m/z 84.0736^a [²H₅] GP). (***546.5** - fragmented m/z in plasma and brain samples only, excluded in CSF). The daughter ions fragmented for MS³ are underlined in the table below.

Sample type	Method name	Method time (min)	Masses and precursors for MS ³ fragmentation (m/z) \pm 5 ppm
Plasma, CSF, brain	A	17	522.3 \rightarrow <u>443.3</u> ; 527.4 \rightarrow <u>443.3</u> ; 532.4 \rightarrow <u>453.4</u> ; 537.4 \rightarrow <u>453.4</u>
	B	17	534.4 \rightarrow <u>455.4</u> ; 539.4 \rightarrow <u>455.4</u> ; 550.4 \rightarrow <u>471.4</u> ; 555.4 \rightarrow <u>471.4</u>
	C	17	546.4 \rightarrow 467.4; 551.4 \rightarrow 467.4; 564.4 \rightarrow 485.3; 569.4 \rightarrow 485.3
	D	17	548.4 \rightarrow <u>469.3</u> ; 553.4 \rightarrow <u>469.3</u> ; 580.4 \rightarrow <u>501.3</u> ; 585.4 \rightarrow <u>501.3</u> ; * 546.5 \rightarrow <u>462.4</u>
Plasma, CSF	E	17	562.4 \rightarrow <u>483.3</u> ; 567.4 \rightarrow <u>483.3</u> ; 566.4 \rightarrow <u>487.4</u> ; 571.4 \rightarrow <u>487.4</u>
	F	17	537.4 \rightarrow <u>435.3</u> ; 543.5 \rightarrow <u>441.4</u> ; 556.4 \rightarrow <u>477.4</u> ; 561.5 \rightarrow <u>477.4</u>
	G	17	614.4 \rightarrow <u>535.3</u> ; 619.4 \rightarrow <u>535.3</u> ; 710.4 \rightarrow <u>631.4</u> ; 715.5 \rightarrow <u>631.4</u>
	H	17	506.3 \rightarrow <u>427.3</u> ; 511.4 \rightarrow <u>427.3</u> ; 552.4 \rightarrow <u>473.4</u> ; 557.5 \rightarrow <u>473.4</u> ; 578.4 \rightarrow <u>499.3</u> ; 583.4 \rightarrow <u>499.3</u>
Plasma, CSF, brain	I	37	539.4 \rightarrow <u>455.4</u> ; 546.5 \rightarrow <u>462.4</u> ; 550.4 \rightarrow <u>471.4</u> ; 555.4 \rightarrow <u>471.4</u>
Plasma, CSF	J	17	540.4 \rightarrow <u>461.4</u> ; 545.5 \rightarrow <u>461.4</u> ; 541.5 \rightarrow <u>462.4</u> ; 546.5 \rightarrow <u>462.4</u>
	K	17	504.3 \rightarrow <u>425.3</u> ; 509.4 \rightarrow <u>425.3</u> ; 540.3 \rightarrow <u>461.3</u> ; 545.4 \rightarrow <u>461.3</u>
	L	17	579.4 \rightarrow <u>500.3</u> ; 584.4 \rightarrow <u>500.3</u> ; 597.4 \rightarrow <u>518.3</u> ; 602.4 \rightarrow <u>518.3</u> ; 629.3 \rightarrow <u>550.3</u> ; 634.4 \rightarrow <u>550.3</u>

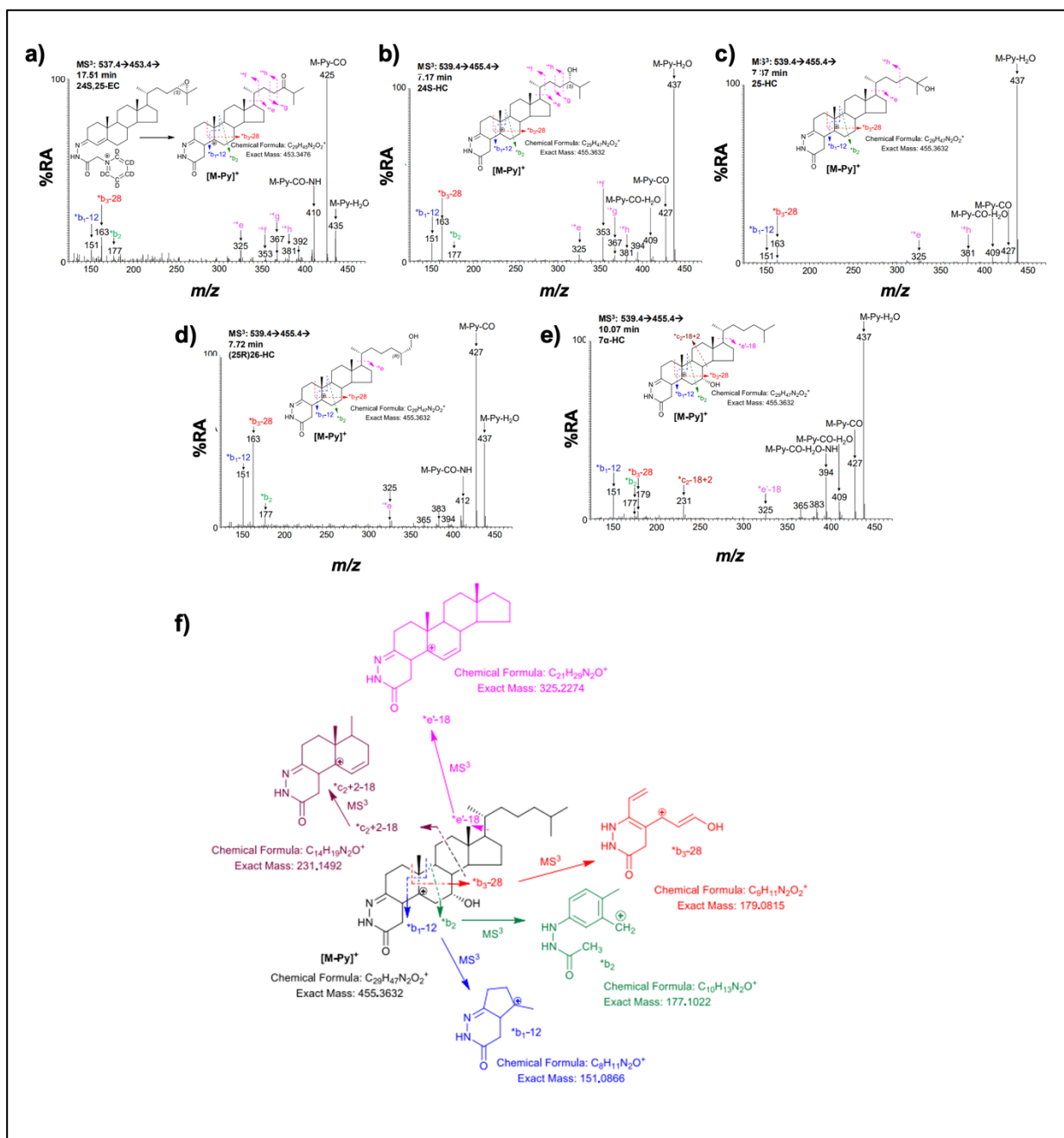


Figure 2.5. The MS³ fragmentation and corresponding fragments from several oxysterols. The fragmentation from 24S,25-EC, 24S-HC, 25-HC, (25R)26-HC and 7α-HC, with the specific fragmentation and subsequent fragment formation (see f).

2.2.10. Analysis of tissue using AP-MALDI

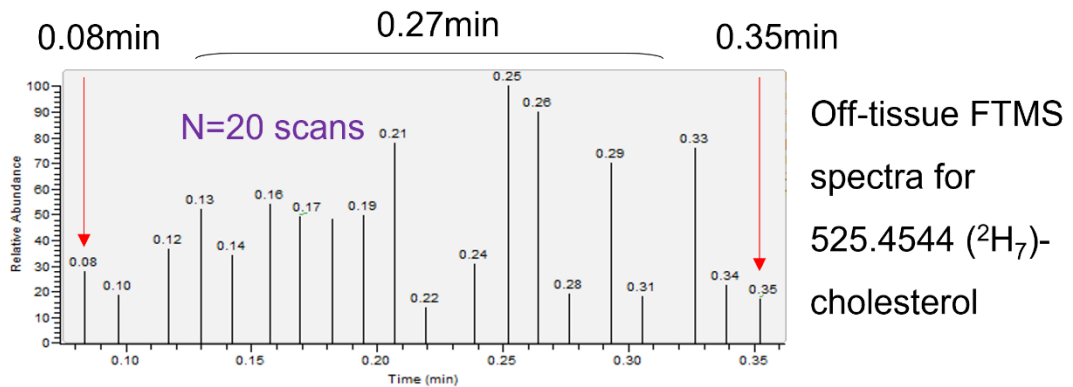
The MALDI analysis within this project was achieved using a 5th generation AP-MALDI UHR source from Mass-Tech and the Orbitrap ID-X from Thermo.

A neodymium-doped yttrium aluminium garnet (Nd:YAG) laser at a wavelength of 355 nm, with an output frequency of 10kHz, with a focused laser spot of around 10 micron (10 μ m) resolution was utilised.

The ITO-coated glass slide loaded with tissue, which has been derivatised and sprayed with matrix, was first cut to 5cm length before being fitted onto the target plate which sits on the target holder in the MALDI source. The MassTech MALDI source software was Target software, which was used to identify the dimensions of the sample area (tissue section) and worked in conjunction with the Thermo Tune software for the Orbitrap ID-X (see Figure 2.6).

As the Orbitrap IDX has automatic gain control (this defines the scan time to prevent overfilling of the trap), an off-tissue test was performed before each individual data acquirement to calculate the scan rate (scan/unit time) utilised by the Orbitrap for the scan method to be used for the subsequent acquisition on-tissue. The scan rate was calculated using the FTMS full scan event and using twenty individual scans to calculate the average time of one scan (see Figure 2.6). Calculating the scan rate (scan/time), or pixel duration (mins/scan), and using the spatial resolution required for the acquisition (in μ m) then allowed for the velocity of the stage movement (mm/min) to be calculated (see Figures 2.6 and 2.7 for worked example).

For 50µm (0.050mm) resolution run:



Time (mins) ÷ No. of scans = Pixel duration (mins)

0.27min ÷ 20 scans = 0.0135min per scan

Resolution (mm) = **Velocity (mm/min)**
Pixel duration (min)

0.050mm = **3.7037mm/min**
0.0135min

Figure 2.6. Calculation of the stage velocity (distance/time) based on a 50µm spatial resolution acquisition.

The width (columns) and height (rows) of the acquisition were decided using the Target software drawing the acquisition area to allow for the whole tissue to be covered. The measurement of the width/ column and the velocity of the stage helped to calculate the total run time, with the addition of the transition time (the time taken for the stage to go from the end of one row to the beginning of the next row), and number of rows contributing to the total time of the acquisition (see Figure 2.7).

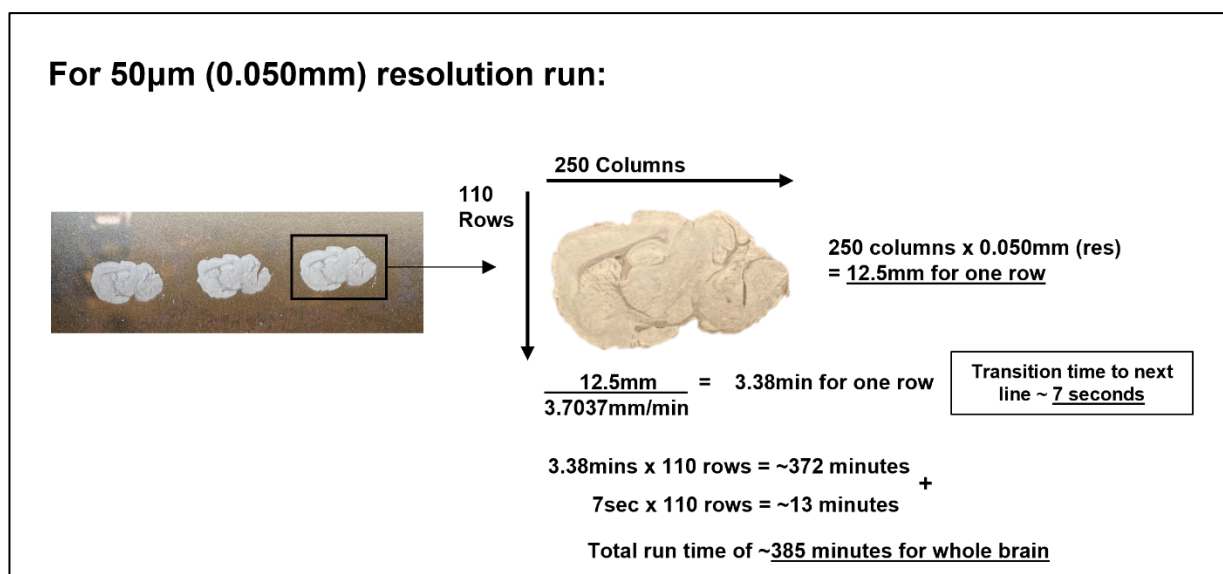


Figure 2.7. Determining the sample area, transition time and calculating the total acquisition time based on parameters from a 50 μ m resolution acquisition.

2.2.11. Orbitrap Elite and Orbitrap ID-X

All mass spectral work within this thesis was performed using the Orbitrap Elite and the Orbitrap ID-X mass spectrometers (Thermo Fisher Scientific, UK).

The Orbitrap Elite hybrid system (for schematic, see Figure 1.24 in introduction) with an ESI source was used for the analysis of plasma and brain homogenate samples for fractions 1 and 3 which was paired with a Dionex Ultimate 3000 Micro UHPLC system (Dionex, UK). For CSF analysis, a separate Dionex Ultimate 3000 NCS2 UHPLC system was used.

The Orbitrap ID-X tribrid system (see Figure 2.8) was used for analysis of mouse and human tissue sections using the Mass-Tech atmospheric pressure - matrix assisted laser desorption/ionisation ultra-high resolution (AP-MALDI UHR) source (Mass-Tech, Maryland, USA).

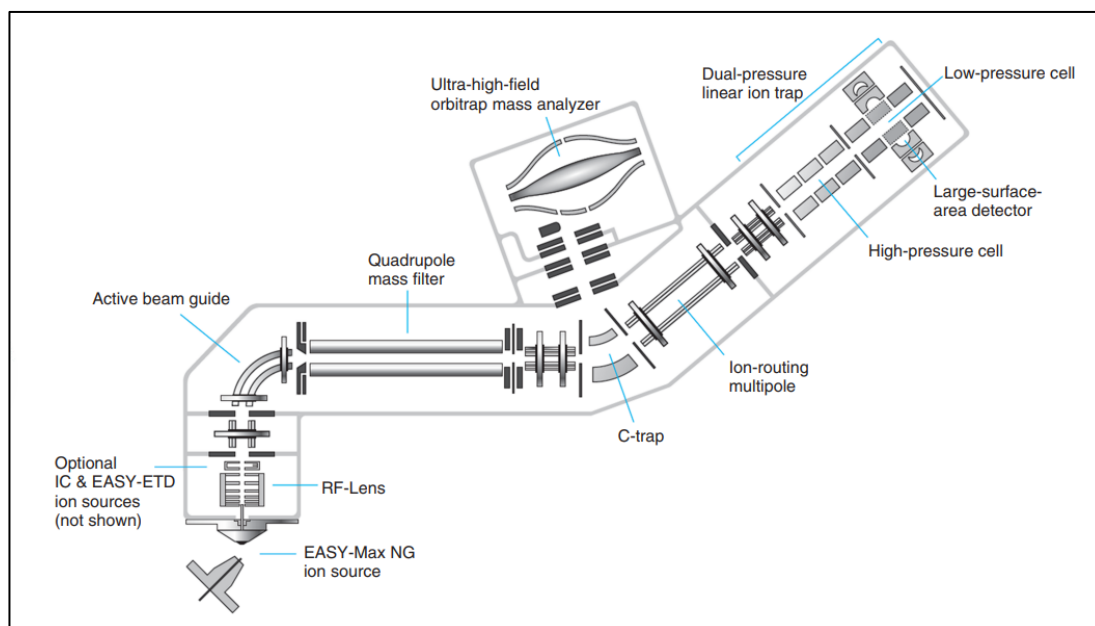


Figure 2.8. Schematic of the Orbitrap ID-X tribrid mass spectrometer. Reproduced from Hecht et al, 2019⁶.

2.2.12. Relative quantitation of analytes

As no calibration curves were calculated, all oxysterols (Fr1) were relatively quantified against the [$^2\text{H}_7$] 24R/S-hydroxycholesterol standard peak using Thermo Xcalibur software. This has been shown to be an acceptable internal standard for a broad range of oxysterols².

[$^2\text{H}_7$]22R-Hydroxycholest-4-en-3-one standard was used to relatively quantify the ratio of oxysterols that had a natural 3-oxo group without enzyme conversion (GP-d0). All other sterols (Fr3) were relatively quantified against the [$^2\text{H}_7$] cholesterol standard peak.

For the analysis of biofluid, oxysterols were reported as ng/mL concentration based on the volume of fluid used as a starting material (see Figure 2.9 on the next page for a worked example).

For brain tissue homogenisation in Chapter 4 (Alzheimer's disease), results were reported as ng per mg of tissue (ng/mg) used. Within Chapters 3 and 5, brain tissue analysis via homogenisation was unable to be calculated via tissue weight and therefore required the normalisation to cholesterol. This was due to either subpar tissue quality from long periods of storage (cerebrotendinous xanthomatosis tissue in Chapter 3), or the use of cryostat shavings resulting in increased condensation on the tissue samples which fluctuated the final weight of the tissue (multiple sclerosis

tissue in Chapter 5). The normalisation to cholesterol was performed to normalise to an internal factor within the tissue.

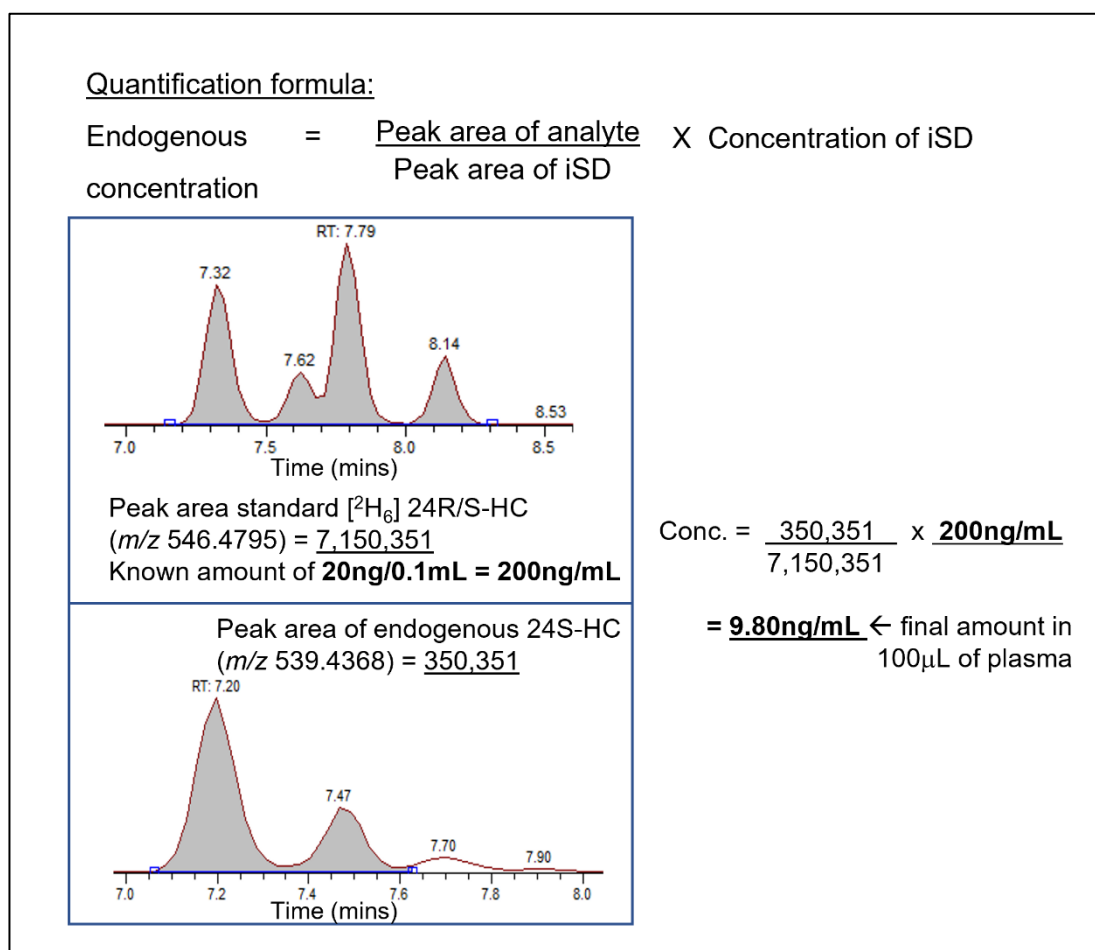


Figure 2.9. A worked example showing the relative quantification of endogenous oxysterol 24S-HC from control plasma using a deuterated internal standard.

2.3. References

1. Höflinger, P. *et al.* Metabolic profiling in serum, cerebrospinal fluid, and brain of patients with cerebrotendinous xanthomatosis. *J. Lipid Res.* **62**, 100078 (2021).
2. Yutuc, E. *et al.* Deep mining of oxysterols and cholestenoic acids in human plasma and cerebrospinal fluid: Quantification using isotope dilution mass spectrometry. *Anal. Chim. Acta* **1154**, 338259 (2021).
3. Griffiths, W. J. *et al.* Analysis of oxysterols by electrospray tandem mass spectrometry. *J. Am. Soc. Mass Spectrom.* **17**, 341–362 (2006).
4. Karu, K. *et al.* Liquid chromatography-mass spectrometry utilizing multi-stage fragmentation for the identification of oxysterols. *J. Lipid Res.* **48**, 976–987 (2007).
5. Yutuc, E. *et al.* Localization of sterols and oxysterols in mouse brain reveals distinct spatial cholesterol metabolism. *Proc. Natl. Acad. Sci.* **117**, 5749–5760 (2020).
6. Hecht, E. S., Scigelova, M., Eliuk, S. & Makarov, A. Fundamentals and Advances of Orbitrap Mass Spectrometry. in *Encyclopedia of Analytical Chemistry* 1–40 (Wiley, 2019). doi:10.1002/9780470027318.a9309.pub2.

Chapter 3: The profiling of oxysterols and sterols in cerebrotendinous xanthomatosis (CTX)

3.1. Introduction

Cerebrotendinous xanthomatosis (CTX) is a rare autosomal recessive disease where a mutation in the *CYP27A1* gene, coding for the sterol-27-hydroxylase enzyme of the same name (*CYP27A1*)¹, causes detrimental effects to protein activity and results in lack or complete loss of important oxysterols and bile acid precursors that derive from cholesterol metabolism².

The disease presents with a vast range of complex symptoms centring around progressive neurological dysfunction including cognitive decline, psychiatric disorders and spastic-ataxic gait disorder occurring later in life which means generally patients experience a diagnostic delay, averaging around 16 years²⁻⁴. After symptoms present, diagnosis can be confirmed with either plasma or CSF analysis of bile alcohol or cholestanol levels which all derive from cholesterol. This fluid analysis is also accompanied with magnetic resonance imaging to observe possible brain abnormalities including general brain atrophy, specific cerebellar atrophy, and brain xanthomas (deposition of lipid nodules) which are common in CTX^{3,5}.

The pathways most affected by this disease centre around cholesterol metabolism, with a major lack or loss of metabolites coming from the alternative pathway (also known as the 26-hydroxylation or acidic pathway) which heavily relies on the *CYP27A1* enzyme. The enzyme plays a crucial role in cholesterol homeostasis and bile acid synthesis via the classical and alternative pathways in the liver (see Figure 3.1), with the mutation significantly affecting the conversion of excess cholesterol to a number of bile acid precursors including (25R)26-HC (more commonly known as 27-HC), and downstream metabolites 3 β -HCA and 3 β ,7 α -diHCA³. As previously mentioned, the consequence of the mutation can range from either a partial decrease or complete lack of synthesis of these oxysterols and results in low levels of chenodeoxycholic acid (CDCA), the final product of the 26-hydroxylation pathway. Raised cholestanol levels via increased production and accumulation are also witnessed, which can be used as a positive biomarker³.

Treatment options are limited; however, bile acid replacement therapy is an option using CDCA supplementation⁴. The supplementation of CDCA works by reducing accumulation of pathway metabolites through down regulation of the *CYP7A1* gene and subsequently the *CYP7A1* enzyme, and drastically reduces 7 α -HC and 3 β -cholestanol formation (see Figure 3.1). Supplementation of cholic acid can also have

a positive effect on CTX patients, however this is usually used when individuals experience non-neurological symptoms exclusively^{3,6,7}.

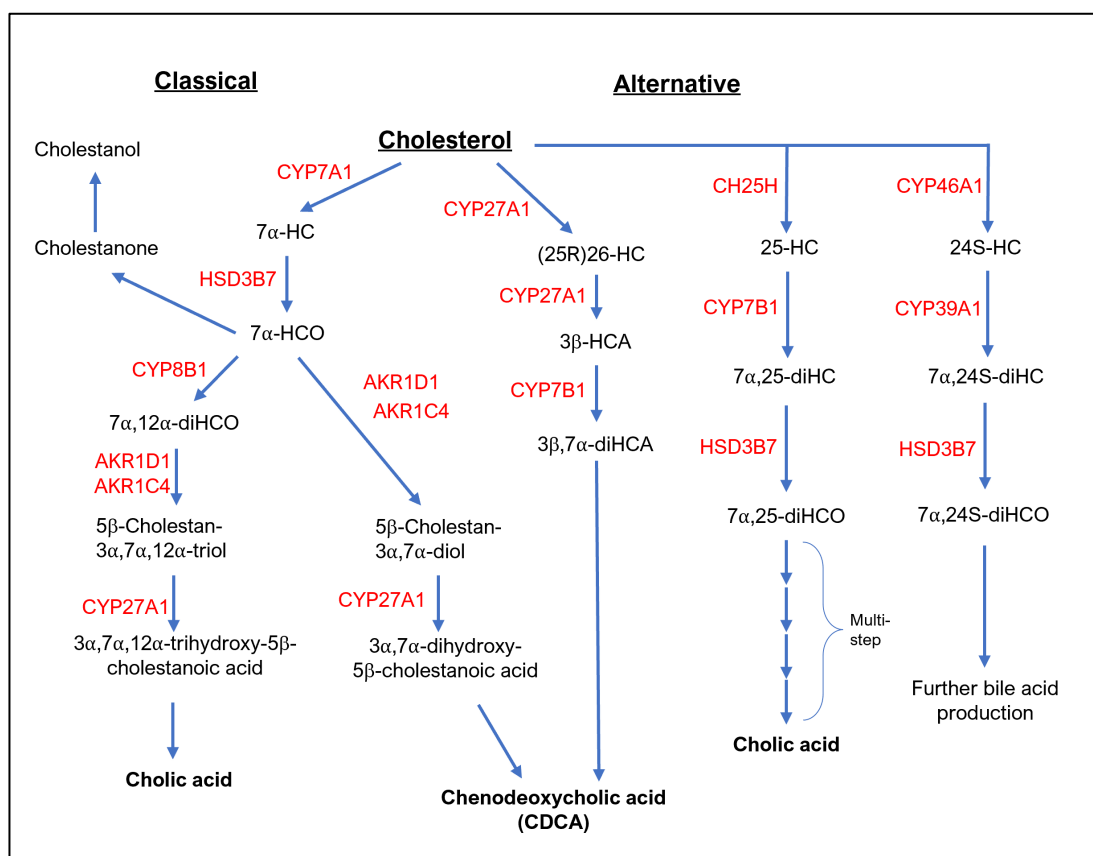


Figure 3.1. Cholesterol metabolism pathways for the synthesis of bile acids.

3.1.1. Aims

The aims of this study were to analyse biofluid samples and regional human brain tissue in CTX and control individuals to identify the severity of the mutation, identify potential metabolites and pathways that may have been compromised from the alteration in the CYP27A1 activity, and whether any other of these metabolites could potentially be used as an additional biomarker for CTX disease.

3.2. Materials and methods

3.2.1. CTX serum, control plasma and CSF cohort

The serum samples (n=4) used for the profiling of sterols and oxysterols in CTX were provided by Professor Ludger Schöls from the University of Tübingen in Germany (ethical approval from University of Tübingen, Germany; 199/2011BO1). There were four samples obtained from four individuals, one female and three males (demographics in Table 3.1). The CSF samples were also obtained from the same four individuals.

A control reference plasma (CRF plasma) obtained from a healthy 61-year-old female individual from Swansea University (n=1), where we performed four ‘technical’ replicates (multiple analysis from the same sample to check for variability). Data for the NIST 1950 standard reference material (SRM)⁸, representative of the population of the US reported in Yutuc et al, 2021⁹ was also reported in this chapter as an additional value for comparison to the single control reference plasma sample.

The control CSF sample was pooled CSF generated by combining individual CSF samples from multiple donors (n=67) obtained from the University Hospital of Umeå, Sweden and elsewhere (all participants or their parents/guardians provided informed consent and the studies were performed with institutional review board approval and adhered to the principles of the Declaration of Helsinki⁹). Again, four technical replicates were performed with the control CSF.

3.2.2. CTX brain tissue cohort

The brain tissue samples used within this study were provided by Dr Andrea DeBarber from the Oregon Health and Science University (OHSU) in Portland, Oregon (IRB00007099; Oregon Health and Science University)². The brain tissue samples provided were taken from one male individual diagnosed with CTX (demographics in Table 3.2), sampling areas from multiple brain regions including medulla oblongata, substantia nigra, basal ganglia, an area of the cerebellum with a CTX-defined lesion present and cerebrum tissue which for this work, we have defined as tissue containing cortical grey matter and white matter tissue. The condition of these tissues was subpar, with the loss of water content giving it a

sponge-like consistency. As a result, all brain tissue analysis and findings must be taken as exploratory.

Table 3.1. Demographics for CTX and control serum and CSF samples. The available demographics for the human serum and CSF CTX samples provided by Prof. Ludger Schöls from Tübingen, Germany².

Sample	Age at sampling	Gender (F/M)	Clinical features
CTX 31294	29	F	Tendon xanthomas
CTX 31761	60	M	Spastic paraparesis, tendon xanthomas
CTX 28965	35	M	Epilepsy, diarrhoea, cerebellar ataxia, cognitive deficit, spastic tetraparesis.
CTX 26932	47	M	Cognitive deficit, cerebellar ataxia, depression, cataracts.
Control CRF092 reference plasma	61	F	N/A
Control CSF	N/A	N/A	N/A

The control tissue was obtained from the Thomas-Willis Brain Bank in Oxford, UK (ethical approval from South Wales REC 13/WA/0292). The tissue was acquired from the cingulate gyrus region of the cortex which contained cortical grey and white matter tissue.

Table 3.2. Demographics for CTX and control brain tissue. A table containing all clinical information available for both the CTX and control brain tissue used. CTX tissue was obtained from Dr Andrea DeBarber in Portland, Oregon, US. Control brain was obtained from Thomas-Willis Brain Bank in Oxford, UK.

Brain sample	Brain region	Gender	Age at death	Cause of death
CTX	Cerebrum	M	26	Accidental fall
	Medulla oblongata (MO)			
	Cerebellar lesion (CBX L)			
	Substantia nigra (SN)			
	Basal ganglia (BG)			
Control 13/126	Cingulate gyrus	M	56	Cardiac arrest

3.2.3. Serum/ plasma extraction and sample preparation

For extraction, 100µL CTX serum (n=4) or control plasma (n=1) was added to EtOH-isotope labelled standard mix dropwise under sonication, then diluted to 70% EtOH (see section 2.2.1 for detailed description). After centrifugation, the solution underwent solid phase extraction (SPE) followed by enzyme-assisted derivatisation with cholesterol oxidase and Girard-P reagent before a final SPE which generates the MeOH sterol-containing eluents (see section 2.2.4 for details).

The eluted samples were diluted and processed at 60% MeOH, injecting 35 µL of this diluted sample into a Dionex Micro HPLC system coupled with an Orbitrap Elite mass spectrometer (see section 2.2.10 for more detail).

3.2.4. CSF extraction and sample preparation

For extraction, 250µL CSF (CTX - n=4; control – n=1) was added to EtOH-isotope labelled standard mix dropwise under sonication, then diluted to 70% EtOH (see section 2.2.2 for details). After centrifugation the solution underwent solid phase extraction (SPE) followed by enzyme-assisted derivatisation with Girard-P reagent before a final SPE which generates the MeOH sterol-containing eluents (see section 2.2.4 for details).

The eluted samples were diluted and processed at 60% MeOH, injecting 100 μ L of sample into a Dionex NCS2 HPLC system coupled with an Orbitrap Elite mass spectrometer (see section 2.2.10 for more detail).

3.2.5. Brain tissue homogenisation, extraction, and sample preparation

For the analysis of cerebrum tissue (n=1), we performed three ‘technical’ replicates (multiple analysis from the same sample to check for variability), and for the analysis of the different brain areas seen in Table 3.2 (all n=1), only one homogenisation was performed purely for exploratory purposes. For homogenisation, samples of brain between 40 and 250 mg were homogenised in an EtOH-isotope labelled standard mix to extract maximum sterol amount collecting a total of 4.2 mL of solution, which was diluted to 6 mL at 70% EtOH.

For extraction, 600 μ L of solution (i.e. 10% of the extract) was added to absolute EtOH dropwise under sonification, then diluted to 70% EtOH (see section 2.2.3 for details). The solution underwent solid phase extraction (SPE) followed by enzyme-assisted derivatisation with Girard-P reagent before a final SPE which generates the MeOH sterol-containing eluents (see section 2.2.4 for details).

The eluted samples were diluted and processed at 60% MeOH, injecting 35 μ L of sample into a Dionex Micro HPLC system coupled with an Orbitrap Elite mass spectrometer (see section 2.2.10 for more detail), where a 17-minute run was used to quantify all data.

3.2.6. Oxysterol analysis

The quantification of peaks was carried out using mass spectrometry software Xcalibur from Thermo-Fisher.

All oxysterols were quantified against the [$^2\text{H}_7$] 24R/S-hydroxycholesterol ([$^2\text{H}_7$] 24R/S-HC) standard peak. Once derivatised [$^2\text{H}_7$] 24R/S-HC has proved to be an acceptable surrogate for the quantification of oxysterols in general¹⁰. Other sterols were quantified against [$^2\text{H}_7$] cholesterol. The [$^2\text{H}_7$] 22R-hydroxycholest-4-en-3-one standard was used to quantify oxysterols that had a natural 3-oxo group.

For the brain tissue analysis, all data was normalised to the cholesterol (ng/mg of cholesterol) from each sample. This was due to the condition of the CTX brain samples having lost much of the water from the brain after many years of storage,

with the samples becoming porous and dry. This meant the weight of the CTX brain tissue was not comparable to the weight of the control brain tissue. The normalisation to cholesterol meant the CTX and control data could be comparable. For this chapter, no statistical analysis was performed due to the low sample numbers for both control plasma (see section 3.2.1), control CSF (see section 3.2.1) and CTX brain tissue (see section 3.2.5). Due to performing technical replicates ($n=1$), we were unable to perform any statistical tests on this dataset, so therefore the find this chapter should be interpreted as observational only, with further controls and disease cases need to confirm these findings.

For all ITMS³ structural fragmentation information, please refer to Figure 2.5 on page 84 (section 2.2.9) for further details on the b_1 -12, b_2 and b_3 -28 labelled fragment peaks.

3.3. Results

3.3.1. Cholesterol

Cholesterol is the main precursor for all bile acid analytes, and in CTX its metabolism is compromised due to the mutation within the *CYP27A1* gene. For this study, we quantified the free cholesterol levels (m/z 523.4414; see Figure 3.2) in all sample types in CTX and control.

In serum, cholesterol levels showed a decrease in CTX samples compared to the female reference control at an average of 411.5 $\mu\text{g/mL}$ compared to 669.9 $\mu\text{g/mL}$ respectively, however the levels in the CTX samples were comparable to the NIST SRM (402.5 $\mu\text{g/mL}$)⁹. In CSF samples the level of cholesterol showed no differences, with the average quantity in CTX at 1.52 $\mu\text{g/mL}$ and in control 1.54 $\mu\text{g/mL}$ (see Figure 3.3).

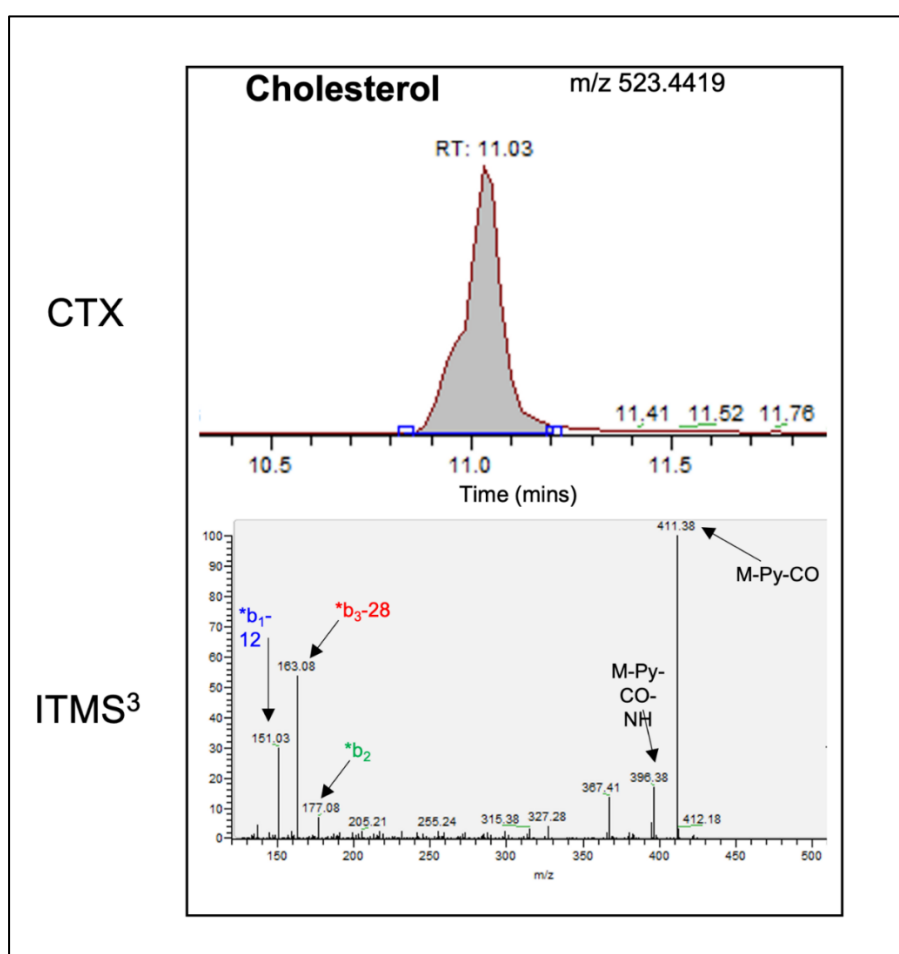


Figure 3.2. Identification of cholesterol using mass spectra and ion trap fragmentation (ITMS³) from CTX serum. The cholesterol peak is found at m/z 523.4419, eluting at around 11 minutes with fragmentation giving a large 411 fragment, and smaller 396, 177, 163 and 151 fragments. The grey shaded area shows the quantified area.

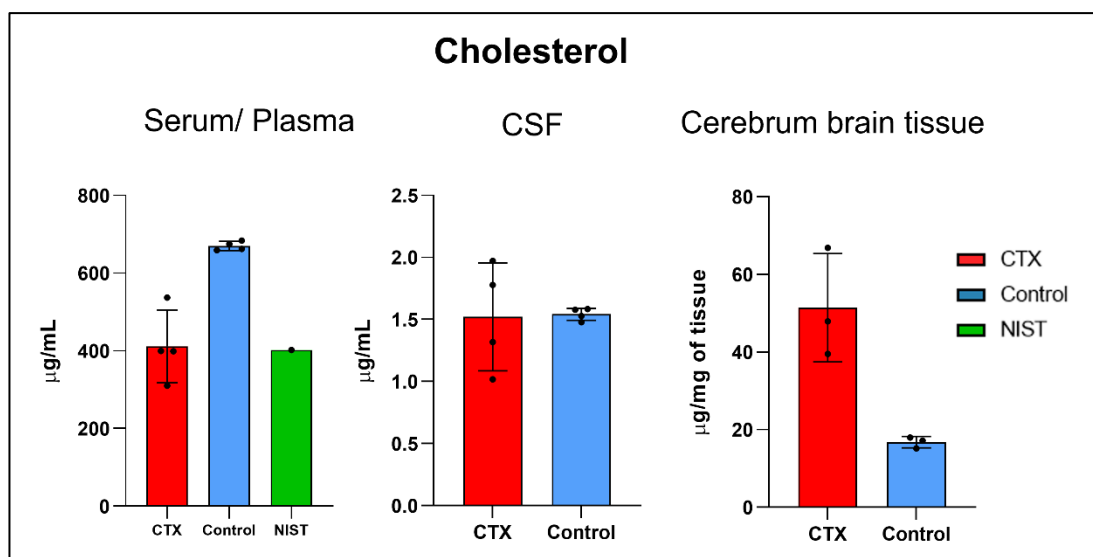


Figure 3.3. Analysis comparing CTX and control cholesterol levels in serum and CSF. All plots above display average values with SD.

In cerebrum brain tissue, free levels were over three-fold higher in CTX tissue compared to control (51.41 ± 13.99 µg/mg of tissue and 16.66 ± 1.34 µg/mg of tissue respectively). However, due to the condition of the brain tissue (discussed in section 3.2.2), this result can only be discussed as observational. It should also be noted that for the CTX samples the standard deviation was large for most metabolites quantified during this chapter. This is due to CTX being unique in every individual ($n=4$) depending on the severity of the mutation which can alter the levels of each individual metabolite, and whether the patient has received treatment. This means that the quantified levels of sterols from one individual can be vastly different compared to another, which will increase the range and standard deviation of the cohort.

For the analysis of the different brain areas taken from the individual with CTX, the free cholesterol was lowest in the basal ganglia brain region tissue (50.11 µg/mg of tissue), a large deep grey matter structure made up for subcortical nuclei.

Interestingly, the region with the highest cholesterol was the substantia nigra, a deep grey matter structure found within the basal ganglia where dopaminergic neurons are located (75.23 µg/mg of tissue), suggesting that the substantia nigra and dopaminergic neurons are more cholesterol rich in comparison to other regions of the basal ganglia in CTX. However, this data needs to be treated with caution considering the desiccated nature of the brain tissue. Recent studies researching cholesterol in the substantia nigra suggested increased cholesterol leads to

dopaminergic neuronal loss, resulting in Parkinson's disease¹¹. It has been reported that in some cases of CTX, symptoms resembling Parkinson's disease can be experienced by the individual known as atypical parkinsonism¹², which could link to the increase of cholesterol observed here in the substantia nigra.

The other regions of interest analysed included the medulla oblongata (68.91 µg/mg of tissue), a white matter structure located in the uppermost region of the brain stem, and cerebellar lesion tissue (60.92 µg/mg of tissue), which is an area of the cerebellum containing a xanthoma (lipid deposit).

3.3.2. Alternative pathway (26-hydroxylation)

CTX disease results from a mutation in the *CYP27A1* gene, coding for the enzyme of the same name. The mutation results in functional dysregulation of the enzyme, causing products of the 26-hydroxylation pathway to be absent or greatly diminished including (25R)26-HC, 3β-HCA, 3β,7α-diHCA and 7α-hydroxy-3-oxocholestenoic acid (7αH,3O-CA). The presence, or lack of, these metabolites was confirmed using MS³ ion-trap fragmentation where MS² gives a neutral loss of Girard P d0 (*m/z* 79.0) or Girard P d5 (*m/z* 84.1) and MS³ of the daughter ion gives a unique fragment pattern for each metabolite (see Figure 3.5; ITMS³ panel – annotated ITMS³ spectra for all analytes can be found in Table 9.1 in Appendix).

Across all samples analysed, three of these four metabolites were undetectable in CTX, the exception being 3β-HCA which showed depleted levels in both serum and CSF (see Figure 3.4 for quantified levels, and Figure 3.5 for confirmation of the metabolites using MS³ fragmentation). In serum, all metabolites were reduced in CTX compared with the female reference plasma and the NIST SRM⁹. The average level of 3β-HCA in CTX was 1.76 ng/mL, compared to the female reference at 130.17ng/mL and a value of 124.08 ng/mL for the NIST 1950 standard reference material⁹, with a unique fragmentation pattern of a high 441, and lower 451, 423 and 408 fragment ions (see Figure 3.4 and 3.5). In the female reference plasma, levels of (25R)26-HC were 42.83 ng/mL with a unique fragmentation pattern of a high 427, and lower 437, 421 and 409 fragment ions, 3β,7α-diHCA 26.70 ng/mL and 7αH,3O-CA 60.98 ng/mL with a unique fragmentation pattern of a high 467, and lower 457, 439, 424 and 421 fragment ions, for comparison the values from NIST 1950 were 24.02 ng/mL ((25R)26-HC), 41.57 ng/mL (3β,7α-diHCA) and 99.13 ng/mL (7αH,3O-CA)⁹ (see Figure 3.4).

In CSF, again metabolites in CTX serum were reduced compared to the control plasma. The average level of 3 β -HCA in CTX was 0.41 ng/mL, compared to the control at 1.55 ng/mL. In control CSF, (25R)26-HC was undetected due to lower levels found in CSF compared to plasma, however average level of 3 β ,7 α -diHCA was 4.46 ng/mL and 7 α H,3O-CA was 28.81 ng/mL. All metabolites quantified showed an observed decrease in control pooled CSF compared to CTX (see Figure 3.4). In cerebrum brain tissue analysis, there was a similar trend to that seen in serum, with all four metabolites undetectable in the CTX brain tissue samples, and generally all other metabolites were increased compared with the control.

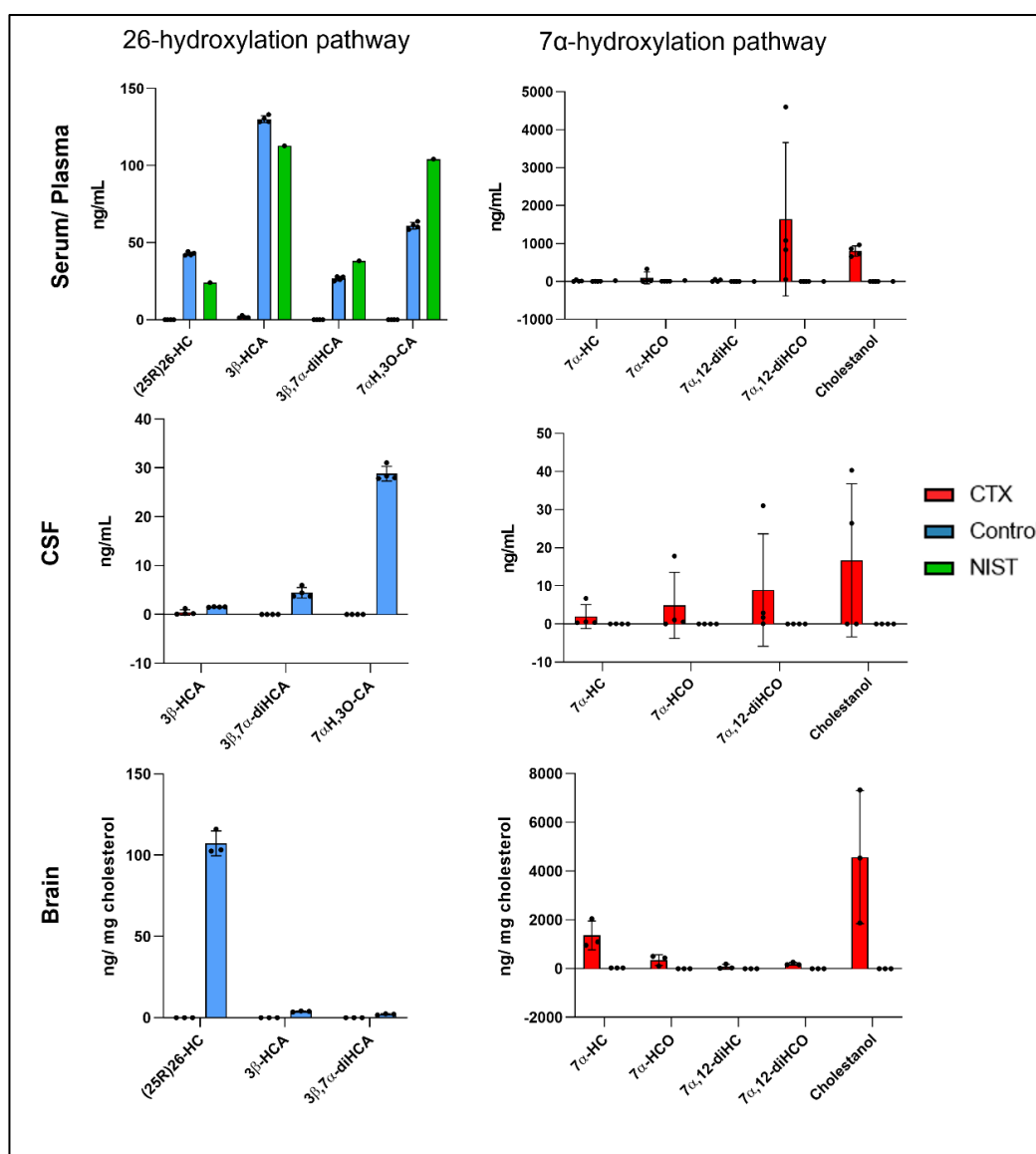


Figure 3.4. Reduced levels of several cholesterol metabolites involved in the 26-hydroxylation and 7 α -hydroxylation pathways observed in CTX serum, CSF and brain tissue. All plots above display average values with SD.

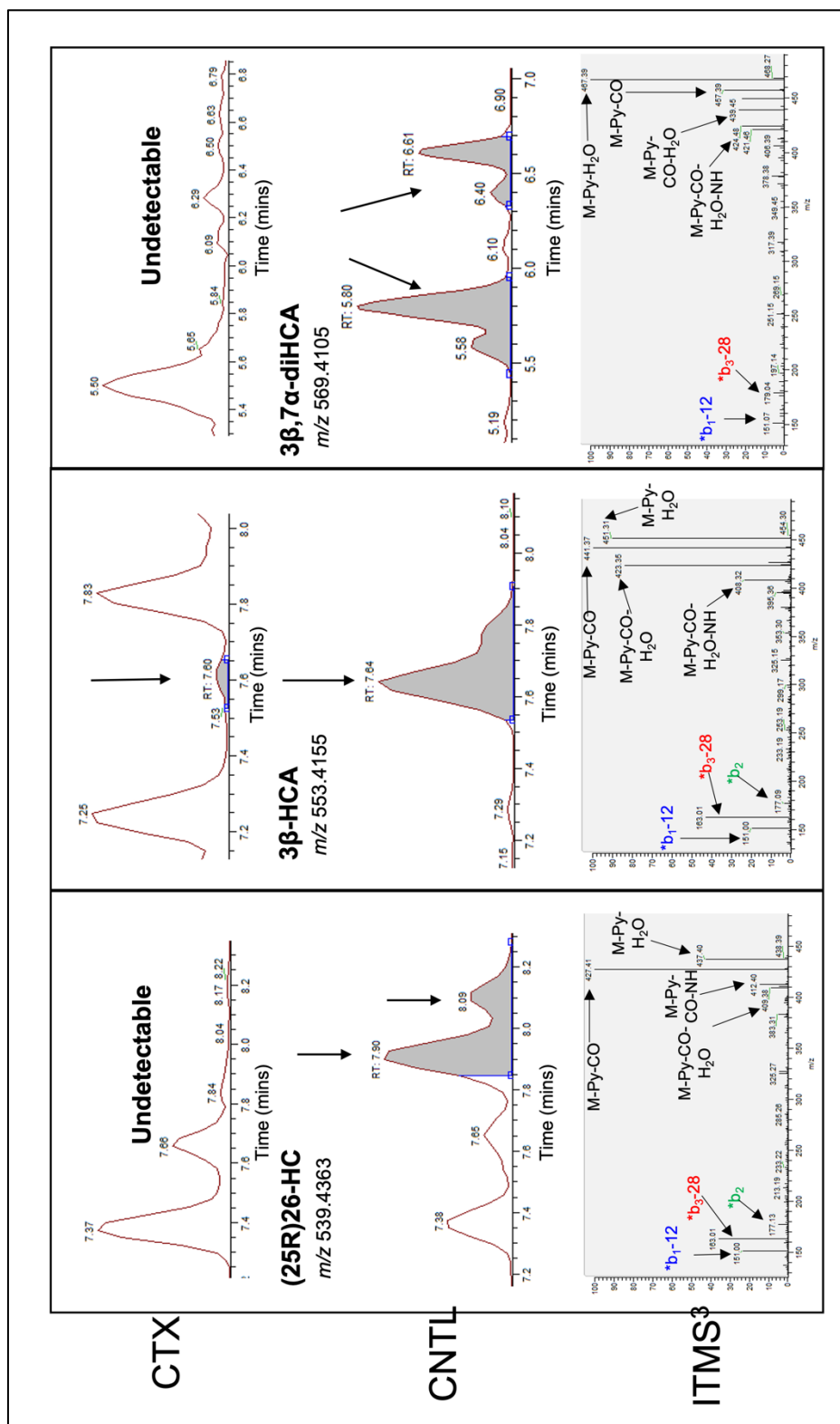


Figure 3.5. Spectra of metabolites of the 26-hydroxylation pathway from the serum/plasma data with the corresponding ITMS³ fragmentation. Peaks of (25R)26-HC, 3β-HCA and 3β,7α-diHCA identified with LC-MS³, with the unique ITMS³ fragmentation spectra.

In control brain the average levels seen for (25R)26-HC was 107.32 ng/mg of cholesterol, 3 β -HCA was 3.91, and 3 β ,7 α -diHCA was 2.07 (all units ng/mg of cholesterol).

Observations from CTX regional brain tissue analysis established there were no detectable levels of the metabolites from the 26-hydroxylation pathway from the four regions of interest.

3.3.3. Classical pathway (7 α -hydroxylation)

The classical pathway is responsible for ~90% of bile acid products synthesised from cholesterol metabolism and is reliant on the CYP7A1 enzyme for 7 α -hydroxylation. Several upregulated classical pathway products are observed in CTX, including 7 α ,12 α -diHC. All the metabolites quantified from the classical pathway had a large standard deviation, which is explained by CTX presenting differently in every individual. This means the levels in each individual vary widely which increased the range of the quantified sterols in biofluid and brain tissue. Again, the presence, or lack of, were confirmed using MS³ ion-trap fragmentation where MS² gives a neutral loss of Girard P d0 (m/z 79.0) or Girard P d5 (m/z 84.1) and MS³ of the daughter ion gives a unique fragment pattern for each metabolite (see Figure 3.6; ITMS³ panel - annotated ITMS³ spectra for all analytes can be found in Table 9.1 in Appendix).

The levels of 7 α -HC measured by LCMS showed a five-fold increase in CTX serum compared to the reference sample, with the 3-oxo form, 7 α -hydroxycholest-4-en-3-one (7 α -HCO) displaying a much larger difference with average levels in CTX of 91.35 ng/mL and the reference plasma at 7.06 ng/mL, the corresponding value for the NIST 1950 is 25.96 ng/mL⁹. Other metabolites within the classical pathway identified in these samples were 7 α ,12 α -diHC and its oxidised form 7 α ,12 α -diHCO. Both these metabolites and 3 β -cholestanol showed increases in CTX serum compared with the reference and the NIST SRM (see Figure 3.4).

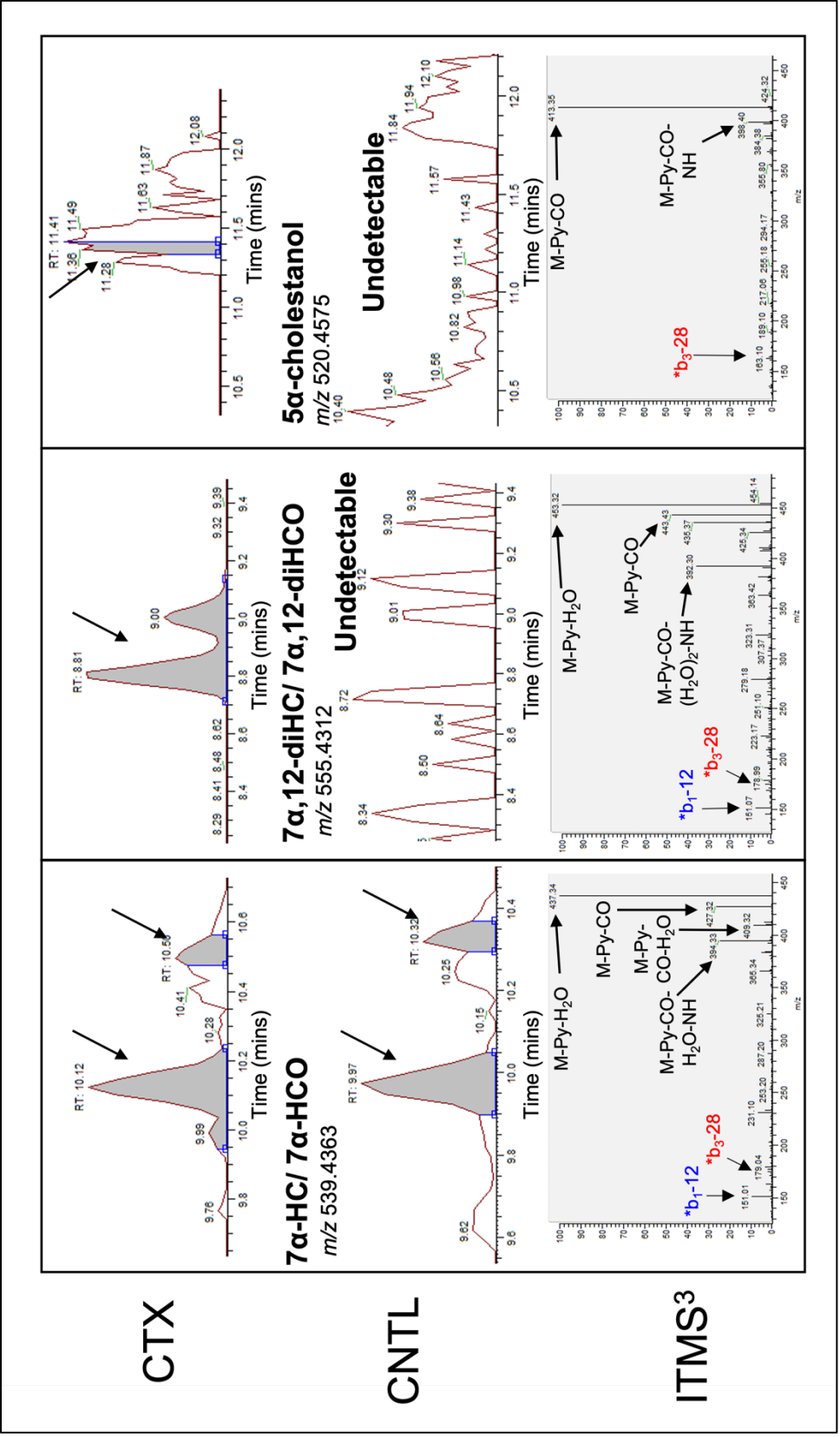


Figure 3.6. Spectra of metabolites of the 7 α -hydroxylation pathway and of 3 β -cholestanol from the serum data with the corresponding ITMS³ fragmentation. Peaks of 7 α -HC and 7 α -HCO, 7 α ,12 α -diHC and 7 α ,12 α -diHCO, and 3 β -cholestanol identified with LC-MS³, with the unique ITMS³ fragmentation spectra.

In CSF, a similar trend was seen in CTX CSF where 7α -HC, 7α -HCO, and $7\alpha,12\alpha$ -diHCO were increased compared to the control, however $7\alpha,12\alpha$ -diHC was undetectable. The analysis of cerebrum brain tissue again showed a similar trend to that seen in both the serum/plasma and CSF, with levels of 7α -HC, 7α -HCO, $7\alpha,12\alpha$ -diHC, $7\alpha,12\alpha$ -diHCO and cholesterol being higher in CTX compared with control brain tissue (see Figure 3.4).

3.3.4. Cerebral pathway (24-hydroxylation)

The cerebral pathway initiates with the CYP46A1 enzyme, an enzyme that catalyses 24-hydroxylation which is almost exclusively expressed in neuronal cells within the cerebral cortex and deep grey matter regions of the brain. Again, the presence, or lack of, were confirmed using MS³ ion-trap fragmentation where MS² gives a neutral loss of Girard P d0 (m/z 79.0) or Girard P d5 (m/z 84.1) and MS³ of the daughter ion gives a unique fragment pattern for each metabolite (see Figure 3.7; ITMS³ panel - annotated ITMS³ spectra for all analytes can be found in Table 9.1 in Appendix).

The 24S-HC peak, found at m/z 539.4368 (see Figure 3.7) was identified in all three sample types analysed. The levels of 24S in CTX serum and the reference plasma were similar at 21.66 ng/mL and 22.97 ng/mL respectively, however the CTX serum did show a large increase compared with the NIST SRM (9.19 ng/mL)⁹. In CTX CSF samples 24S-HC was detected with an average level of 0.06 ng/mL but not detected in the control sample. In cerebrum brain tissue, 24S-HC was increased in CTX after normalisation to cholesterol (average levels in CTX 1653.38 ng/mg cholesterol and controls 1314.34 ng/mg cholesterol).

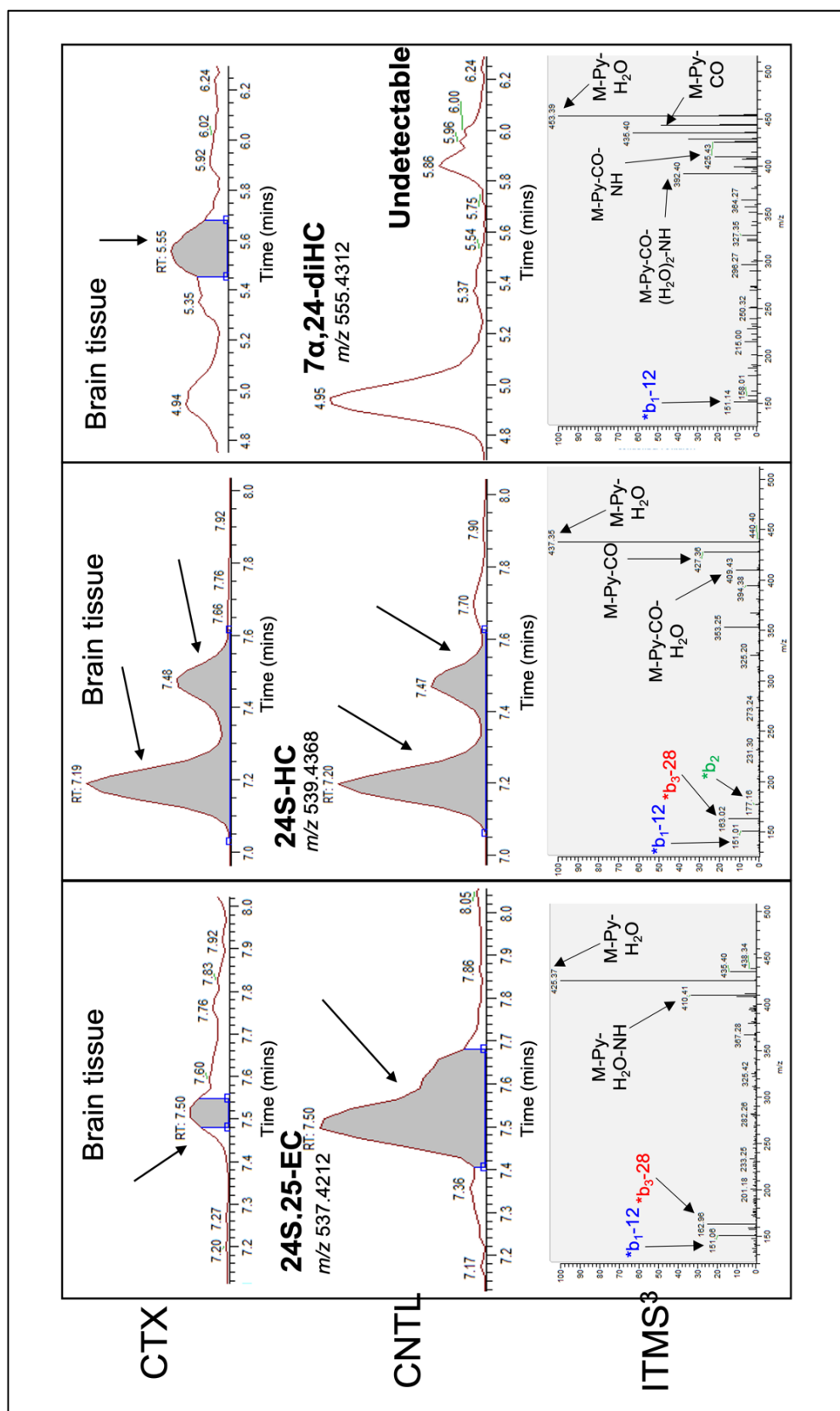


Figure 3.7. The metabolites identified from the cerebral pathway in CTX and control. Peaks of 24S,25-EC, 24S-HC and 7α,24-diHC identified with LC-MS³, with the unique ITMS³ fragmentation spectra. To note, the ITMS³ spectrum of *m/z* 555.4312 confirms the peak seen at 5.37 mins does not correspond to 7α,24-diHC in the control brain.

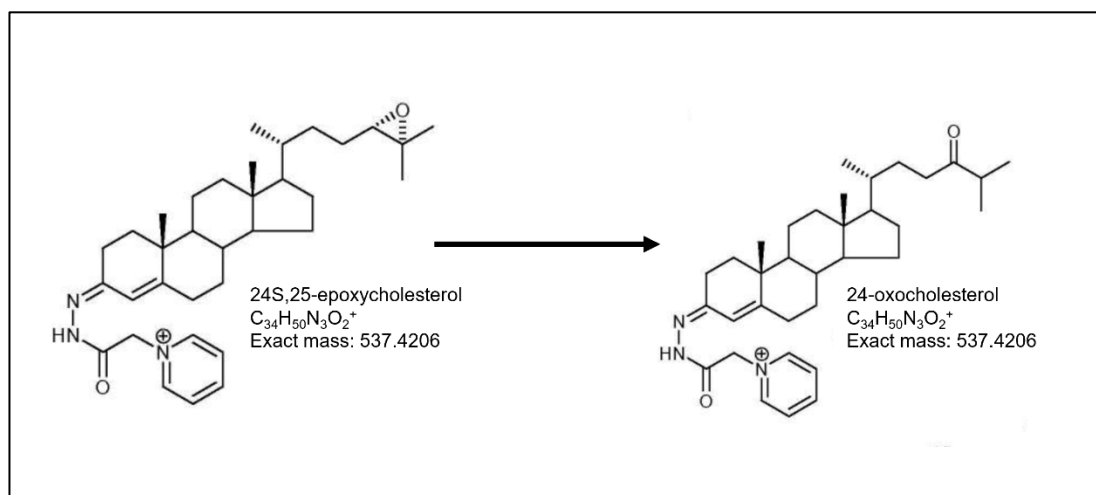


Figure 3.8. The conversion of 24S,25-epoxycholesterol (24S,25-EC) to 24-oxocholesterol (24-OC).

Peaks at m/z 537.4206 were identified as 24S,25-EC, which isomerises to 24-OC during sample preparation (see Figure 3.8 for structures). Here we consider 24S,25-EC to be a member of the 24-hydroxylation pathway as it can be formed by the CYP46A1 oxidation of desmosterol. These specific compounds were not seen in serum samples; however, they were identified in the control CSF and both the CTX and control brain tissue samples analysed (see Figure 3.9).

Finally, $7\alpha,24$ -diHC was detected in cerebrum brain tissue exclusively within the CTX samples. The average levels quantified in CTX brain tissue was 21.72 ng/mg of cholesterol.

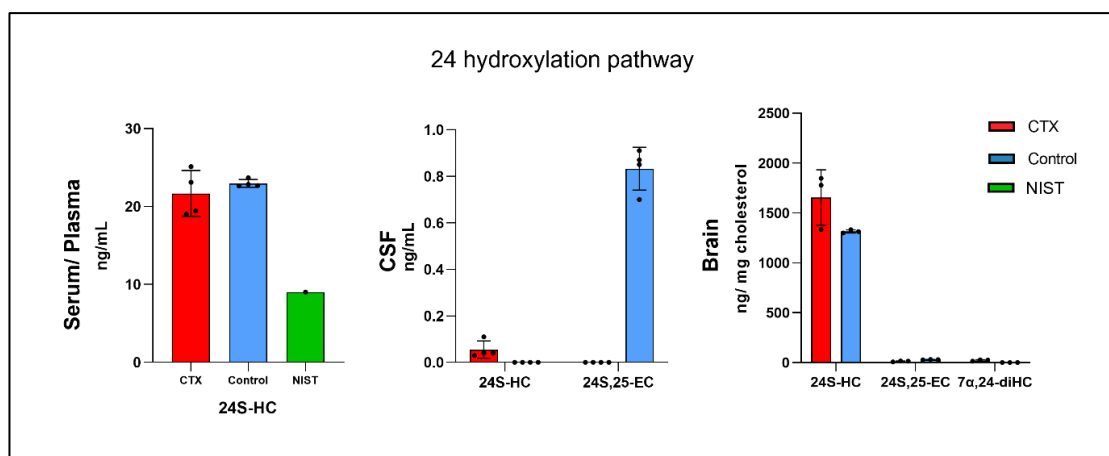


Figure 3.9. Analysis of metabolites within the 24S-hydroxylation pathway identified within CTX serum and reference plasma, CSF, and cerebrum brain tissue. All plots above display average values with SD.

3.3.5. 25-hydroxylation pathway

25-Hydroxylation of cholesterol is performed by the CH25H enzyme, most known for its presence in macrophage immune cells. Other CYP enzymes can also behave as sterol 25-hydroxylases including CYP3A enzymes^{13,14}. There were several metabolites potentially involved in the 25-hydroxylation pathways identified within the CTX biofluid, including 25-HC at m/z 539.4363 with an ITMS³ spectra of a high 437 peak only, 3β,22-dihydroxycholest-5-en-24-one (or possibly 3β,20-dihydroxycholest-5-en-22-one) at m/z 553.4155 with an ITMS³ spectra of a moderate 325 accompanied by higher 423 and 441 fragments and its downstream metabolite 3β,22,25-trihydroxycholest-5-en-24-one at m/z 569.4105 with an ITMS³ spectra of a large 385 fragment, with a smaller 467 peak (see Figure 3.10 - annotated ITMS³ spectra for all analytes can be found in Table 9.1 in Appendix). Again, the presence, or lack of, were confirmed using MS³ ion-trap fragmentation where MS² gives a neutral loss of Girard P d0 (m/z 79.0) or Girard P d5 (m/z 84.1) and MS³ spectra of the daughter ion gives a unique fragment pattern for each metabolite (see Figure 3.10; ITMS³ panel). In serum, both 3β,22-dihydroxycholesta-5-en-24-one and 3β,22,25-trihydroxycholest-5-en-24-one were observed to be increased in CTX patients with average levels at 45.76 ng/mL and 27.29 ng/mL respectively, compared with 3.74 ng/mL and 3.61 ng/mL respectively for in the reference plasma (see Figure 3.11).

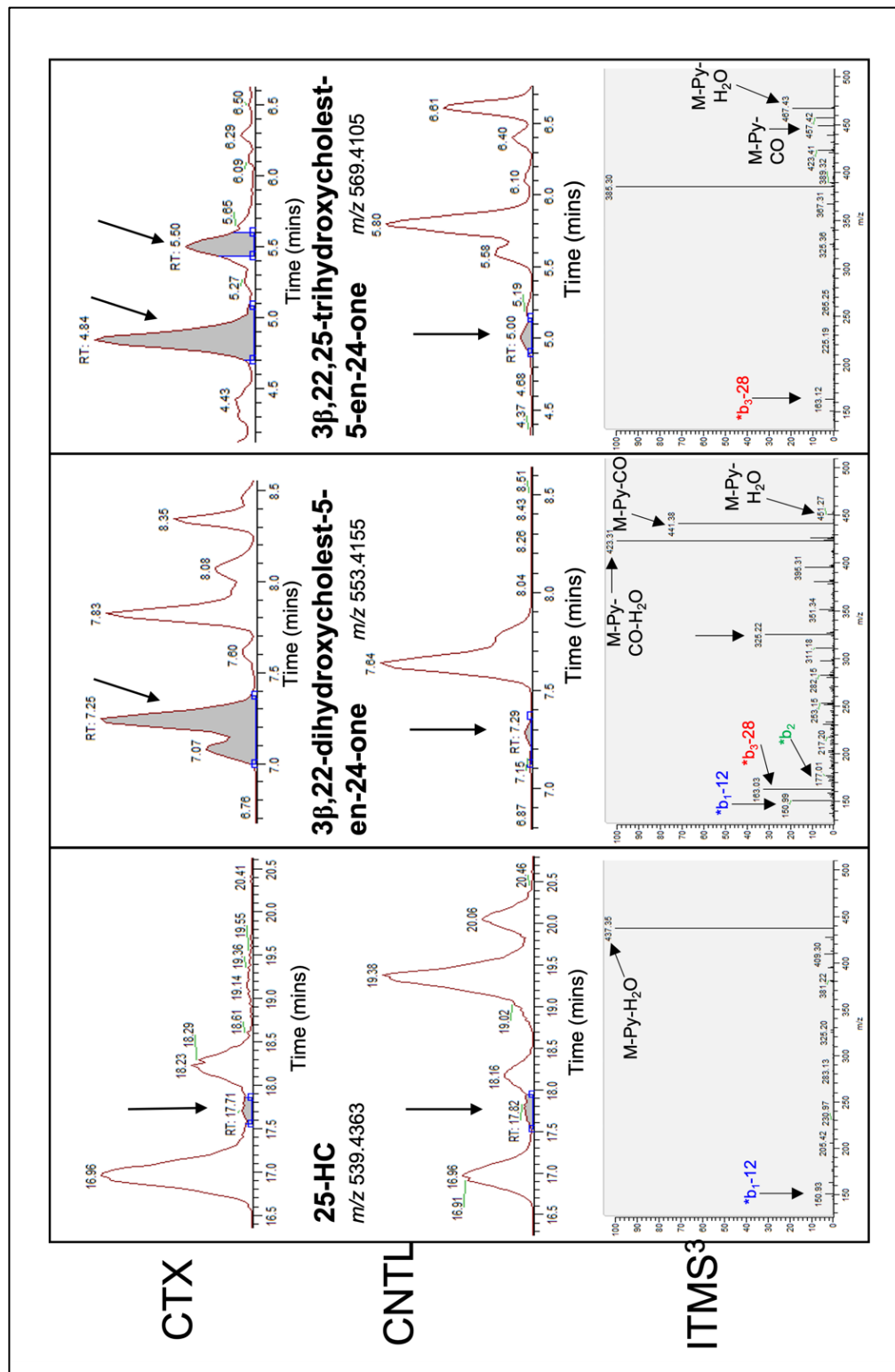


Figure 3.10. Spectra of metabolites from the 25-hydroxylation pathway identified in CTX serum and control plasma. Peaks of 25-HC, 3β,22-dihydroxycholesta-5-en-24-one, and 3β,22,25-trihydroxycholest-5-en-24-one identified with LC-MS³, with the unique ITMS³ fragmentation spectra

25-HC showed a slight increase in CTX serum compared to the reference plasma and to the NIST SRM (average levels of 2.21 ng/mL in CTX compared to 1.70 ng/mL in reference plasma and 1.10 ng/mL in NIST SRM).

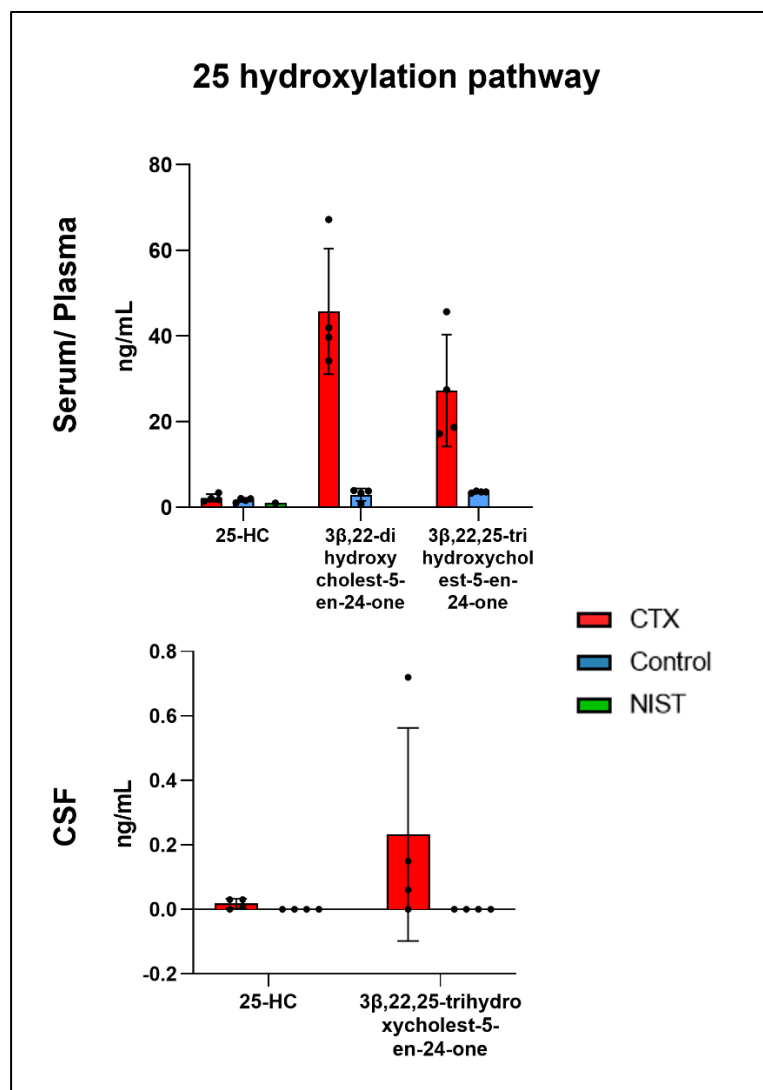


Figure 3.11. Analysis of metabolites within the 25-hydroxylation pathway identified within CTX serum, control plasma and CSF. All plots display average values with SD.

In CSF samples, data was only quantified for 25-HC and 3β,22,25-trihydroxycholest-5-en-24-one in CTX, with 3β,22-dihydroxycholesta-5-en-24-one being undetectable. Both metabolites showed increased levels in CTX samples, with 25-HC showing average levels of 0.018 ng/mL and 3β,22,25-trihydroxycholest-5-en-24-one with 0.233 ng/mL compared with control CSF, where both metabolites were undetected. The only metabolite identified from the 25-hydroxylation pathway in cerebrum brain tissue was 25-HC, which when normalised to cholesterol showed an increase in CTX

compared to control where it was undetected (average levels of 57.50 ng/mg cholesterol).

3.3.6. Analysis from regional brain tissue in CTX

The CTX patient who donated the cerebrum brain tissue also had samples taken from several other brain regions, including medulla oblongata (the upper most part of the brain stem), a cerebellar lesion (cerebellum is the structure used for balance and movement, with a CTX xanthoma lipid deposit), basal ganglia (a large deep grey matter region filled with subcortical neurons) and the substantia nigra (a specific region of the basal ganglia containing dopaminergic neurons). Due to a limited sample amount of each region, we only performed an n=1 of each region with no technical replicates. For this reason, all reported data below is observational, with more samples needed to confirm any observations we have reported below.

Numerous metabolites were quantified from all four regions of interest (see Figure 3.12), with the basal ganglia highest for monohydroxycholesterol products including 24S-HC, 25-HC and 7 α -HC. The cerebellar lesion also showed relatively high levels of each metabolite. Medulla showed the lowest amount of 24S-HC (expected due to it being the only white matter region analysed) but did show the highest levels of cholestanol by almost 2-fold compared to other regions. The substantia nigra did not show the highest levels for any of the metabolites quantified, and instead showed the lowest levels of cholestanol, 7 α -HC and the dihydroxycholestenone 7 α ,12 α -diHCO of all the regions analysed.

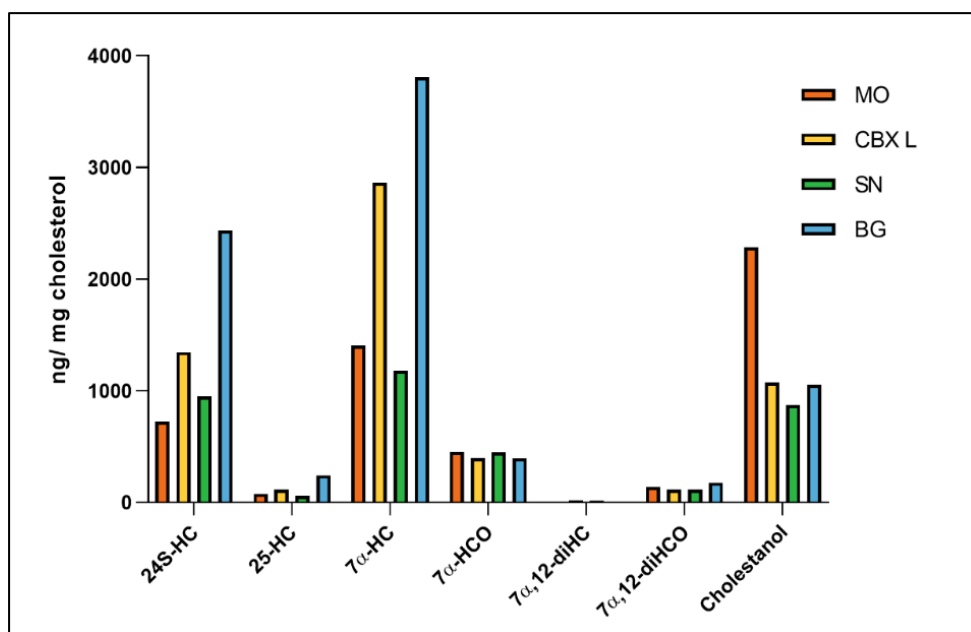


Figure 3.12. Observations from regional brain tissue samples from an individual with CTX.

Analysis of brain tissue homogenates normalised to cholesterol content showed regional differences for specific metabolites. This includes 24S-HC, which was observed to be highest in the basal ganglia, a deep grey matter regions filled with subcortical neurons, and lowest in the medulla oblongata, a white matter region located in the brain stem. As all metabolites from the 26-hydroxylation pathway were undetectable in all the brain regions analysed. (MO - medulla oblongata; CBX L - cerebellar lesion; SN - substantia nigra; BG - basal ganglia).

After cholesterol oxidase and GP-tagging			Mean concentration (ng/mL ± SD)						
Mass (± 5ppm)	Sterol/ Oxysterol Systematic name	Sterol/ Oxysterol Common name	Elemental composition	Abbreviation	CTX plasma (n=4)	Control plasma (n=1)	NIST 1950 SRM	CTX CSF (n=4)	Control CSF (n=1)
523.4419	(GP ^{[2} H ₅]) Cholest-4-en-3-one	Cholesterol	C ₃₄ H ₄₇ D ₅ N ₃ O ⁺	-	411,478.5 ± 93664	669,858.5 ± 11640.48	402,515	1,524.05 ± 436.23	1,542.25 ± 49.08
525.4575	(GP ^{[2} H ₅]) Cholestan-3-one	Cholestanol	C ₃₄ H ₄₉ D ₅ N ₃ O ⁺	-	802.49 ± 136.81	ND	NR	16.69 ± 20.09	ND
537.4211	(GP ^{[2} H ₅]) 24S,25-Epoxycholest-4-en-3-one	24S,25-Epoxycholesterol/ 24-oxocholesterol	C ₃₄ H ₄₅ D ₅ N ₃ O ₂ ⁺	24S,25-EC/ 24-OC	ND	ND	NR	ND	0.83 ± 0.09
534.4054	(GP ^{[2} H ₀]) 3β-Hydroxycholest-5-en-7-one	7-Oxocholesterol	C ₃₄ H ₅₂ N ₃ O ₂ ⁺	7-OC	1.79 ± 0.60	3.31 ± 0.67	9.27	2.05 ± 3.09	0.48 ± 0.31
534.4054	(GP ^{[2} H ₀]) 7α-Hydroxycholest-4-en-3-one	7α-Hydroxycholestenone	C ₃₄ H ₅₂ N ₃ O ⁺	7α-HCO	91.35 ± 157.87	7.06 ± 1.16	25.96	4.88 ± 8.64	ND
539.4368	(GP ^{[2} H ₅]) 24S-Hydroxycholest-4-en-3-one	24S-Hydroxycholesterol	C ₃₄ H ₄₇ D ₅ N ₃ O ₂ ⁺	24S-HC	21.66 ± 2.94	22.97 ± 0.49	9.19	0.06 ± 0.03	ND
539.4368	(GP ^{[2} H ₅]) 25-Hydroxycholest-4-en-3-one	25-Hydroxycholesterol	C ₃₄ H ₄₇ D ₅ N ₃ O ₂ ⁺	25-HC	2.21 ± 0.86	1.70 ± 0.46	1.10	0.02 ± 0.01	ND
539.4368	(GP ^{[2} H ₅]) (25R)26-Hydroxycholest-4-en-3-one	(25R)26-Hydroxycholesterol	C ₃₄ H ₄₇ D ₅ N ₃ O ₂ ⁺	(25R)26-HC	ND	42.83 ± 1.13	24.11	ND	ND
539.4368	(GP ^{[2} H ₅]) 7α-Hydroxycholest-4-en-3-one	7α-Hydroxycholesterol	C ₃₄ H ₄₇ D ₅ N ₃ O ₂ ⁺	7α-HC	15.96 ± 20.08	3.53 ± 1.59	21.44	1.99 ± 3.15	0.03 ± 0.03
539.4368	(GP ^{[2} H ₅]) 6β-Hydroxycholest-4-en-3-one	6β-Hydroxycholesterol	C ₃₄ H ₄₇ D ₅ N ₃ O ₂ ⁺	6β-HC	3.42 ± 1.20	ND	NR	0.56 ± 0.13	0.48 ± 0.35
553.4161	(GP ^{[2} H ₅]) 3-Oxocholest-4-en-25R)26-oic acid	3β-Hydroxycholestenonic acid	C ₃₄ H ₄₅ D ₅ N ₃ O ₃ ⁺	3β-HCA	1.76 ±0.67	130.17 ± 2.19	124.08	0.41 ± 0.56	1.55 ± 0.05
553.4161	(GP ^{[2} H ₅]) 22-Hydroxycholest-4-en-3,24-dione	3β,22-Dihydroxycholesta-5-en-24-one	C ₃₄ H ₄₅ D ₅ N ₃ O ₃ ⁺	-	45.76 ± 14.65	3.74 ± 0.27	NR	ND	ND
550.4003	(GP ^{[2} H ₀]) 7α, 12α-Dihydroxycholest-4-en-3-one	7α, 12α-Dihydroxycholestenone	C ₃₄ H ₅₂ N ₃ O ₃ ⁺	7α, 12α-diHCO	1640 ± 2020.82	ND	NR	8.93 ± 14.76	ND
550.4003	(GP ^{[2} H ₀]) 7α, 25-Dihydroxycholest-4-en-3-one	7α, 25-Dihydroxycholestenone	C ₃₄ H ₅₂ N ₃ O ₃ ⁺	7α, 25-diHCO	ND	2.14 ± 0.11	1.92	ND	ND
550.4003	(GP ^{[2} H ₀]) 7α, (25R)26-dihydroxycholest-4-en-3-one	7α, (25R)26-dihydroxycholestenone	C ₃₄ H ₅₂ N ₃ O ₃ ⁺	7α, (25R)26-diHCO	ND	5.28 ± 2.17	7.70	ND	ND

555.4317	(GP[² H ₅]) 7 α ,12 α -Dihydroxycholest-4-en-3-one	7 α ,12 α -Dihydroxycholesterol	C ₃₄ H ₄₇ D ₅ N ₃ O ₃ ⁺	7 α ,12 α -diHC	24.82 \pm 28.25	ND	NR	ND	ND
555.4317	(GP[² H ₅]) 7 α ,25-Dihydroxycholest-4-en-3-one	7 α ,25-Dihydroxycholesterol	C ₃₄ H ₄₇ D ₅ N ₃ O ₃ ⁺	7 α ,25-diHC	ND	0.60 \pm 0.08	NR	ND	ND
555.4317	(GP[² H ₅]) 7 α , (25R)26-Dihydroxycholest-4-en-3-one	7 α , (25R)26-Dihydroxycholesterol	C ₃₄ H ₄₇ D ₅ N ₃ O ₃ ⁺	7 α , (25R)26-diHC	ND	2.14 \pm 0.57	NR	ND	ND
564.3796	(GP[² H ₀]) 7 α -Hydroxy-3-oxocholest-4-en-(25R/S),26-oic acid	7 α -hydroxy-3-oxocholest-4-en-(25R/S),26-oic acid	C ₃₄ H ₅₀ N ₃ O ₄ ⁺	7 α H ₃ ,3O-CA	ND	60.98 \pm 2.19	99.13	ND	28.81 \pm 1.51
569.4110	(GP[² H ₅]) 3 β ,7 α -dihydroxycholest-5-en-(25R/S),26-oic acid GP-d5	3 β ,7 α -dihydroxycholest-5-en-(25R/S),26-oic acid	C ₃₄ H ₄₅ D ₅ N ₃ O ₄ ⁺	3 β ,7 α -diHCA	ND	26.70 \pm 1.39	41.57	ND	4.46 \pm 1.06
569.4110	(GP[² H ₅]) 3 β ,22,25-Trihydroxycholest-5-en-24-one GP-d5	3 β ,22,25-Trihydroxycholest-5-en-24-one	C ₃₄ H ₄₅ D ₅ N ₃ O ₄ ⁺	-	27.29 \pm 13.07	3.61 \pm 0.19	NR	0.23 \pm 0.33	ND

Table 3.3. Average values of sterols found in CTX and control serum/plasma and CSF samples. The mean concentration of each oxysterol seen in each sample, with the standard deviation. ND = analyte below detection level; NR = not reported in Yutuc et al, 2021 for NIST SRM; HC = hydroxycholesterol; diHC = dihydroxycholesterol; CA = cholestenic acid; diHCA = dihydroxycholestenic acid.

After cholesterol oxidase and GP-tagging		Sterol/ Oxysterol Common name	Elemental composition	Abbreviation	Mean concentration (ng/mg of tissue \pm SD)		
Mass (\pm 5ppm)	Sterol/ Oxysterol Systematic name				CTX cerebrum (n=1)	Control brain (n=1)	Mean concentration (ng/ mg cholesterol \pm SD)
523.4419	(GP[² H ₅]) Cholest-4-en-3-one	Cholesterol	C ₃₄ H ₄₇ D ₅ N ₃ O ⁺	-	51407 \pm 13985	16658 \pm 1339.90	CTX cerebrum NTC (n=1) 7.76mg \pm 5.92
525.4575	(GP[² H ₅]) Cholestan-3-one	Cholestanol	C ₃₄ H ₄₉ D ₅ N ₃ O ⁺	-	259.43 \pm 212.22	ND	4577.60 \pm 2728.90
537.4211	(GP[² H ₅]) 24S,25-Epoxycholest-4-en-3-one	24S,25-Epoxycholesterol/ 24-oxocholesterol	C ₃₄ H ₄₃ D ₅ N ₃ O ₂ ⁺	24S,25-EC	0.55 \pm 0.14	0.49 \pm 0.08	11.73 \pm 5.19
534.4054	(GP[² H ₀]) 3 β -Hydroxycholest-5-en-7-one	7-Oxocholesterol	C ₃₄ H ₅₂ N ₃ O ₂ ⁺	7-OC	388.24 \pm 270.79	0.07 \pm 0.01	7175.60 \pm 4810.90
534.4054	(GP[² H ₀]) 7 α -Hydroxycholest-4-en-3-one	7 α -Hydroxycholestenone	C ₃₄ H ₅₂ N ₃ O ⁺	7 α -HCO	15.95 \pm 8.83	ND	349.30 \pm 218.03
539.4368	(GP[² H ₅]) 24S-Hydroxycholest-4-en-3-one	24S-Hydroxycholesterol	C ₃₄ H ₄₇ D ₅ N ₃ O ₂ ⁺	24S-HC	81.65 \pm 9.78	21.87 \pm 1.78	1653.38 \pm 278.37
539.4368	(GP[² H ₅]) 25-Hydroxycholest-4-en-3-one	25-Hydroxycholesterol	C ₃₄ H ₄₇ D ₅ N ₃ O ₂ ⁺	25-HC	2.98 \pm 1.36	ND	57.50 \pm 13.03
539.4368	(GP[² H ₅]) (25R)26-Hydroxycholest-4-en-3-one	(25R)26-Hydroxycholesterol	C ₃₄ H ₄₇ D ₅ N ₃ O ₂ ⁺	(25R)26-HC	ND	1.78 \pm 0.038	ND
539.4368	(GP[² H ₅]) 7 α -Hydroxycholest-4-en-3-one	7 α -Hydroxycholesterol	C ₃₄ H ₄₇ D ₅ N ₃ O ₂ ⁺	7 α -HC	74.75 \pm 53.57	0.45 \pm 0.01	1365.38 \pm 592.00
539.4368	(GP[² H ₅]) 6 β -Hydroxycholest-4-en-3-one	6 β -Hydroxycholesterol	C ₃₄ H ₄₇ D ₅ N ₃ O ₂ ⁺	6 β -HC	27.42 \pm 8.20	0.16 \pm 0.03	539.56 \pm 58.98
553.4161	(GP[² H ₅]) 3-Oxocholest-4-en-(25R)26-oic acid	3 β -Hydroxycholestenonic acid	C ₃₄ H ₄₅ D ₅ N ₃ O ₃ ⁺	3 β -HCA	ND	0.065 \pm 0.0050	ND
550.4003	(GP[² H ₀]) 7 α ,12 α -Dihydroxycholest-4-en-3-one	7 α ,12 α -Dihydroxycholestenone	C ₃₄ H ₅₂ N ₃ O ₃ ⁺	7 α ,12 α -diHCO	9.54 \pm 1.50	ND	195.90 \pm 59.79
							ND

550.4003	(GP[² H ₀]) 7 α ,25-Dihydroxycholest-4-en-3-one-	7 α ,25-Dihydroxycholestenone	C ₃₄ H ₅₂ N ₃ O ₃ ⁺	7 α ,25-diHCO	ND	ND	ND	ND
550.4003	(GP[² H ₀]) 7 α , (25R)26-dihydroxycholest-4-en-3-one	7 α , (25R)26-dihydroxycholestenone	C ₃₄ H ₅₂ N ₃ O ₃ ⁺	7 α , (25R)26-diHCO	ND	0.0046 \pm 0.0009	ND	0.27 \pm 0.04
555.4317	(GP[² H ₅]) 7 α , 12 α -Dihydroxycholest-4-en-3-one	7 α , 12 α -Dihydroxycholesterol	C ₃₄ H ₄₇ D ₅ N ₃ O ₃ ⁺	7 α , 12 α -diHHC	3.85 \pm 4.45	ND	77.20 \pm 94.61	ND
555.4317	(GP[² H ₅]) 7 α , 24-Dihydroxycholest-4-en-3-one	7 α , 24-Dihydroxycholesterol	C ₃₄ H ₄₇ D ₅ N ₃ O ₃ ⁺	7 α , 24-diHHC	1.040 \pm 0.151	ND	21.72 \pm 7.25	ND
555.4317	(GP[² H ₅]) 7 α , 25-Dihydroxycholest-4-en-3-one	7 α , 25-Dihydroxycholesterol	C ₃₄ H ₄₇ D ₅ N ₃ O ₃ ⁺	7 α , 25-diHHC	ND	ND	ND	ND
555.4317	(GP[² H ₅]) 7 α , (25R)26-Dihydroxycholest-4-en-3-one	7 α , (25R)26-Dihydroxycholesterol	C ₃₄ H ₄₇ D ₅ N ₃ O ₃ ⁺	7 α , (25R)26-diHHC	ND	0.12 \pm 0.02	ND	7.46 \pm 1.73
564.3796	(GP[² H ₀]) 7 α -Hydroxy-3-oxocholest-4-en-(25R/S), 26-oic acid	7 α -hydroxy-3-oxocholest-4-en-(25R/S), 26-oic acid	C ₃₄ H ₅₀ N ₃ O ₄ ⁺	7 α H, 3O-CA	ND	ND	ND	ND
569.4110	(GP[² H ₅]) 3 β , 7 α -dihydroxycholest-5-en-(25R/S), 26-oic acid GP-d5	3 β , 7 α -dihydroxycholest-5-en-(25R/S), 26-oic acid	C ₃₄ H ₄₅ D ₅ N ₃ O ₄ ⁺	3 β , 7 α -diHCA	ND	0.033 \pm 0.007	ND	2.07 \pm 0.38

Table 3.4. Average values of sterols found in CTX and control cerebrum brain tissue. The mean concentration (units ng/mg of tissue) of each oxysterol quantified, shown with the standard deviation (units for normalised data is ng/mg cholesterol). NTC = normalised to cholesterol; ND = analyte below detection level; HC = hydroxycholesterol; diHHC = dihydroxycholesterol; CA = cholestenic acid; diHCA = dihydroxycholestenic acid.

After cholesterol oxidase and GP-tagging			Mean concentration (ng/mg cholesterol)					
Mass (\pm 5ppm)	Sterol/ Oxysterol Systematic name	Sterol/ Oxysterol Common name	Elemental composition	Abbreviation	CTX MO (n=1)	CTX CBXL (n=1)	CTX SN (n=1)	CTX BG (n=1)
523.4419	(GP[² H ₅]) Cholest-4-en-3-one	Cholesterol	C ₃₄ H ₄₇ D ₅ N ₃ O ⁺	-	1.771mg	2.083mg	1.914mg	1.488mg
525.4575	(GP[² H ₅]) Cholestan-3-one	Cholestanol	C ₃₄ H ₄₉ D ₅ N ₃ O ⁺	-	2284.86	1072.62	871.69	1052.04
537.4211	(GP[² H ₅]) 24S,25-Epoxycholest-4-en-3-one	24S,25-Epoxycholesterol/ 24-oxocholesterol	C ₃₄ H ₄₅ D ₅ N ₃ O ₂ ⁺	24S,25-EC	11.39	15.55	9.44	47.24
534.4054	(GP[² H ₀]) 3 β -Hydroxycholest-5-en-7-one	7-Oxocholesterol	C ₃₄ H ₅₂ N ₃ O ₂ ⁺	7-OC	3208.77	5458.93	2468.63	10,147.18
534.4054	(GP[² H ₀]) 7 α -Hydroxycholest-4-en-3-one	7 α -Hydroxycholestenone	C ₃₄ H ₅₂ N ₃ O ⁺	7 α -HCO	452.57	398.19	448.27	395.25
539.4368	(GP[² H ₅]) 24S-Hydroxycholest-4-en-3-one	24S-Hydroxycholesterol	C ₃₄ H ₄₇ D ₅ N ₃ O ₂ ⁺	24S-HC	722.54	1346.56	949.10	2434.67
539.4368	(GP[² H ₅]) 25-Hydroxycholest-4-en-3-one	25-Hydroxycholesterol	C ₃₄ H ₄₇ D ₅ N ₃ O ₂ ⁺	25-HC	76.92	112.41	58.73	242.33
539.4368	(GP[² H ₅]) (25R)26-Hydroxycholest-4-en-3-one	(25R)26-Hydroxycholesterol	C ₃₄ H ₄₇ D ₅ N ₃ O ₂ ⁺	(25R)26-HC	ND	ND	ND	ND
539.4368	(GP[² H ₅]) 7 α -Hydroxycholest-4-en-3-one	7 α -Hydroxycholesterol	C ₃₄ H ₄₇ D ₅ N ₃ O ₂ ⁺	7 α -HC	1405.78	2861.25	1178.87	3808.84
539.4368	(GP[² H ₅]) 6 β -Hydroxycholest-4-en-3-one	6 β -Hydroxycholesterol	C ₃₄ H ₄₇ D ₅ N ₃ O ₂ ⁺	6 β -HC	491.20	812.15	384.68	1577.33
553.4161	(GP[² H ₅]) 3-Oxocholest-4-en-(25R)26-oic acid	3 β -Hydroxycholestenic acid	C ₃₄ H ₄₅ D ₅ N ₃ O ₃ ⁺	3 β -HCA	ND	ND	ND	ND
550.4003	(GP[² H ₀]) 7 α , 12 α -Dihydroxycholest-4-en-3-one	7 α , 12 α -Dihydroxycholestenone	C ₃₄ H ₅₂ N ₃ O ₃ ⁺	7 α , 12 α -diHCO	136.78	112.29	112.27	177.89

550.4003	(GP ^[2]H₀] 7 α ,25-Dihydroxycholest-4-en-3-one	7 α ,25-Dihydroxycholest-4-en-3-one	7 α ,25-Dihydroxycholest-4-en-3-one	C ₃₄ H ₅₂ N ₃ O ₃ ⁺	7 α ,25-diHC	ND	ND	ND	ND
550.4003	(GP ^[2]H₀] 7 α , (25R)26-dihydroxycholest-4-en-3-one	7 α , (25R)26-dihydroxycholest-4-en-3-one	7 α , (25R)26-dihydroxycholest-4-en-3-one	C ₃₄ H ₅₂ N ₃ O ₃ ⁺	7 α , (25R)26-diHC	ND	ND	ND	ND
555.4317	(GP ^[2]H₃] 7 α , 12 α -Dihydroxycholest-4-en-3-one	7 α , 12 α -Dihydroxycholest-4-en-3-one	7 α , 12 α -Dihydroxycholest-4-en-3-one	C ₃₄ H ₄₇ D ₅ N ₃ O ₃ ⁺	7 α , 12 α -diHC	8.97	19.69	13.28	ND
555.4317	(GP ^[2]H₃] 7 α , 24-Dihydroxycholest-4-en-3-one	7 α , 24-Dihydroxycholest-4-en-3-one	7 α , 24-Dihydroxycholest-4-en-3-one	C ₃₄ H ₄₇ D ₅ N ₃ O ₃ ⁺	7 α , 24-diHC	ND	3.70	1.92	18.82
555.4317	(GP ^[2]H₃] 7 α , 25-Dihydroxycholest-4-en-3-one	7 α , 25-Dihydroxycholest-4-en-3-one	7 α , 25-Dihydroxycholest-4-en-3-one	C ₃₄ H ₄₇ D ₅ N ₃ O ₃ ⁺	7 α , 25-diHC	ND	2.38	1.38	2.74
555.4317	(GP ^[2]H₃] 7 α , (25R)26-Dihydroxycholest-4-en-3-one	7 α , (25R)26-Dihydroxycholest-4-en-3-one	7 α , (25R)26-Dihydroxycholest-4-en-3-one	C ₃₄ H ₄₇ D ₅ N ₃ O ₃ ⁺	7 α , (25R)26-diHC	ND	ND	ND	ND
564.3796	(GP ^[2]H₀] 7 α -Hydroxy-3-oxocholest-4-en-(25R/S), 26-oic acid	7 α -hydroxy-3-oxocholest-4-en-(25R/S), 26-oic acid	7 α -hydroxy-3-oxocholest-4-en-(25R/S), 26-oic acid	C ₃₄ H ₅₀ N ₃ O ₄ ⁺	7 α H, 3O-CA	ND	ND	ND	ND
569.4110	(GP ^[2]H₃] 3 β , 7 α -dihydroxycholest-5-en-(25R/S), 26-oic acid GP-d5	3 β , 7 α -dihydroxycholest-5-en-(25R/S), 26-oic acid	3 β , 7 α -dihydroxycholest-5-en-(25R/S), 26-oic acid	C ₃₄ H ₄₅ D ₅ N ₃ O ₄ ⁺	3 β , 7 α -diHCA	ND	ND	ND	ND

Table 3.5. Average values of sterols found in CTX regional brain tissue. The mean concentration (units ng/mg of cholesterol) of each oxysterol quantified. MO = medulla oblongata; CBXL = cerebellar lesion; SN = substantia nigra; BG = basal ganglia; ND = analyte below detection level; HC = hydroxycholesterol; diHC = dihydroxycholesterol; CA = cholestenoic acid; diHCA = dihydroxycholestenoic acid.

3.4. Discussion

It is clear from the data obtained during this study that the mutations in the CYP27A1 gene and subsequent lack of enzyme activity have resulted in severe depletion of intermediate metabolites from the 26-hydroxylation pathway and generally affected the balance of oxysterols both in the peripheral fluid and the brain tissue.

The complete lack of (25R)26-HC, $3\beta,7\alpha$ -diHCA and 7α H,3O-CA, and the reduction of 3β -HCA suggests the mutations has caused almost a complete loss of enzyme activity, and this lack of activity has affected synthesis of the whole 26-hydroxylation pathway in all sample types analysed, a finding that has previously been reported in several other studies⁹. The impaired availability of this pathway results in compensatory mechanisms via other means to decrease the burden of excess cholesterol, i.e. up-regulation of CYP7A1⁵.

The results from the data analysis conducted within this study suggest a reliance on other key pathways within bile acid synthesis resulting in higher-than-normal levels of several oxysterols in CTX including 7α -HC, $3\beta,22$ -dihydroxycholest-5-en-24-one and $3\beta,22,25$ -trihydroxycholest-5-en-24-one. However, the sterols with the biggest change are $7\alpha,12\alpha$ -diHCO and cholestanol, which are undetected in all control samples analysed. This finding, like many other studies have concluded^{2,3,15-17}, suggests that both these metabolites are good markers for disease using a less invasive plasma sample.

Our study has also highlighted the importance of the 25-hydroxylation pathway in CTX with the increase of specific metabolites $3\beta,22$ -dihydroxycholest-5-en-24-one and $3\beta,22,25$ -trihydroxycholest-5-en-24-one both of which are greatly increased in plasma and could also be possible biomarkers used to diagnose disease.

To conclude, the confirmation of all four metabolites mentioned here along with decreased levels of cholesterol and a depletion of all metabolites within the 26-hydroxylation pathway in plasma would suggest a high possibility an individual has CTX. These findings could aid in assisting with diagnosing CTX earlier in life resulting in earlier treatment and therefore a more manageable disease with less severe and life-altering symptoms.

Further experimentation is needed to confirm these findings as the samples numbers are low, however CTX is a rare disease and increasing sample numbers could be

difficult as a result. Increasing the control number is also needed but again, obtaining control plasma can be difficult.

3.5. References

1. Verrips, A. *et al.* Clinical and molecular genetic characteristics of patients with cerebrotendinous xanthomatosis. *Brain* **123**, 908–919 (2000).
2. Höflinger, P. *et al.* Metabolic profiling in serum, cerebrospinal fluid, and brain of patients with cerebrotendinous xanthomatosis. *J. Lipid Res.* **62**, 100078 (2021).
3. Nie, S., Chen, G., Cao, X. & Zhang, Y. Cerebrotendinous xanthomatosis: a comprehensive review of pathogenesis, clinical manifestations, diagnosis, and management. *Orphanet J. Rare Dis.* **9**, 179 (2014).
4. Pilo de la Fuente, B. *et al.* Usefulness of cholestanol levels in the diagnosis and follow-up of patients with cerebrotendinous xanthomatosis. *Neurol. (English Ed.)* **26**, 397–404 (2011).
5. Björkhem, I. Cerebrotendinous xanthomatosis. *Curr. Opin. Lipidol.* **24**, 283–287 (2013).
6. Duell, P. B. *et al.* Diagnosis, treatment, and clinical outcomes in 43 cases with cerebrotendinous xanthomatosis. *J. Clin. Lipidol.* **12**, 1169–1178 (2018).
7. Stelten, B. M. L. *et al.* Long-term treatment effect in cerebrotendinous xanthomatosis depends on age at treatment start. *Neurology* **92**, e83–e95 (2019).
8. Phinney, K. W. *et al.* Development of a Standard Reference Material for metabolomics research. *Anal. Chem.* **85**, 11732–8 (2013).
9. Yutuc, E. *et al.* Deep mining of oxysterols and cholestenoic acids in human plasma and cerebrospinal fluid: Quantification using isotope dilution mass spectrometry. *Anal. Chim. Acta* **1154**, (2021).
10. Crick, P. J. *et al.* Quantitative charge-tags for sterol and oxysterol analysis. *Clin. Chem.* **61**, 400–11 (2015).
11. Paul, R. *et al.* Accumulation of Cholesterol and Homocysteine in the Nigrostriatal Pathway of Brain Contributes to the Dopaminergic Neurodegeneration in Mice. *Neuroscience* **388**, 347–356 (2018).
12. Stamelou, M., Quinn, N. P. & Bhatia, K. P. ‘Atypical’ atypical parkinsonism: New genetic conditions presenting with features of progressive supranuclear palsy, corticobasal degeneration, or multiple system atrophy-A diagnostic guide. *Mov. Disord.* **28**, 1184–1199 (2013).
13. Russell, D. W. The enzymes, regulation, and genetics of bile acid synthesis. *Annu. Rev. Biochem.* **72**, 137–74 (2003).
14. Honda, A. *et al.* Side chain hydroxylations in bile acid biosynthesis catalyzed by CYP3A are markedly up-regulated in Cyp27^{-/-} mice but not in cerebrotendinous xanthomatosis. *J. Biol. Chem.* **276**, 34579–85 (2001).
15. DeBarber, A. E. *et al.* Profiling sterols in cerebrotendinous xanthomatosis: Utility of Girard derivatization and high resolution exact mass LC-ESI-MSn analysis. *J. Chromatogr. B Anal. Technol. Biomed. Life Sci.* **879**, 1384–1392 (2011).
16. DeBarber, A. E. *et al.* A blood test for cerebrotendinous xanthomatosis with potential for disease detection in newborns. *J. Lipid Res.* **55**, 146–154 (2014).
17. Bhattacharyya, A. K., Lin, D. S. & Connor, W. E. Cholestanol metabolism in patients with cerebrotendinous xanthomatosis: Absorption, turnover, and tissue deposition. *J. Lipid Res.* **48**, 185–192 (2007).

Chapter 4: The profiling of sterols in human Alzheimer's disease brain tissue

4.1. Introduction

AD is a neurodegenerative disease that affects memory, behaviour, and cognitive thinking accompanied by severe brain atrophy, with a progressive worsening of symptoms over time¹. Although the main symptoms associated with AD revolve around memory deficit and cognition, other symptoms include a lack of spatial awareness, inability to communicate, depression and behavioural changes² accompanied by the presence of pathological hallmarks of disease, specifically A β plaques and NFT depositions³.

AD is the most common form of dementia, with between 50-75% of all dementia cases being confirmed as an AD diagnosis¹, with currently over 30 million people worldwide diagnosed⁴. There are several risk factors associated with AD, including associations with gender, age, and genetics. The gender differences associate females with a two-fold likelihood of being diagnosed with AD compared to their male counterparts⁵, however, age is the most influential risk factor with prevalence increasing significantly with age⁶. AD has two possible disease subtypes, mainly dependant on age of onset but also linked with possible genetic susceptibilities. The first and most common subtype is late onset AD (LOAD), or sporadic AD, which is characterised by an onset age of 65 years or above, and tends to have a less-severe disease course compared with the other subtype^{6,7}. The second is known as early onset AD (or EOAD) with this subtype much rarer, and accounts for around 1% of all AD cases and frequently has a genetic origin.

Each subtype is associated with a relative risk associated with single or multiple gene loci which is most evident in EOAD, with the most common gene susceptibilities being beta secretase 1 (*BACE1*), *APP*, presenilin 1 (*PSEN1*) and *PSEN2* (genes stated in italics; enzymes in non-italics), of which BACE1 and APP have possible links to cholesterol and lipid raft formation in AD⁸. *APOE* has also been noted as a gene of interest with LOAD, which is a lipid transporter responsible for the movement of cholesterol within the brain (see Figure 4.1 for mechanistic information)^{6,9}.

Unfortunately, there is no known cure for AD, however there are treatments available to some individuals that can manage the symptoms that coincide with disease and aid in slowing progression of both symptoms and disability. These treatments, such as cholinesterase inhibitors (ChEI's) and NMDA antagonists, help

to compensate for cholinergic neuronal loss and excitatory NMDAR activity. However, they have limited efficacy and unfortunately do not target the neurodegenerative disease mechanisms but instead aim in reducing symptomatic load¹⁰. AD is a complex neurological disorder with many different mechanisms of action working in tangent to cause the progressive neurodegeneration associated with the disease. The most studied and understood mechanisms are those that centre around the hypotheses of A β protein deposits, abnormal tau protein phosphorylation and NFT protein deposits within the brain¹¹. Future pioneering treatments are looking to target these important pathological pathways to prevent and lower the accumulation of these products with anti-amyloid and anti-tau disease modifying therapies (DMTs)¹², for example aducanumab, a drug which aids to help clear amyloid deposition within the brain has recently been approved by the Food and Drug Association (FDA), actively aiming to reduce the levels of neurotoxic amyloid and slowing cognitive decline¹³.

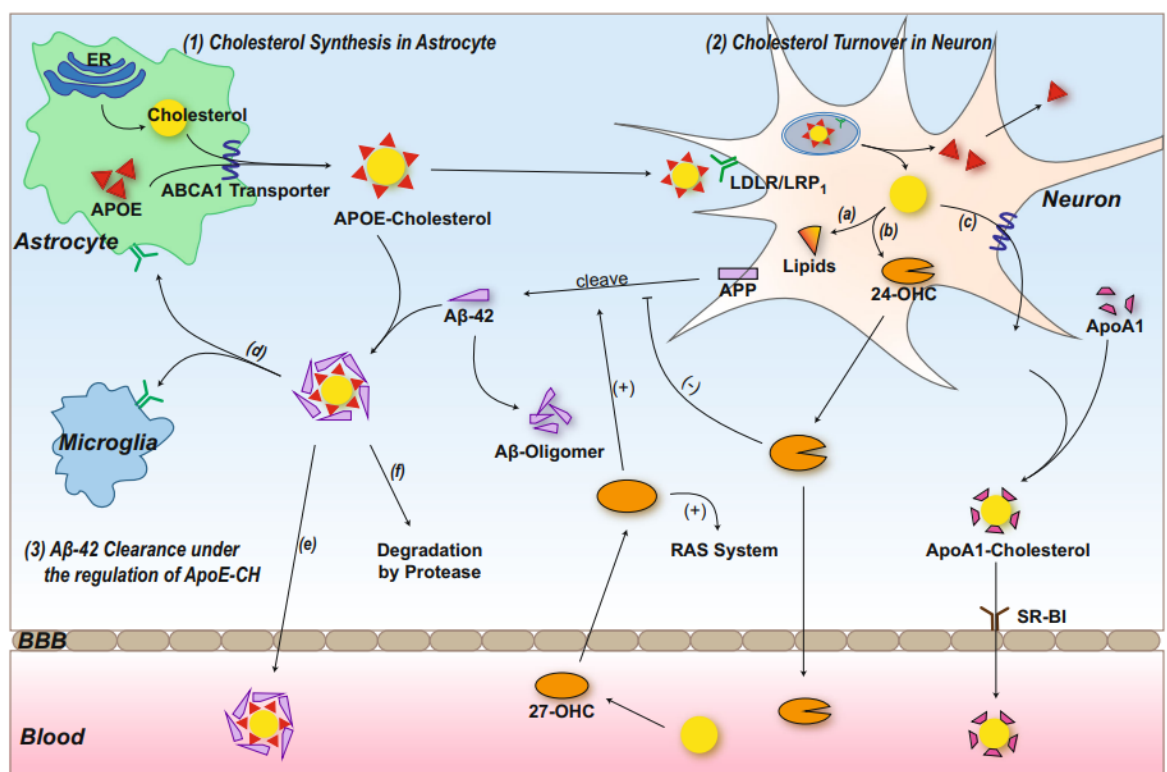


Figure 4.1. The role of APOE in cholesterol transport in the brain and the influence of A β and sterols. Reproduced from Dai et al, 2021¹⁴, with permission taken from the Molecular Neurobiology journal.

The A β protein depositions have associations with APOE, which as previously mentioned is a cholesterol transporter that is important within the brain. It has three genotypes/isoforms; *APO* ϵ 2, *APO* ϵ 3 and *APO* ϵ 4, and as well as its role in moving cholesterol between astrocytes and neurons, APOE also has a responsibility in mediating A β clearance in conjunction with specific oxysterols including 24S-HC and (25R)26-HC, more commonly referred to as 27-HC (see Figure 4.1)^{14,15}. APOE binds to synthesised cholesterol (APOE-Ch) within the astrocyte, is either transported to the neuron or forms a complex with A β oligomers. Cholesterol is metabolised within the neuron by lipid droplet formation (Figure 4.1a), conversion to 24S-HC by CYP46A1 enzyme and crossing the blood brain barrier (Figure 4.1b), or by exiting the cell and binding to ApoA1 (Figure 4.1c). 24S-HC inhibits A β production, but (25R)26-HC (27-HC) promotes its production. The APOE-Ch A β complex is either endocytosed (Figure 4.1d), secreted into the periphery (Figure 4.1e) or degraded by proteases (Figure 4.1f).

The different isoforms of APOE have different capabilities for both of these roles, and it has been shown there is a superior uptake of *APO* ϵ 2 and *APO* ϵ 3-bound cholesterol than *APO* ϵ 4-bound cholesterol by neurons and astrocytes in rat neuronal cells¹⁶. In a separate study, *APO* ϵ 4 has also shown the worst ability to mediate the clearance of A β of all three genotypes and in addition, preferentially encourages plaque formation¹⁷. A β deposits within the brain are used for diagnosis and are seen as a pathological feature of AD, with studies showing these plaques have a neurotoxic effect resulting in progressive neurodegeneration³, with compromised clearance meaning more aggregate formation resulting in quicker disease progression.

In addition to A β being linked with ApoE, it has also shown links to cholesterol although not directly. A study from 2000 showed that increased dietary cholesterol can increase A β accumulation in mice overexpressing APP¹⁸, however as cholesterol cannot cross the BBB this effect must be indirect. Another study from 2001 showed that simvastatin treatment (which inhibits cholesterol synthesis) reduced A β peptides in rat neuronal cells, and in the CSF and brain homogenates of guinea pigs¹⁹, which suggests that cholesterol levels could affect the amount of A β accumulation in AD patients.

4.1.1. Aims

We hypothesise that there is an altered sterol profile in AD, which is linked with the *APOE* status of an individual. To address this, we aim to analyse the human brain tissue of AD, mild cognitive impairment (MCI) and control individuals, and analyse the free sterol content of each subgroup. We also plan to analyse the oxysterol data based on *APOE* isoform status to look at whether these changes may be linked with the APOE cholesterol transport mechanism.

4.2. Materials and Methods

4.2.1. AD brain tissue cohort

The brain samples used within this study were provided by the Rush Alzheimer's Disease Centre located in Rush University, Chicago, Illinois, USA. The cohort consisted of forty-eight individual post-mortem brain tissue samples from the dorsolateral prefrontal cortex (see Figure 4.2 for location). The samples were obtained from a monastery, explaining the male-heavy cohort and suggests environment and lifestyle would have been comparable to some extent. Ethical permission was approved by Institutional Review Board #1 at Rush University Medical Centre (ORA Number: L91020181-CR14 Principal Investigator: David Bennett). The cohort consisted of fourteen females and thirty-four males, with a mix of established AD, MCI (defined as the clinical and neuropsychological syndrome of emerging cognitive impairment²⁰) and control (CNTL) cases based upon brain diagnosis. Out of the forty-eight samples, three were removed from statistical analysis either for missing genetic information (n=1) or for heterogeneity in APOE status (n=2). The details of these three cases are highlighted in Table 4.1. For quality control purposes to check for variation in sample preparation between batches, control mouse brain tissue was also processed alongside each batch of eight samples in addition to a water blank, with the redundant mouse brain tissue provided by Cardiff University, UK.

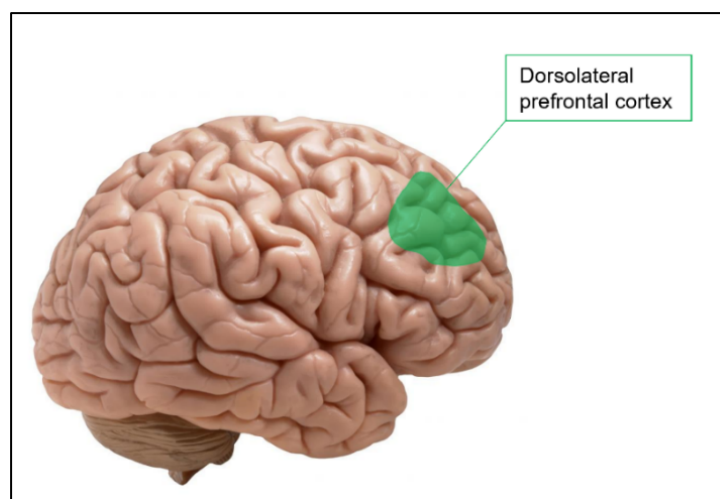


Figure 4.2. Position of the dorsolateral prefrontal cortex within the human brain. This region is primarily affected in later stages of disease.

4.2.2. Brain tissue homogenisation, extraction, and sample preparation

For homogenisation, tissue was pre-weighed between 50-100 mg in the Rush Alzheimer's Disease Centre and placed into Precellys soft tissue homogenisation 2 mL tubes with 1.4 mm ceramic beads. The tissue was homogenised in an EtOH-isotope labelled standard mix to extract maximum sterol amount collecting a total of 4.2 mL of solution in four 1.05 mL increments, which was diluted to 6 mL at 70% EtOH. For extraction, 600 µL of supernatant (i.e. 10% of the extract) was added to absolute EtOH dropwise under sonification, then diluted to 70% EtOH (see section 2.2.3 – Alzheimer's disease for details). The solution underwent SPE followed by enzyme-assisted derivatisation with Girard-P reagent, before a final SPE which generates the MeOH sterol-containing eluents (see section 2.2.4 for details). The eluted samples were diluted and processed at 60% MeOH, injecting 35 µL of sample into a Dionex Micro HPLC system coupled with an Orbitrap Elite mass spectrometer (see section 2.2.10 for more details), where 17-minute runs were used to quantify all data.

4.2.3. Oxysterol analysis

The quantification of peaks was carried out using mass spectrometry software Xcalibur from Thermo-Fisher. All oxysterols were quantified against the [$^2\text{H}_7$] 24R/S-hydroxycholesterol ([$^2\text{H}_7$] 24R/S-HC) standard. Once derivatised [$^2\text{H}_7$] 24R/S-HC has proved to be an acceptable surrogate for the quantification of oxysterols in general²¹. Other sterols were quantified against [$^2\text{H}_7$] cholesterol. The [$^2\text{H}_7$] 22R-hydroxycholest-4-en-3-one standard was used to quantify oxysterols that had a natural 3-oxo group. All sterols analysed were converted into ng per mg of tissue (ng/mg tissue) concentration. For the full ITMS³ fragmentation spectra for each oxysterol, refer to Table 9.1 in the Appendix.

4.2.4. Statistical analysis

The statistical analysis was carried out using GraphPad Prism 7 analysis software. The data set was first tested for normalised distribution using the D'Agostino and Pearson normality test (for full normality data see Appendix Tables 9.2 and 9.3). If the data followed Gaussian distribution (normally distributed), a one-way ANOVA was performed with a Tukey multiple comparison post-test. If the data did not follow

Gaussian distribution (non-normally distributed), a Kruskal-Wallis test was performed with a Dunn's multiple comparison post-test. For both multiple comparison tests, the adjusted P-value was taken and used for significance, with the significance levels as follows: * $P < 0.05$, ** $P < 0.005$; *** $P < 0.0005$; **** $P < 0.0001$. Data was screened for outliers using the ROUT test, with identified outliers subsequently removed from data analysis.

Table 4.1. Demographics of the Alzheimer's/ MCI brain tissue cohort. A list of all clinical details obtained for the RUSH samples. All brain material analysed was supplied from the dorsolateral prefrontal cortex (AD - Alzheimer's disease; MCI – mild cognitive impairment; CN – control). For statistical analysis, the three cases highlighted were removed due to a lack of genetic information (green) or due to heterogeneity in *APOE* status (yellow).

ID number	Brain weight (mg)	Sex (M/F)	Age at death	<i>APOE2</i>	<i>APOE3</i>	<i>APOE4</i>	Brain diagnosis	Blood diagnosis
73177635	70	F	92.11		Y		AD	MCI
97130008	69	M	95.29		Y		AD	MCI
10371937	77	M	81.03			Y	AD	AD
18455382	60	M	94.09			Y	AD	CN
82325110	54	M	100.42		Y		AD	AD
57597479	51	M	95.06		Y		AD	CN
18500138	65	M	80.08			Y	AD	AD
53355949	72	M	85.19			Y	AD	MCI
33332646	80	M	89.03			Y	AD	MCI
71806467	57	M	87.81		Y		AD	MCI
45212640	55	M	100.90		Y		AD	AD
20634274	52	M	99.35	Y			AD	CN
70636113	62	M	98.07			Y	AD	MCI
51864085	54	M	85.28			Y	AD	MCI
69924281	79	M	87.39			Y	AD	AD
77180612	75	M	86.71		Y		AD	AD
26631069	71	M	89.37			Y	AD	MCI
51650969	68	M	85.02		Y		AD	AD
90821208	59	M	83.76	-	-	-	MCI	MCI
73146926	51	M	84.33			Y	MCI	MCI
23892088	71	M	93.76			Y	MCI	MCI
17260313	67	M	92.89		Y		MCI	MCI
51791453	69	M	86.53			Y	MCI	CN
97882751	88	F	99.61		Y		MCI	MCI
74203334	65	M	85.79		Y		MCI	MCI
92371267	64	M	88.16		Y		MCI	MCI
18659212	56	F	91.73		Y		MCI	MCI
46910335	54	M	88.83	Y		Y	MCI	MCI
39721045	80	M	96.63			Y	MCI	MCI
39484737	82	F	86.29		Y		MCI	CN
17615774	61	M	101.61		Y		MCI	MCI
54104440	64	F	84.88		Y		MCI	MCI
6804844	55	F	86.97	Y		Y	MCI	CN
42543978	83	F	82.09		Y		CN	CN
82335720	65	M	78.44			Y	CN	CN
71514280	56	F	101.07	Y			CN	CN
84896566	70	M	92.16		Y		CN	CN
85584353	56	M	87.32	Y			CN	CN
79938680	52	M	90.21			Y	CN	CN
50301701	76	M	91.84			Y	CN	CN
44842532	71	F	97.10			Y	CN	CN
16068769	62	F	92.07			Y	CN	CN
20712597	76	M	84.58	Y			CN	CN
33321607	66	F	92.56		Y		CN	CN
4127190	69	M	88.64	Y			CN	CN
10459674	67	F	91.27	Y			CN	CN
31728786	66	F	80.72	Y			CN	CN
19785885	73	F	93.65		Y		CN	CN

4.3. Results

4.3.1. Identification of 25-hydroxycholestenone and (25R)26-hydroxycholestenone

The derivatisation agent [$^2\text{H}_0$]GP is used in the protocol in the absence of cholesterol oxidase enzyme. This means that following derivatisation, oxysterols with an even m/z must possess an endogenous oxo group prior to derivatisation.

At m/z 534.4054 we found the presence of two weak peaks, with a similar retention time and the same fragmentation pattern to 25-HC and (25R)26-HC reference standards. They were not present in every sample analysed and were not seen in the mouse brain quality control homogenate sample carried out with each sample batch processed, indicating that these compounds are present within the human brain tissue samples (see structures in Figure 4.3).

Interestingly, recent data shows that (25R)26-HCO can be present in human formed by HSD3B1 mediated oxidation of (25R)26-HC²². This enzyme may also be responsible for formation of 25-HCO, however additional work would be needed to prove this. The *HSD3B1* gene has also been detected in human brain suggesting that these two compounds could be formed cerebrally²³. The 25-hydroxycholestenone (25-HCO) was identified in twenty-four of the forty-five brain homogenates analysed, nine being females and the other fifteen being males. After analysing the data using *APOE* status and brain diagnosis (both shown in Table 4.1) in both male plus female and male-only groupings we observed no statistical significance between any of the groupings.

Although there were no significant findings, we did observe some differences within the groups. For the mixed male and female brain diagnosis, the MCI group showed an increase in 25-HCO compared to both AD and control groups (see Figure 4.4).

For *APOE* status, individuals with the *APOE*2 isoform showed a large decrease in 25-HCO ($P=0.0803$; Dunn's post-test) compared with the *APOE*3 isoform. The removal of females from the cohort resulted in the same trends, with both MCI and *APOE*3 groups showing a higher mean concentration compared to their counterpart groups. The (25R)26-hydroxycholestenone ((25R)26-HCO) was identified in thirty-one of the forty-five samples analysed, present in slightly more cases compared with the 25-HCO.

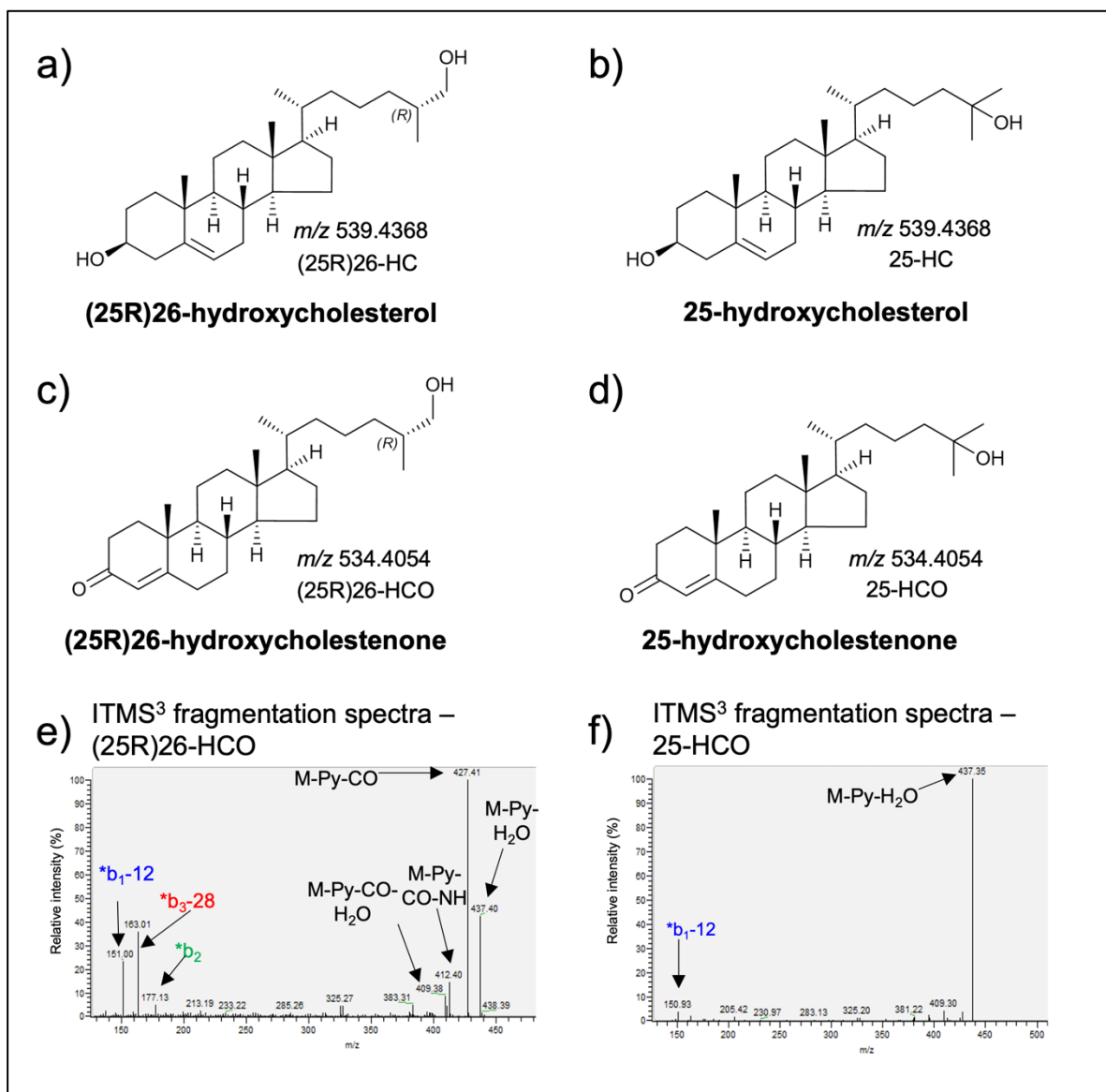


Figure 4.3. The structures of 25-hydroxycholestenone (25-HCO) and (25R)26-hydroxycholestenone ((25R)26-HCO) with ITMS³ fragmentation confirmation. The structures of both (25R)26-HC (a) and 25-HC (b) at m/z 539.4368 \pm 5ppm compared with (25R)26-HCO (c) and 25-HCO (d) at m/z 534.4054 \pm 5ppm, with confirmation of the structure from the ITMS³ fragmentation pattern (e for (25R)26-HC; f for 25-HCO).

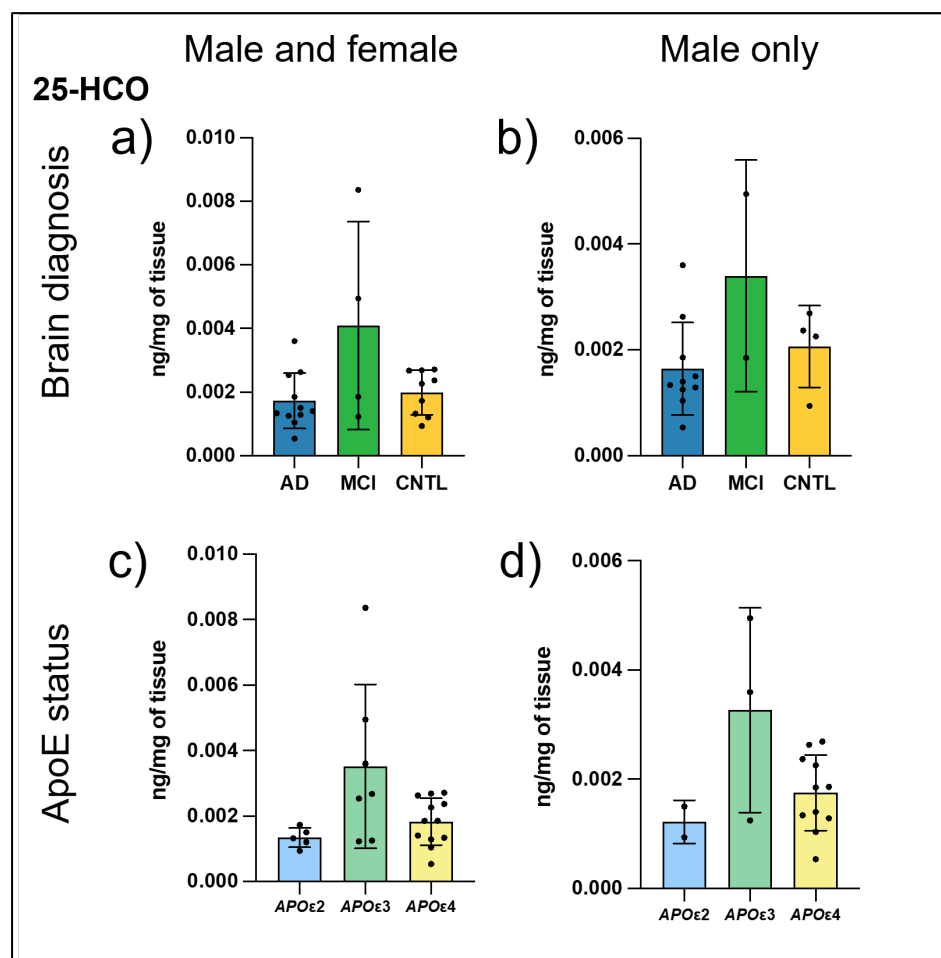


Figure 4.4. Concentrations of 25-hydroxycholestenone (25-HCO) in the human brain. The 25-HCO data using both brain diagnosis (a & b) and ApoE status (c & d) for both male and female (a & c), and male only groupings (b & d).

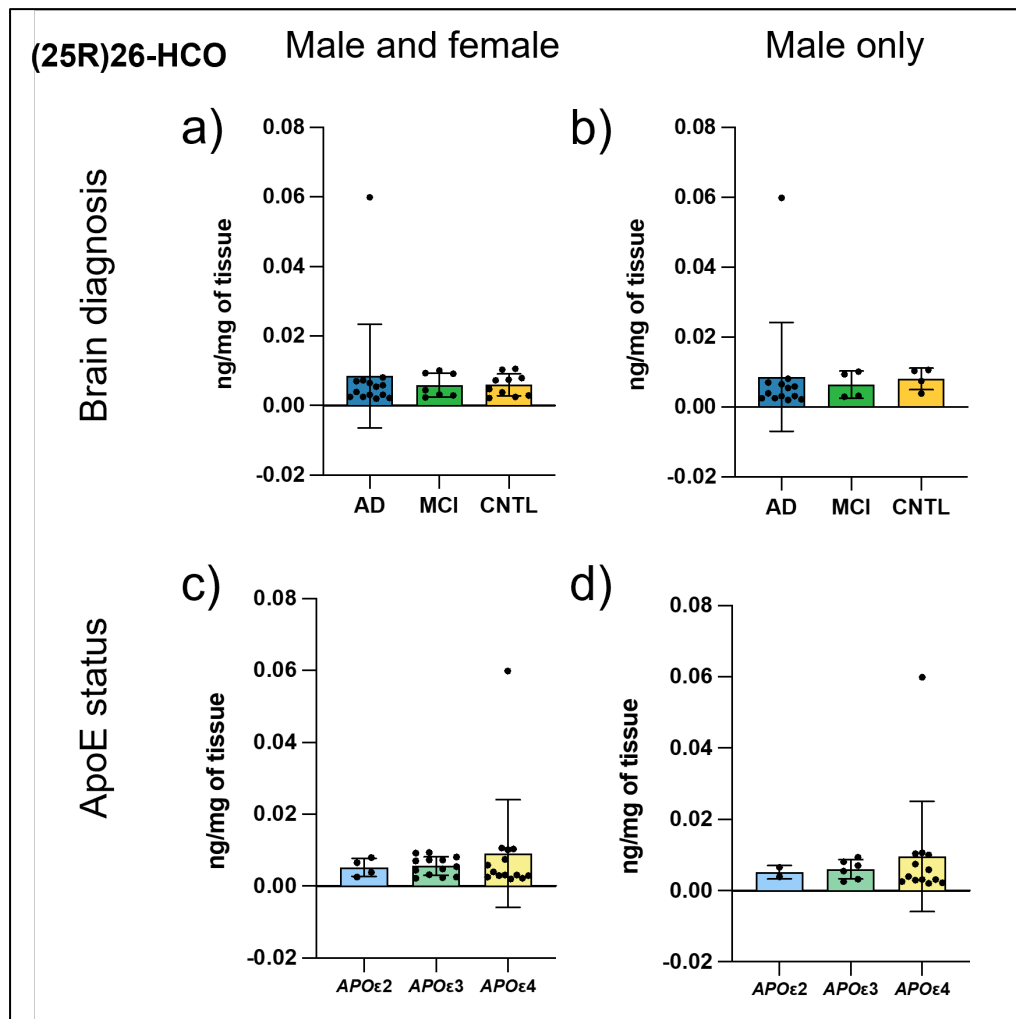


Figure 4.5. Concentrations of (25R)26-hydroxycholestenone ((25R)26-HCO) in the human brain. The (25R)26-HCO data using both brain diagnosis (a & b) and ApoE status (c & d) for both male and female (a & c), and male only groupings (b & d).

The data was analysed using the same grouping system, brain diagnosis and *APOE* status with male plus female and male-only groupings. Again, no statistical significance was observed, however there were some small differences observed between the groups (see Figure 4.5). For both groupings using brain diagnosis, the AD group showed a small increase in (25R)26-HCO compared with MCI and control cases. In *APOE* status, the *APOε4* isoform group showed an increase of (25R)26-HCO compared with both the *APOε2* and *APOε3* isoforms.

4.3.2. Analysis of sterols using brain diagnosis grouping

For this study, the data was first analysed using the brain diagnosis provided by Rush Institute (AD, MCI or CNTL), with the data further split using gender; either male plus female, or male-only due to the lack of females within the AD cohort.

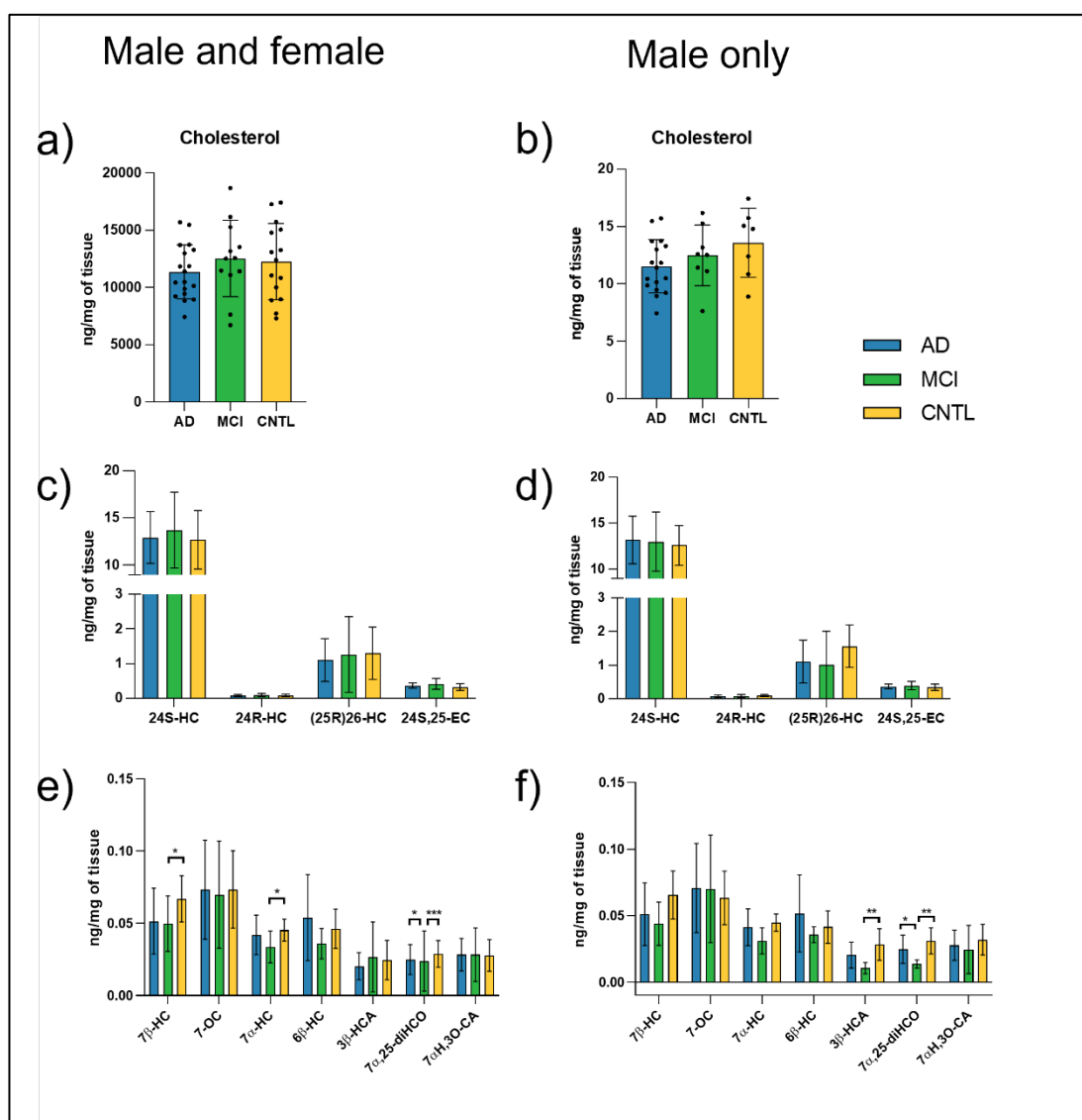


Figure 4.6. Statistical analysis of sterols identified in AD, MCI and control brain. Plotted data of sterols quantified using brain diagnosis status for both male and female (a, c & e), and male only groupings (b, d & f), showing cholesterol (a & b), key monohydroxycholesterols (c & d), and other sterols of interest (e & f).

The brain diagnosis analysis did not show any significance between groups with cholesterol; however, it did show a consistent decrease in the amount of cholesterol seen in the AD group compared with MCI and control cases for both the mixed gender and male-only analyses (see Figure 4.6).

The 24S-HC quantified also showed no significant differences but did show MCI cases increased on average in the mixed gender grouping, and AD slightly increased in male-only. In both groupings (25R)26-HC showed decreased levels in AD compared to both MCI and control but again no significance was observed.

The significant findings were mainly found in 7 β -HC and 7 α -HC analysis. In the mixed gender grouping, 7 β -HC was significantly lower in MCI ($P=0.0327$; Dunn's) compared with the control group, and in the male-only analysis, 7 β -HC did show a decrease in the MCI grouping compared with the control group, however no significance was observed.

For 7 α -HC, in the mixed gender grouping MCI was significantly lower compared with control ($P=0.0351$; Dunn's), with the same trend seen in the male only analysis but without a significant value.

There was also significance identified with 7 α ,25-diHCO in the mixed gender grouping, where MCI was significantly lower compared to control ($P=0.0004$; Dunn's) and compared to AD ($P=0.0262$; Dunn's). Again, in the male-only grouping the same trend was seen, with significantly lower levels in MCI compared to control ($P=0.0048$; Tukey's) and AD ($P=0.0362$; Tukey's post-test). There was also significance seen for 3 β -HCA, with levels significantly decreased in MCI compared with control ($P=0.0093$; Dunn's).

4.3.3. Analysis of sterols using *APOE* status

In addition to the brain diagnosis analysis, data was also investigated using the *APOE* status of the individuals using the three isoforms as groupings (*APOE*2, *APOE*3 or *APOE*4). For the purpose of this study, cases with a heterozygous *APOE* status were removed from the cohort (see Table 4.1 for case details).

The cholesterol levels quantified within the mixed gender grouping showed no large differences between isoforms, however in the male-only group cholesterol was observed to be increased in individuals with the *APOE*2 isoform compared with *APOE*3 and *APOE*4 (see Figure 4.7), but no significance was observed.

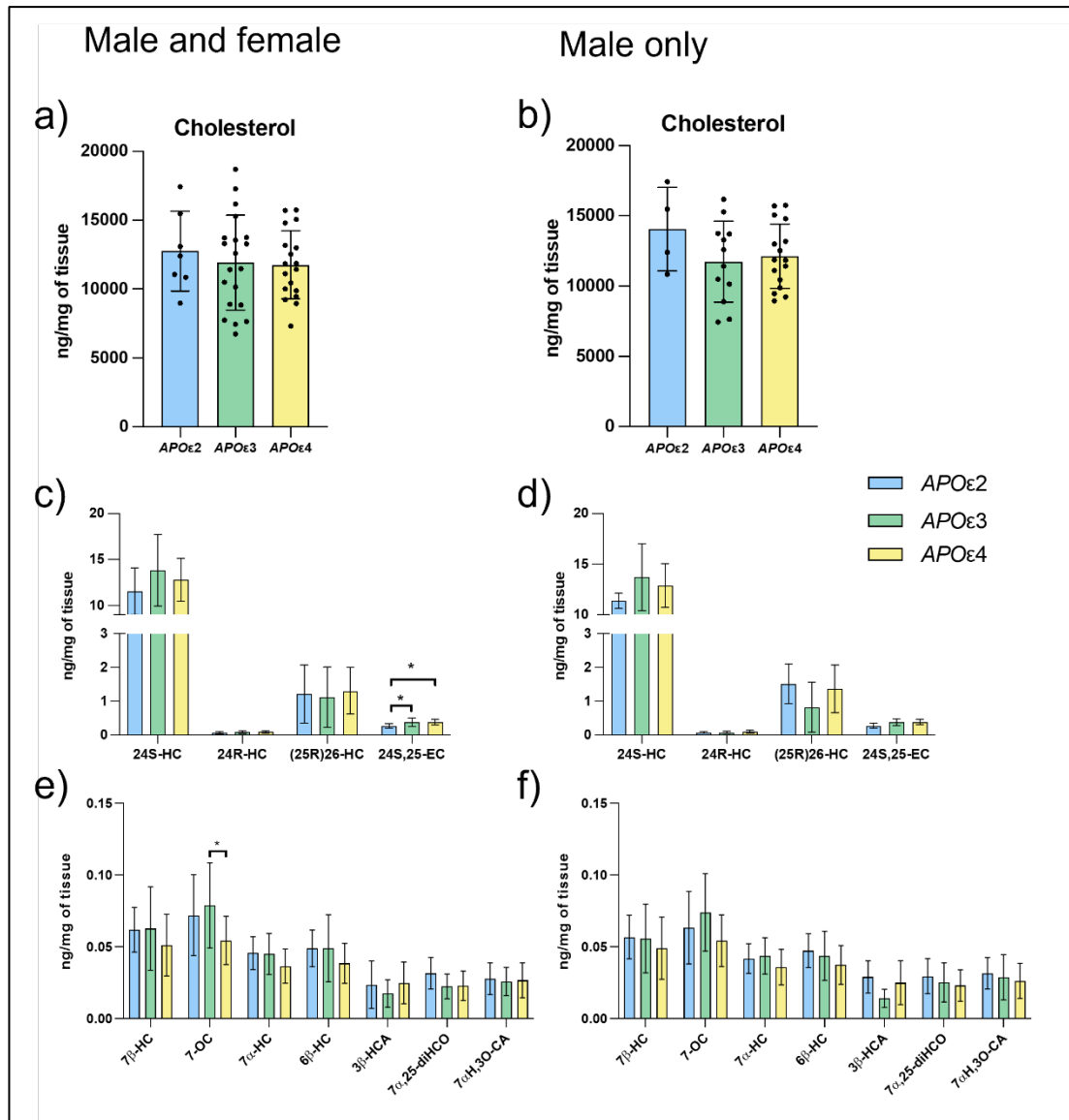


Figure 4.7. The statistical analysis of sterols using the *APOE* status of individuals. Plotted data of sterols quantified using ApoE status for both male and female (a, c & e), and male only groupings (b, d & f), showing cholesterol (a & b), key monohydroxycholesterols (c & d), and other sterols of interest (e & f).

The 24S-HC quantified within the mixed grouping and male-only showed a decrease in individuals with *APOε2* and *APOε4* isoforms compared with *APOε3*, however, no statistical significance was observed. For (25R)26-HC in the mixed gender grouping, although not significant, levels were slightly increased in the *APOε2* and *APOε4* isoforms compared with *APOε3*. This difference was much more pronounced in the male-only grouping, where both *APOε2* and *APOε4* had higher mean concentrations of (25R)26-HC compared with individuals with the *APOε3* isoform group but again did not show significance (see Figure 4.7).

There was statistical significance observed with 24S,25-EC, which isomerises to 24-oxocholesterol (24-OC) in our analytical method. In the mixed gender grouping, 24S,25-EC was significantly increased in *APOε3* ($P=0.0372$; Dunn's) and *APOε4* ($P=0.0254$; Dunn's) compared with the *APOε2* isoform group. Again, the same trend was witnessed in the male-only grouping however no significance was observed. The other sterols analysed followed the same trends in both the mixed and male-only groupings, and there was significant observed in the mixed group, where 7-OC was significantly increased in MCI compared with control ($P=0.0176$; Tukey's), however the remaining data did not show any significant results which could be due to the relatively low sample numbers (e.g., male-only grouping).

After cholesterol oxidase and GP-tagging			Mean concentration (ng/mg tissue ± SD)				
Mass (± 5ppm)	Sterol/ Oxysterol Systematic name	Sterol/ Oxysterol Common name	Elemental composition	Abbreviation	AD brain tissue (n=18)	MCI brain tissue (n=12)	CNTL brain tissue (n=15)
523.4419	(GP ^{[2} H ₅]) Cholest-4-en-3-one	Cholesterol	C ₃₄ H ₄₇ D ₅ N ₃ O ⁺	-	11381±2362	12527±3331	12258±3330
537.4211	(GP ^{[2} H ₅]) 24S,25-Epoxycholest-4-en-3-one	24S,25-Epoxycholesterol/24-oxocholesterol	C ₃₄ H ₄₅ D ₅ N ₃ O ₂ ⁺	24S,25-EC/24-OC	0.364±0.079	0.413±0.151	0.326±0.095
534.4054	(GP ^{[2} H ₀]) 25-Hydroxycholest-4-en-3-one	25-Hydroxycholestenone	C ₃₄ H ₅₂ N ₃ O ₂ ⁺	25-HCO	0.0011±0.0011	0.0014±0.0026	0.0012±0.0011
534.4054	(GP ^{[2} H ₀]) (25R)26-Hydroxycholest-4-en-3-one	(25R)26-Hydroxycholestenone	C ₃₄ H ₅₂ N ₃ O ₂ ⁺	(25R)26-HCO	0.0067±0.0136	0.0035±0.0040	0.0040±0.0039
534.4054	(GP ^{[2} H ₀]) 3β-Hydroxycholest-5-en-7-one	7-Oxocholesterol	C ₃₄ H ₅₂ N ₃ O ₂ ⁺	7-OC	0.073±0.034	0.070±0.037	0.073±0.027
539.4368	(GP ^{[2} H ₅]) 24S-Hydroxycholest-4-en-3-one	24S-Hydroxycholesterol	C ₃₄ H ₄₇ D ₅ N ₃ O ₂ ⁺	24S-HC	12.920±2.754	13.703±4.016	12.710±3.095
539.4368	(GP ^{[2} H ₅]) 24R-Hydroxycholest-4-en-3-one	24R-Hydroxycholesterol	C ₃₄ H ₄₇ D ₅ N ₃ O ₂ ⁺	24R-HC	0.081±0.033	0.096±0.051	0.085±0.039
539.4368	(GP ^{[2} H ₅]) (25R)26-Hydroxycholest-4-en-3-one	(25R)26-Hydroxycholesterol	C ₃₄ H ₄₇ D ₅ N ₃ O ₂ ⁺	(25R)26-HC	1.099±0.621	1.260±1.093	1.299±0.755
539.4368	(GP ^{[2} H ₅]) 7β-Hydroxycholest-4-en-3-one	7β-Hydroxycholesterol	C ₃₄ H ₄₇ D ₅ N ₃ O ₂ ⁺	7β-HC	0.051±0.023	0.050±0.019	0.067±0.016
539.4368	(GP ^{[2} H ₅]) 7α-Hydroxycholest-4-en-3-one	7α-Hydroxycholesterol	C ₃₄ H ₄₇ D ₅ N ₃ O ₂ ⁺	7α-HC	0.042±0.030	0.034±0.011	0.045±0.006
539.4368	(GP ^{[2} H ₅]) 6β-Hydroxycholest-4-en-3-one	6β-Hydroxycholesterol	C ₃₄ H ₄₇ D ₅ N ₃ O ₂ ⁺	6β-HC	0.054±0.030	0.036±0.011	0.046±0.013
553.4161	(GP ^{[2} H ₅]) 3-Oxocholest-4-en-(25R)26-oic acid	3β-Hydroxycholestenic acid	C ₃₄ H ₄₅ D ₅ N ₃ O ₃ ⁺	3β-HCA	0.020±0.009	0.027±0.024	0.025±0.014
550.4003	(GP ^{[2} H ₀]) 7α,25-Dihydroxycholest-4-en-3-one	7α,25-Dihydroxycholestenone	C ₃₄ H ₅₂ N ₃ O ₃ ⁺	7α,25-diHCO	0.025±0.010	0.016±0.004	0.029±0.009
550.4003	(GP ^{[2} H ₀]) 7α,(25R)26-dihydroxycholest-4-en-3-one	7α,(25R)26-dihydroxycholestenone	C ₃₄ H ₅₂ N ₃ O ₃ ⁺	7α,26-diHCO	0.072±0.032	0.074±0.051	0.080±0.038

555.4317	(GP[² H ₅]) 7 α ,25-Dihydroxycholest-4-en-3-one	7 α ,25-Dihydroxycholesterol	C ₃₄ H ₄₇ D ₅ N ₃ O ₃ ⁺	7 α ,25-diHHC	0.010 \pm 0.007	0.007 \pm 0.007	0.010 \pm 0.007
555.4317	(GP[² H ₅]) 7 α , (25R)26-Dihydroxycholest-4-en-3-one	7 α , (25R)26-Dihydroxycholesterol	C ₃₄ H ₄₇ D ₅ N ₃ O ₃ ⁺	7 α ,26-diHHC	0.017 \pm 0.013	0.018 \pm 0.028	0.015 \pm 0.011
564.3796	(GP[² H ₀]) 7 α -Hydroxy-3-oxocholest-4-en-(25R/S),26-oic acid	7 α -hydroxy-3-oxocholest-4-en-(25R/S),26-oic acid	C ₃₄ H ₅₀ N ₃ O ₄ ⁺	7 α H,3O-CA	0.028 \pm 0.011	0.028 \pm 0.019	0.028 \pm 0.011
569.4110	(GP[² H ₅]) 3 β ,7 α -dihydroxycholest-5-en-(25R/S),26-oic acid GP-d5	3 β ,7 α -dihydroxycholest-5-en-(25R/S)26-oic acid	C ₃₄ H ₄₅ D ₅ N ₃ O ₄ ⁺	3 β ,7 α -diHCA	0.001 \pm 0.002	0.002 \pm 0.002	0.003 \pm 0.003

Table 4.2. Average values of cholesterol and oxysterols found in AD, MCI and CNTL brain tissue homogenates across total cohort (male and female). The mean concentration of each oxysterol seen in each sample, with the standard deviation. EC = epoxycholesterol; OC = oxocholesterol; HC = hydroxycholesterol; diHHC = dihydroxycholesterol; CA = cholestenoic acid; diHCA = dihydroxycholestenoic acid.

After cholesterol oxidase and GP-tagging			Mean concentration (ng/mg tissue ± SD)				
Mass (± 5ppm)	Sterol/ Oxysterol Systematic name	Sterol/ Oxysterol Common name	Elemental composition	Abbreviation	AD brain tissue (n=17)	MCI brain tissue (n=8)	CNTL brain tissue (n=7)
523.4419	(GP ² H ₅) Cholest-4-en-3-one	Cholesterol	C ₃₄ H ₄₇ D ₅ N ₃ O ⁺	-	11531±2346	12488±2627	13591±3001
537.4211	(GP ² H ₅) 24S,25-Epoxycholest-4-en-3-one	24S,25-Epoxycholesterol/ 24-oxocholesterol	C ₃₄ H ₄₅ D ₅ N ₃ O ₂ ⁺	24S,25-EC/ 24-OC	0.371±0.075	0.393±0.121	0.342±0.092
534.4054	(GP ² H ₀) 25-Hydroxycholest-4-en-3-one	25-Hydroxycholestenone	C ₃₄ H ₅₂ N ₃ O ₂ ⁺	25-HCO	0.0010±0.0011	0.0008±0.0018	0.0012±0.0012
534.4054	(GP ² H ₀) (25R)26-Hydroxycholest-4-en-3-one	(25R)26-Hydroxycholestenone	C ₃₄ H ₅₂ N ₃ O ₂ ⁺	(25R)26-HCO	0.0066±0.0140	0.0032±0.0043	0.0046±0.0049
534.4054	(GP ² H ₀) 3β-Hydroxycholest-5-en-7-one	7-Oxocholesterol	C ₃₄ H ₅₂ N ₃ O ₂ ⁺	7-OC	0.071±0.033	0.070±0.041	0.063±0.020
539.4368	(GP ² H ₅) 24S-Hydroxycholest-4-en-3-one	24S-Hydroxycholesterol	C ₃₄ H ₄₇ D ₅ N ₃ O ₂ ⁺	24S-HC	13.181±2.600	12.979±3.202	12.595±2.153
539.4368	(GP ² H ₅) 24R-Hydroxycholest-4-en-3-one	24R-Hydroxycholesterol	C ₃₄ H ₄₇ D ₅ N ₃ O ₂ ⁺	24R-HC	0.082±0.033	0.085±0.040	0.094±0.029
539.4368	(GP ² H ₅) (25R)26-Hydroxycholest-4-en-3-one	(25R)26-Hydroxycholesterol	C ₃₄ H ₄₇ D ₅ N ₃ O ₂ ⁺	(25R)26-HC	1.109±0.639	1.012±0.997	1.560±0.623
539.4368	(GP ² H ₅) 7β-Hydroxycholest-4-en-3-one	7β-Hydroxycholesterol	C ₃₄ H ₄₇ D ₅ N ₃ O ₂ ⁺	7β-HC	0.051±0.024	0.044±0.016	0.065±0.018
539.4368	(GP ² H ₅) 7α-Hydroxycholest-4-en-3-one	7α-Hydroxycholesterol	C ₃₄ H ₄₇ D ₅ N ₃ O ₂ ⁺	7α-HC	0.041±0.014	0.031±0.010	0.045±0.006
539.4368	(GP ² H ₅) 6β-Hydroxycholest-4-en-3-one	6β-Hydroxycholesterol	C ₃₄ H ₄₇ D ₅ N ₃ O ₂ ⁺	6β-HC	0.052±0.029	0.036±0.006	0.042±0.012
553.4161	(GP ² H ₅) 3-Oxocholest-4-en-(25R)26-oic acid	3β-Hydroxycholestenonic acid	C ₃₄ H ₄₅ D ₅ N ₃ O ₃ ⁺	3β-HCA	0.020±0.010	0.010±0.004	0.028±0.012
550.4003	(GP ² H ₀) 7α,25-Dihydroxycholest-4-en-3-one	7α,25-Dihydroxycholestenone	C ₃₄ H ₅₂ N ₃ O ₃ ⁺	7α,25-diHCO	0.025±0.011	0.014±0.003	0.031±0.010
550.4003	(GP ² H ₀) 7α,(25R)26-dihydroxycholest-4-en-3-one	7α,(25R)26-dihydroxycholestenone	C ₃₄ H ₅₂ N ₃ O ₃ ⁺	7α,26-diHCO	0.067±0.023	0.058±0.026	0.078±0.016

555.4317	(GP[² H ₅]) 7 α ,25-Dihydroxycholest-4-en-3-one	7 α ,25-Dihydroxycholesterol	C ₃₄ H ₄₇ D ₅ N ₃ O ₃ ⁺	7 α ,25-diHC	0.010 \pm 0.006	0.009 \pm 0.008	0.012 \pm 0.008
555.4317	(GP[² H ₅]) 7 α , (25R)26-Dihydroxycholest-4-en-3-one	7 α , (25R)26-Dihydroxycholesterol	C ₃₄ H ₄₇ D ₅ N ₃ O ₃ ⁺	7 α ,26-diHC	0.016 \pm 0.013	0.022 \pm 0.033	0.014 \pm 0.008
564.3796	(GP[² H ₀]) 7 α -Hydroxy-3-oxocholest-4-en-(25R/S),26-oic acid	7 α -hydroxy-3-oxocholest-4-en-(25R/S),26-oic acid	C ₃₄ H ₅₀ N ₃ O ₄ ⁺	7 α H,3O-CA	0.028 \pm 0.011	0.025 \pm 0.018	0.032 \pm 0.012
569.4110	(GP[² H ₅]) 3 β ,7 α -dihydroxycholest-5-en-(25R/S),26-oic acid GP-d5	3 β ,7 α -dihydroxycholest-5-en-(25R/S)26-oic acid	C ₃₄ H ₄₅ D ₅ N ₃ O ₄ ⁺	3 β ,7 α -diHCA	0.001 \pm 0.002	0.001 \pm 0.002	0.001 \pm 0.002

Table 4.3. Average values of cholesterol and oxysterols found in AD, MCI and CNTL brain tissue homogenates in males only. The mean concentration of each oxysterol seen in each sample, with the standard deviation. EC = epoxcholesterol; OC = oxocholesterol; HC = hydroxycholesterol; diHC = dihydroxycholesterol; CA = cholestenoic acid; diHCA = dihydroxycholestenenoic acid.

After cholesterol oxidase and GP-tagging			Mean concentration (ng/mg tissue ± SD)				
Mass (± 5ppm)	Sterol/ Oxysterol Systematic name	Sterol/ Oxysterol Common name	Elemental composition	Abbreviation	<i>APO</i> ε2 isoform (n=7)	<i>APO</i> ε3 isoform (n=20)	<i>APO</i> ε4 isoform (n=18)
523.4419	(GP[² H ₅]) Cholest-4-en-3-one	Cholesterol	C ₃₄ H ₄₇ D ₅ N ₃ O ⁺	-	12753±2895	11917±3435	11747±2472
537.4211	(GP[² H ₅]) 24S,25-Epoxycholest-4-en-3-one	24S,25-Epoxycholesterol/ 24-oxocholesterol	C ₃₄ H ₄₅ D ₅ N ₃ O ₂ ⁺	24S,25-EC/ 24-OC	0.266±0.069	0.383±0.126	0.382±0.086
534.4054	(GP[² H ₀]) 25-Hydroxycholest-4-en-3-one	25-Hydroxycholestenone	C ₃₄ H ₅₂ N ₃ O ₂ ⁺	25-HCO	0.0010±0.0007	0.0012±0.0022	0.0012±0.0011
534.4054	(GP[² H ₀]) (25R)26-Hydroxycholest-4-en-3-one	(25R)26-Hydroxycholestenone	C ₃₄ H ₅₂ N ₃ O ₂ ⁺	(25R)26-HCO	0.0030±0.0033	0.0037±0.0034	0.0071±0.0137
534.4054	(GP[² H ₀]) 3β-Hydroxycholest-5-en-7-one	7-Oxocholesterol	C ₃₄ H ₅₂ N ₃ O ₂ ⁺	7-OC	0.072±0.028	0.079±0.030	0.054±0.017
539.4368	(GP[² H ₅]) 24S-Hydroxycholest-4-en-3-one	24S-Hydroxycholesterol	C ₃₄ H ₄₇ D ₅ N ₃ O ₂ ⁺	24S-HC	11.556±2.552	13.834±3.889	12.781±2.324
539.4368	(GP[² H ₅]) 24R-Hydroxycholest-4-en-3-one	24R-Hydroxycholesterol	C ₃₄ H ₄₇ D ₅ N ₃ O ₂ ⁺	24R-HC	0.067±0.035	0.086±0.042	0.094±0.037
539.4368	(GP[² H ₅]) (25R)26-Hydroxycholest-4-en-3-one	(25R)26-Hydroxycholesterol	C ₃₄ H ₄₇ D ₅ N ₃ O ₂ ⁺	(25R)26-HC	1.216±0.858	1.117±0.894	1.308±0.691
539.4368	(GP[² H ₅]) 7β-Hydroxycholest-4-en-3-one	7β-Hydroxycholesterol	C ₃₄ H ₄₇ D ₅ N ₃ O ₂ ⁺	7β-HC	0.062±0.015	0.063±0.029	0.051±0.021
539.4368	(GP[² H ₅]) 7α-Hydroxycholest-4-en-3-one	7α-Hydroxycholesterol	C ₃₄ H ₄₇ D ₅ N ₃ O ₂ ⁺	7α-HC	0.045±0.011	0.045±0.014	0.036±0.012
539.4368	(GP[² H ₅]) 6β-Hydroxycholest-4-en-3-one	6β-Hydroxycholesterol	C ₃₄ H ₄₇ D ₅ N ₃ O ₂ ⁺	6β-HC	0.049±0.011	0.049±0.023	0.039±0.014
553.4161	(GP[² H ₅]) 3-Oxocholest-4-en-(25R)26-oic acid	3β-Hydroxycholestenic acid	C ₃₄ H ₄₅ D ₅ N ₃ O ₃ ⁺	3β-HCA	0.024±0.016	0.017±0.010	0.025±0.015
550.4003	(GP[² H ₀]) 7α,25-Dihydroxycholest-4-en-3-one	7α,25-Dihydroxycholestenone	C ₃₄ H ₅₂ N ₃ O ₃ ⁺	7α,25-diHCO	0.031±0.011	0.022±0.008	0.023±0.010
550.4003	(GP[² H ₀]) 7α,(25R)26-dihydroxycholest-4-en-3-one	7α,(25R)26-dihydroxycholestenone	C ₃₄ H ₅₂ N ₃ O ₃ ⁺	7α,26-diHCO	0.067±0.020	0.067±0.020	0.066±0.023

555.4317	(GP[² H ₅]) 7 α ,25-Dihydroxycholest-4-en-3-one	7 α ,25-Dihydroxycholesterol	C ₃₄ H ₄₇ D ₅ N ₃ O ₃ ⁺	7 α ,25-diHC	0.009 \pm 0.008	0.009 \pm 0.007	0.009 \pm 0.007
555.4317	(GP[² H ₅]) 7 α , (25R)26-Dihydroxycholest-4-en-3-one	7 α , (25R)26-Dihydroxycholesterol	C ₃₄ H ₄₇ D ₅ N ₃ O ₃ ⁺	7 α ,26-diHC	0.021 \pm 0.022	0.013 \pm 0.011	0.018 \pm 0.021
564.3796	(GP[² H ₀]) 7 α -Hydroxy-3-oxocholest-4-en-(25R/S),26-oic acid	7 α -hydroxy-3-oxocholest-4-en-(25R/S),26-oic acid	C ₃₄ H ₅₀ N ₃ O ₄ ⁺	7 α H,3O-CA	0.028 \pm 0.011	0.026 \pm 0.010	0.027 \pm 0.012
569.4110	(GP[² H ₅]) 3 β ,7 α -dihydroxycholest-5-en-(25R/S),26-oic acid GP-d ₅	3 β ,7 α -dihydroxycholest-5-en-(25R/S),26-oic acid	C ₃₄ H ₄₅ D ₅ N ₃ O ₄ ⁺	3 β ,7 α -diHCA	0.002 \pm 0.003	0.001 \pm 0.002	0.002 \pm 0.003

Table 4.4. Average values of cholesterol and oxysterols found in the brain homogenate cohort using *APOE* status grouping *APOε2*, *APOε3* and *APOε4* (male and female).

The mean concentration of each oxysterol seen in each sample, with the standard deviation. EC = epoxycholesterol; OC = oxocholesterol; HC = hydroxycholesterol; diHC = dihydroxycholesterol; CA = cholestenic acid; diHCA = dihydroxycholestenic acid.

After cholesterol oxidase and GP-tagging			Mean concentration (ng/mg tissue \pm SD)				
Mass (\pm 5ppm)	Sterol/ Oxysterol Systematic name	Sterol/ Oxysterol Common name	Elemental composition	Abbreviation	<i>APO</i> ϵ 2 isoform (n=4)	<i>APO</i> ϵ 3 isoform (n=12)	<i>APO</i> ϵ 4 isoform (n=16)
523.4419	(GP[² H ₅]) Cholest-4-en-3-one	Cholesterol	C ₃₄ H ₄₇ D ₅ N ₃ O ⁺	-	14037 \pm 2970	11732 \pm 2873	12133 \pm 2293
537.4211	(GP[² H ₅]) 24S,25-Epoxycholesterol/ Epoxycholest-4-en-3-one	24S,25-Epoxycholesterol/ 24-oxocholesterol	C ₃₄ H ₄₅ D ₅ N ₃ O ₂ ⁺	24S,25-EC/ 24-OC	0.279 \pm 0.082	0.379 \pm 0.096	0.387 \pm 0.079
534.4054	(GP[² H ₀]) 25-Hydroxycholest-4-en-3-one	25-Hydroxycholestenone	C ₃₄ H ₅₂ N ₃ O ₂ ⁺	25-HCO	0.0006 \pm 0.0007	0.0008 \pm 0.0017	0.0012 \pm 0.0010
534.4054	(GP[² H ₀]) (25R)26-Hydroxycholest-4-en-3-one	(25R)26-Hydroxycholestenone	C ₃₄ H ₅₂ N ₃ O ₂ ⁺	(25R)26-HCO	0.0026 \pm 0.0032	0.0030 \pm 0.0036	0.0043 \pm 0.0037
534.4054	(GP[² H ₀]) 3 β -Hydroxycholest-5-en-7-one	7-Oxocholesterol	C ₃₄ H ₅₂ N ₃ O ₂ ⁺	7-OC	0.063 \pm 0.025	0.074 \pm 0.027	0.054 \pm 0.018
539.4368	(GP[² H ₅]) 24S-Hydroxycholest-4-en-3-one	24S-Hydroxycholesterol	C ₃₄ H ₄₇ D ₅ N ₃ O ₂ ⁺	24S-HC	11.351 \pm 0.759	13.710 \pm 3.312	12.885 \pm 2.159
539.4368	(GP[² H ₅]) 24R-Hydroxycholest-4-en-3-one	24R-Hydroxycholesterol	C ₃₄ H ₄₇ D ₅ N ₃ O ₂ ⁺	24R-HC	0.077 \pm 0.020	0.075 \pm 0.029	0.096 \pm 0.038
539.4368	(GP[² H ₅]) (25R)26-Hydroxycholest-4-en-3-one	(25R)26-Hydroxycholesterol	C ₃₄ H ₄₇ D ₅ N ₃ O ₂ ⁺	(25R)26-HC	1.512 \pm 0.586	0.823 \pm 0.741	1.372 \pm 0.707
539.4368	(GP[² H ₅]) 7 β -Hydroxycholest-4-en-3-one	7 β -Hydroxycholesterol	C ₃₄ H ₄₇ D ₅ N ₃ O ₂ ⁺	7 β -HC	0.057 \pm 0.015	0.056 \pm 0.024	0.049 \pm 0.022
539.4368	(GP[² H ₅]) 7 α -Hydroxycholest-4-en-3-one	7 α -Hydroxycholesterol	C ₃₄ H ₄₇ D ₅ N ₃ O ₂ ⁺	7 α -HC	0.042 \pm 0.010	0.044 \pm 0.013	0.036 \pm 0.012
539.4368	(GP[² H ₅]) 6 β -Hydroxycholest-4-en-3-one	6 β -Hydroxycholesterol	C ₃₄ H ₄₇ D ₅ N ₃ O ₂ ⁺	6 β -HC	0.047 \pm 0.011	0.044 \pm 0.017	0.037 \pm 0.014
553.4161	(GP[² H ₅]) 3-Oxocholest-4-en-(25R)26-oic acid	3 β -Hydroxycholestenonic acid	C ₃₄ H ₄₅ D ₅ N ₃ O ₃ ⁺	3 β -HCA	0.029 \pm 0.011	0.014 \pm 0.006	0.025 \pm 0.015
550.4003	(GP[² H ₀]) 7 α ,25-Dihydroxycholest-4-en-3-one	7 α ,25-Dihydroxycholestenone	C ₃₄ H ₅₂ N ₃ O ₃ ⁺	7 α ,25-diHCO	0.030 \pm 0.012	0.025 \pm 0.013	0.023 \pm 0.011
550.4003	(GP[² H ₀]) 7 α , (25R)26-dihydroxycholest-4-en-3-one	7 α , (25R)26-dihydroxycholestenone	C ₃₄ H ₅₂ N ₃ O ₃ ⁺	7 α ,26-diHCO	0.079 \pm 0.014	0.063 \pm 0.023	0.066 \pm 0.024

555.4317	(GP[² H ₅]) 7 α ,25-Dihydroxycholest-4-en-3-one	7 α ,25-Dihydroxycholesterol	C ₃₄ H ₄₇ D ₅ N ₃ O ₃ ⁺	7 α ,25-diHC	0.013 \pm 0.009	0.009 \pm 0.007	0.010 \pm 0.007
555.4317	(GP[² H ₅]) 7 α , (25R)26-Dihydroxycholest-4-en-3-one	7 α , (25R)26-Dihydroxycholesterol	C ₃₄ H ₄₇ D ₅ N ₃ O ₃ ⁺	7 α ,26-diHC	0.023 \pm 0.023	0.012 \pm 0.011	0.019 \pm 0.023
564.3796	(GP[² H ₀]) 7 α -Hydroxy-3-oxocholest-4-en-(25R/S),26-oic acid	7 α -hydroxy-3-oxocholest-4-en-(25R/S),26-oic acid	C ₃₄ H ₅₀ N ₃ O ₄ ⁺	7 α H,3O-CA	0.031 \pm 0.011	0.029 \pm 0.016	0.026 \pm 0.012
569.4110	(GP[² H ₅]) 3 β ,7 α -dihydroxycholest-5-en-(25R/S),26-oic acid GP-d5	3 β ,7 α -dihydroxycholest-5-en-(25R/S)26-oic acid	C ₃₄ H ₄₅ D ₅ N ₃ O ₄ ⁺	3 β ,7 α -diHCA	0.001 \pm 0.002	0.001 \pm 0.002	0.002 \pm 0.002

Table 4.5. Average values of cholesterol and oxysterols found in brain homogenate cohort using *APOE* status grouping *APOε2*, *APOε3* and *APOε4* (male only). The mean concentration of each oxysterol seen in each sample, with the standard deviation. EC = epoxycholesterol; OC = oxocholesterol; HC = hydroxycholesterol; diHC = dihydroxycholesterol; CA = cholestenoic acid; diHCA = dihydroxycholestenoic acid.

4.4. Discussion

The justification for this study came from previously published data showing altered levels of oxysterols in the brain tissue of AD patients^{24,25}, and for this work in addition to brain diagnosis we also looked at the relevance of ApoE status of an individual. This was of interest to us, primarily due to its role in cholesterol transport but also from the various other studies that had identified ApoE status could play a role in AD. The general aim of this study was to analyse oxysterol content at different stages of cognitive decline to identify possible discrepancies in comparison to control cases, which was achieved. After analysis we did identify significantly differing levels of analytes in the 7α - and 7β -hydroxylation pathways, specifically 7α -HC, 7β -HC and $7\alpha,25$ -diHCO based on brain diagnosis, with most significance observed between MCI and control, where MCI cases had significantly decreased levels compared with control. In addition, levels of $7\alpha,25$ -diHCO in AD were also significantly decreased compared with control. We did not observe any increase in cholesterol levels in AD compared with both MCI and control cases, suggesting that there may not be any strong direct link between cholesterol concentration in the brain and AD.

There was a difference seen between AD and control cases for 7β -HC showing decreased levels in AD compared with control. The MCI grouping showed a significant decrease for this metabolite compared with control, however these findings were contrasting to previously published data from Testa in 2016²⁵.

The study looked at many oxysterols including 7α -HC, 7-OC and 7β -HC, which were all increased in late-stage AD compared to control cases²⁵. It also reported on 24S-HC and (25R)26-HC in brain tissue, showing a significant decrease of 24S-HC and a significant increase of (25R)26-HC in late-stage AD compared with controls. This data was also seen in a study by Heverin in 2004 who showed that levels of 24S-HC were decreased in the cortex of AD compared with controls, with (25R)26-HC significantly increased in cortical brain tissue of individuals with AD²⁴. In comparison, the results of this study showed no significance between groups for those two metabolites. It should be noted that care should be taken when interpreting data with respect to 7α -HC, 7β -HC and 7-OC as these can all be formed from cholesterol by oxidation in air. In dealing with human brain this is difficult to control^{26,27}.

The main difference between this study and the Testa research from 2016 was the decision of splitting the AD cohort based on disease stage using Braak scoring. Alzheimer's is a complex and progressive disease, where in later disease stages important pathological mechanisms are more advanced and are paired with increased cortical atrophy, greater neuronal loss, and more pronounced pathological hallmarks including A β plaques and NFT deposition which could mean a substantial difference in oxysterol concentrations in the preliminary stages of disease, where mechanisms may not be fully dysfunctional, to later-stage disease where there is increased accumulation of disease pathology. The ability to split our cohort was not available, however, it could have given us additional analysis opportunities for our datasets and highlighted possible differences at distinct stages of neurological impairment in combination with MCI, telling a broader story about neurodegeneration in dementias like Alzheimer's.

The most interesting findings from our study centred around the analysis of the *APOE* genotype status, where ApoE is the dominant apolipoprotein in the brain primarily involved in the transport of cholesterol from astrocytes to neurons. Established research has shown a difference in the ability to uptake ApoE-bound cholesterol into astrocytes and neuronal cells between several isoforms of ApoE, with uptake lower for APO ϵ 4-bound cholesterol compared to ϵ 2 and ϵ 3¹⁶.

Using the ApoE grouping we identified significance with 24S,25-EC (isomerising to 24-oxocholesterol), which is a potent ligand for LXR's. The levels of 24S,25-EC were significantly increased in *APO* ϵ 4 and *APO* ϵ 3 genotype in comparison to *APO* ϵ 2 in the mixed gender grouping. This was the opposite trend observed in the cholesterol analysis, where cholesterol levels were increased in the *APO* ϵ 2 grouping compared with *APO* ϵ 3 and *APO* ϵ 4 which were lower, although no significance was observed. This agrees with the understanding that binding of 24S,25-EC to INSIG decreases the synthesis of HMGCR via SREBP and subsequently lowers levels of cholesterol^{28,29}, as well as being a potent ligand to LXRs. LXRs have the ability to directly regulate the transcription of *APOE*³⁰⁻³³, which could aid the removal of excess cholesterol from neurons.

In addition to 24S,25-EC, we also saw some large differences in the male-only grouping for (25R)26-HC, although not significantly so possibly due to the low sample number (n=4) for the *APO* ϵ 2 grouping. The current understanding of the

APOε4 isoform, and the poor ability of the protein's lipid-bound complex to be taken into neuronal cells and failing to clear Aβ effectively from the brain, means it is a known risk factor for AD. Our findings from this study supports the theory of the possible dysregulation an *APOε4* genotype is associated with, beginning with the differences identified with (25R)26-HC in males only ((25R)26-HC shows a sex difference, with males showing higher compared with females in plasma^{34,35}), which shows both *APOε4* and *APOε2* isoforms show an increase of (25R)26-HC in comparison to *APOε3*. This finding is supported by Jenner et al, 2010, which showed increased (25R)26-HC in *APOε4* and *APOε2* mouse models at one year old in comparison to *APOε3* mice³⁶. This increase of (25R)26-HC could cause cholesterol and oxysterol imbalances within the brain, cause upregulated cleavage of APP and generating the formation of Aβ₄₂, fragments that are more likely to form plaques. The inability of the *APOε4* isoform to clear these toxic plaques results in neurotoxic effect and eventually neuronal loss with this cycle continuing and leading to progressive disease¹⁴.

To conclude, during this study we have seen altered levels of oxysterols in AD, MCI and control brain tissue, where levels in MCI tend to be generally depleted in comparison to established AD, with exception to some metabolites. In control samples, data was more varied with no true trend across all metabolites. However, we found that *APOE* status of individuals could be more telling for the dysregulation of important oxysterols including (25R)26-HC and 24S,25-EC, given its role in cholesterol transport and the subpar ability of the *APOε4* isoform. More work is needed to truly understand *APOE* and its effects in AD and on sterol profiles in individuals to build on the findings we have found in this study. The possibility of analysing different Braak groupings for *APOE* and sterol content could be something to consider, to further analyse oxysterols at different stages of neurological impairment as this study has highlighted distinctions between established AD and early cognitive impairment and could be key to gaining a better understanding of the progression of an individual than just using the disease diagnosis.

4.5. References

1. Jahn, H. Memory loss in Alzheimer's disease. *Dialogues Clin. Neurosci.* **15**, 445–454 (2013).
2. Lanctôt, K. L. *et al.* Neuropsychiatric signs and symptoms of Alzheimer's disease: New treatment paradigms. *Alzheimer's Dement. Transl. Res. Clin. Interv.* **3**, 440–449 (2017).
3. Lane, C. A., Hardy, J. & Schott, J. M. Alzheimer's disease. *Eur. J. Neurol.* **25**, 59–70 (2018).
4. Alzheimer's Society. *Alzheimer's Society's view on demography.* (2020).
5. Beam, C. R. *et al.* Differences Between Women and Men in Incidence Rates of Dementia and Alzheimer's Disease. *J. Alzheimer's Dis.* **64**, 1077–1083 (2018).
6. Bekris, L. M., Yu, C.-E., Bird, T. D. & Tsuang, D. W. Review Article: Genetics of Alzheimer Disease. *J. Geriatr. Psychiatry Neurol.* **23**, 213–227 (2010).
7. Blennow, K. & Zetterberg, H. Biomarkers for Alzheimer's disease: current status and prospects for the future. *J. Intern. Med.* **284**, 643–663 (2018).
8. Wong, M. W. *et al.* Dysregulation of lipids in Alzheimer's disease and their role as potential biomarkers. *Alzheimer's Dement.* **13**, 810–827 (2017).
9. Bertram, L. & Tanzi, R. E. The Genetics of Alzheimer's Disease. in 79–100 (2012). doi:10.1016/B978-0-12-385883-2.00008-4.
10. Vaz, M. & Silvestre, S. Alzheimer's disease: Recent treatment strategies. *Eur. J. Pharmacol.* **887**, 173554 (2020).
11. Kocahan, S. & Doğan, Z. Mechanisms of Alzheimer's Disease Pathogenesis and Prevention: The Brain, Neural Pathology, N-methyl-D-aspartate Receptors, Tau Protein and Other Risk Factors. *Clin. Psychopharmacol. Neurosci.* **15**, 1–8 (2017).
12. Atri, A. Current and Future Treatments in Alzheimer's Disease. *Semin. Neurol.* **39**, 227–240 (2019).
13. Mullard, A. Landmark Alzheimer's drug approval confounds research community. *Nature* **594**, 309–310 (2021).
14. Dai, L. *et al.* Cholesterol Metabolism in Neurodegenerative Diseases: Molecular Mechanisms and Therapeutic Targets. *Mol. Neurobiol.* **58**, 2183–2201 (2021).
15. Saint-Pol, J., Candela, P., Boucau, M.-C., Fenart, L. & Gosselet, F. Oxysterols decrease apical-to-basolateral transport of A β peptides via an ABCB1-mediated process in an in vitro Blood-brain barrier model constituted of bovine brain capillary endothelial cells. *Brain Res.* **1517**, 1–15 (2013).
16. Rapp, A., Gmeiner, B. & Hüttinger, M. Implication of apoE isoforms in cholesterol metabolism by primary rat hippocampal neurons and astrocytes. *Biochimie* **88**, 473–483 (2006).
17. Ma, J., Yee, A., Brewer, H. B., Das, S. & Potter, H. Amyloid-associated proteins α 1-antichymotrypsin and apolipoprotein E promote assembly of Alzheimer β -protein into filaments. *Nature* **372**, 92–94 (1994).
18. Refolo, L. M. *et al.* Hypercholesterolemia Accelerates the Alzheimer's Amyloid Pathology in a Transgenic Mouse Model. *Neurobiol. Dis.* **7**, 321–331 (2000).
19. Fassbender, K. *et al.* Simvastatin strongly reduces levels of Alzheimer's disease β -amyloid peptides A β 42 and A β 40 in vitro and in vivo. *Proc. Natl.*

- Acad. Sci.* **98**, 5856–5861 (2001).
20. Petersen, R. C. *et al.* Aging, Memory, and Mild Cognitive Impairment. *Int. Psychogeriatrics* **9**, 65–69 (1997).
 21. Crick, P. J. *et al.* Quantitative charge-tags for sterol and oxysterol analysis. *Clin. Chem.* **61**, 400–11 (2015).
 22. Dickson, A. *et al.* HSD3B1 is an Oxysterol 3 β -Hydroxysteroid Dehydrogenase in Human Placenta. *bioRxiv* 2022.04.01.486576 (2022) doi:10.1101/2022.04.01.486576.
 23. Uhlen, M. *et al.* Tissue-based map of the human proteome. *Science* (80-.). **347**, (2015).
 24. Heverin, M. *et al.* Changes in the levels of cerebral and extracerebral sterols in the brain of patients with Alzheimer's disease. *J. Lipid Res.* **45**, 186–193 (2004).
 25. Testa, G. *et al.* Changes in brain oxysterols at different stages of Alzheimer's disease: Their involvement in neuroinflammation. *Redox Biol.* **10**, 24–33 (2016).
 26. Murphy, R. C. & Johnson, K. M. Cholesterol, reactive oxygen species, and the formation of biologically active mediators. *J. Biol. Chem.* **283**, 15521–5 (2008).
 27. Schroepfer, G. J. Oxysterols: modulators of cholesterol metabolism and other processes. *Physiol. Rev.* **80**, 361–554 (2000).
 28. Brown, A. J. 24(S),25-Epoxycholesterol: A messenger for cholesterol homeostasis. *Int. J. Biochem. Cell Biol.* **41**, 744–747 (2009).
 29. Radhakrishnan, A., Ikeda, Y., Kwon, H. J., Brown, M. S. & Goldstein, J. L. Sterol-regulated transport of SREBPs from endoplasmic reticulum to Golgi: Oxysterols block transport by binding to Insig. *Proc. Natl. Acad. Sci.* **104**, 6511–6518 (2007).
 30. Laffitte, B. A. *et al.* LXRs control lipid-inducible expression of the apolipoprotein E gene in macrophages and adipocytes. *Proc. Natl. Acad. Sci.* **98**, 507–512 (2001).
 31. Hong, C. & Tontonoz, P. Liver X receptors in lipid metabolism: opportunities for drug discovery. *Nat. Rev. Drug Discov.* **13**, 433–444 (2014).
 32. Repa, J. J. *et al.* Regulation of Absorption and ABC1-Mediated Efflux of Cholesterol by RXR Heterodimers. *Science* (80-.). **289**, 1524–1529 (2000).
 33. Bradley, M. N. *et al.* Ligand activation of LXR β reverses atherosclerosis and cellular cholesterol overload in mice lacking LXR α and apoE. *J. Clin. Invest.* **117**, 2337–2346 (2007).
 34. Burkard, I., von Eckardstein, A., Waeber, G., Vollenweider, P. & Rentsch, K. M. Lipoprotein distribution and biological variation of 24S- and 27-hydroxycholesterol in healthy volunteers. *Atherosclerosis* **194**, 71–78 (2007).
 35. Brown, A. J. & Jessup, W. Oxysterols and atherosclerosis. *Atherosclerosis* **142**, 1–28 (1999).
 36. Jenner, A. M. *et al.* The effect of APOE genotype on brain levels of oxysterols in young and old human APOE ϵ 2, ϵ 3 and ϵ 4 knock-in mice. *Neuroscience* **169**, 109–115 (2010).

Chapter 5: The profiling of sterols in multiple sclerosis brain tissue

5.1. Introduction

Multiple sclerosis is an autoimmune, demyelinating and neurodegenerative disease of the CNS, characterised by an extensive loss of myelin (demyelination) accompanied by chronic inflammation¹. Myelin is a structure made up of proteins and lipids, one of the most abundant being cholesterol, and is produced in the CNS from oligodendrocyte cells to encompass the axonal length of a nerve cell, allowing efficient signal transduction to occur between neurons and their targets².

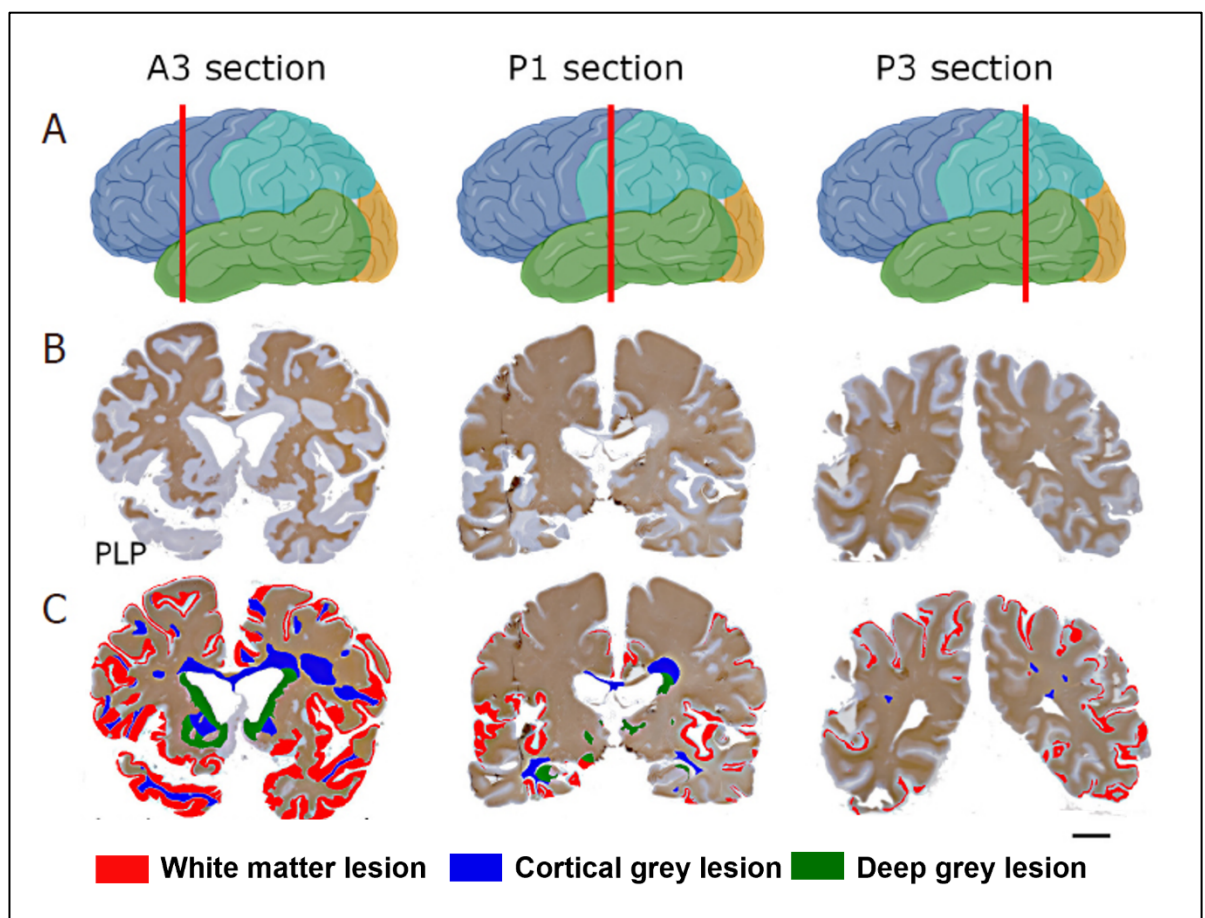


Figure 5.1. The vast number and types of lesions present in a multiple sclerosis brain. Whole coronal sections of progressive multiple sclerosis brain highlight the extensive demyelination in the white, cortical grey and deep grey matter regions across the whole brain using proteolipid protein (PLP – myelin marker) immunohistochemical staining (scale bar = 2cm) – taken with permission from Griffiths et al, 2020³.

The demyelination of the axons within multiple sclerosis creates lesions in the grey and white matter of the brain and spinal cord, resulting in affected neurotransmission and an increased propensity for the underlying nerve cells to degenerate. Damaged

myelin membranes are phagocytosed by activated microglial cells, the resident immune cells of the CNS⁴ and by infiltrating monocytes that enter the CNS across the BBB. These lesions can vary in size and occur within all different regions of the CNS (see Figure 5.1), which, in conjunction with the large amounts of pathology seen in the non-lesioned regions of the brain including neuronal and axonal injury, compromise signal transduction along the axon and add to the diffuse global pathology seen in long-standing multiple sclerosis⁵.

The non-lesioned areas of the brain, also called the normal-appearing tissue as macroscopically it seems unaffected in comparison to the demyelinated areas, is also acutely abnormal⁶⁻⁸. This normal-appearing brain tissue is histologically and biochemically different with, for example, increased lysosomal enzyme damage, altered properties of both axons and myelin alongside extensive axon and myelin degeneration, perivascular inflammation and astrocyte activation^{8,9}.

This pathology in both the lesioned and non-lesioned areas correspond to the complex symptomology experienced by the individual. The symptoms of multiple sclerosis can vary widely, depending on where the lesion lies within the brain, how many and how large the lesions are, the relative extent of normal-appearing tissue pathology and the extent of neuro- and axonal- loss. Common symptoms include cognitive impairment, severe fatigue, muscle weakness and spasticity, optical disturbances and incontinence¹⁰.

Multiple sclerosis can present in several forms with the most common being relapsing remitting (RRMS), characterised by periods of acute worsening of neurological function, followed by either partial or complete recovery¹¹. Progressive disease is generally associated with increased and progressive neurological disability over time^{12,13}. There are two types of progressive disease; secondary progressive (SPMS) which commonly follows RRMS, or primary progressive (PPMS), which happens without the initial relapsing stage, where individuals experience a gradual worsening of disability and neurological function from onset¹¹. During progressive disease, there is increased cortical demyelination and atrophy, substantial axonal and neuronal injury and loss, a widespread inflammatory phenotype throughout the brain from activated microglia/macrophage cells and increasing cognitive dysfunction¹⁴⁻¹⁶. Due to the very limited treatment options for progressive disease, the disease progresses with the gradual worsening of life-changing disability.

Multiple sclerosis risk is complex and is best viewed as an interplay of one or more genetic and/ or environmental/ life-style factors. For example, smoking, exposure to Epstein-Barr virus (EBV) and vitamin D deficiency¹⁷ are known risk factors. In relation to vitamin D, several genetic susceptibilities have been reported within the sterol pathway of Vitamin D₃. Specific genes linked to cholesterol including DHCR7, CYP27A1 and CYP27B1 have all been identified as factors increasing the risk of being diagnosed with multiple sclerosis¹⁸.

In recent years, cholesterol and its derivatives have been highlighted in many neurodegenerative and neurological conditions as being significant in disease biochemistry, showing altered levels of various oxysterols (oxygenated cholesterol derivatives) in disease compared to healthy controls^{19–22}. In multiple sclerosis, cholesterol synthesis and regulation is important due to the vast amount of cholesterol found in myelin (~30% of total myelin makeup²³), with cholesterol being the rate-limiting compound for myelin membrane formation²⁴. Those related pathways and metabolites are associated with several pathological and immunological processes, which are disease hallmarks of multiple sclerosis, with the demyelination and axonal degradation witnessed in disease affecting cholesterol concentration within the brain²⁵. The significant neurodegeneration witnessed in later disease stages means a depletion of CYP46A1²⁶. This enzyme is almost exclusively expressed in neuronal cells and aids the conversion of the cerebrosterol 24S-hydroxycholesterol, an oxysterol which is permeable to the BBB and one of the major pathways for the efflux of cholesterol from the CNS²⁷.

The cholesterol from myelin degradation is usually ingested by microglia/ macrophage cells. When activated these cells highly express *CH25H*, which codes for the enzyme to produce 25-hydroxycholesterol (25-HC). This oxysterol has been linked to the production of lipid droplets via SOAT1 and promotion of macrophage foam cell formation (macrophages that are lipid laden with cholesterol), which have been observed during the preparation of post-mortem tissue^{28–30}. These foamy cells have been reported to cause a pro-inflammatory response and promote multiple sclerosis disease progression; firstly by internalising the myelin debris and presenting this as an antigen to autoreactive T-cells^{30,31}, as well as being toxic to the myelin-laden macrophage itself³². Other evidence suggests high levels of 25-HC could indicate a more severe disease course in other autoimmune diseases such as atherosclerosis^{33,34}. However, some studies have shown altering the regulation of

CH25H and subsequent production of 25-HC helps to regulate inflammatory responses in macrophage cells and experimental autoimmune encephalomyelitis (EAE) mouse models, with increased 25-HC levels suppressing interleukin-1-driven inflammation³⁵ and *CH25H* knock-out mice overproducing IL-1 β in response to a pathogen³⁶. This suggests 25-HC is required for a normal inflammatory response. Another oxysterol thought to be important within the immune response is (25R)26-HC, more commonly referred to as 27-HC. The enzyme responsible for its synthesis, CYP27A1 – also linked with vitamin D deficiency¹⁸ – is again highly expressed in macrophage cells, with increased levels in the CNS being linked to a defective BBB^{37,38} which has been suggested in multiple sclerosis³⁹. It has also been linked with promoting atherosclerosis, another inflammatory condition, through upregulation of proinflammatory mechanisms⁴⁰ and is known to block post-synaptic signalling, cause apoptosis and neurodegeneration³⁷. Although a lot of the research into oxysterols and multiple sclerosis focus on the pro-inflammatory involvement and neuronal loss, several research studies have also highlighted the importance these sterol synthesis pathways have on the regulation of neuroprotective mechanisms in disease, such as the remyelination repair process. New therapies targeting the regulation of cholesterol-linked pathways including retinoid X receptors (RXRs), mitogen-activated protein (MAP) kinase and peroxisome proliferator-activated receptor (PPAR) are being investigated as a possible alternative treatment to disease modifying therapies (DMTs)^{41–44} by promoting remyelination, with one study highlighting how an increase in dietary cholesterol promoted remyelination in mouse models of disease⁴⁵.

5.1.1. Aims

The aims of this study were to analyse levels of oxysterols from brain tissue samples directly using homogenisation methods and liquid chromatography-mass spectrometry. We would use this data to explore possible alterations in sterol concentration in primary and secondary progressive multiple sclerosis and control brain tissue and analyse whether there are differences between disease and controls groups to learn more about the role of cholesterol and its metabolites in progressive multiple sclerosis.

5.2. Materials and Methods

5.2.1. Multiple sclerosis brain tissue cohort

The sample set for this study consisted of snap-frozen human brain tissue from both progressive multiple sclerosis (n=16) and control (n=5) tissue blocks, which were shipped using dry ice, still frozen on arrival. For the multiple sclerosis cohort, there were three cases with two tissue blocks, therefore the total case number was 13. The tissue analysed was collected from cryostat cuttings, with the weight of tissue ranging from 10 to 260mg. The disease tissue blocks used within this study were provided by the UK Multiple Sclerosis Tissue Bank, Imperial College London, with appropriate ethical approval (08/MRE09/31+5).

The control tissue blocks were acquired from Oxford University with appropriate research ethics committee approval (13/WA/092).

The multiple sclerosis cohort consisted of ten females and three males, and control cases consisted of two females and three males. The details of these cases are highlighted in Table 5.1 (page 143). For quality control purposes, control mouse brain tissue was also processed alongside each batch of eight samples, which was provided by Cardiff University, with the animals killed by schedule 1 under license. Brain tissue sections corresponding to the homogenates were cut at 10 µm thickness and immunohistochemically stained to identify pathological regions of interest within the brain tissue. Myelin oligodendrocyte glycoprotein (MOG) was used to identify lesions, and co-staining of the microglia/ macrophage marker human leukocyte antigen (HLA) and myelin chemical stain Luxol Fast Blue (LFB) was used to identify immunopathological regions in the tissue (see example in Figure 5.2). All staining within this thesis was performed by PhD student Kristen Hawkins of Swansea University.

5.2.2. Brain tissue homogenisation, extraction, and sample preparation

For homogenisation, tissue was placed into Precellys soft tissue homogenisation 2 mL tubes with 1.4 mm ceramic beads. The tissue was homogenised in an EtOH-internal standard mix to extract maximum sterol amount collecting a total of 4.2 mL of 100% EtOH supernatant in four 1.0 5mL increments and transferred to a 15 mL tube, which was diluted to 6 mL at 70% EtOH.

For extraction, 600 μL of solution (i.e., 10% of the extract) was added to absolute EtOH dropwise under sonification, then diluted to 70% EtOH (see section 2.2.3 – Multiple sclerosis for details). The solution underwent solid phase extraction (SPE) followed by enzyme-assisted derivatisation with Girard-P reagent before a final SPE which generates the MeOH sterol-containing eluents (see section 2.2.4 for details). The eluted samples were diluted and processed at 60% MeOH, injecting 35 μL of sample into a Dionex Micro HPLC system coupled with an Orbitrap Elite mass spectrometer (see section 2.2.10 for more details), where a 17-minute run was used to quantify all data displayed in this chapter.

5.2.3. Oxysterol analysis

The quantification of oxysterols was carried out using mass spectrometry software Xcalibur from Thermo-Fisher. All oxysterols were quantified against the [$^2\text{H}_7$]24R/S-hydroxycholesterol ([$^2\text{H}_7$]24R/S-HC) internal standard. Once derivatised [$^2\text{H}_7$]24R/S-HC has proved to be an acceptable surrogate for the quantification of oxysterols in general⁴⁶. Other sterols were quantified against [$^2\text{H}_7$] cholesterol. The [$^2\text{H}_7$]22R-hydroxycholest-4-en-3-one standard was used to quantify oxysterols that had a natural 3-oxo group. For the full ITMS³ fragmentation spectra for each oxysterol, refer to Table 9.1 in the Appendix.

For the three cases that had multiple tissue blocks, the data was averaged per case. Concentrations of all sterols are given in ng/ μg of cholesterol, after normalising all quantified data to the μg of cholesterol present per sample.

The rationale behind the cholesterol normalisation stems from the concern over the accuracy of the tissue weight. The tissue obtained for this study came from 10 μm thick cryostat shavings from blocks of snap frozen post-mortem tissue and not from a predetermined dissected piece as used in Chapter 4 (see section 4.2.1 for details) due to the rarity of the human multiple sclerosis tissue and the availability we had specific to blocks used for sectioning and histochemical staining. Cryo-sectioned tissue unavoidably becomes coated with condensation from air, resulting in an increase of the actual mass measured. Each tissue block sampled has varying degrees of pathology, made up of different percentages of white and grey matter, lesioned and non-lesioned tissue, with some containing active inflammation. Therefore, the normalisation to cholesterol aimed to reduce the concern regarding inaccuracies in

the quantified levels of oxysterols based on imprecise weight by normalising to an internal factor. For this purpose, we assumed cholesterol did not change between disease and control as we were unable to relatively quantify the levels in tissue without the mass, which admittedly is a weakness of this study.

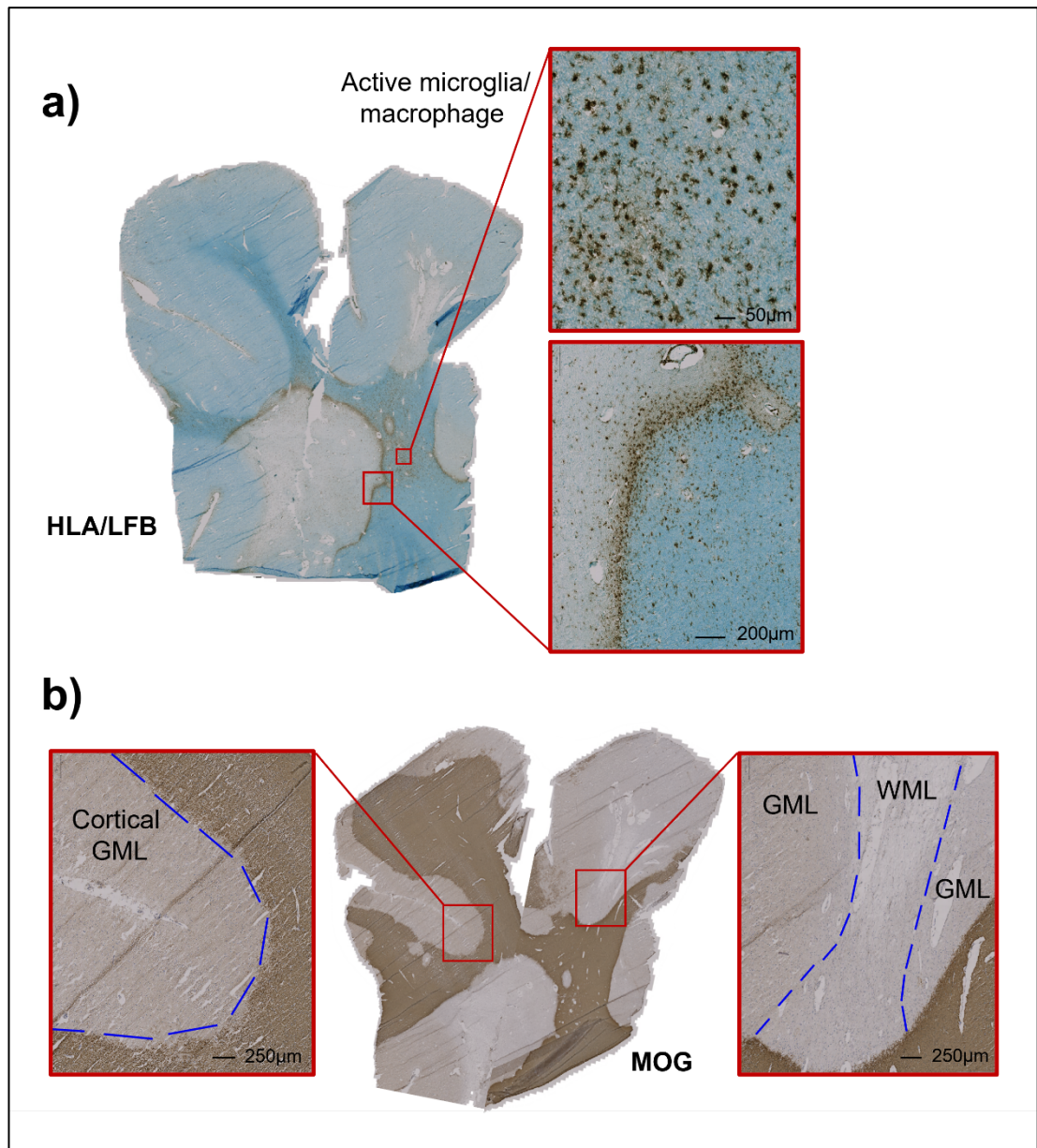


Figure 5.2. Chronic active inflammation and extensive demyelinating pathologies witnessed in the multiple sclerosis disease course. Case MS513 block A3A3 from this cohort highlights cortical grey (GML) and white matter lesioned (WML) areas with MOG antibody-stained tissue. Inflammation highlighted with HLA immunostained section dually stained with Luxol Fast Blue (LFB).

Table 5.1. Demographics of the multiple sclerosis and control brain sample cohort. A list of all clinical details obtained for the multiple sclerosis and control human brain samples. (MS – multiple sclerosis; NP – control; F – female; M – male; PMD – post-mortem delay; DD – disease duration; SPMS – secondary progressive; PPMS – primary progressive; U – unknown; TTP – time to progressive; TTW – time to wheelchair).

Case	Sex	Age	PMD (hrs)	Cause of death	MS Subtype	DD (yrs)	TTP (yrs)	TTW (yrs)
MS402	M	46	12	Bronchopneumonia, MS	SPMS	20	9	7
MS407	F	44	22	Septicaemia, pneumonia	SPMS	19	11	10
MS422	M	58	25	Chest infection, MS	SPMS	23	U	U
MS423	F	54	10	Pneumonia	SPMS	30	21	18
MS438	F	53	17	MS	SPMS	18	U	14
MS473	F	39	9	Bronchopneumonia, MS	PPMS	13	10	6
MS485	F	57	24	Bronchopneumonia, MS	PPMS	29	29	23
MS491	F	64	9	Anaphylactic reaction	SPMS	26	U	U
MS492	F	66	15	Sigmoid cancer	PPMS	31	31	9
MS510	F	38	19	Pneumonia, MS	SPMS	22	15	15
MS513	M	51	17	Respiratory failure, MS	SPMS	18	15	14
MS541	F	68	< 24	MS	SPMS	49	32	37
MS543	F	66	< 24	MS	SPMS	40	32	20
NP13/128	M	68	48	Cardiac arrest	-	-	-	-
NP13/012	F	60	48	Metastatic breast cancer	-	-	-	-
NP13/011	F	62	24	Metastatic colorectal cancer	-	-	-	-
NP13/127	M	60	30	Cardiac arrest	-	-	-	-
NP13/126	M	56	40	Cardiac arrest	-	-	-	-

5.2.4. Statistical analysis

The statistical analysis was carried out using GraphPad Prism 7 analysis software. As the data did not follow Gaussian distribution (see full normality test results in Appendix Table 9.4), all analysis was performed using the appropriate non-parametric Mann-Whitney U test. The level of statistical significance was as indicated:

* $P < 0.05$, ** $P < 0.005$; *** $P < 0.0005$; **** $P < 0.0001$.

A ROUT outlier test was performed to identify outliers from nonlinear regression (maximum desired false discovery rate (Q) set at 1%). The Bartlett's test was used to interpret the variance within the cohort.

5.3. Results

The cohort of tissue used during this study was representative of the varying pathologies found in progressive multiple sclerosis. Cases presented with extensive demyelination within the grey and white matter, associated with active/inactive lesion edges, and areas with high levels of inflammation in the normal-appearing tissue with myelin-laden macrophage cells present (Figure 5.2).

5.3.1. Confirmation of the presence of 25- and (25R)26-hydroxycholestenone in multiple sclerosis and control human brain tissue.

As we reported in the previous chapter (Chapter 4), the presence of both 25-HCO and (25R)26-HCO with an endogenous 3-oxo group was observed in the human brain tissue homogenates at m/z 534.4054 \pm 5 ppm.

Within this study, we establish the presence of both metabolites in the disease and control brain tissue, however the levels were undetectable in some of the samples analysed due to the small amounts of brain tissue homogenised (see Figure 5.3).

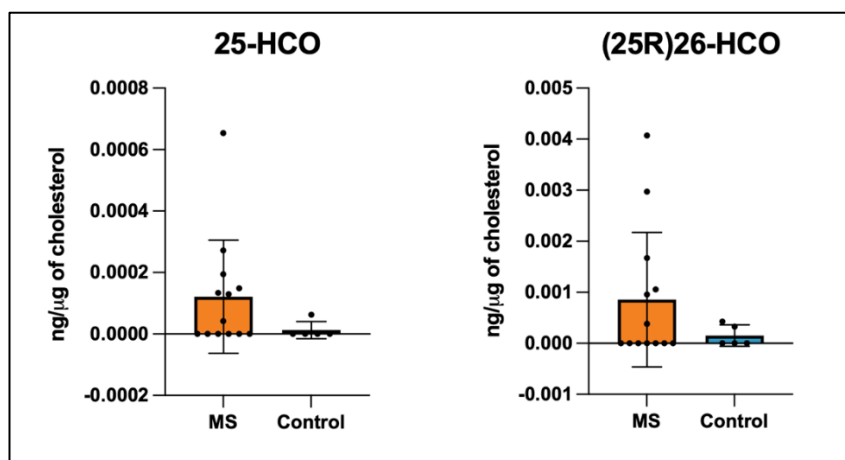


Figure 5.3. Concentrations of 25- and (25R)26-hydroxycholestenone relatively quantified from human multiple sclerosis and control brain tissue. All plots display the mean value per group with SD.

Overall, both the levels of 25-HCO and (25R)26-HCO were higher in multiple sclerosis tissue compared with control, however neither showed significant differences. Although we do not see significance between the groups, it should be noted that we do observe the same multiple sclerosis cases give elevated levels of both 25-HCO and (25R)26-HCO.

5.3.2. Analysis of 24S-HC, 25-HC and (25R)26-HC

The monohydroxycholesterol metabolites are the oxysterols most reported on in multiple sclerosis, specifically 24S-HC, which we identified at m/z 539.4363 \pm 5 ppm (see Figure 5.4 b & c). Within this study we found no significant difference within 24S-HC analyses, however the level was lower in the disease group compared with control brain (see Figure 5.5). There was significance with its counterpart, 24R-HC, but with the reverse trend showing the level increased in the multiple sclerosis group compared with the control group ($P=0.0268$).

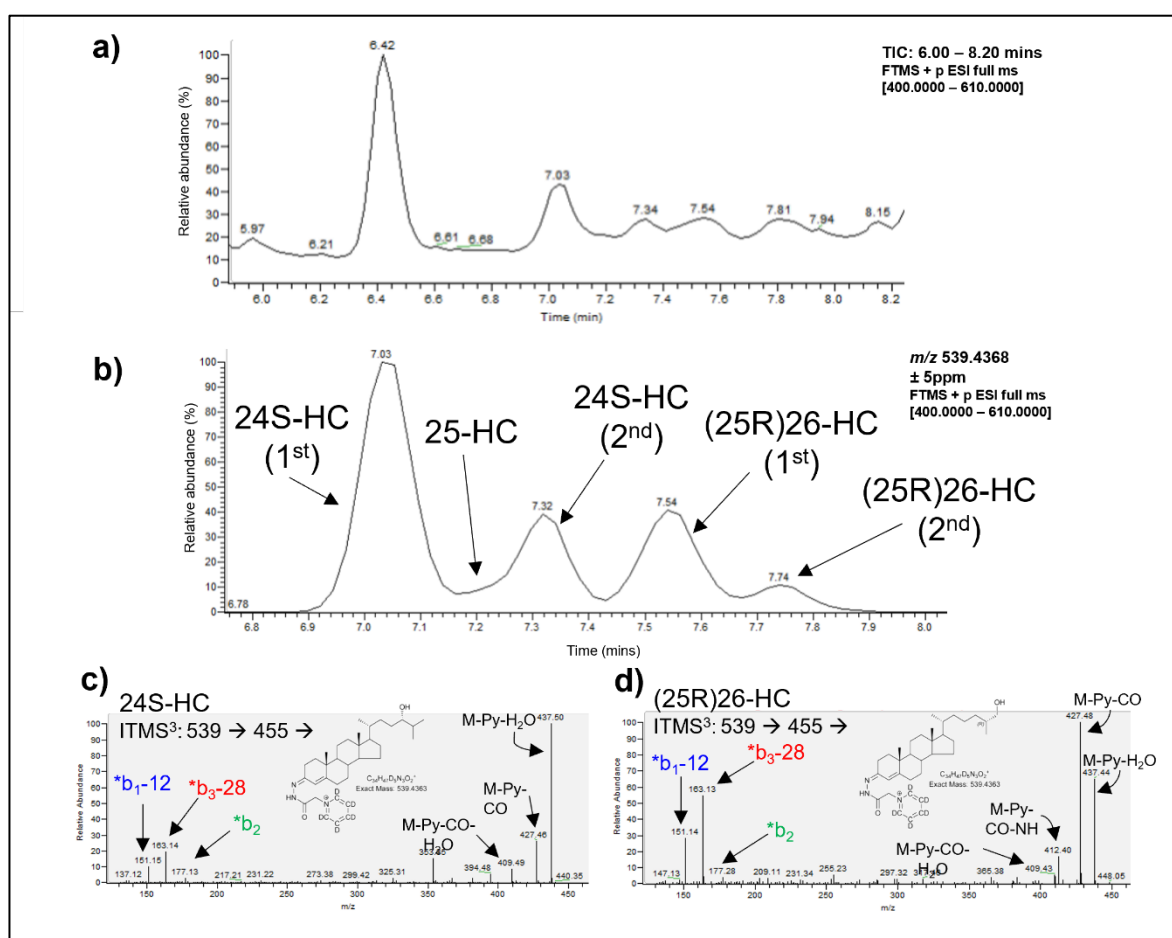


Figure 5.4. A chromatogram of monohydroxycholesterols at m/z 539.4363 \pm 5 ppm from multiple sclerosis brain tissue using long gradient LC MS³. a) Total ion count (TIC) spectra from sample MS423 between 6 and 8.2 minutes. b) LCMS chromatogram at m/z 539.4368 from sample MS423 showing 24S-HC, 25-HC and (25R)26-HC. c) ITMS³ fragmentation spectra of 24S-HC. d) ITMS³ fragmentation spectra of (25R)26-HC. The primary fragments from ITMS³ relate back to structure (f) in Figure 2.5. Structural images of oxysterols taken with permission from Griffiths et al, 2016⁴⁷.

The 25-HC, also a widely reported oxysterol within multiple sclerosis disease, did show an average increase in disease compared with control, however this observation was not significant (see Figure 5.5).

(25R)26-HC, which has been reported in several other neurodegenerative diseases as showing altered levels compared with controls, showed a significant increase in multiple sclerosis brain tissue in comparison to the control tissue, even after the removal of an outlying datapoint identified from the ROUT outlier test ($P=0.0136$). We looked at the ratio of 24S-HC to (25R)26-HC and found ratios were significantly decreased in the multiple sclerosis grouping compared with the control cohort ($P=0.0365$), suggesting impaired levels of both analytes in progressive multiple sclerosis (see Figure 5.5).

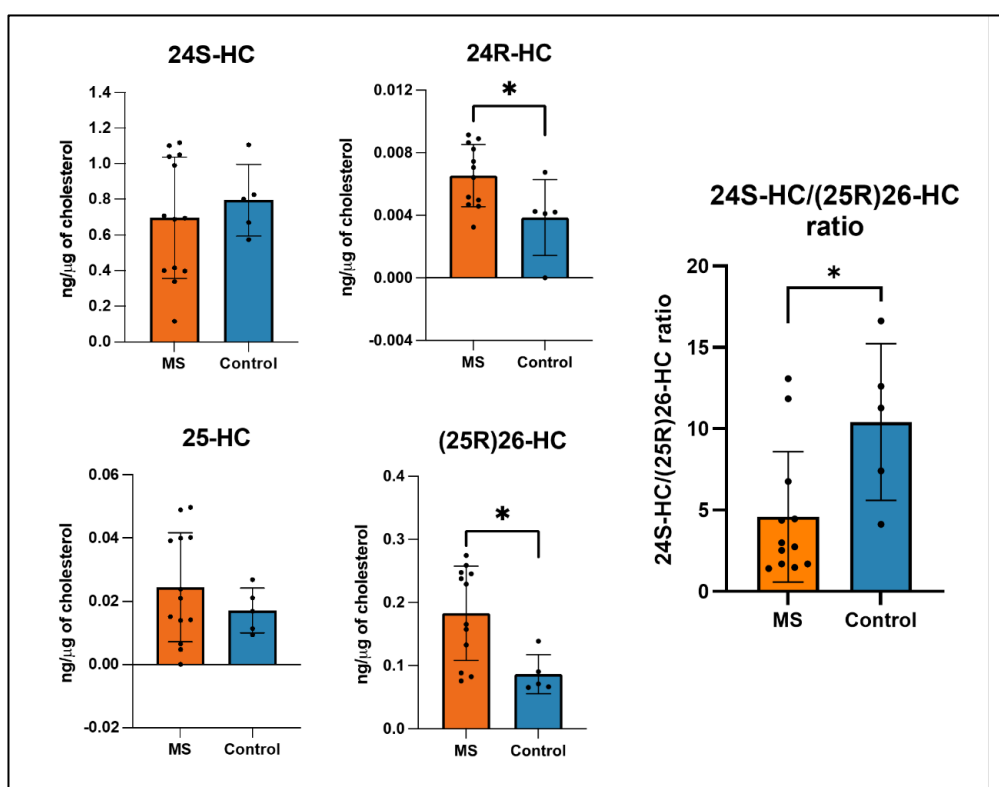


Figure 5.5. Analysis of monohydroxycholesterols shows significance in (25R)26-HC and 24R-HC. The graphs plotting the data of 24S-HC, 24R-HC, 25-HC, (25R)26-HC and the ratio between 24S-HC and (25R)26-HC in MS and control brain tissue homogenates. A single outlier point has been removed from the multiple sclerosis data set for (25R)26-HC. All plots above display mean values with SD.

5.3.3. Analysis of other monohydroxycholesterols of interest

In addition to the previously discussed oxysterols in this chapter, there are several other sterols that were quantified within this study including 7α -HC, 7β -HC, 7-OC and 6β -HC, quantified using FTMS spectra using their exact mass (m/z 539.4368 ± 5 ppm for 7α -HC, 7β -HC and 6β -HC, and m/z 534.4054 ± 5 ppm for 7-OC).

Both the concentrations of 7β -HC and 7α -HC were found to be significantly increased in the multiple sclerosis brain tissue compared with control ($P=0.0380$ and $P=0.0133$ respectively; - see Figure 5.6 a). This significant value was after the removal of outlying datapoints by the ROUT test.

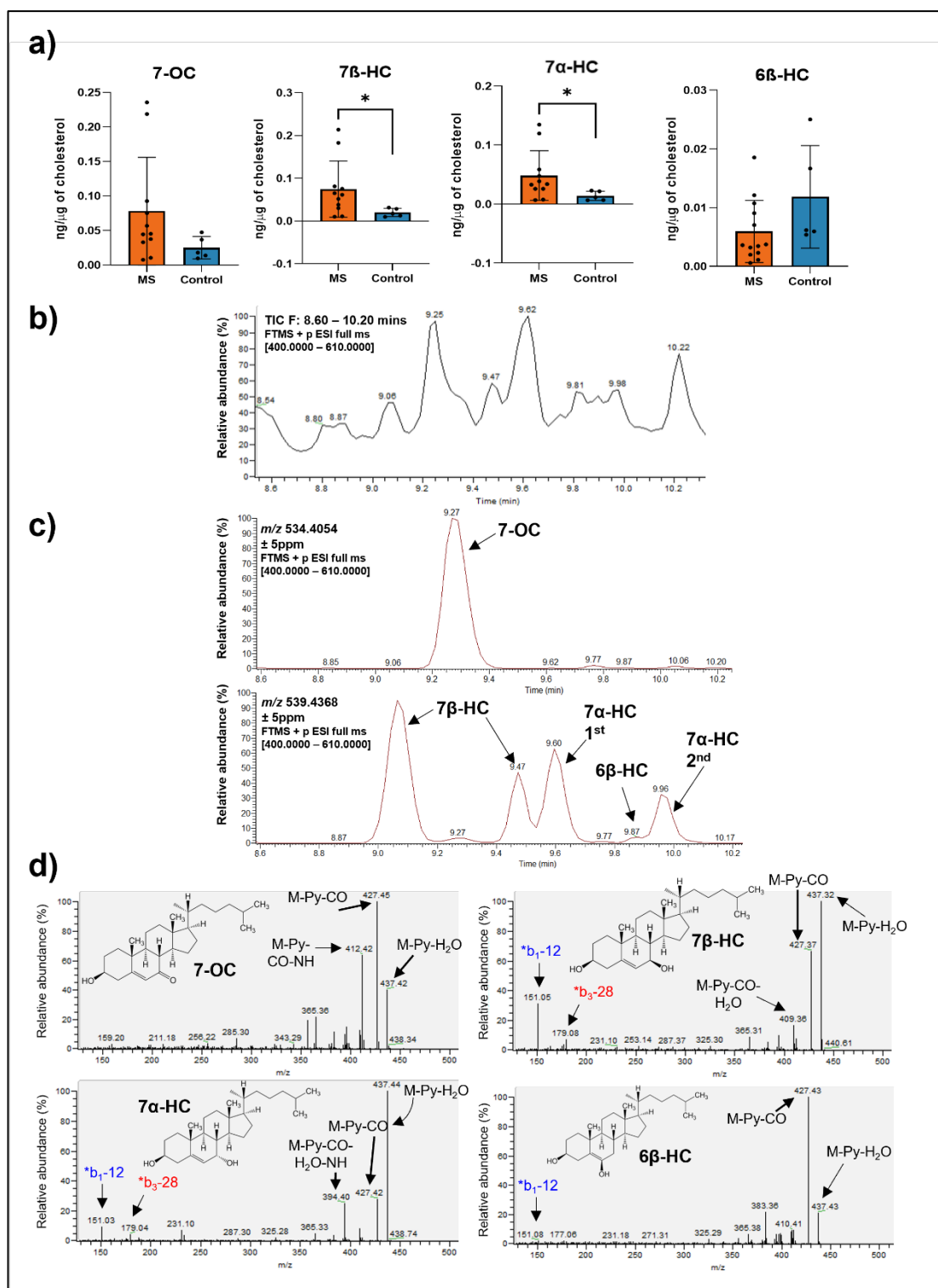


Figure 5.6. A significant difference in the levels of 7 β -HC and 7 α -HC quantified from multiple sclerosis and control brain tissue. a) The data graphs plotting 7-OC, 7 β -HC, 7 α -HC and 6 β -HC, with 7 β -HC and 7 α -HC showing significant differences (plots show mean value with SD). b) A TIC FTMS spectra between 8.6 and 10.2 minutes. c) The LCMS chromatogram at m/z 534.4054 and 539.4368 for sample MS423. d) The labelled ITMS³ spectra for 7-OC, 7 β -HC, 7 α -HC and 6 β -HC. All plots above display average values with SD. Primary fragments relate back to structure (f) in Figure 2.5.

The analysis of 7-OC showed the same relationship as both 7 β -HC and 7 α -HC, with increased concentrations in disease compared to control, however no significance was observed (see Figure 5.6). The levels of 6 β -HC were also quantified within the homogenate samples which showed an inverse relationship compared to the other three metabolites, with increased concentrations in control compared with multiple sclerosis. Again, no significance was observed.

5.3.4. The quantification of other sterol molecules, dihydrocholesterols and cholestenic acid metabolites.

There were several other sterols that were quantified from the brain tissue homogenates which showed trends between disease and control samples but did lack significance between the datasets, which includes 24S,25-EC, 3 β -HCA and 7 α ,26-diHC (see Figure 5.7). Most of these metabolites quantified from the brain homogenate data did show the same trend, where levels were slightly increased in the multiple sclerosis brain tissue in comparison to the control, with the exception of 7 α ,25-diHC which was significantly decreased in disease after outlier exclusion ($P=0.0070$).

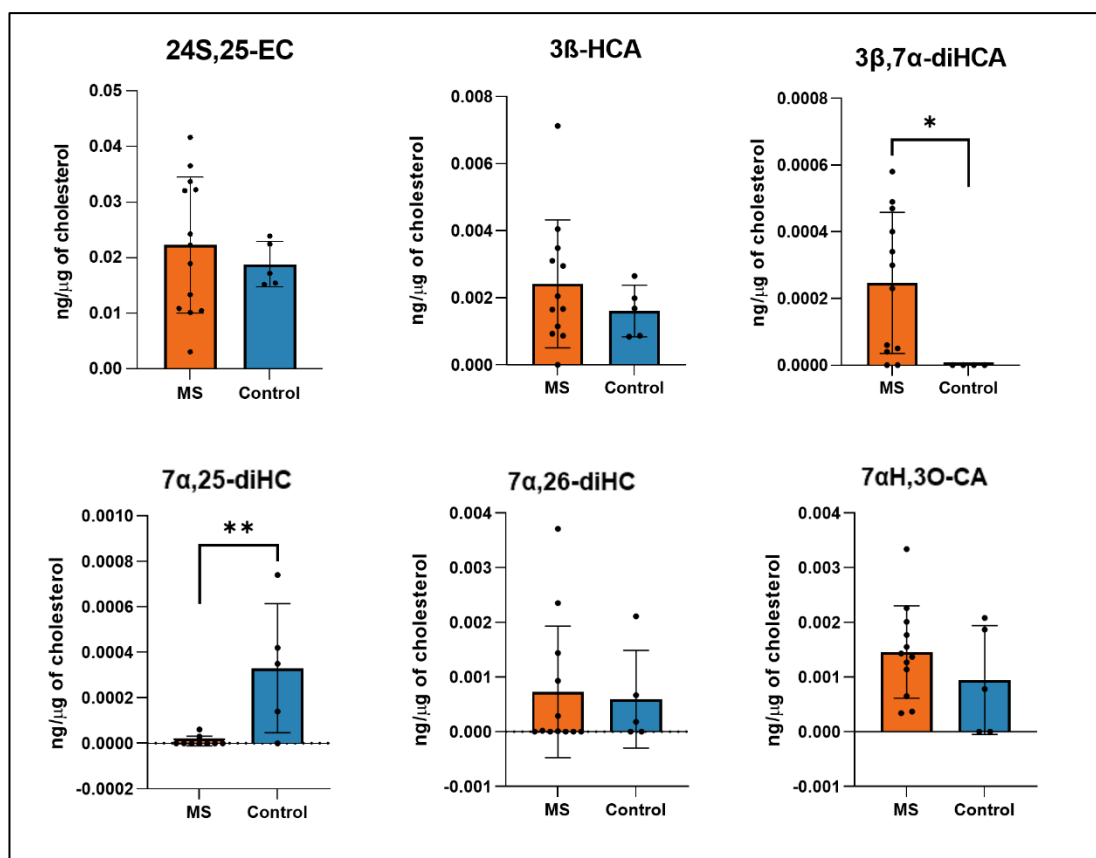


Figure 5.7. Concentrations of other sterol metabolites showed trends but no significance. All plots above display mean values with SD.

Another significant finding was the increased level of 3 β ,7 α -diHCA in the multiple sclerosis group after the exclusion of outlying data points ($P=0.0148$). All other metabolites showed no significance (see Figure 5.7).

After cholesterol oxidase and GP-tagging					Mean concentration (ng/μg of cholesterol ± SD)	
Mass (± 5 ppm)	Sterol/ Oxysterol Systematic name	Sterol/ Oxysterol Common name	Abbreviation	MS brain tissue (n=13)	Control brain tissue (n=5)	
523.4414	(GP ^[2]H₅]) Cholest-4-en-3-one	Cholesterol	-	3790.79±4033.59	477.05±184.81	
537.4206	(GP ^[2]H₅]) 24S,25-Epoxycholest-4-en-3-one	24S,25-Epoxycholesterol/ 24-oxocholesterol	24S,25-EC/ 24-OC	0.022±0.012	0.019±0.004	
534.4054	(GP ^[2]H₀]) 25-Hydroxycholest-4-en-3-one	25-Hydroxycholestenone	25-HCO	0.0001±0.0001*	ND	
534.4054	(GP ^[2]H₀]) (25R)26-Hydroxycholest-4-en-3-one	(25R)26-Hydroxycholestenone	(25R)26-HCO	0.001±0.001	0.0002±0.0002*	
534.4054	(GP ^[2]H₀]) 3β-Hydroxycholest-5-en-7-one	7-Oxocholesterol	7-OC	0.078±0.078	0.025±0.016	
539.4363	(GP ^[2]H₅]) 24S-Hydroxycholest-4-en-3-one	24S-Hydroxycholesterol	24S-HC	0.697±0.340	0.796±0.201	
539.4363	(GP ^[2]H₅]) 24R-Hydroxycholest-4-en-3-one	24R-Hydroxycholesterol	24R-HC	0.007±0.002	0.004±0.002	
539.4363	(GP ^[2]H₅]) 25-Hydroxycholest-4-en-3-one	25-Hydroxycholesterol	25-HC	0.024±0.017	0.017±0.007	
539.4363	(GP ^[2]H₅]) (25R)26-Hydroxycholest-4-en-3-one	(25R)26-Hydroxycholesterol	(25R)26-HC	0.183±0.075	0.087±0.031	
539.4363	(GP ^[2]H₅]) 7β-Hydroxycholest-4-en-3-one	7β-Hydroxycholesterol	7β-HC	0.075±0.066	0.020±0.010	
539.4363	(GP ^[2]H₅]) 7α-Hydroxycholest-4-en-3-one	7α-Hydroxycholesterol	7α-HC	0.048±0.042	0.014±0.008	
539.4363	(GP ^[2]H₅]) 6β-Hydroxycholest-4-en-3-one	6β-Hydroxycholesterol	6β-HC	0.006±0.005	0.012±0.009	
553.4155	(GP ^[2]H₅]) 3-Oxocholest-4-en-(25R)26-oic acid	3β-Hydroxycholestenic acid	3β-HCA	0.002±0.002	0.002±0.001	
550.4003	(GP ^[2]H₀]) 7α,25-Dihydroxycholest-4-en-3-one	7α,25-Dihydroxycholestenone	7α,25-diHCO	0.001±0.001	ND	
550.4003	(GP ^[2]H₀]) 7α,(25R)26-dihydroxycholest-4-en-3-one	7α,(25R)26-dihydroxycholestenone	7α,26-diHCO	0.005±0.003	0.003±0.002	

555.4312	(GP[² H ₅]) 7 α ,25-Dihydroxycholest-4-en-3-one	7 α ,25-Dihydroxycholesterol	7 α ,25-diHC	0.00001 \pm 0.00002**	0.0003 \pm 0.0003*
555.4312	(GP[² H ₅]) 7 α , (25R)26-Dihydroxycholest-4-en-3-one	7 α , (25R)26-Dihydroxycholesterol	7 α ,26-diHC	0.001 \pm 0.001	0.001 \pm 0.001
564.3796	(GP[² H ₆]) 7 α -Hydroxy-3-oxocholest-4-en-(25R/S),26-oic acid	7 α -hydroxy-3-oxocholest-4-en-(25R/S),26-oic acid	7 α H,3O-CA	0.001 \pm 0.001	0.001 \pm 0.001
569.4105	(GP[² H ₅]) 7 α -Hydroxy-3-oxocholest-4-en-(25R/S),26-oic acid GP-d5	3 β ,7 α -dihydroxycholest-5-en-(25R/S)26-oic acid	3 β ,7 α -diHCA	0.0004 \pm 0.0004*	ND

Table 5.2. Average values of cholesterol and oxysterols found in multiple sclerosis and control brain tissue homogenates in total cohort. The mean concentration of each oxysterol seen in each sample, with the standard deviation. HC = hydroxycholesterol; diHC = dihydroxycholesterol; CA = cholestenoic acid; diHCA = dihydroxycholestenoic acid. * = 4 d.p; ** = 5.d.p; ND = Not detectable. Cholesterol information in **bold** and values given in μ g.

5.4. Discussion

The aim of this study was to analyse the concentrations of different sterols within brain tissue samples from progressive multiple sclerosis and control individuals to look for any differences between the groups to better understand the association between cholesterol metabolism and multiple sclerosis pathology.

The multiple sclerosis tissue cohort in this study highlights the vast variability in pathology that can be seen in this disease. Although all cases were classified as progressive, the pathology in each case ranged from the extent of cortical lesion load and a remyelinating area seen in case MS510 to the presence of active/inactive white matter lesions and extensive cortical demyelination seen in case MS513. Another example includes in Figure 5.5, where although data looks to be ‘clustering’ on the graphs displayed, with a closer analysis there is no correlation between analytes with each data point from a different individual, with the individuality of peoples disease course recently been proven using single nuclei RNA sequencing⁴⁸. The difference in pathology reflects the variability in abundance of the different of sterols (Bartlett's test ($P < 0.0001$) - see Appendix Table 9.5) and demonstrates the value of fully characterising samples to help interpret analytical findings.

Although variability across the cohort was large, we have identified that 24R-HC, (25R)26-HC, 7 α -HC and 7 β -HC all showed significantly increased concentrations in multiple sclerosis brain compared with control.

The significant increase of (25R)26-HC in multiple sclerosis compared to control in brain tissue is in contrast to that reported in plasma samples from multiple sclerosis patients²⁵. However, our finding does agree with several papers analysing CSF from multiple sclerosis and control patients^{22,25,49} which show either an increase or significant increase in (25R)26-HC in multiple sclerosis CSF samples, with a disturbance in the blood brain barrier (BBB) and an associated efflux of (25R)26-HC cited as a possible reason for this^{50,51}.

This trend to an increase in (25R)26-HC is also seen in other neurodegenerative diseases. The Heverin study in 2004 showed a significant increase in (25R)26-HC in Alzheimer's disease (AD) patients in comparison to controls within frontal, occipital cortex and the basal ganglia⁵². These values were also normalised to μg of cholesterol as in our study, and were in the same range as our data⁵².

The Testa study in 2016 also showed a trend to increased (25R)26-HC in late AD (Braak stage IV-VI where significant neuronal loss and atrophy has occurred) in comparison to control¹⁹. Our 7 α -HC and 7 β -HC findings were also in agreement with the work of Testa et al¹⁹. However, it is important to consider that both 7 α -HC and 7 β -HC, as well as 7-OC and 6 β -HC (which is derived indirectly from 5,6-EC) can be formed by ex vivo oxidation in air⁵³.

Another interesting finding was the significant decrease of 7 α ,25-diHC levels in multiple sclerosis group compared with controls, which is the same trend seen between MCI and control in Chapter 4 with 7 α ,25-diHCO. 7 α ,25-diHC is a potent ligand of the EBI2 receptor, which has previously been implicated in immune cell function and multiple sclerosis. Previous literature has shown the activation of EBI2 can regulate B cell migration⁵⁴, with others showing EBI2 expression and 7 α ,25-diHC levels are increased in demyelinating lesions in the experimental autoimmune encephalomyelitis (EAE) multiple sclerosis model⁵⁵. The reduced 7 α ,25-diHC would suggest lower B cell migration in progressive multiple sclerosis, where new inflammatory attacks and waves of B cell infiltration to the brain are rare in comparison to early disease stages.

Although not significant, we also observed reduced 24S-HC concentrations in multiple sclerosis tissue compared with control. Neuronal loss in late disease multiple sclerosis is linked with cortical demyelination, which can be extensive, with our previous research showing that in some cases, up to 60% of the cortex can be demyelinated³. This loss of myelin and subsequent damage within the cortical layers would lead to the significant loss of neurons and therefore available CYP46A1, resulting in lower 24S-HC levels. Reduced 24S-HC is seen in other neurodegenerative disease^{26,56,57}. As previously discussed in the introduction of this chapter, neuronal loss seen in the latter stages of multiple sclerosis has been linked to a decrease of *CYP46A1* expression, the gene of the enzyme which converts excess cholesterol into 24S-HC in neuronal cells²⁶. The study of Leoni in 2002, also showed the link between the neurodegeneration and decreased levels of 24S-HC in plasma samples based on age groups, where older age groups who have had multiple sclerosis for longer would therefore have greater neuronal and CYP46A1 loss compared with younger age groups.

Our data also highlighted significant differences between the 24S/(25R)26-HC ratio in both groupings, with the progressive multiple sclerosis tissue cohort having a lower ratio compared with control tissue. Again, this could relate to the significant cortical pathology found in our cohort. Therefore, progressive disease results in a lower level of 24S-HC (neurodegeneration) and increased (25R)26-HC (BBB dysfunction), in comparison to control. The previously published data from other neurodegenerative diseases suggests the combination of both 24S-HC and (25R)26-HC concentrations gives a good indication of neurodegeneration within the brain, and with our results using multiple sclerosis tissue, we show it could be also true of late-stage progressive multiple sclerosis.

Our findings from this study of the altered sterol profiles in multiple sclerosis brain tissue leads to questions over whether this is the result of a gradual change due to the build-up of significant damage over time from the loss of important structures including myelin, axons, and neurons. If so, could this relate to other biomarkers of multiple sclerosis disease severity, such as neurofilament proteins in the CSF, which represent neuro-axonal loss⁵⁸, or the extent and distribution of lesions, which can be visualised by MRI. We would also be interested to know if individual oxysterol levels change after therapeutic treatments.

The pathology is incredibly varied across the tissue blocks in this cohort, with the homogenisation techniques carried out in the study unable to analyse specific pathological regions of interest individually. This means we cannot explicitly state if these altered profiles are a result of one pathology, or multiple pathological mechanisms combined. A future direction for this study could be to utilise novel mass spectrometry techniques on this tissue cohort to quantify oxysterols across intact tissue sections, such as liquid extraction for surface analysis (LESA) techniques⁵⁹. In addition to oxysterols, cholesterol is also hugely important in multiple sclerosis due to the vast amount of myelin lost throughout disease. As we were not able to look at cholesterol specifically in this chapter, we address the visualisation and quantification of cholesterol in these identified pathologies in a later chapter using novel imaging techniques with mass spectrometry⁶⁰ (Chapter 7 – The analysis of cholesterol in multiple sclerosis and Huntington’s disease brain tissue using mass spectrometry imaging).

5.5. References

1. Goldenberg, M. M. Multiple sclerosis review. *P T* **37**, 175–84 (2012).
2. Stadelmann, C., Timmler, S., Barrantes-Freer, A. & Simons, M. Myelin in the Central Nervous System: Structure, Function, and Pathology. *Physiol. Rev.* **99**, 1381–1431 (2019).
3. Griffiths, L. *et al.* Substantial subpial cortical demyelination in progressive multiple sclerosis: have we underestimated the extent of cortical pathology? *Neuroimmunol. Neuroinflammation* (2020) doi:10.20517/2347-8659.2019.21.
4. Lassmann, H. Multiple Sclerosis Pathology. *Cold Spring Harb. Perspect. Med.* **8**, a028936 (2018).
5. Kutzelnigg, A. *et al.* Cortical demyelination and diffuse white matter injury in multiple sclerosis. *Brain* **128**, 2705–2712 (2005).
6. Kolind, S. *et al.* Myelin water imaging reflects clinical variability in multiple sclerosis. *Neuroimage* **60**, 263–270 (2012).
7. Bodini, B. *et al.* Exploring the relationship between white matter and gray matter damage in early primary progressive multiple sclerosis: An in vivo study with TBSS and VBM. *Hum. Brain Mapp.* **30**, 2852–2861 (2009).
8. Elliott, C. *et al.* Abnormalities in normal-appearing white matter from which multiple sclerosis lesions arise. *Brain Commun.* **3**, (2021).
9. Allen, I. V. & McKeown, S. R. A histological, histochemical and biochemical study of the macroscopically normal white matter in multiple sclerosis. *J. Neurol. Sci.* **41**, 81–91 (1979).
10. Compston, A. & Coles, A. Multiple sclerosis. *Lancet* **372**, 1502–17 (2008).
11. Noseworthy, J. H., Lucchinetti, C., Rodriguez, M. & Weinshenker, B. G. Multiple sclerosis. *N. Engl. J. Med.* **343**, 938–952 (2000).
12. Lassmann, H., van Horssen, J. & Mahad, D. Progressive multiple sclerosis: pathology and pathogenesis. *Nat. Rev. Neurol.* **8**, 647–656 (2012).
13. Mahad, D. H., Trapp, B. D. & Lassmann, H. Pathological mechanisms in progressive multiple sclerosis. *Lancet Neurol.* **14**, 183–193 (2015).
14. Pitteri, M., Romualdi, C., Magliozzi, R., Monaco, S. & Calabrese, M. Cognitive impairment predicts disability progression and cortical thinning in MS: An 8-year study. *Mult. Scler.* **23**, 848–854 (2017).
15. Frischer, J. M. *et al.* Clinical and pathological insights into the dynamic nature of the white matter multiple sclerosis plaque. *Ann. Neurol.* **78**, 710–721 (2015).
16. Curti, E., Graziuso, S., Tsantes, E., Crisi, G. & Granella, F. Correlation between cortical lesions and cognitive impairment in multiple sclerosis. 1–8 (2018) doi:10.1002/brb3.955.
17. Olsson, T., Barcellos, L. F. & Alfredsson, L. Interactions between genetic, lifestyle and environmental risk factors for multiple sclerosis. *Nat. Rev. Neurol.* **13**, 25–36 (2017).
18. Scazzone, C., Agnello, L., Bivona, G., Lo Sasso, B. & Ciaccio, M. Vitamin D and Genetic Susceptibility to Multiple Sclerosis. *Biochem. Genet.* **59**, 1–30 (2021).
19. Testa, G. *et al.* Changes in brain oxysterols at different stages of Alzheimer's disease: Their involvement in neuroinflammation. *Redox Biol.* **10**, 24–33 (2016).
20. Grayaa, S. *et al.* Plasma oxysterol profiling in children reveals 24-hydroxycholesterol as a potential marker for Autism Spectrum Disorders.

- Biochimie* **153**, 80–85 (2018).
21. Björkhem, I., Patra, K., Boxer, A. L. & Svenningsson, P. 24S-Hydroxycholesterol Correlates With Tau and Is Increased in Cerebrospinal Fluid in Parkinson's Disease and Corticobasal Syndrome. *Front. Neurol.* **9**, (2018).
 22. Crick, P. J. *et al.* Reduced Plasma Levels of 25-Hydroxycholesterol and Increased Cerebrospinal Fluid Levels of Bile Acid Precursors in Multiple Sclerosis Patients. *Mol. Neurobiol.* **54**, 8009–8020 (2017).
 23. Morell, P. & Quarles, R. H. Characteristic Composition of Myelin. in *Basic Neurochemistry: Molecular, Cellular and Medical Aspects* (eds. Siegel, G. J., Agranoff, B. W., Albers, R. W., Fisher, S. K. & Uhler, M. D.) 81–82 (Lippincott-Raven, 1999).
 24. Saher, G. *et al.* High cholesterol level is essential for myelin membrane growth. *Nat. Neurosci.* **8**, 468–475 (2005).
 25. van de Kraats, C. *et al.* Oxysterols and cholesterol precursors correlate to magnetic resonance imaging measures of neurodegeneration in multiple sclerosis. *Mult. Scler. J.* **20**, 412–417 (2014).
 26. Leoni, V. *et al.* Changes in human plasma levels of the brain specific oxysterol 24S-hydroxycholesterol during progression of multiple sclerosis. *Neurosci. Lett.* **331**, 163–166 (2002).
 27. Dai, L. *et al.* Cholesterol Metabolism in Neurodegenerative Diseases: Molecular Mechanisms and Therapeutic Targets. *Mol. Neurobiol.* **58**, 2183–2201 (2021).
 28. Chang, T.-Y., Chang, C. C. Y., Ohgami, N. & Yamauchi, Y. Cholesterol Sensing, Trafficking, and Esterification. *Annu. Rev. Cell Dev. Biol.* **22**, 129–157 (2006).
 29. Gold, E. S. *et al.* ATF3 protects against atherosclerosis by suppressing 25-hydroxycholesterol-induced lipid body formation. *J. Exp. Med.* **209**, 807–817 (2012).
 30. Grajchen, E., Hendriks, J. J. A. & Bogie, J. F. J. The physiology of foamy phagocytes in multiple sclerosis. *Acta Neuropathol. Commun.* **6**, 124 (2018).
 31. Grau-López, L. *et al.* Myelin peptides in multiple sclerosis. *Autoimmun. Rev.* **8**, 650–653 (2009).
 32. Cantuti-Castelvetri, L. *et al.* Defective cholesterol clearance limits remyelination in the aged central nervous system. *Science (80-.).* **359**, 684–688 (2018).
 33. Li-Hawkins, J., Lund, E. G., Turley, S. D. & Russell, D. W. Disruption of the Oxysterol 7 α -Hydroxylase Gene in Mice. *J. Biol. Chem.* **275**, 16536–16542 (2000).
 34. Cyster, J. G., Dang, E. V., Reboldi, A. & Yi, T. 25-Hydroxycholesterols in innate and adaptive immunity. *Nat. Rev. Immunol.* **14**, 731–743 (2014).
 35. Reboldi, A. *et al.* 25-Hydroxycholesterol suppresses interleukin-1-driven inflammation downstream of type I interferon. *Science (80-.).* **345**, 679–684 (2014).
 36. Dang, E. V., McDonald, J. G., Russell, D. W. & Cyster, J. G. Oxysterol Restraint of Cholesterol Synthesis Prevents AIM2 Inflammasome Activation. *Cell* **171**, 1057-1071.e11 (2017).
 37. Zmysłowski, A. & Szterk, A. Oxysterols as a biomarker in diseases. *Clin. Chim. Acta* **491**, 103–113 (2019).
 38. Jiang, X. *et al.* Simvastatin Blocks Blood-Brain Barrier Disruptions Induced

- by Elevated Cholesterol Both In Vivo and In Vitro. *Int. J. Alzheimers. Dis.* **2012**, 1–7 (2012).
39. Cramer, S. P., Simonsen, H., Frederiksen, J. L., Rostrup, E. & Larsson, H. B. W. Abnormal blood-brain barrier permeability in normal appearing white matter in multiple sclerosis investigated by MRI. *NeuroImage Clin.* **4**, 182–189 (2014).
 40. Umetani, M. *et al.* The Cholesterol Metabolite 27-Hydroxycholesterol Promotes Atherosclerosis via Proinflammatory Processes Mediated by Estrogen Receptor Alpha. *Cell Metab.* **20**, 172–182 (2014).
 41. Natrajan, M. S. *et al.* Retinoid X receptor activation reverses age-related deficiencies in myelin debris phagocytosis and remyelination. *Brain* **138**, 3581–3597 (2015).
 42. Liu, P., Ying, Y. -s. & Anderson, R. G. W. Platelet-derived growth factor activates mitogen-activated protein kinase in isolated caveolae. *Proc. Natl. Acad. Sci.* **94**, 13666–13670 (1997).
 43. Chinetti, G. *et al.* PPAR- α and PPAR- γ activators induce cholesterol removal from human macrophage foam cells through stimulation of the ABCA1 pathway. *Nat. Med.* **7**, 53–58 (2001).
 44. Quinn, C. M., Jessup, W., Wong, J., Kritharides, L. & Brown, A. J. Expression and regulation of sterol 27-hydroxylase (CYP27A1) in human macrophages: a role for RXR and PPAR γ ligands. *Biochem. J.* **385**, 823–830 (2005).
 45. Berghoff, S. A. *et al.* Dietary cholesterol promotes repair of demyelinated lesions in the adult brain. *Nat. Commun.* **8**, 14241 (2017).
 46. Crick, P. J. *et al.* Quantitative charge-tags for sterol and oxysterol analysis. *Clin. Chem.* **61**, 400–11 (2015).
 47. Griffiths, W. J., Abdel-Khalik, J., Crick, P. J., Yutuc, E. & Wang, Y. New methods for analysis of oxysterols and related compounds by LC–MS. *J. Steroid Biochem. Mol. Biol.* **162**, 4–26 (2016).
 48. Macnair, W. *et al.* Single nuclei RNAseq stratifies multiple sclerosis patients into three distinct white matter glia responses. *bioRxiv* 2022.04.06.487263 (2022) doi:10.1101/2022.04.06.487263.
 49. Leoni, V. *et al.* Diagnostic use of cerebral and extracerebral oxysterols. *Clin. Chem. Lab. Med.* **42**, (2004).
 50. Leoni, V. *et al.* Side chain oxidized oxysterols in cerebrospinal fluid and the integrity of blood-brain and blood-cerebrospinal fluid barriers. *J. Lipid Res.* **44**, 793–799 (2003).
 51. Bjorkhem, I., Heverin, M., Leoni, V., Meaney, S. & Diczfalusy, U. Oxysterols and Alzheimer's disease. *Acta Neurol. Scand.* **114**, 43–49 (2006).
 52. Heverin, M. *et al.* Changes in the levels of cerebral and extracerebral sterols in the brain of patients with Alzheimer's disease. *J. Lipid Res.* **45**, 186–193 (2004).
 53. Griffiths, W. J. & Wang, Y. Oxysterols as lipid mediators: Their biosynthetic genes, enzymes and metabolites. *Prostaglandins Other Lipid Mediat.* **147**, 106381 (2020).
 54. Hannedouche, S. *et al.* Oxysterols direct immune cell migration via EBI2. *Nature* **475**, 524–527 (2011).
 55. Wanke, F. *et al.* EBI2 Is Highly Expressed in Multiple Sclerosis Lesions and Promotes Early CNS Migration of Encephalitogenic CD4 T Cells. *Cell Rep.* **18**, 1270–1284 (2017).

56. Teunissen, C. . *et al.* Decreased levels of the brain specific 24S-hydroxycholesterol and cholesterol precursors in serum of multiple sclerosis patients. *Neurosci. Lett.* **347**, 159–162 (2003).
57. Karrenbauer, V. D. *et al.* Plasma cerebrosterol and magnetic resonance imaging measures in multiple sclerosis. *Clin. Neurol. Neurosurg.* **108**, 456–460 (2006).
58. Giovannoni, G. Cerebrospinal fluid neurofilament: the biomarker that will resuscitate the ‘Spinal Tap’. *Mult. Scler. J.* **16**, 285–286 (2010).
59. Yutuc, E. *et al.* Localization of sterols and oxysterols in mouse brain reveals distinct spatial cholesterol metabolism. *Proc. Natl. Acad. Sci.* **117**, 5749–5760 (2020).
60. Angelini, R. *et al.* Visualizing Cholesterol in the Brain by On-Tissue Derivatization and Quantitative Mass Spectrometry Imaging. *Anal. Chem.* **93**, 4932–4943 (2021).

**Chapter 6 – The optimisation of an imaging
method to analyse cholesterol using AP-MALDI
mass spectrometry imaging**

6.1. Introduction

As shown throughout this thesis, the abundance of sterols within the brain is vast and has long been reported, specifically in relation to neurodegenerative diseases and the potential of disrupted or altered cholesterol and sterol synthesis^{1–5}. The traditional method of quantifying these sterols is through the homogenisation of brain tissue followed by lipid extraction and analysis using GC-MS or LC-MS/MS, or by monitoring brain-derived sterols in peripheral fluids including CSF or plasma, which are the chosen methods used in the papers referenced above. Although these methods do allow for exact quantification, they simultaneously destroy the integrity of the tissue and results in a loss of spatial information, meaning the sterol makeup in specific regions of interest cannot be characterised accurately. For better understanding of the sterol biochemistry and resulting pathological changes within neurodegenerative disease, we need to be able to isolate and analyse these regions with precision.

Mass spectrometry imaging (MSI) combines the selectivity and sensitivity of a mass spectrometer with the spatial information of histology⁶. It is a modern development for the detection, localization, and identification of biomolecules, including proteins, peptides and lipids whilst preserving the sampling material, and can be applied to acquire a large amount of data to visualise the spatial distribution of many biomolecules across an intact tissue section⁷. There are several ionisation techniques available for MSI, including secondary ion MS (SIMS), desorption electrospray ionisation (DESI), easy ambient sonic spray ionization (EASI), and the technique used for our methodology, matrix-assisted laser desorption/ionisation (MALDI)^{8,9}. These techniques result in a large amount of information being extracted from the sample surface e.g., tissue, allowing for a more precise analysis of specific regions of interest within tissue sections, which are important in diseases which have pathological hallmarks including amyloid beta plaques in Alzheimer's disease or myelin-deficient lesions in multiple sclerosis.

MALDI is a soft ionisation technique used mainly for qualitative analysis of a wide range of biomolecules¹⁰. MALDI uses a low molecular weight compound known as the matrix, which for MSI is sprayed onto the sample in solvent, or deposited by sublimation, resulting in a matrix co-crystal formation with the top layer of the sample of interest¹¹. The matrix has two major roles; it absorbs laser energy resulting

in explosive desorption of the matrix crystals and transfers energy to the analyte to help ionisation (see Figure 6.1). The matrix also aids the ionisation of the analyte via the usually acidic compound creating an abundance of protons¹². Some of the advantages of using MALDI over other imaging ionisation techniques like DESI is the large mass range that can be detected, and the high spatial resolution that can be achieved¹³, although previously MALDI has mainly been targeted towards the analysis of larger molecules such as peptides and oligonucleotides rather than lower molecular weight compounds¹⁴.

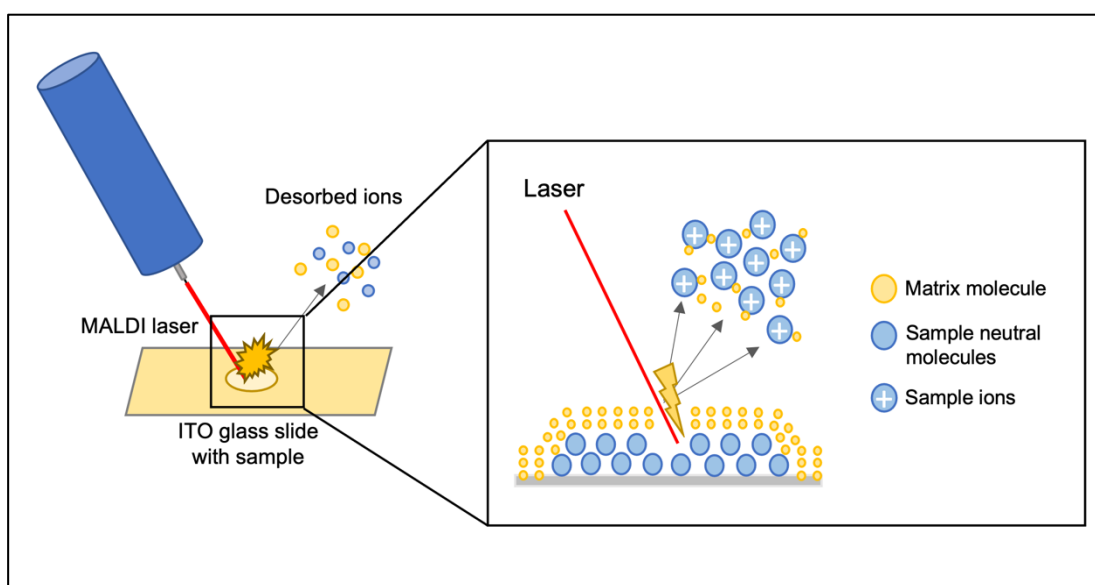


Figure 6.1. A schematic of MALDI imaging. MALDI imaging uses a laser to desorb and ionise molecules from the sample surface which has been covered with a matrix layer.

Cholesterol and other sterol molecules are highly abundant within the CNS, with about 25% of the body's cholesterol found in the brain¹⁵. Due to cholesterol's inability to pass through the blood-brain barrier, brain cholesterol is maintained and synthesised *in-situ*, with its synthesis relying upon several imperative brain cells including neurons, astrocytes and other cells of the CNS utilising this production, for example oligodendrocytes which produce myelin, of which cholesterol is a major component^{16,17}. The high level of cholesterol in the brain invites the question of whether cholesterol dysregulation could play a role in neurodegenerative diseases, with several studies suggesting defective sterol synthesis and transport is present in diseases including Alzheimer's disease, Huntington's disease and multiple sclerosis^{4,5,18,19}. Although several studies have reported cholesterol and sterol levels

within these diseases in brain tissue, it is an area that is generally underreported due to the difficulty of ionising these molecules meaning mass spectrometry has issues detecting and therefore reporting the relative levels.

6.2. Methodological differences

A paper from Angelini *et al* in 2021 reported an MSI method for the analysis of cholesterol using the EADSA method, where a pre-charged hydrazine molecule was added to the cholesterol via an enzyme derivatisation protocol using cholesterol oxidase, as previously discussed in section 2.2.5²⁰. This method on tissue allowed for the full amount of free cholesterol to be visualised and quantified across tissue for the first time (Figure 6.2).

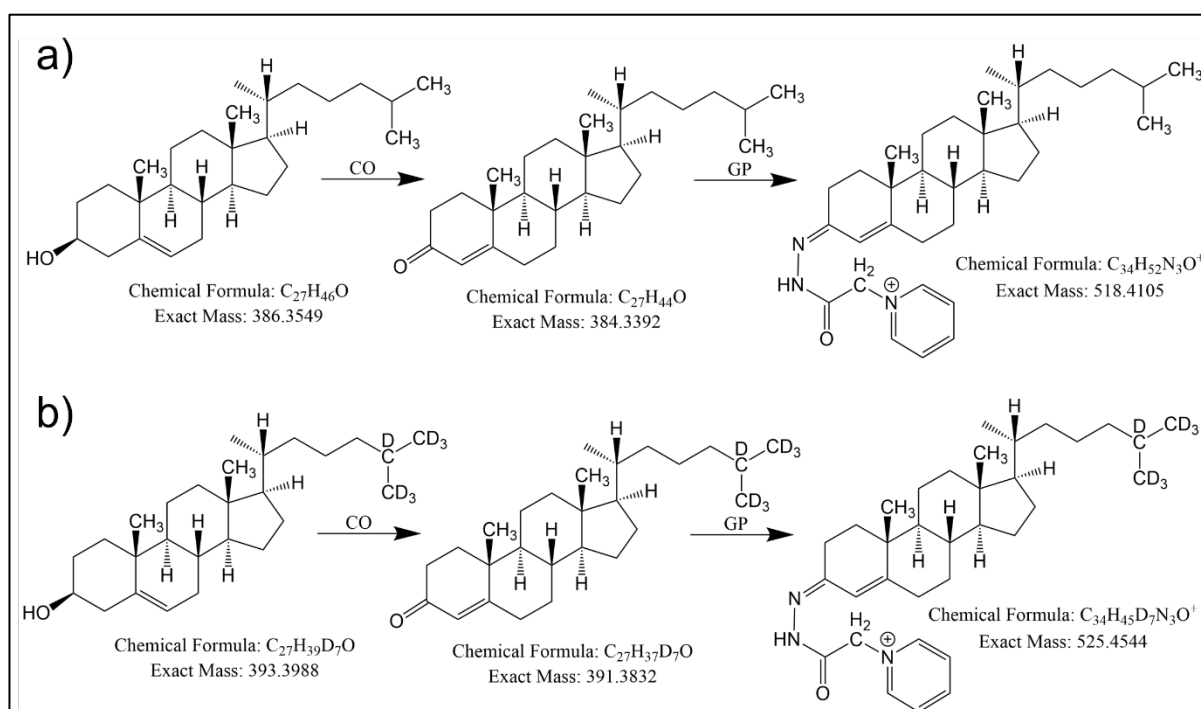


Figure 6.2. Enzyme-assisted derivatisation of endogenous cholesterol with Girard P. Treatment with cholesterol oxidase enzyme is used to convert the 3 β -hydroxyl group to a 3-ketone of the endogenous cholesterol (a), and the internal standard (b). Girard P hydrazine adds a charge-tag to the cholesterol molecule, with a final m/z 518.4105 ± 5 ppm for endogenous cholesterol (a), and m/z 525.4544 ± 5 ppm for the internal standard (b).

One of the main aims of this chapter and PhD project was to apply this method to disease tissues and aim to quantify cholesterol within the tissue against an isotope-labelled standard, however, specific instrumentation was not available to us to repeat the published method including the vacuum ultrafleXtreme MALDI-ToF/ToF from Bruker, and the HTX TM-matrix sprayer. In conjunction with the change of instrumentation, we identified key areas within the methodology that could be

improved including the amount of isotope-labelled standard used, and the buffer concentration for the enzyme reaction.

For this chapter, the main aim was to create a reproducible and reliable MALDI imaging method that would allow for the visualisation and quantification of cholesterol from brain tissue sections at a high spatial resolution. To reach this we had to identify key areas of the method to optimise and achieve the optimal signal of derivatised cholesterol (m/z 518.4105 \pm 5 ppm) within the mouse brain tissue sections we used. These conditions were appropriate for the new instrumentation used, with all our data obtained using an AP-MALDI UHR source from MassTech coupled with an Orbitrap ID-X tribrid mass spectrometer from Thermo-Fisher Scientific.

6.2.1. Original published method

Frozen brain tissue sections at 10 μ m thickness were thaw-mounted on ITO-coated glass slides as they possess a high level of conductivity needed for the excitation and desorption of ions, and placed into a vacuum desiccator. After the tissue was free of surface moisture, the tissue sections were placed into a SunCollect pneumatic sprayer system and sprayed with 200 ng/ μ L [2 H₇] cholesterol isotope-labelled standard in 99% EtOH (18 layers; 20 μ L/min flowrate; 900 mm/min velocity; 2 mm line distance; final density of 40 ng/mm²). Following the isotope-labelled standard, cholesterol oxidase enzyme was sprayed in 0.1 mM potassium phosphate (KH₂PO₄) buffer at pH 7.0 at a concentration of 0.264 units/mL (18 layers; 1st layer 10 μ L/min, 2nd layer 15 μ L/min, all other layers 20 μ L/min flowrate; 900 mm/min velocity; 2 mm line distance; final density of 52.8 μ U/mm²). The slides were incubated in a water bath glass chamber on a PTFE bed above 30 mL of pre-warmed HPLC-grade water to create humid conditions for the oxidation reaction to occur for one hour at 37°C, then placed into a desiccator under vacuum to remove excess moisture on the slide. Once dry, the slide was again placed into the sprayer system and sprayed with a [2 H₀] Girard-P solution in delivery solvent (70% MeOH, 5% glacial acetic acid), at a concentration of 0.5 mg/mL (18 layers; 1st layer 10 μ L/min, 2nd layer 15 μ L/min, all other layers 20 μ L/min flowrate; 900 mm/min velocity; final density of 0.1 μ g/mm²). The slides were again incubated within the above chamber on the PTFE bed above 10mL of pre-warmed GP incubation solvent (50% MeOH, 5% glacial acetic acid) at 37°C for one hour. After incubation, the slides were removed from the chamber and

placed in the desiccator under vacuum to remove excess moisture. The slide was sprayed with CHCA matrix in a 3:4:3 mix of water/propan-2-ol/acetonitrile at a concentration of 5 mg/mL (8 layers; 80 μ L/min flowrate; 1200 mm/min velocity; 2 mm line distance; final density of 1.33 μ g/mm²) using a HTX TM-sprayer with sprayer nozzle heated to 70°C and analysed immediately after this step or stored in a vacuum desiccator at 4°C in a dark environment.

6.2.2. Cryosectioning and histological staining

All tissue analysed within this chapter was snap-frozen mouse brain tissue, cut using a Leica Cryostat CM1900 (Leica Microsystems, Milton Keynes, UK) at a temperature between -16 and -18°C at 10 μ m thickness. Tissue was thaw-mounted onto indium tin oxide (ITO) coated slides (8 – 12 ohm/sq resistance) from Diamond Coatings (Halesowen, UK), with each slide containing three sections (each adjacent section was separated by 100 μ m) and stored at -80°C until use.

Mouse brain tissue was residual material from earlier studies. The CYP46A1 overexpressed mouse brains used for the imaging software optimisation were obtained from the Karolinska Institutet in Stockholm, Sweden. Further details regarding these mice can be found in Saeed *et al*, 2014²¹. All animal experiments received full approval from the local ethical committee of Karolinska Institutet. The Q150 negative (Q150^{-/-}) were C57/Bl6 mice used for the isotope-labelled standard optimisation and reproducibility experiments were gifted from Professor Anne Rosser and Dr Mariah Lelos from the School of Biosciences in Cardiff University, Wales, UK.

The wild-type brain tissue from *Npc1*^{+/+} mice used for buffer optimisation were provided by Dr Stephanie Cologna from the University of Illinois, Chicago, US (see Angelini *et al* for more details of this mouse²⁰). All procedures performed were in accordance with the Guide for the Humane Use and Care of Laboratory Animals, with all experiments performed in accordance with University of Illinois at Chicago IACUC approved protocols.

The wild type (WT1) mouse brains used for both Girard P and matrix optimisation were gifted from Dr Irina Pikuleva from Case Western Reserve University in Cleveland, Ohio, US (see Yutuc *et al* for more details about this mouse²²). The brains were from male mice who were euthanised at 4 months old. All animal experiments

were approved by the Case Western Reserve University's Institutional Animal Care and Use Committee.

The histological staining of Luxol Fast Blue with a counterstain of Cresyl Violet was performed in accordance with Klüver and Barrera²³. The stained sections were digitalised by scanning at x400 magnification using a Zeiss AutoScanner.

6.3. Optimisation of an AP-MALDI-MSI method for the visualisation of cholesterol

6.3.1. Imaging software for the visualisation and quantification of cholesterol

The imaging software used in the methodology published by Angelini was mainly SCiLS Lab from Bruker, with the majority of that data/experimentation obtained using the Bruker ultrafleXtreme MALDI-ToF/ToF, where the data file produced from an acquisition has the imzML format required for SCiLS. Some of the higher spatial resolution data that was acquired using an AP-MALDI source and Orbitrap Elite mass spectrometer was in a RAW data format, and analysed using ImageQuest, a Thermo Scientific software.

For our data analysis, we wanted to test three different imaging software packages to decide which was the best for the requirements we had for analysis; (i) SciLS Lab from Bruker Daltonics, (ii) ImageQuest (Thermo Scientific) / MsiReader (freeware²⁴); and (iii) Multimaging by Imabiotech .

The format of the data provided from our AP-MALDI source / Thermo Scientific instrument combination was in a RAW data format. This meant that for both the use of SciLS and MsiReader softwares we would have to convert the data into an imzML format, which we did using ImageQuest.

We found that, although ImageQuest did convert full scan data, it was selective in the type of the dataset it would convert (for example, it would not convert ion trap fragmentation data) and did not always successfully convert Orbitrap data, meaning it was unreliable. In addition, ImageQuest is not supported on computers where the more recent versions of Xcalibur (versions 4.0 or above) are installed. We did test another imzML converter provided by MassTech (MT imzML Converter) which was more consistent in conversion compared with ImageQuest and therefore used it to test both SciLS and MsiReader.

Multimaging is a relatively new software from Imabiotech, which allowed us to have some input into the development of key areas within the software, which included using the RAW dataset without having to convert the data to imzML; analyse the ion trap fragmentation (ITMS³) data to look at ion fragmentation, which is key for identification of specific ions; and customise the spectra into stick format rather than standard peaks.

Once we were able to analyse the data, we found that the images provided from SciLS were overcompensated (an extreme colour scale, based on a colour maximum of the most intense ion) specifically when normalised to internal standard, in comparison to both MsiReader and Multimaging (see Figure 6.3). The MsiReader software did give a good quality normalised image of cholesterol in the full-scan dataset with peaks quantified at an m/z accuracy of 20 ppm, however, it was unable to open and analyse any ion trap fragmentation data which was an issue for what we wanted to achieve with the method and data we acquired. Due to the input we provided to Imabiotech, we were able to ensure the Multimaging software had the ability to analyse ITMS³ data and normalise that data to the isotope-labelled standard to produce normalised images in both full scan (with peaks quantified at an m/z accuracy of 20 ppm) and ITMS³ datasets. We were also able to isolate specific regions of interest which gave us the opportunity to be able to quantify cholesterol in those regions and calculate the relative amount of endogenous cholesterol in each region based on a ratio value which was multiplied by the isotope-labelled standard concentrations used. It also gave very high-quality normalised images of cholesterol (comparable to MsiReader) not only in the full scan acquisition but also in the ITMS³ data.

After looking at the handling of data, the quality of images produced, and the capabilities of all the software packages, we decided to choose Multimaging to analyse all our MALDI datasets throughout the project. Throughout the rest of the thesis, we used a 10 ppm window for all imaging analysis.

6.3.2. Isotope-labelled standard density on tissue

The isotope-labelled standard concentration used in the original methodology to spray onto tissue was stated at 200 ng/ μ L giving a final areal density of 40 ng/mm². We used these parameters for most experiments during the optimisation process. However, we encountered an issue when using the control Q150^{-/-} mouse model brain tissue (full description of mouse model in section 6.2.2) where 200 ng/ μ L and 40 ng/mm² density seemed too low for the endogenous cholesterol, where we saw black pixels in the normalised image that when analysing the spectra from these pixels, showed a lack of a peak at m/z 525.4544 \pm 5 ppm, the mass for the deuterated cholesterol isotope-labelled standard.

We decided to increase the final areal density by spraying extra layers onto the tissue at the same 200 ng/ μ L concentration, minimising the possibility of carryover from the pneumatic sprayer that increasing the concentration could cause, and instigating interference in other projects performed in the laboratory.

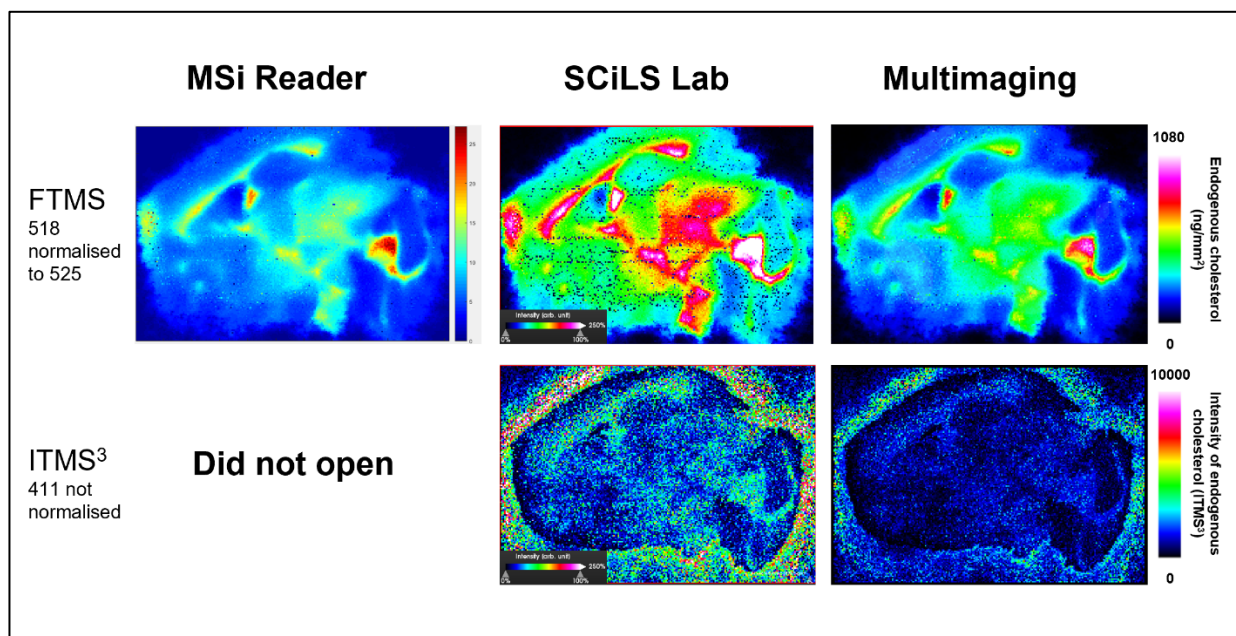


Figure 6.3. The comparison of several imaging softwares based on software ability, image quality and data handling. There were issues with both MsiReader not opening fragmentation data, and SciLS Lab having over compensated normalised images of cholesterol. The Multimaging software was chosen based on its many favourable functions including regional quantification, good quality images provided for both full scan and fragmentation data, and the ability to show the full data set without changing or compromising the raw data (which was an issue with SciLS). All images shown in this figure were acquired at a 50 μ m spatial resolution.

We tested 40 ng/mm², 80 ng/mm² and 120 ng/mm² as final areal densities of isotope-labelled standard (see Figure 6.4) and compared the number of black pixels present in the final images, and the ratio of m/z 525.4544 \pm 5 ppm present compared with m/z 518.4105 \pm 5 ppm.

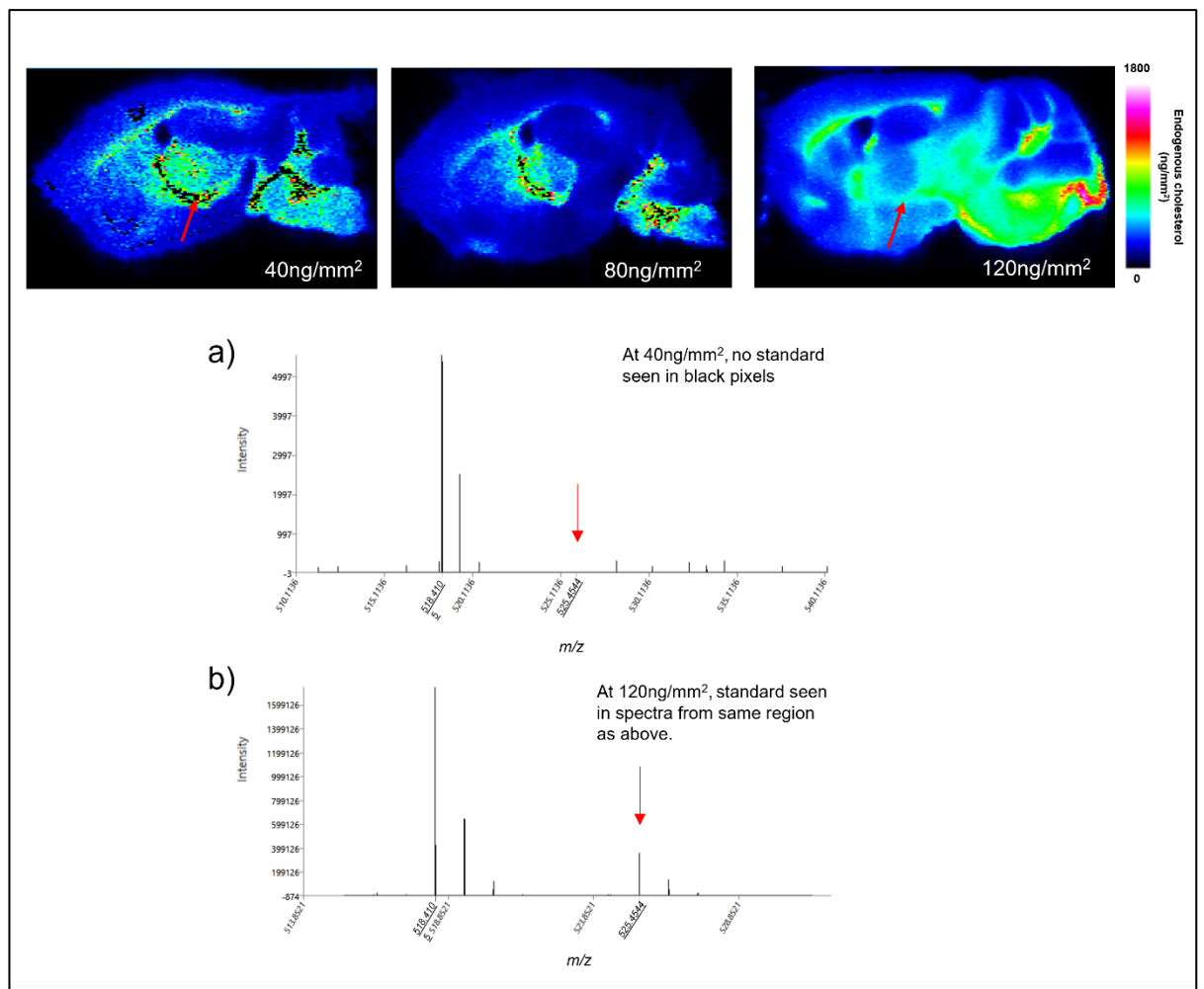


Figure 6.4. An increase in isotope-labelled standard density showed better image quality and removed 'black pixels'. (a) Spectra from black pixel showing a lack of isotope-labelled standard detected (m/z 525.4544 \pm 5 ppm) (identified with red arrow). (b) Spectra from image with 120 ng/mm² standard meant the peak at m/z 525.4544 \pm 5 ppm was present (shown with red arrow). All images shown in this figure were acquired at a 50 μ m spatial resolution.

From the data analysed (shown in Figure 6.4), the image using 120 ng/mm² showed no black pixels in white matter regions of brain in contrast to the lower densities at 40 ng/mm² and 80 ng/mm². This suggests that the higher spatial density of isotope-labelled standard (120 ng/mm²) was sufficient for the detection of m/z 525.4544 \pm 5 ppm on-tissue from the mass spectrometer in comparison to the original 40 ng/mm² (see Figure 6.4 a and b). Therefore, for the finalised methodology for application, a final density of 120 ng/mm² of isotope-labelled cholesterol standard was used.

6.3.3. Potassium phosphate buffer concentration for the enzyme reaction

The enzyme buffer established in the method published by Angelini *et al* was at 0.1 mM concentration of KH_2PO_4 at a pH 7.0. When applying that method, we found instability of the pH which subsequently meant the cholesterol oxidase enzyme efficiency could have been compromised. The aim was to increase the concentration enough so that the buffer would give a stable pH 7.0 but not so that the salt crystal formation would interfere with the MALDI image obtained.

We tested three concentrations; 0.1 mM as published by Angelini *et al*, 5 mM and 50 mM (the concentration used during in-solution derivatisation of plasma, CSF and brain extracts).

The analysis showed that overall, the 0.1 mM buffer did give a slightly better signal across the whole brain for both m/z 518.4105 ± 5 ppm and m/z 525.4544 ± 5 ppm, with the 5 mM buffer giving a slightly lower signal of around 2-fold difference (see Figure 6.5). The 50 mM buffer saturated the slide with salt crystals and as a result the image created was of very poor quality due to the difficulty of desorbing off the salt crystal layer.

The 0.1 mM did give the better signal, however due to the inconsistencies of the buffer pH at that concentration, and reproducibility problems of the enzyme reaction (previously noted by Angelini *et al*²⁰), we decided to use the 5 mM buffer for future experiments as the image quality was not compromised and was much more stable in terms of pH, which gave us confidence that the enzymatic reaction would be consistent for each run.

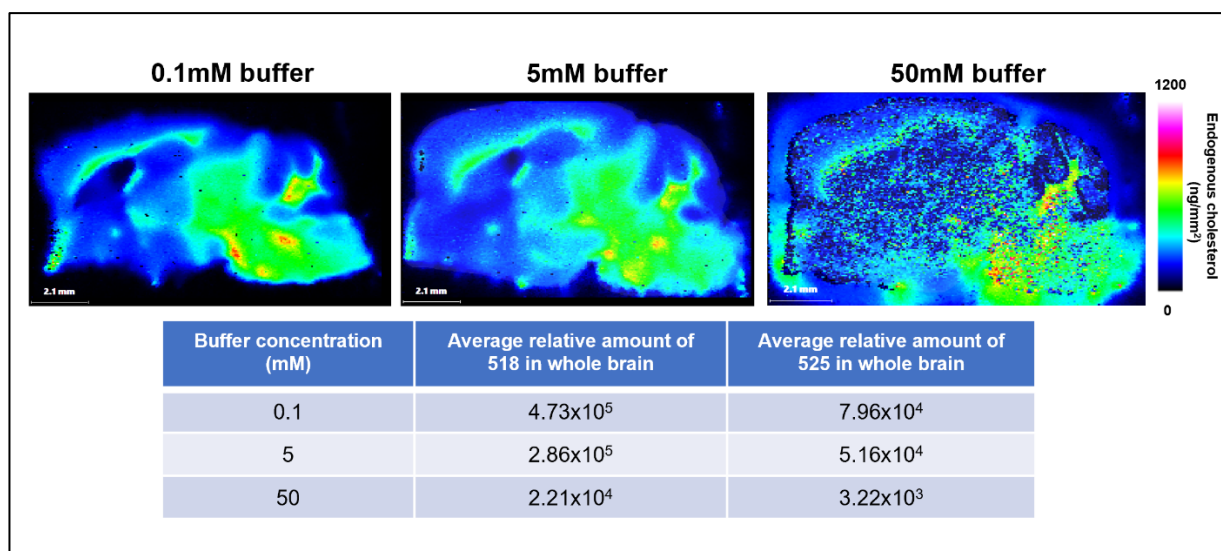


Figure 6.5. Changing the concentration of buffer from 0.1 mM to 5 mM did not affect image quality but introduced a better pH stability for the enzymatic reaction.

6.3.4. Girard-P reagent density on tissue

The next condition analysed was the Girard P on-tissue density. We tested two final areal densities of 96 ng/mm² and 192 ng/mm². We used regions of interest homogeneous throughout the brain to look at the effect the GP density had on cholesterol signal, using both the cortex and the cerebellar white matter centre. For these experiments we used the Case Western wild-type 1 (WT1) mouse brain tissue and sprayed 18 layers of 0.5 mg/mL GP solution for 96 ng/mm² and 36 layers for 192 ng/mm².

After analysing specific spectra from both the cortex (Figure 6.6, left arrow on the brains) and the cerebellar white matter arbor vitae (cerebellar nuclei – Figure 6.6, right arrow on the brains), the average signal for cholesterol was higher at the lower density of 96 ng/mm² compared with the higher density (see Figure 6.6 table), suggesting that a density of 96 ng/mm² of GP is sufficient for the reaction to occur, and by increasing the density seems to compromise the signal of endogenous cholesterol (m/z 518.4105 \pm 5 ppm), suggesting any unreacted reagent inhibits ionisation.

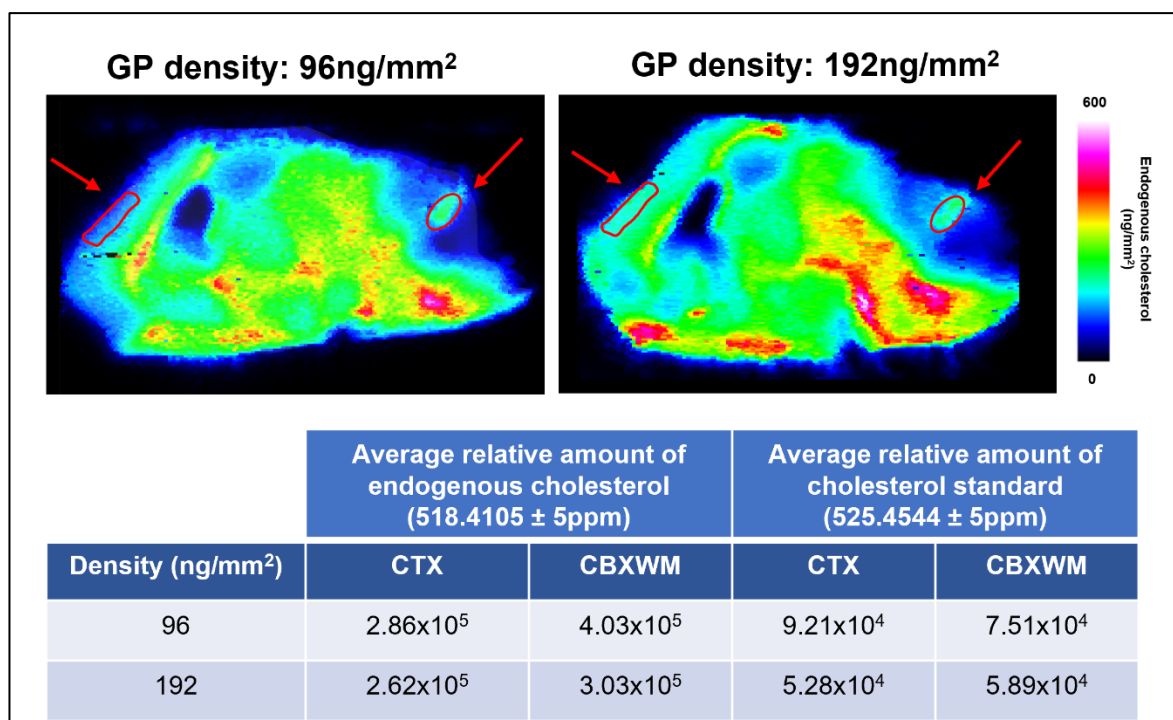


Figure 6.6. The intensity of both endogenous cholesterol and the isotope-labelled standard does not increase as areal density of Girard P (GP) reagent increases. Both images shown in this figure are acquired at a 50 μm spatial resolution.

6.3.5. Matrix density on tissue and sprayer system

For matrix application, we continued using the α -cyano-4-hydroxycinnamic acid (CHCA) after previous experimentation by Angelini *et al* and also other published literature supported its role in positive ion detection experimentation at lower mass ranges^{20,25,26}.

The biggest challenge for this condition was the change in sprayer systems being used for matrix deposition. Previously the Angelini *et al* method had used a HTX TM sprayer, with the heated nozzle function ensuring a homogeneous layer of matrix was applied to the surface of the slide and tissue. Due to the inability to access this machine, we used a SunCollect sprayer system, the same specification used to apply the isotope-labelled standard, enzyme, and Girard P reagents. As there was no heated nozzle option for the SunCollect sprayer, we had to adjust the previous parameters to ensure enough matrix was present on the tissue to allow sufficient desorption without in-source fragmentation (where there is not enough matrix and therefore excess laser energy causing the ion of interest to fragment before detection).

The previous parameters for spraying matrix were 8 layers sprayed at a flow rate of 80 $\mu\text{L}/\text{min}$, and a linear velocity of 1200 mm/min, with a final areal density of 1.33 $\mu\text{g}/\text{mm}^2$ with a nozzle temperature of 70°C.

We wanted to test the current methodology on the new SunCollect sprayer system to see if the conditions were optimum for matrix application without a heated nozzle.

We also tested double this density by using the same parameters, spraying 16 layers, creating a final density of 2.67 $\mu\text{g}/\text{mm}^2$. For this experiment, we used the Case Western WT1 mouse brain tissue, and prepared the tissue spraying standard, cholesterol oxidase and GP reagent, followed by spraying with the two matrix parameters.

After acquiring the data, we found that the signal was increased in the sample sprayed with 16 layers of matrix and a final density of 2.67 $\mu\text{g}/\text{mm}^2$ (see Figure 6.7 a, right panel). We quantified the average relative intensity of m/z 518.4105 \pm 5 ppm for endogenous cholesterol, but also quantified the isotope-labelled standard at m/z 525.4054 \pm 5 ppm as a quality control across the whole brain section analysed, which showed there was increased intensity detected in the higher density compared with the low, showing an almost 2-fold increase in intensity (see Figure 6.7 b with table). This data suggested that for this sprayer system, double the density of matrix gave a better signal intensity of ions.

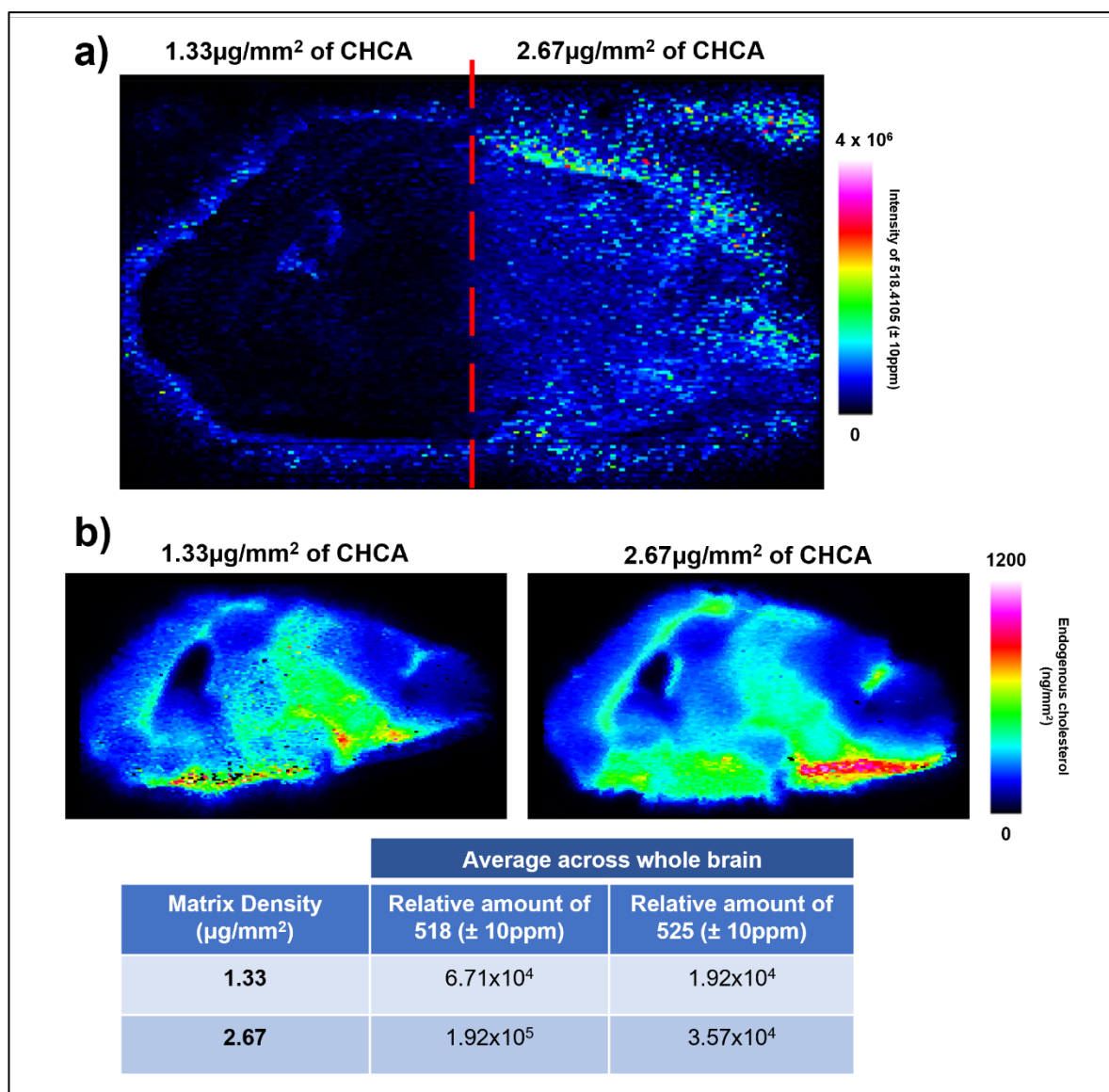


Figure 6.7. A more intense cholesterol signal is obtained at a CHCA areal density of 2.67 $\mu\text{g}/\text{mm}^2$. (a) The mouse brain was sprayed with both 1.33 $\mu\text{g}/\text{mm}^2$ and 2.67 $\mu\text{g}/\text{mm}^2$ final density of matrix, shown from the image of m/z 518.4105 ± 5 ppm without normalisation. (b) Image of cholesterol after normalisation to isotope labelled standard for both 1.33 $\mu\text{g}/\text{mm}^2$ and 2.67 $\mu\text{g}/\text{mm}^2$ GP density.

6.3.6. AP-MALDI UHR source and Orbitrap ID-X mass spectrometer parameters

For the data acquisition, there were specific settings for both the Orbitrap ID-X and the MassTech AP-MALDI source to achieve optimal performance.

Both full scan (MS^1) and ion-trap fragmentation (ITMS^3) data were acquired simultaneously but as different scan events. This meant we could confirm in every

run the fragmentation pattern of both cholesterol (m/z 518.4105 \pm 5 ppm) and the isotope-labelled standard (m/z 525.4544 \pm 5 ppm).

For MS¹ imaging analysis, data was acquired in the positive mode with an m/z range of 400-1000 at a 120,000 resolution with the RF lens set at 120% and a maximum injection time of 500 ms in profile acquisition mode.

For the MS³ imaging analysis, data was again acquired in positive mode with precursor ions isolated and fragmented at 521.9 with a wide isolation window of 8 (to include both the endogenous and isotope-labelled standard masses) for both MS² and MS³, with a collision-induced dissociation (CID) energy of 30% for MS² and 35% for MS³. The fragmentation data was detected using the ion-trap detector under a rapid IT scan rate with the RF lens at 120% with 5 microscans within the 35 ms maximum injection time under centroid acquisition.

The AP-MALDI source, equipped with a Nd:YAG laser emitting at 355 nm, was set to 11% laser energy at a laser frequency of 3000 Hz. After identifying lines in the non-normalised images (observed in Figure 6.10a, page 181), we later changed the parameters to 4% laser energy at 5000 Hz. This removed the problem. Data was acquired in a constant speed raster (CSR) at a speed of between 2.7 and 5 mm/min and a pixel size of 50 μ m, with the average time taken to acquire one whole mouse brain tissue with an average area of around 7.25 mm by 12.25 mm between 10 to 12 hours. For higher resolution images, the CSR speed was slower, for example 20 μ m pixel size would give a speed of around 1.7 mm/min.

6.3.7. Fourier-transform data from Orbitrap ID-X; Reproducibility of the methodology at 50 μ m spatial resolution

The established and optimised method above needed to show reproducibility, therefore we applied the above method to six control Q150^{-/-} mouse brain tissues, each at 30 μ m distance apart at a spatial resolution of 50 μ m (standard resolution used for our images).

We used a Luxol Fast Blue (LFB) staining to map the grey and white matter regions within the mouse brain tissue to show the different brain regions and to differentiate between white and grey matter within the brain (white stained with a darker blue colour; grey matter regions stained with a lighter blue – see Figure 6.8) to see if the MSI image created matched in terms of expected cholesterol content, with white matter containing more cholesterol compared with grey.

The data was relatively quantified using Multimaging by highlighting the region of interest (in this case the whole brain) and looking at the relative amount of m/z 518.4105 \pm 5 ppm, and 525.4544 \pm 5 ppm, and calculated the ratio between these two masses. The relative amount of cholesterol across the whole brain was calculated by multiplying the ratio by the density of isotope-labelled standard (120 ng/mm²) (see Figure 6.8).

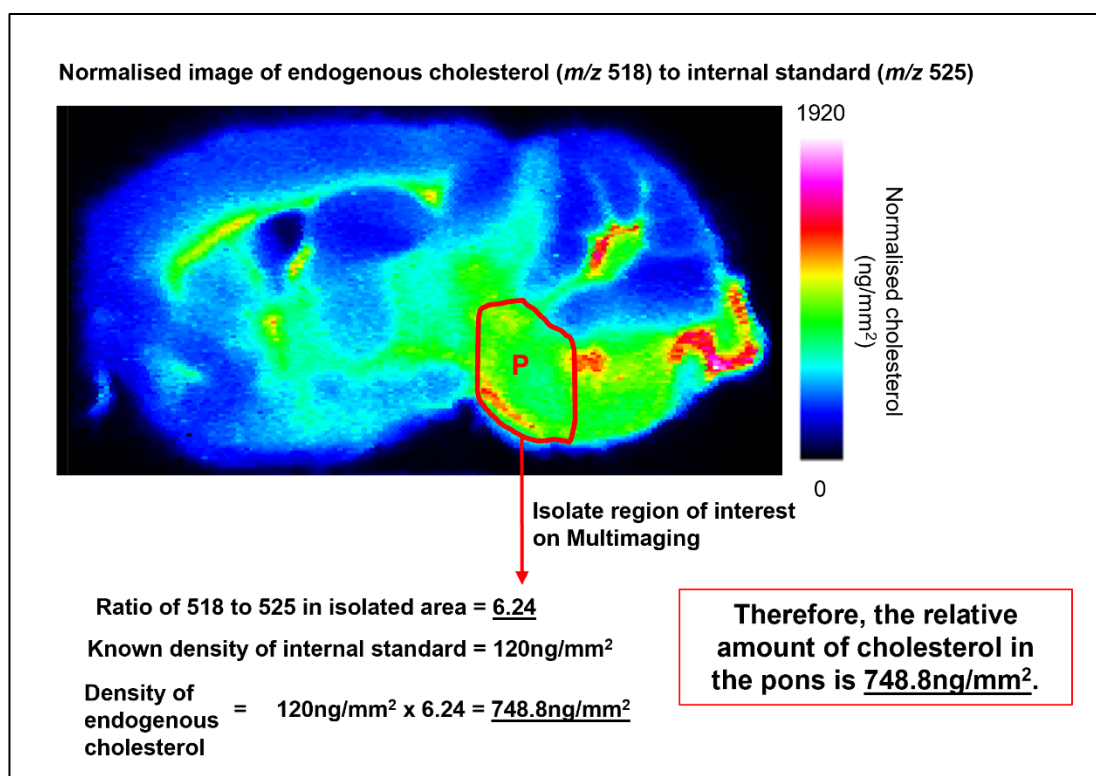


Figure 6.8. A worked example for the calculation of the areal density of endogenous cholesterol on tissue (in ng/mm²) in a specific region of interest (the pons) using internal standard density (at 120 ng/mm²).

The data in Figure 6.9 shows the relative amount of cholesterol across all six tissues are within 5.04% of each other, suggesting good reproducibility with the optimised method. This value was despite the relative intensity of both 518 and 525 increasing over time, proving that the addition of the isotope-labelled standard not only allows for the quantification of cholesterol, but also accounts and corrects for differences in intensity acquired by the mass spectrometer that are not biological. Each section of control brain tissue analysed (shown in Figure 6.9) was performed at 50 μ m spatial resolution (pixel size), where each brain tissue slice used an acquisition area of 13.5

mm x 6.9 mm, with a velocity of around 4 mm/min and took 8 hr 15 mins to acquire (average time across six brain sections).

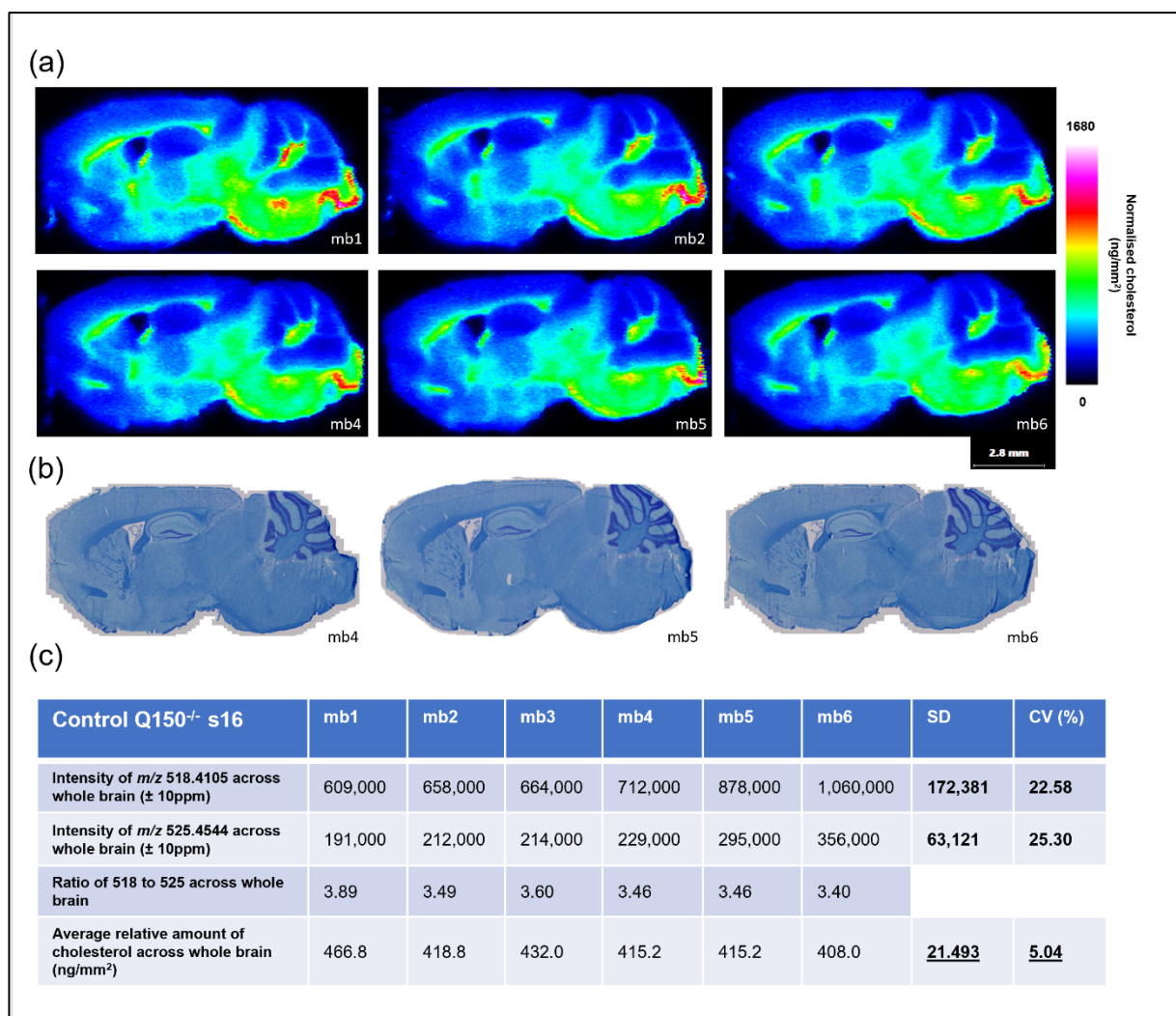


Figure 6.9. The reproducibility of the method proven by staining confirmation and quantification of relative cholesterol. (a) Six sections of mouse brain analysed, with the normalised images of cholesterol in control brain tissue displaying good reproducibility and matched with the Luxol Fast Blue (LFB) stained sections (b) which differentiated between the white and grey matter regions in the brain (where white matter regions stained a darker blue correlated with the increased cholesterol shown in the normalised MSI images with a green/yellow/red colour). (c) The quantified data showed a gradual increase in the intensity of both endogenous cholesterol (518) and the standard (525) across the days acquired, however the relative amount of cholesterol shown was consistent with a coefficient of variance (CV) of around 5%. All images in the above figure were acquired at 50 μ m spatial resolution.

6.3.8. Ion-trap fragmentation confirmation of cholesterol and isotope-labelled standard

The presence of both the endogenous cholesterol (m/z 518.4105 \pm 5 ppm) and the deuterated cholesterol standard (m/z 525.4544 \pm 5 ppm) using the Orbitrap for FT analysis was confirmed using ion-trap fragmentation (ITMS³).

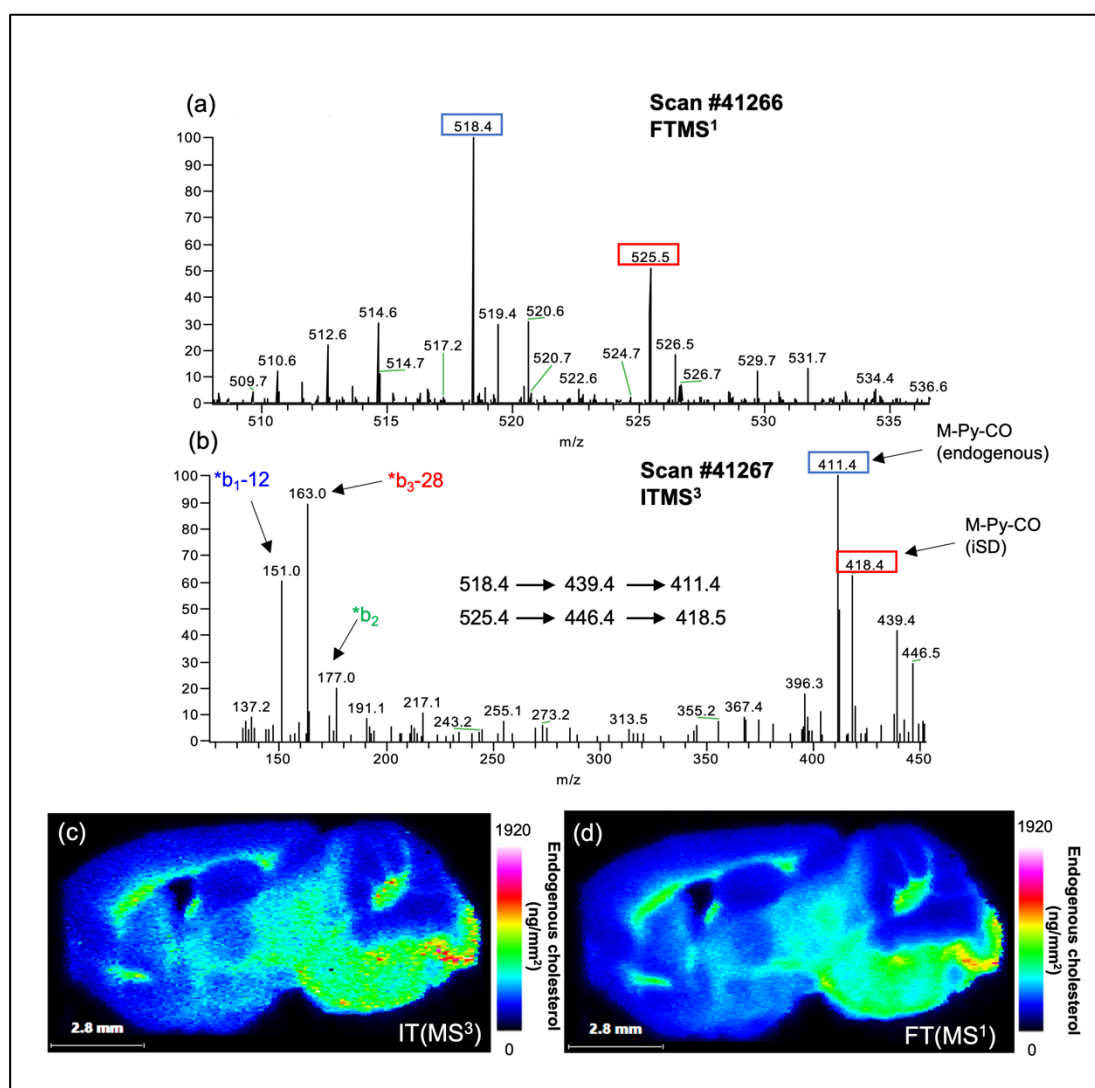


Figure 6.10. Ion-trap fragmentation (ITMS³) data confirms the identity of cholesterol and the isotope-labelled standard in mouse brain tissue sections. (a & b) Spectra confirming the MS³ fragmentation of 518.4 and 525.4 (central fragmentation mass of 521.9 and isolation window of 8) results in a 411.4 and 418.5 fragment associated with endogenous cholesterol and standard respectively, with labelled fragments shown. (c,d) MS³ data fragmenting 521.9 to 442.9 both with an isolation window of 8 captures both 518.4 \rightarrow 439.4 \rightarrow and 525.4 \rightarrow 446.4 \rightarrow transitions. A normalised image of 411.4 to 418.5 provides the ratio of endogenous cholesterol to internal standard (c) showing a similar image compared with the FT normalised image (518.4105 \pm 5 ppm to 525.4544 \pm 5 ppm) with no fragmentation (d).

The raw fragmentation data analysed in Thermo Xcalibur (shown in Figure 6.10 a & b) confirms the presence of cholesterol from the fragmentation of 518.4 → 439.4 → 411.4 in the ion trap, where the MS² displays the neutral loss of the pyridine ring structure from the GP group (neutral loss of 79.0). The same is shown for the cholesterol standard from the fragmentation pattern of 525.4 → 446.4 → 418.5, again showing a neutral loss of pyridine at MS² level, which were simultaneously identified using one MS³ method for 521.9, with a wide isolation window of 8 to fragment both the endogenous and standard in the same scan. By doing this we were able to use the Multimaging software to create a normalised image of cholesterol using the fragments of 411.4 and 418.5 (Figure 6.10 c). The signal was much lower compared to the intensity from the full scan data (no fragmentation), so the image needed slight compensation using Multimaging software. After compensation, the ITMS³ normalised image was comparable to the full scan normalised image of cholesterol. The LFB stained tissue as expected showed similarity to the MALDI images of cholesterol, where a darker blue stain reflects increased cholesterol levels.

6.3.9. High resolution imaging advantages of AP-MALDI UHR source

The majority of the MSI experimentation was performed at a 50 µm spatial resolution which we found gave us a good quality image and showed the different brain regions well. However, the AP-MALDI source from MassTech has the capability of producing images at better than 10 µm spatial resolution so we wanted to test this and look at the images created to see the difference in spatial resolution for image quality.

We first tested a 20 µm spatial resolution on some CYP46A1 overexpressed mouse brain tissue from Karolinska Institute in Stockholm. The sample preparation was the same, however the parameters of the AP-MALDI were changed, including the pixel size reduced to 20 µm, the CSR was slower at around 1.4 mm/min with a pixel duration of 0.8571 seconds. The area of analysis was 4.0 mm by 3.0 mm. The whole brain acquisition was not possible within one run due to a 16.5 hour maximum run time set on the Orbitrap ID-X, however, we were able to acquire smaller regions of interest at higher resolution, for example the cerebellum shown in Figure 6.11, which is located at the rear of the brain, and it used for balance (see Figure 6.11 c for location).

The data from the 20 μm acquisition of mouse brain cerebellum using the Orbitrap FT scan at high mass resolution (120,000) created a higher spatial resolution image for both endogenous cholesterol at m/z 518.4105 \pm 5 ppm and of the image of cholesterol normalised to the isotope-labelled standard (m/z 525.4544 \pm 5 ppm) (see Figure 6.11 a and b). The image shows a stark contrast of cholesterol intensity between the outer grey matter region and the inner white matter tracts of the cerebellum, confirming that cholesterol is increased in the white matter (see Figure 6.11).

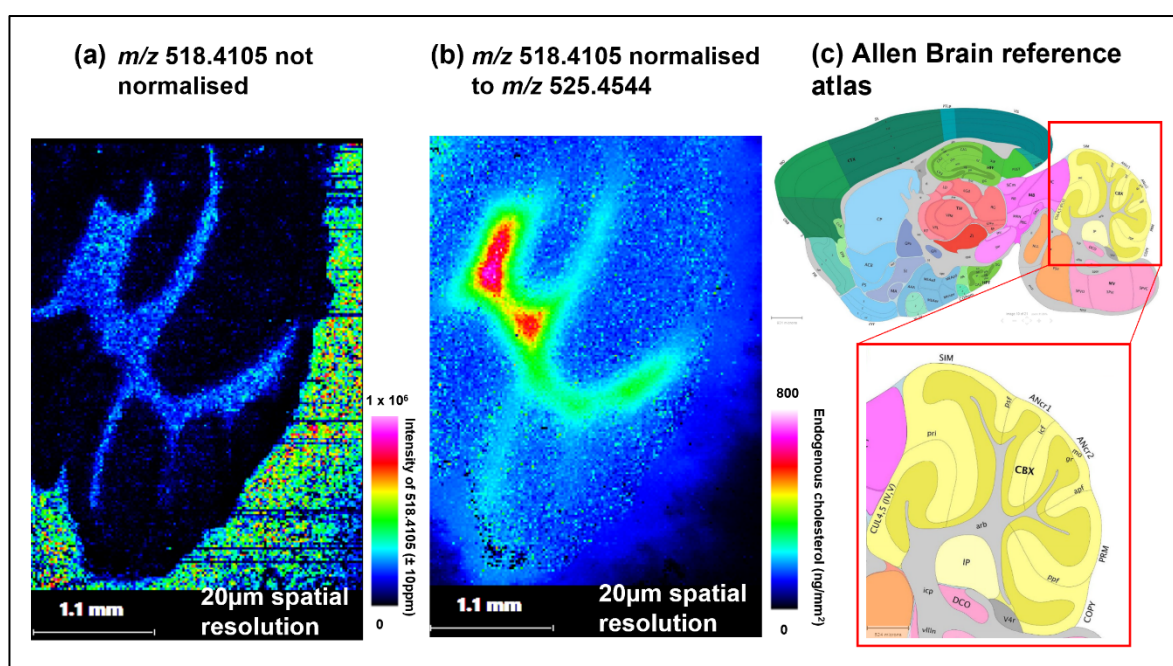


Figure 6.11. The analysis of CYP46A1 overexpressed mouse brain cerebellum at 20 μm higher spatial resolution. (a) The mapping of endogenous cholesterol (m/z 518.4105 \pm 5 ppm) of cerebellum at 20 μm spatial resolution. (b) Normalised image of cholesterol of mouse cerebellum at 20 μm spatial resolution. (c) The cerebellum, presented from the Allen Interactive Brain Atlas, a region which has both grey (shown in yellow) and white matter (shown in grey) present, which has been included to identify where in the mouse brain the region is located.

After successfully creating a 20 μm spatial resolution image of normalised cholesterol in mouse brain, we then wanted to test what the maximum spatial resolution the machine could successfully achieve. We tested at both 5 μm and 10 μm resolution on the striatal, or caudate putamen (CP) region of the brain. This region is specifically affected in Huntington's disease, resulting in a region-specific

loss of neuronal cell bodies, so we therefore used a Huntington's mouse model to look at this (see Figure 6.12).

For the analysis at 5 μm spatial resolution, again sample preparation was applied within the same way, however the AP-MALDI the pixel size was reduced to 5 μm with the scan speed decreasing to 0.3868 mm/min and a pixel duration of 0.7755 seconds. The maximum area of analysis in 16 hours at 5 μm was only 1.35 mm by 1.37 mm, meaning only a very small area of the striatum could be analysed, meaning the acquisition time was slower for a smaller area of analysis due to the higher spatial resolution (smaller pixel size).

Again, this was the case for the 10 μm spatial resolution, where the pixel size was set to 10 μm with a CSR of 0.7918 mm/min and a pixel duration of 0.7577 seconds. The maximum area of analysis in the 16 hour period was 2.75 mm by 2.75 mm, which was large enough to cover the whole striatal region.

From the data acquired and image produced, it seemed that in the 5 μm spatial resolution image (see Figure 6.12 b) there were a number of black pixels. This could be a consequence of oversampling (where the laser overlaps its sample area and results in a loss of signal due to laser overexposure) or more likely a result of reduced signal of both cholesterol and internal standard as pixel area is proportional to the square of its radius. In Figure 6.12 b some "streaking" can be observed, additional optimisation of the MALDI software proved that this can be avoided by altering the laser energy from 11% to 4%, and the laser frequency from 3000 Hz to 5000 Hz (as mentioned previously in section 6.3.6).

At 10 μm spatial resolution we acquired a very detailed image of the CP region of the brain, which also displayed a high intensity from the corpus callosum white matter tract sitting directly above (Figure 6.12 a). In comparison to the 50 μm image, the data was much more informative and gave a more detailed view of the structure, highlighting some areas within the CP where the intensity on endogenous cholesterol was increased, which may be visualising the individual neuronal cells present in the grey matter region.

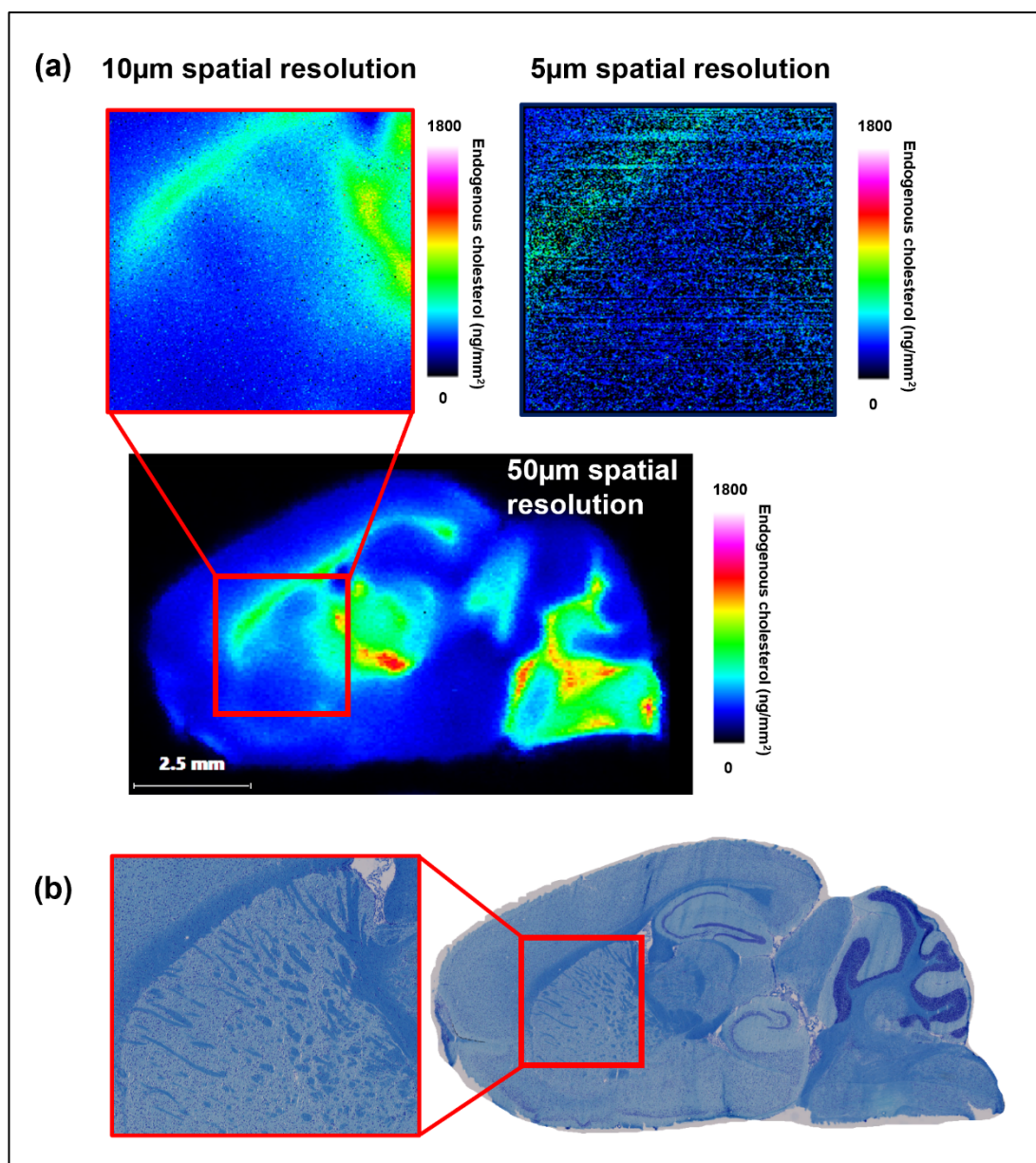


Figure 6.12. The mass spectrometry image created of the striatal / caudate putamen (CP) region of Q150⁺ mouse brain tissue at 10 µm and 5 µm spatial resolution. (a) The CP region at 10 µm resolution created a detailed image showing the distribution of cholesterol. (b) At 5 µm resolution, the greatly reduced area of sample available in each pixel, and thus amount of cholesterol and internal standard, resulted in black pixels in the white matter region. (c) At 50 µm resolution, the image does not look as detailed in the smaller regions of interest such as the CP. (d) The CP/ striatum is located just below the white matter structure of the corpus callosum (grey) highlighted in purple on the Allen Interactive Brain Atlas image. (e) The LFB stained section in the CP shows the fine white matter tracts within the structure. These are not seen by the MSI image suggesting the cholesterol difference here may not be significant to the surrounding deep grey matter.

6.4. Conclusion

This chapter focused on the optimisation of a published mass spectrometry imaging method for the visualisation and quantification of cholesterol within brain tissue samples. After optimisation of key sections of the method, we confirm we have a reproducible method for the visualisation of cholesterol at 50 μm (and higher) spatial resolution, and are able to quantify cholesterol within the brain to give a relative amount of cholesterol in ng/mm^2 .

The new method we have optimised is as followed, with changes highlighted in **bold**:

Frozen brain tissue cut at 10 μm thickness was thaw-mounted on ITO-coated glass slides and stored at -80°C . Slides for analysis were removed from the -80°C freezer and placed into a vacuum desiccator. After the tissue was free of surface moisture, the tissue sections were placed into a SunCollect pneumatic sprayer system and sprayed with 200 $\text{ng}/\mu\text{L}$ [$^2\text{H}_7$] cholesterol isotope-labelled standard in 99% EtOH (**54 layers**; 20 $\mu\text{L}/\text{min}$ flowrate; 900 mm/min velocity; 2 mm line distance; final density of **120 ng/mm^2**). Following the isotope-labelled standard, cholesterol oxidase enzyme was sprayed in **5 mM** potassium phosphate (KH_2PO_4) buffer at pH 7.0 at a final concentration of 0.264 units/mL (18 layers; 1st layer 10 $\mu\text{L}/\text{min}$, 2nd layer 15 $\mu\text{L}/\text{min}$, all other layers 20 $\mu\text{L}/\text{min}$ flowrate; 900 mm/min velocity; 2 mm line distance; final density of 52.8 $\mu\text{U}/\text{mm}^2$). The slides were incubated in a **plastic chamber** (pipette box) above 30 mL of pre-warmed HPLC-grade water to create humid conditions for the oxidation reaction to occur for one hour set at 37°C , then placed into a desiccator under vacuum to remove excess moisture on the slide. Once dry, the slide was again placed into the sprayer system and sprayed with a [$^2\text{H}_0$] Girard-P solution in delivery solvent (70% MeOH, 5% glacial acetic acid), at a final concentration of 0.5 mg/mL (18 layers; 1st layer 10 $\mu\text{L}/\text{min}$, 2nd layer 15 $\mu\text{L}/\text{min}$, all other layers 20 $\mu\text{L}/\text{min}$ flowrate; 900 mm/min velocity; final density of 0.1 $\mu\text{g}/\text{mm}^2$). The slides were again incubated within **the chamber described above**, placed above 10 mL of pre-warmed GP incubation solvent (50% MeOH, 5% glacial acetic acid) at 37°C for one hour. After incubation, the slides were removed from the chamber and placed in the desiccator under vacuum to remove excess moisture. The slide was sprayed with CHCA matrix in a 3:4:3 mix of water/propan-2-ol/acetonitrile at a final concentration of 5 mg/mL (**16 layers**; 80 $\mu\text{L}/\text{min}$ flowrate; 1200 mm/min velocity; 2

mm line distance; final density of **2.66 $\mu\text{g}/\text{mm}^2$**) using a **SunCollect pneumatic sprayer system** and analysed immediately after this step or stored in a vacuum desiccator 4°C in a dark environment.

This finalised method was reproducible in image quality and quantifying of cholesterol data from mouse brain tissue, so we therefore wanted to apply this to disease models. In the next chapter we show the application of this method to both Huntington's disease mouse model brain tissue and human multiple sclerosis brain tissue and corresponding controls to quantify cholesterol in pathological regions of interest.

6.5. References

1. Björkhem, I., Cedazo-Minguez, A., Leoni, V. & Meaney, S. Oxysterols and neurodegenerative diseases. *Mol. Aspects Med.* **30**, 171–179 (2009).
2. Leoni, V. & Caccia, C. Oxysterols as biomarkers in neurodegenerative diseases. *Chem. Phys. Lipids* **164**, 515–524 (2011).
3. Meljon, A., Wang, Y. & Griffiths, W. J. Oxysterols in the brain of the cholesterol 24-hydroxylase knockout mouse. *Biochem. Biophys. Res. Commun.* **446**, 768–774 (2014).
4. Testa, G. *et al.* Changes in brain oxysterols at different stages of Alzheimer's disease: Their involvement in neuroinflammation. *Redox Biol.* **10**, 24–33 (2016).
5. Heverin, M. *et al.* Changes in the levels of cerebral and extracerebral sterols in the brain of patients with Alzheimer's disease. *J. Lipid Res.* **45**, 186–193 (2004).
6. Gessel, M. M., Norris, J. L. & Caprioli, R. M. MALDI imaging mass spectrometry: Spatial molecular analysis to enable a new age of discovery. *J. Proteomics* **107**, 71–82 (2014).
7. Zemski Berry, K. A. *et al.* MALDI Imaging of Lipid Biochemistry in Tissues by Mass Spectrometry. *Chem. Rev.* **111**, 6491–6512 (2011).
8. Buchberger, A. R., DeLaney, K., Johnson, J. & Li, L. Mass Spectrometry Imaging: A Review of Emerging Advancements and Future Insights. *Anal. Chem.* **90**, 240–265 (2018).
9. Amstalden van Hove, E. R., Smith, D. F. & Heeren, R. M. A. A concise review of mass spectrometry imaging. *J. Chromatogr. A* **1217**, 3946–3954 (2010).
10. Hillenkamp, F. & Peter-Katalinic, J. *MALDI MS: Chapter 1: The MALDI Process and Method.* (Wiley, 2007). doi:10.1002/9783527610464.
11. Gustafsson, J. O. R., Oehler, M. K., Ruskiewicz, A., McColl, S. R. & Hoffmann, P. MALDI Imaging Mass Spectrometry (MALDI-IMS)—Application of Spatial Proteomics for Ovarian Cancer Classification and Diagnosis. *Int. J. Mol. Sci.* **12**, 773–794 (2011).
12. Karas, M., Bahr, U. & Gießmann, U. Matrix-assisted laser desorption ionization mass spectrometry. *Mass Spectrom. Rev.* **10**, 335–357 (1991).
13. Shariatgorji, M. *et al.* Simultaneous imaging of multiple neurotransmitters and neuroactive substances in the brain by desorption electrospray ionization mass spectrometry. *Neuroimage* **136**, 129–138 (2016).
14. Calvano, C. D., Monopoli, A., Cataldi, T. R. I. & Palmisano, F. MALDI matrices for low molecular weight compounds: an endless story? *Anal. Bioanal. Chem.* **410**, 4015–4038 (2018).
15. Björkhem, I. & Meaney, S. Brain Cholesterol: Long Secret Life Behind a Barrier. *Arterioscler. Thromb. Vasc. Biol.* **24**, 806–815 (2004).
16. Jin, U., Park, S. J. & Park, S. M. Cholesterol Metabolism in the Brain and Its Association with Parkinson's Disease. *Exp. Neurobiol.* **28**, 554–567 (2019).
17. Petrov, A. M., Kasimov, M. R. & Zefirov, A. L. Brain Cholesterol Metabolism and Its Defects: Linkage to Neurodegenerative Diseases and Synaptic Dysfunction. *Acta Naturae* **8**, 58–73 (2016).
18. Crick, P. J. *et al.* Reduced Plasma Levels of 25-Hydroxycholesterol and Increased Cerebrospinal Fluid Levels of Bile Acid Precursors in Multiple Sclerosis Patients. *Mol. Neurobiol.* **54**, 8009–8020 (2017).

19. Boussicault, L. *et al.* CYP46A1, the rate-limiting enzyme for cholesterol degradation, is neuroprotective in Huntington's disease. *Brain* **139**, 953–970 (2016).
20. Angelini, R. *et al.* Visualizing Cholesterol in the Brain by On-Tissue Derivatization and Quantitative Mass Spectrometry Imaging. *Anal. Chem.* **93**, 4932–4943 (2021).
21. Saeed, A. A. *et al.* Effects of a Disrupted Blood-Brain Barrier on Cholesterol Homeostasis in the Brain. *J. Biol. Chem.* **289**, 23712–23722 (2014).
22. Yutuc, E. *et al.* Localization of sterols and oxysterols in mouse brain reveals distinct spatial cholesterol metabolism. *Proc. Natl. Acad. Sci.* **117**, 5749–5760 (2020).
23. Klüver, H. & Barrera, E. A Method for the Combined Staining of Cells and Fibers in the Nervous System. *J. Neuropathol. Exp. Neurol.* **12**, 400–403 (1953).
24. Robichaud, G., Garrard, K. P., Barry, J. A. & Muddiman, D. C. MSiReader: An Open-Source Interface to View and Analyze High Resolving Power MS Imaging Files on Matlab Platform. *J. Am. Soc. Mass Spectrom.* **24**, 718–721 (2013).
25. Cerruti, C. D. *et al.* MALDI imaging mass spectrometry of lipids by adding lithium salts to the matrix solution. *Anal. Bioanal. Chem.* **401**, 75–87 (2011).
26. Brunelle, A. MALDI Mass Spectrometry Imaging of lipids in positive and negative ion mode. *HTX Imaging* <http://www.htximaging.com/htx-an-35-maldi-mass-spectrometry-imaging-of-lipids-in-positive-and-negative-ion-mode> (2015).

Chapter 7: The analysis of cholesterol in multiple sclerosis and Huntington's disease brain tissue using mass spectrometry imaging

7.1. Introduction

Across this thesis, we have highlighted the importance of cholesterol and oxysterols within the brain, and how in specific diseases the homeostasis of this lipid species can be compromised. We also introduced the benefits of mass spectrometry imaging (MSI) techniques and the amount of information that can be extracted by applying these methods to tissue sections. These techniques specifically utilise the sensitivity and selectivity of mass spectrometry and combine them with spatial information that classical immunohistochemical staining usually provides, which adds valuable information about specific structures and molecules present within the different samples. These techniques have the potential to be incredibly valuable in researching sterols and possibly expand on their links with neurodegenerative disease.

There are several neurodegenerative diseases linked with sterol dysregulation and altered levels of sterols, including Alzheimer's, Parkinson's, and motor neuron disease (MND)¹⁻⁵. In this chapter we are focusing on two diseases with interesting pathological features, multiple sclerosis and Huntington's disease (HD).

Multiple sclerosis is characterised by demyelination – the loss of myelin, which is a complex mix of both proteins and lipids that surround and protect nerve axons in both the grey and white matter of the brain^{6,7}. Other hallmarks of multiple sclerosis include inflammation and neuronal loss in the CNS, where the body's own immune cells actively participate in the degradation of myelin, resulting in foamy macrophage cells that are laden with lipids. The loss of myelin, which is extremely cholesterol-rich⁸, has substantial and devastating effects on the individual who may suffer with life-debilitating disability as a consequence. Demyelination and inflammation leads to the subsequent degeneration of axons and neurons⁹⁻¹⁵, however, we need to better understand the timing and the extent of cholesterol loss with demyelination, and whether visualising cholesterol could identify new areas of myelin disturbance or repair that standard immunohistochemistry and histology cannot routinely identify.

HD is an autosomal-dominant, progressive neurodegenerative disease, where a mutation causing polyglutamine (CAG) expansion in the huntingtin protein results in neurotoxic protein aggregate formation^{16,17}. The effects of this begin in the striatum (specifically the caudate and putamen), with progression of the disease resulting in widespread neuronal loss across the cerebral cortex and other grey matter areas of

the brain, including the brain stem^{18,19}. In 2016, the Betuing group showed significantly increased levels of cholesterol in the striatum of R6/2 mouse models of HD compared with corresponding controls¹⁸. They also showed protein levels of CYP46A1, the enzyme that primarily aid the removal of cholesterol via its conversion to 24S-HC, were significantly decreased in the putamen of HD post-mortem human brain tissue compared with control samples¹⁸. However, published data from the Cattaneo group contradict this, showing dysregulation of cholesterol homeostasis in HD with decreased expression of target genes in the cholesterol biosynthesis pathway in astrocytes via SREBP2, and reduced messenger RNA (mRNA) levels of key enzymes in the cholesterol synthesis pathway in HD cells^{20–22}. The main aim from the previous chapter was to develop a reproducible method for the visualisation and quantification of cholesterol, which was successfully achieved.

7.1.1. Aims

For this chapter, we aim to apply the optimised derivatisation method from Chapter 6 to brain tissue from mouse models of HD and post-mortem human multiple sclerosis, alongside corresponding controls, to look at possible differences in cholesterol by quantification using an isotope-labelled standard in a proof of principle study. In addition, we will also explore the other benefits of MALDI-MSI by looking at underivatized sections of rat brain tissue and mapping other lipids, such as different phospholipid species including phosphatidylcholines (PCs), phosphatidylethanolamines (PEs), and sphingolipids in rat brain tissue.

7.2. Methods and materials

7.2.1. Q150 mouse brain tissue

We used the Huntingtin gene knock-in model of HD (referred to during this chapter as Q150), with ~ 150 CAG/ polyglutamine repeats in the Huntingtin gene (*Hdh*) (model *Hdh*^{Q150/Q150}), which is comparable with the R6/2 model used by both the Betuing and Cattaneo groups^{18,23–25}.

The Q150 mouse brains used in this chapter were provided by Professor Anne Rosser and Dr Mariah Lelos from the Brain Repair Group in Cardiff University, Wales. The brains were from a male Q150 heterogenous positive mouse (ID: 052204; disease) and female Q150 negative/ WT C57BL mouse (ID:052207; control) culled at 6 months 18 days old. The mice were euthanised with 0.2mL of a ketamine/xylazine mix, then perfused with 30 mL phosphate-buffered saline (PBS). The brains were removed, washed with PBS to remove excess blood, and immediately flash frozen in liquid nitrogen. The procedures were conducted under license held by the Brain Repair Group in Cardiff University.

7.2.2 Rat brain tissue

The rat brain coronal tissue sections were provided by Dr Beatriz Abad of the University of Basque Country, Spain. The sections were pre-cut at 25 µm thickness, thaw-mounted onto SuperFrost® Plus Menzel-Gläser peptide-coated glass slides (Thermo Scientific, UK) and stored at -80°C until used for analysis.

7.2.3. Multiple sclerosis and control human brain tissue

The multiple sclerosis snap-frozen brain tissue blocks were provided by the UK Multiple Sclerosis Tissue Bank, Imperial College London with appropriate ethical approval (08/MRE09/31+5). The brains used were from four cases of progressive multiple sclerosis (1 PPMS; 3 SPMS; gender: 1M, 3F; full demographics found in Table 7.1).

The control human snap-frozen brain tissue blocks were acquired from Oxford University with appropriate research ethics committee approval (13/WA/092). All control tissue used in this study were selected for their relatively young age at death

(mean 63.3 yrs) and matched regions of interest to the multiple sclerosis cohort (gender 1M; 2F).

Table 7.1. Demographics of multiple sclerosis and control human brain tissue. All multiple sclerosis cases coded MS, all control cases coded NP (DD – disease duration; TTP – time to progressive)

Case	Block	Sex	Age	DD	TTP	Cause of death
MS423	A1B2	F	54	30	21	Pneumonia
MS473	A1B3	F	39	13	10	Bronchopneumonia, MS
MS510	P2B4	F	38	22	15	Pneumonia, MS
MS513	A3A3	M	51	18	15	Respiratory failure, MS
NP13/011	-	F	62	-	-	Metastatic colorectal cancer
NP13/012	-	F	60	-	-	Metastatic breast cancer
NP13/128	-	M	68	-	-	Cardiac arrest

7.2.4. Tissue cutting

The HD mouse and human multiple sclerosis brain tissues were cut at 10 μ m thickness using a Leica Cryostat CM1860 UV (Leica Microsystems, Milton Keynes, UK) and thaw-mounted on one of three different glass sections; indium tin oxide (ITO) coated glass slides (8 – 12 ohms/sq resistance; 0.7 mm thickness; from Diamond Coatings, Halesowen, UK) for MALDI analysis; SuperFrost® Plus glass slides for histochemical staining (from Thermo Scientific), or normal uncoated glass sections (Thermo Scientific). Each mouse slide comprised six brain sections, each 30 μ m distance from each other (see Figure 7.1 for cutting details). The human tissue sections were cut one section per slide due to their larger size, with three cut consecutively for either ITO, SuperFrost or normal glass slides. After the tissue was thaw mounted, it was stored at -80°C until tissue preparation for MSI.

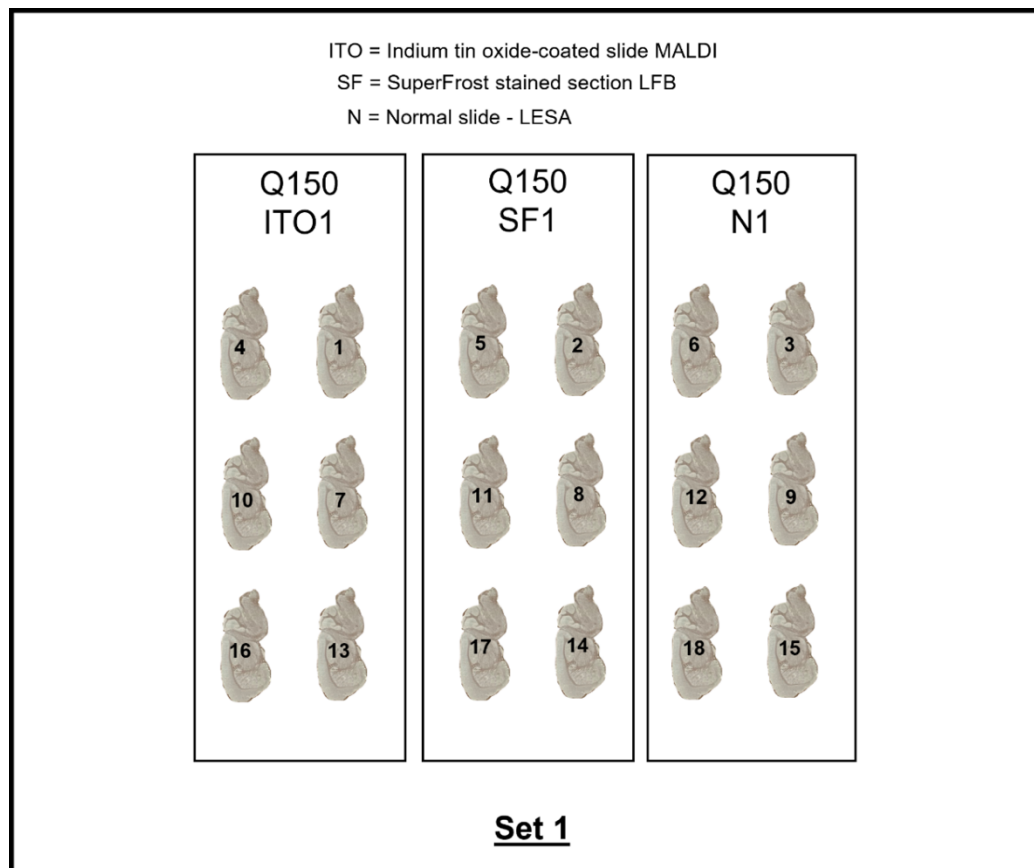


Figure 7.1. Cutting of the Q150 mouse and corresponding control. The mouse brain tissue was cut at 10 μ m thickness and mounted onto slides in sets of three: alternating between ITO (for MALDI), SuperFrost (for histology) and normal sections. Sections were mounted as above (sections 1 to 18, with 6 mouse brain sections on each slide 30 μ m distance from each other, with a total of 16 sets).

7.2.5. Tissue histology

Corresponding histochemical and immunohistochemical staining's were carried out on consecutive sections of tissue to highlight the pathological features within the tissue. All immunohistochemical staining's were carried out by myself and Kristen Hawkins (BSc).

For the Q150 mouse brain tissue, Luxol Fast Blue (LFB) chemical staining was performed to differentiate between the grey and white matter regions and aid in the identification of specific regions of interest for quantification. LFB stained sections allowed for the 'matching' of regions of interest (for example, mouse cerebellum or hippocampus) between control and disease tissues.

For the post-mortem human multiple sclerosis and control brain tissue, several immunohistochemical stains were applied to sequential sections to characterise the

relevant pathological features. Anti-HLA immunostaining was performed on already LFB-stained tissue sections (to identify areas of active inflammatory demyelination). Immunostaining against myelin oligodendrocyte glycoprotein (MOG) on a sequential slide allowed us to visualise myelin and to identify more accurately demyelinated and remyelinating lesions. Optimisation of these histological markers included both negative (no primary antibody) and positive (primary antibody against an essential neural protein raised in the same species as the antibody of interest) controls to ensure the antibody of choice displayed specific binding to the antigen. Following LFB or anti-MOG staining, sections were counterstained with a Nissl stain, such as haematoxylin, to label all nucleated cells. The control human brain tissue was stained with MOG antibody with the haematoxylin counterstain. All slides from a single experiment were stained at the same time to ensure consistency of results.

7.2.6. MALDI sample preparation

The tissue section for analysis (on ITO glass slides) was removed from -80°C storage and immediately placed into a vacuum desiccator with silica gel beads to prevent condensation on the tissue section.

After the tissue was free of surface moisture, the sections were placed into a SunCollect pneumatic sprayer system and sprayed with 200 ng/μL [²H₇] cholesterol isotope-labelled standard in absolute EtOH (54 layers; 20 μL/min flowrate; 900 mm/min velocity; 2 mm line distance; final density of 120 ng/mm²). Following the isotope-labelled standard, cholesterol oxidase enzyme was sprayed in 5 mM potassium phosphate (KH₂PO₄) buffer at pH 7.0 at a final concentration of 0.264 units/mL (18 layers; 1st layer 10 μL/min, 2nd layer 15 μL/min, all other layers 20 μL/min flowrate; 900 mm/min velocity; 2 mm line distance; final density of 52.8 μU/mm²).

The slides were incubated in a plastic chamber above 30 mL of pre-warmed HPLC-grade water to create humid conditions for the oxidation reaction to occur for one hour at 37°C, then placed into a desiccator under vacuum to remove excess moisture on the slide. Once dry, the slide was again placed into the sprayer system and sprayed with a [²H₀] Girard-P solution in delivery solvent (70% MeOH, 5% glacial acetic acid), at a final concentration of 0.5 mg/mL (18 layers; 1st layer 10 μL/min, 2nd layer 15 μL/min, all other layers 20 μL/min flowrate; 900 mm/min velocity; 2 mm

line distance; final density of 0.1 $\mu\text{g}/\text{mm}^2$). The slides were again incubated within a chamber above 10 mL of pre-warmed incubation solvent (50% MeOH, 5% glacial acetic acid) at 37°C for one hour. After incubation, the slides were removed from the chamber and placed in the desiccator under vacuum to remove excess moisture.

7.2.7. Matrix application

The matrix used for analysis was α -cyano-4-hydroxycinnamic acid (CHCA) in a 3:4:3 mix of water/IPA/ACN at a final concentration of 5 mg/mL (16 layers; 80 $\mu\text{L}/\text{min}$ flowrate; 1200 mm/min velocity; final density of 2.66 $\mu\text{g}/\text{mm}^2$). A separate SunCollect pneumatic sprayer system was used to spray on the matrix.

7.2.8. Instrumentation

The instrumentation used for all analysis was a combination of the AP-MALDI from MassTech and an Orbitrap ID-X tribrid mass spectrometer (Thermo Fisher, UK).

All data used within this chapter was acquired at 50 μm spatial resolution. For both the Q150 mouse brain and post-mortem human multiple sclerosis brain tissue sections the slides were prepared as stated in section 7.2.6. They all used the same Orbitrap method, acquiring the RAW data in full scan (FT) in positive-ion mode at a resolution of 120,000 over m/z range 400-1000 with all data quantified within a mass window of 10 ppm, with ion-trap fragmentation data (MS^3) using a central mass of m/z 521.9 with a wide isolation window of 8 mass units. This allowed for the simultaneous fragmentation of both endogenous cholesterol (m/z 518.4105 \pm 5 ppm) and the isotope-labelled standard (m/z 525.4544 \pm 5 ppm).

For the coronal rat brain sections, a wider m/z range of 400–1200 was used, with only an FT scan event only due to the exploratory nature of the experiment.

7.2.9. Software analysis of MALDI-MSI data

All data reported within this chapter was analysed using Multimaging from Imabiotech (France), with the exception of the rat coronal sections. This software was used for the normalisation of data to the isotope-labelled standard to create a normalised image of cholesterol (m/z 518.4105 \pm 5 ppm normalised to m/z 525.4544 \pm 5 ppm) displayed as percentage of normalised intensity, and to provide accurate

quantification of cholesterol. It was also used for the quantification of cholesterol in specific regions of interest using the Region of Interest (ROI) tab. The ROI was marked freehand on the tissue, with the software calculating the ratio of isotope labelled standard to endogenous cholesterol in that chosen region. The ratio was then multiplied by the density of standard on tissue (120 ng/mm²) to get the average relative amount of cholesterol across a given area (see previous chapter 6, section 6.3.7, Figure 6.8 for worked example).

For the data looking at other lipid species with the rat brain coronal sections, we used an online open-source software called Metaspace (<https://metaspace2020.eu/>) that searches the RAW data to identify common lipids within the dataset, and map each individual lipid to create an image^{26,27}.

7.2.10. Statistical analysis

Statistical analysis was generally based on three control and four multiple sclerosis cases, with grouping having three sections from the same tissue block repeated (control n = 9; multiple sclerosis n = 12 for sections analysed). However, these n numbers did vary across the analysis of different subgroups e.g., white matter lesion, lesion edge etc. due to some cases lacking these pathological regions of interest. GraphPad Prism software was used for the statistical analysis of the multiple sclerosis human tissue data. The data was first checked for normal distribution using the D'Agostino and Pearson normality test. The data did not generally follow Gaussian distribution and where there were more than three groups of interest to analyse, a Kruskal-Wallis test with a Dunn's multiple comparison post-test was performed. The adjusted P-value was taken and used for significance, with the significance levels as follows: * P < 0.05, ** P < 0.005, *** P < 0.0005, **** P < 0.0001.

A Mann-Whitney U test and unpaired t-test with Welch's correction were used as additional statistical tests as part of our explorative data analysis to look at the strength of interactions between two groups (significance levels as follows: * P < 0.05, ** P < 0.005, *** P < 0.0005, **** P < 0.0001).

For the Q150 mouse brain analysis, the control and HD groupings only had n=1, therefore no statistical analysis was possible.

A ROUT outlier test was used to identify outlying data points from nonlinear regression (maximum desired false discovery rate (Q) set at 1%).

7.3. Results

7.3.1. Huntington's disease Q150 mouse model

We imaged 18 brain sections from one HD Q150⁺ brain and 18 sections of one control Q150^{-/-} brain, allowing us to visualise the change in cholesterol throughout the brain and to have more accurate data to quantify throughout the brain structures of interest. In addition to the quantification of the striatal region identified by Boussicault et al¹⁸, we also looked at other salient structures within the brain. These included the cortex, cerebellum (both grey and white matter), corpus callosum, hippocampus, pons, and medulla oblongata (brain stem). All regions were isolated and quantified for every brain tissue section analysed, with the relative amount of cholesterol calculated using the density of isotope-labelled standard sprayed (120 ng/mm²) (see Figure 7.2 for isolated quantification areas).

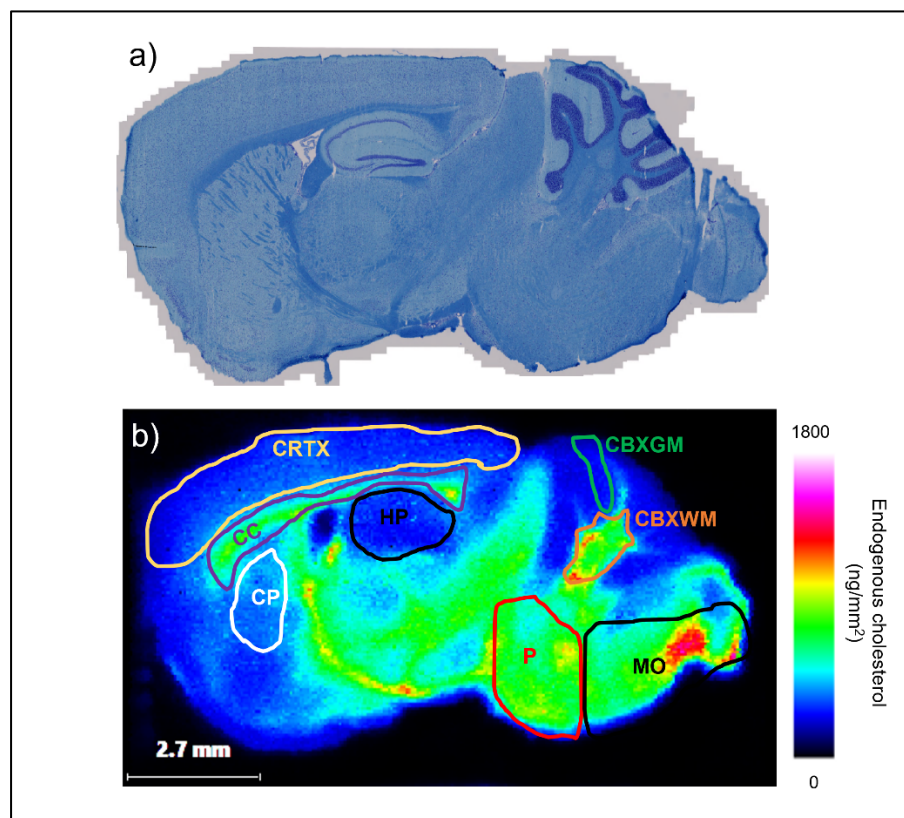


Figure 7.2. Quantification of regions of interest in Q150 MALDI-MSI images based on LFB staining. (a) The LFB-stained sections (darker blue highlighting the white matter regions; lighter blue highlighting the grey) showed good correlation to the MALDI images produced and helped in isolating the areas for quantification (as shown in (b)). CRTX – cortex; CC – corpus callosum; CP – caudate putamen/ striatum; HP – hippocampus; CBXGM – cerebellar grey matter; CBXWM – cerebellar white matter; P – pons; MO – medulla oblongata.

All 36 sections from both the Q150⁺ and Q150^{-/-} model brain tissue analysed were normalised to the isotope-labelled standard, with a subset of these images of normalised cholesterol shown in Figure 7.3. The Allen atlas image was added to show the comparison to both the disease and control brain tissue (Figure 7.3 – C).

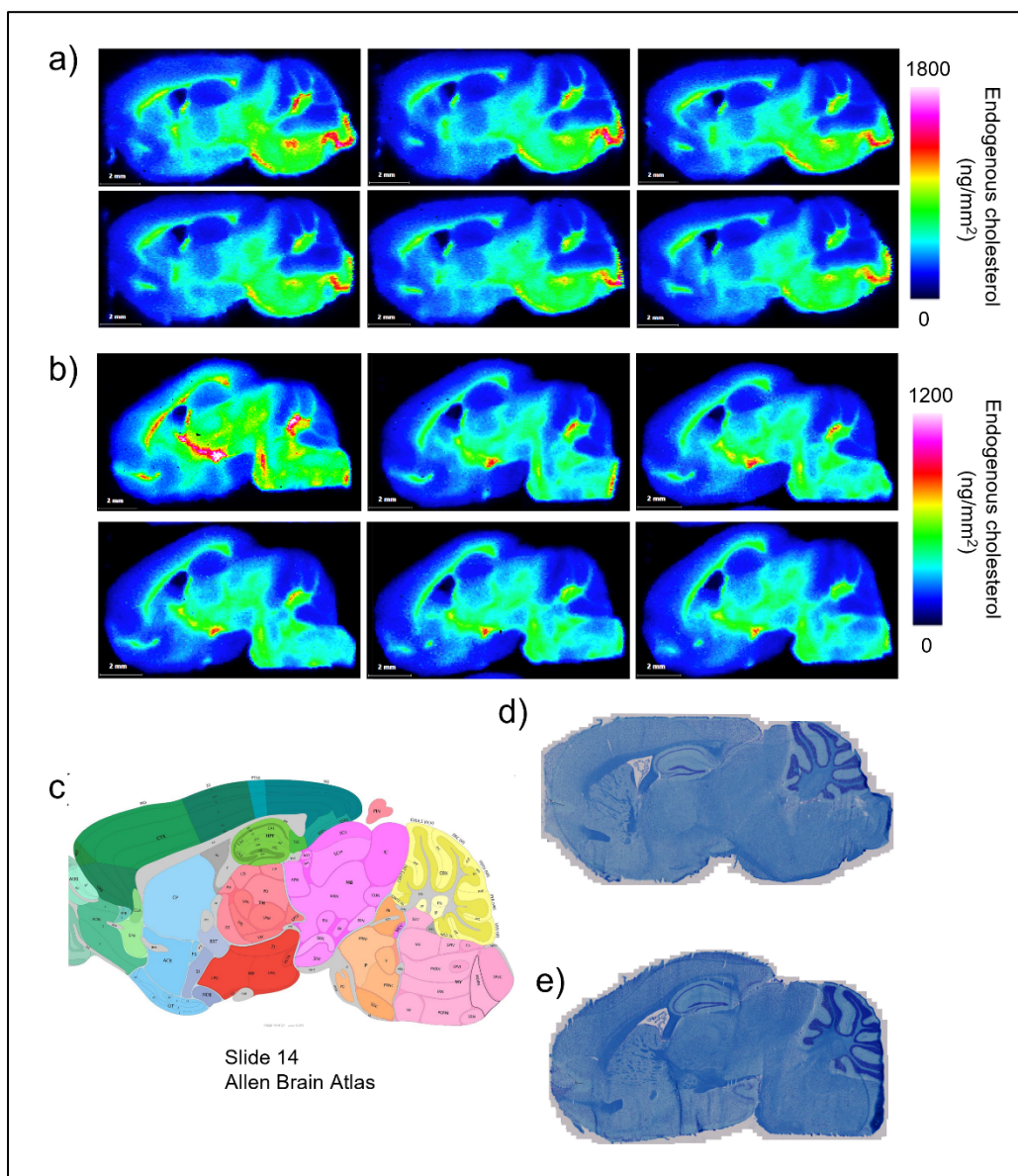


Figure 7.3. The normalised images of cholesterol from the Huntington's and control mouse brain tissue. a) The MALDI-MSI data from control set 16, containing six brain sections 30µm distance from the next. b) The MALDI-MSI data from HD set 7, containing six brain sections, again 30µm distance from each other. c) These sections correspond to slide 14 of the Allen Brain Atlas. d) An LFB stained section from control set 16, matching the MALDI images in a). e) An LFB stained section from HD set 7, matching the MALDI images in b). (All scale bars = 2mm).

In addition to the MALDI imaged tissue, subsequent sections were stained with LFB chemical stain for myelin to show the white and grey matter structures within the brain (details of the stain mentioned in section 7.2.5 - see Figure 7.3 d) for control, and e) for disease (Q150⁺) stained mouse brain tissue). After quantifying all regions of interest, one section was identified as an outlier via the ROUT test and subsequently removed from the data analysis (control slide 12 mb 1 - shown in Table 7.2 – page 210). Across all eight regions of interest, there were differences seen between HD and control brain tissue, however the striatum/caudate putamen (labelled CP in Figure 7.4 b and c) did not show any obvious differences between the animals. Differences in cholesterol (ng/mm²) were seen in the medulla oblongata and pons, where in the pons cholesterol was decreased by 11%, and in the medulla, cholesterol was decreased by 24% in the HD animal compared with the control.

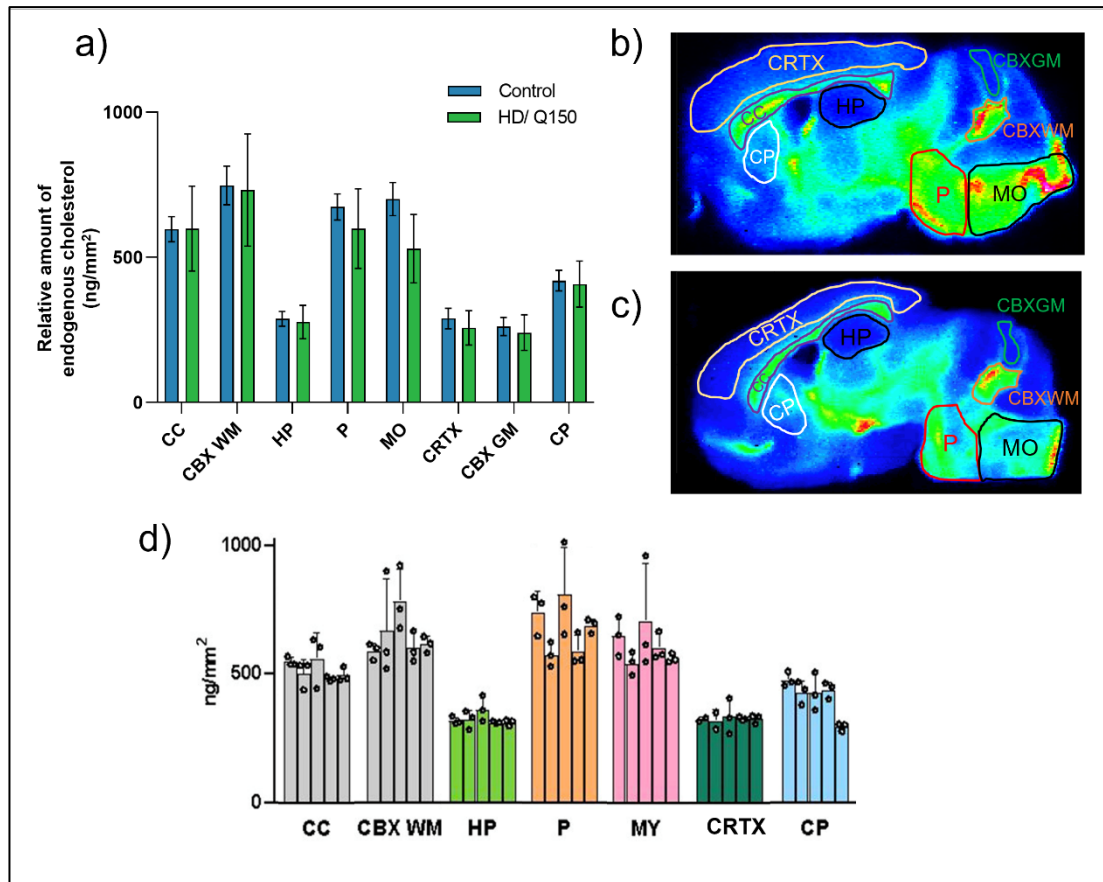


Figure 7.4. The quantification of relative cholesterol across HD mouse model brain tissue and corresponding control. a) Across most regions of interest quantified, the data generally shows a decrease in cholesterol in the disease tissue compared with control. The quantified regions of interest are indicated in b (control) and c (HD). d) Our control data was comparable to published data from Angelini et al, 2021²⁸ (CRTX – cortex; CC – corpus callosum; CP – caudate putamen/striatum; HP – hippocampus; CBXGM – cerebellum grey matter; CBXWM – cerebellum white matter; P – pons; MO/MY – medulla oblongata).

There was also a small change observed in the cortex, with cholesterol decreased by 11% in HD vs. control. Generally the data obtained from the mass spectrometry images was comparable to previously published data from Angelini et al in 2021 (Figure 7.4d)²⁸.

7.3.2. Human multiple sclerosis brain tissue

Our main aim using the MSI method on this cohort was to observe cholesterol distribution in the multiple sclerosis brain and to quantify the cholesterol in specific pathological regions of interest, including normal appearing (non-lesion) white and grey matter, demyelinated lesion centres, and areas representing recent inflammatory

demyelination (lesion edge). For comparison, control human brain white and grey matter was also quantified.

Four multiple sclerosis cases were analysed, each chosen due to the different pathological hallmarks highlighted from characterisation by immunohistochemistry (see Figure 7.5). Three control cases were also analysed.

The multiple sclerosis cases were imaged across three separate sections per case (each section 30 μ m distance from the next). The images were normalised to the isotope-labelled standard and show the normalised cholesterol visualised across the tissue section (m/z 518.4105 normalised to m/z 525.4544), displayed as percentage of normalised intensity. Each multiple sclerosis case was then analysed for the regions of interest unique to that brain tissue section (see Figure 7.5) and were used in quantifying cholesterol in the MALDI image to give an average relative amount of cholesterol present in the region of interest (shown in Figure 7.6), with the control tissue undertaken in the same way (see all data in Tables 7.4 and 7.5).

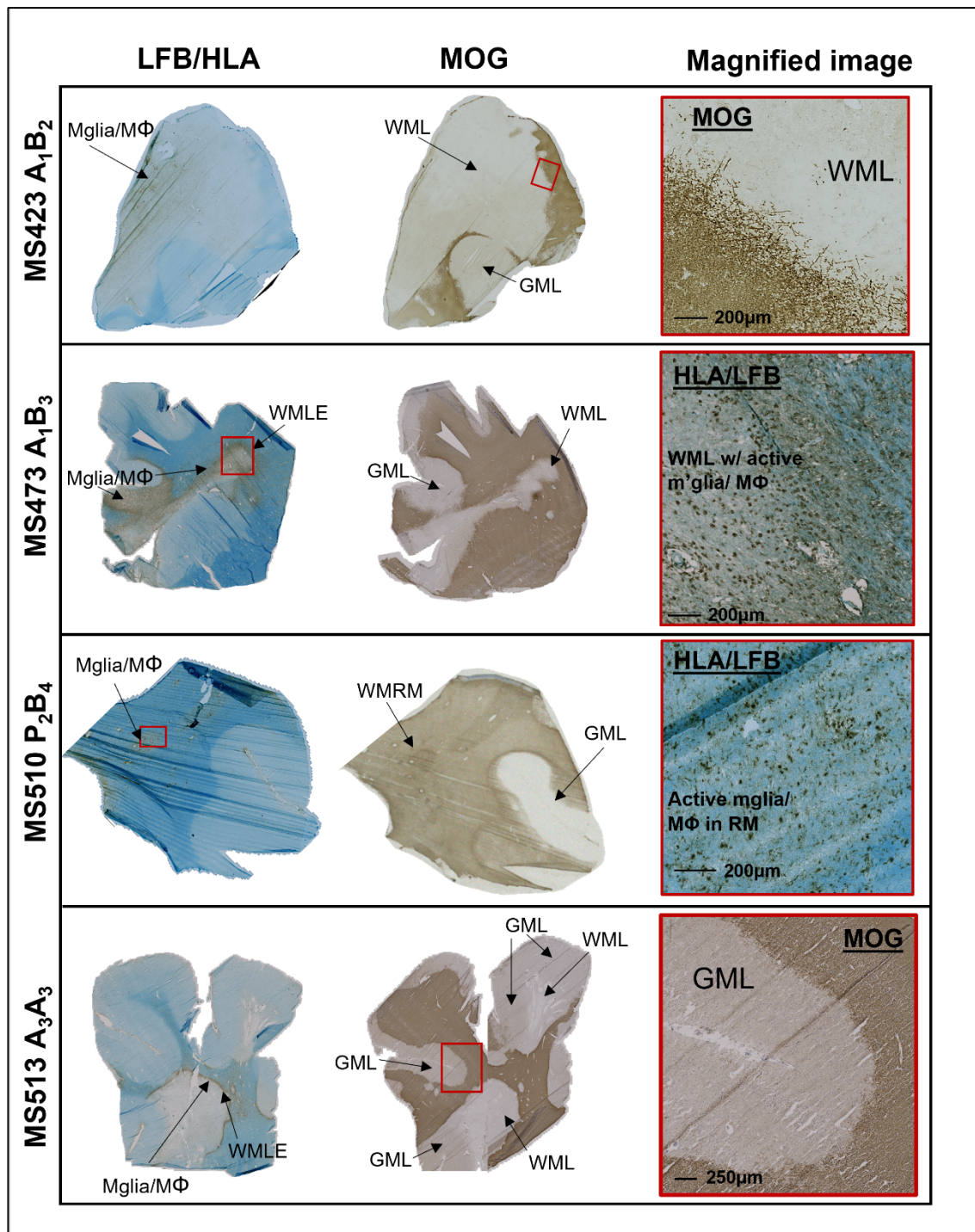


Figure 7.5. The demyelinating and inflammatory pathology seen in the multiple sclerosis cases imaged using the MALDI-MSI method. All four cases imaged show diverse pathology at various levels. The LFB/HLA dual staining shows LFB in blue indicating the differentiation between grey (lighter) and white (darker) matter, and the HLA in brown indicating activated microglia/ macrophage (Mglia/MΦ) cells. The MOG (brown) stain indicates demyelinated lesions and areas of remyelination with active inflammation (when viewed under high magnification). (WML – white matter lesion; GML – grey matter lesion; WMLE – white matter lesion edge; WMRM – white matter remyelination).

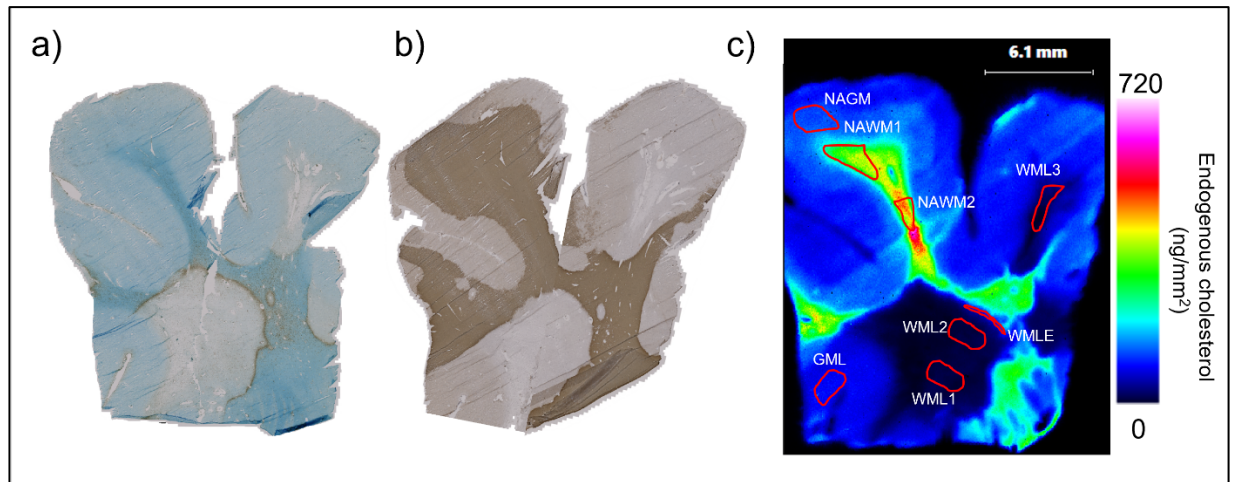


Figure 7.6. Pathological regions of interest quantified for relative amounts of cholesterol using MALDI-MSI. Using the LFB/HLA (a) and MOG (b) staining for case MS513 block A₃A₃, pathological areas of interest were identified and quantified within the MALDI-MS image to calculate the relative amount of cholesterol within those areas (c) (GM – grey matter, WM – white matter, NA – normal appearing, L – lesion centre, LE – lesion edge).

Generally, the MALDI-MS images of normalised cholesterol showed very good correlation to the stained sections of tissue (see Figure 7.6 and 7.7), where the loss of myelin seen from the MOG immunostaining also shows a decrease in cholesterol in the MALDI image, expected given the abundance of cholesterol present in myelin. There were noteworthy and significant changes observed from lesion centres, with both white and grey matter lesion centres having lower levels of cholesterol compared with their normal-appearing counterparts and control tissues. The white matter lesion showed significantly lower levels of cholesterol in comparison to both normal-appearing white matter in multiple sclerosis tissue (16-fold decrease) and control white matter (20-fold decrease) ($P < 0.0001$ for both; Dunn's post-test) (see Figure 7.9).

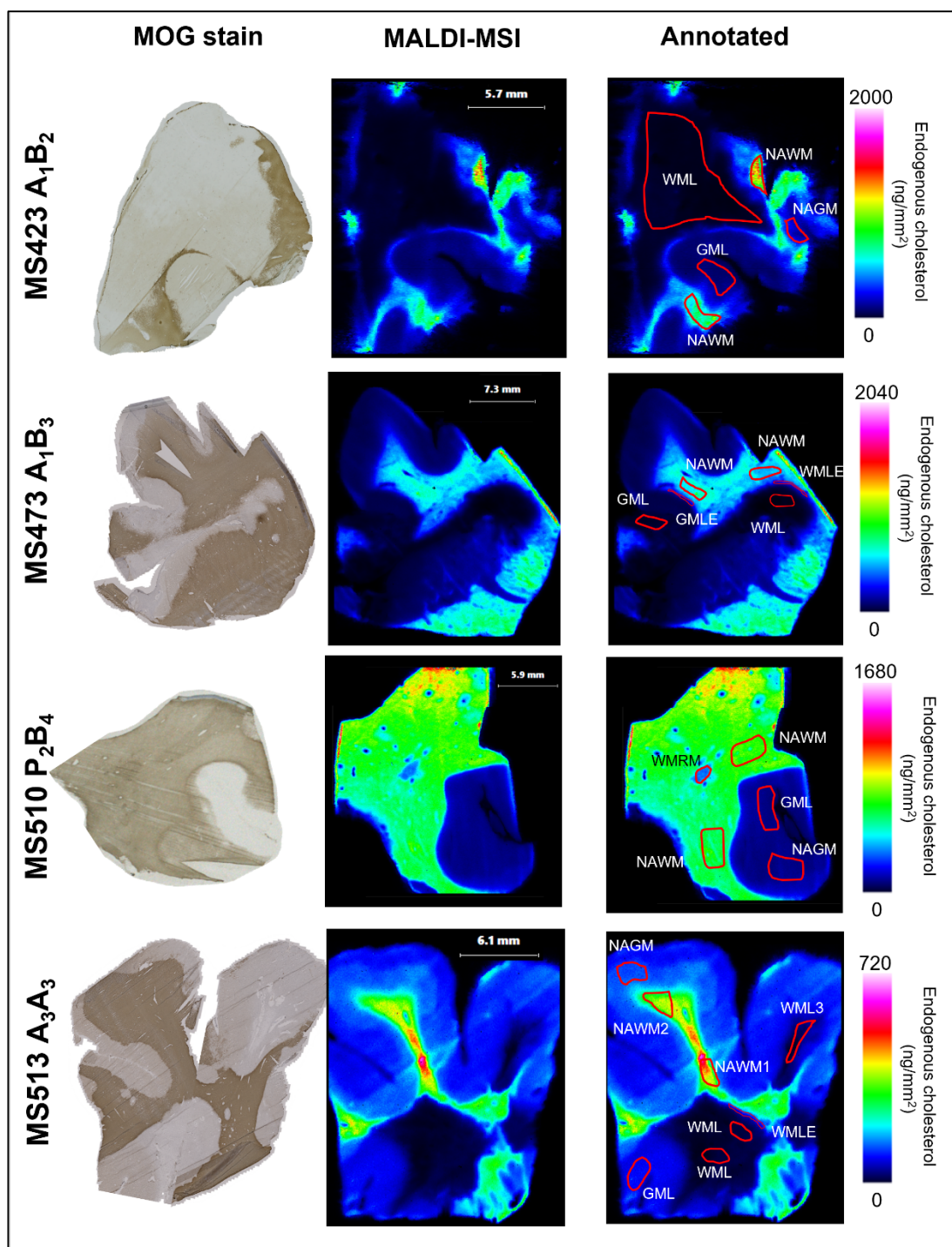


Figure 7.7. MALDI analysis and areas of quantification for calculating relative cholesterol in multiple sclerosis tissue. The four multiple sclerosis cases chosen for analysis above, showing the MALDI image of normalised cholesterol. The MALDI images highlight the vast difference of cholesterol in normal appearing tissue versus white matter lesions (see annotated). It also shows the stark difference in the grey and white matter in terms of cholesterol quantity, with the lower myelin load in grey due to the presence of less myelinated axons²⁹. (GM – grey matter, WM – white matter, NA – normal appearing, L – lesion centre, LE – lesion edge; RM – remyelinating).

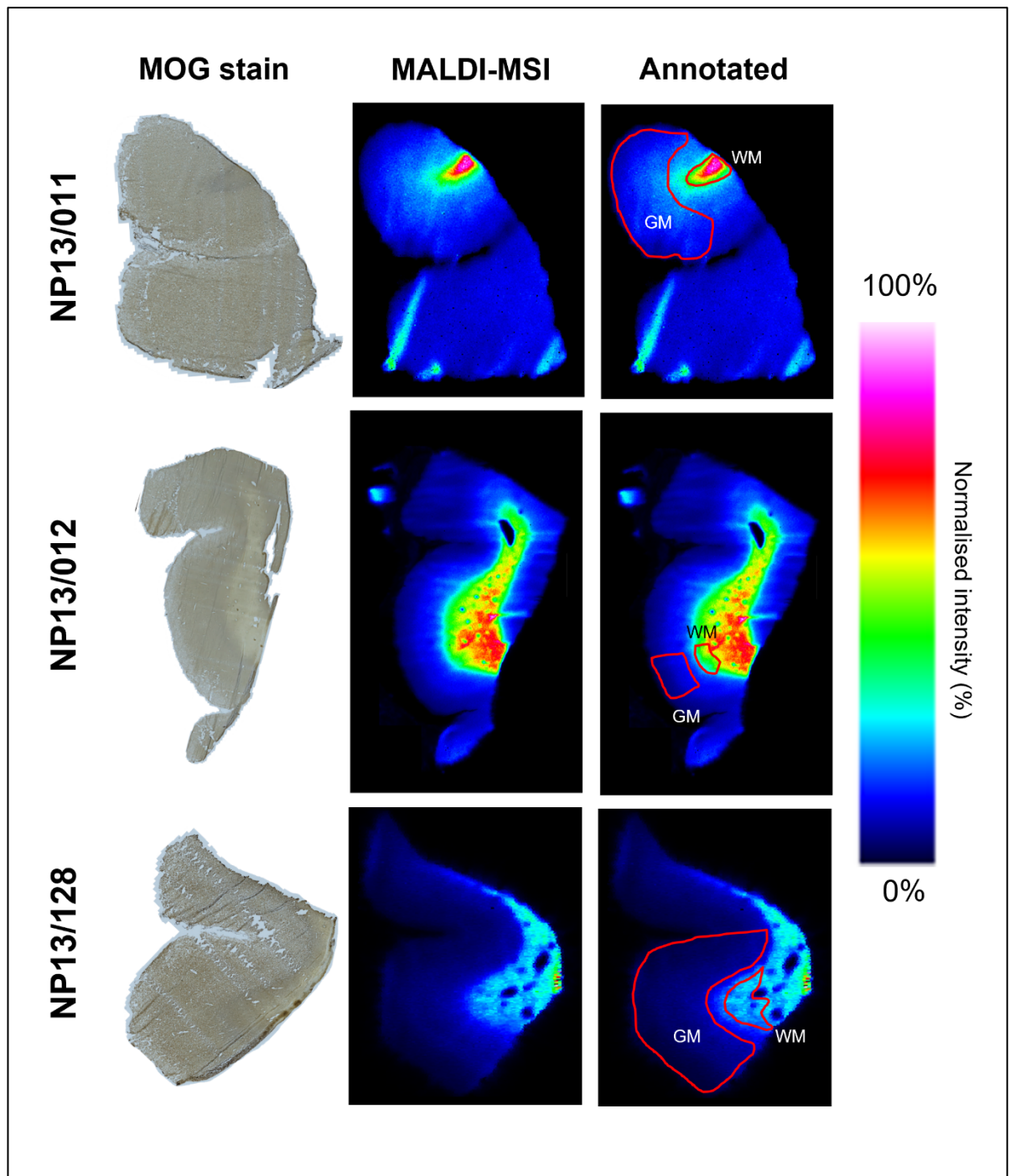


Figure 7.8. MALDI analysis of control brain tissue and areas of quantification used for calculating relative cholesterol. The three neurological control cases chosen for analysis above, showing the MALDI image of normalised cholesterol, and the regions taken for cholesterol quantification, shown in the annotated column highlighted in red. (GM – grey matter; WM – white matter).

The same trend was seen in grey matter tissue but was a far smaller difference in comparison, with no significance observed. The grey matter lesion centre showed a 34% decrease in cholesterol compared with normal appearing grey matter, and a

47% decrease compared with control grey matter. The amount of cholesterol in the grey matter lesion was almost four times the amount compared to the white matter lesion (110.2 ng/mm² compared with 33.2 ng/mm² respectively).

The grey matter lesion edge region, where there is a proliferation of activated microglial/ macrophage cells on the outer rim of the lesion, did contain 2-fold more cholesterol in comparison to the grey matter lesion centre but again, no significance was observed. The grey matter lesion edge also contained more cholesterol compared with both the NAGM and control GM, (220.4 ng/mm² compared with 166.1 ng/mm² and 207.0 ng/mm² respectively – see Figure 7.9 and Tables 7.4 and 7.5). However, the inflammatory grey matter lesion edge was only present in one case, MS473 (n = 3 technical replicates), therefore more cases would need to be analysed to support this observation.

Likewise, the white matter lesion edge of inflammatory active/inactive lesions³⁰ showed an increase of cholesterol compared with the white matter lesion centre, showing significance with a non-parametric Mann-Whitney t test (P=0.0004). The WMLE also displayed a significant decrease in cholesterol in comparison to both the normal appearing white matter (NAWM) (P=0.0001; Mann-Whitney U test) and against the control white matter (P=0.0004; Mann-Whitney U test) (see Figure 7.9). Interestingly, we also observed an increase in cholesterol in a region perceived to be remyelinating in the white matter of case MS510. However, again only one case displayed this pathology, therefore more cases would be needed to explore this finding.

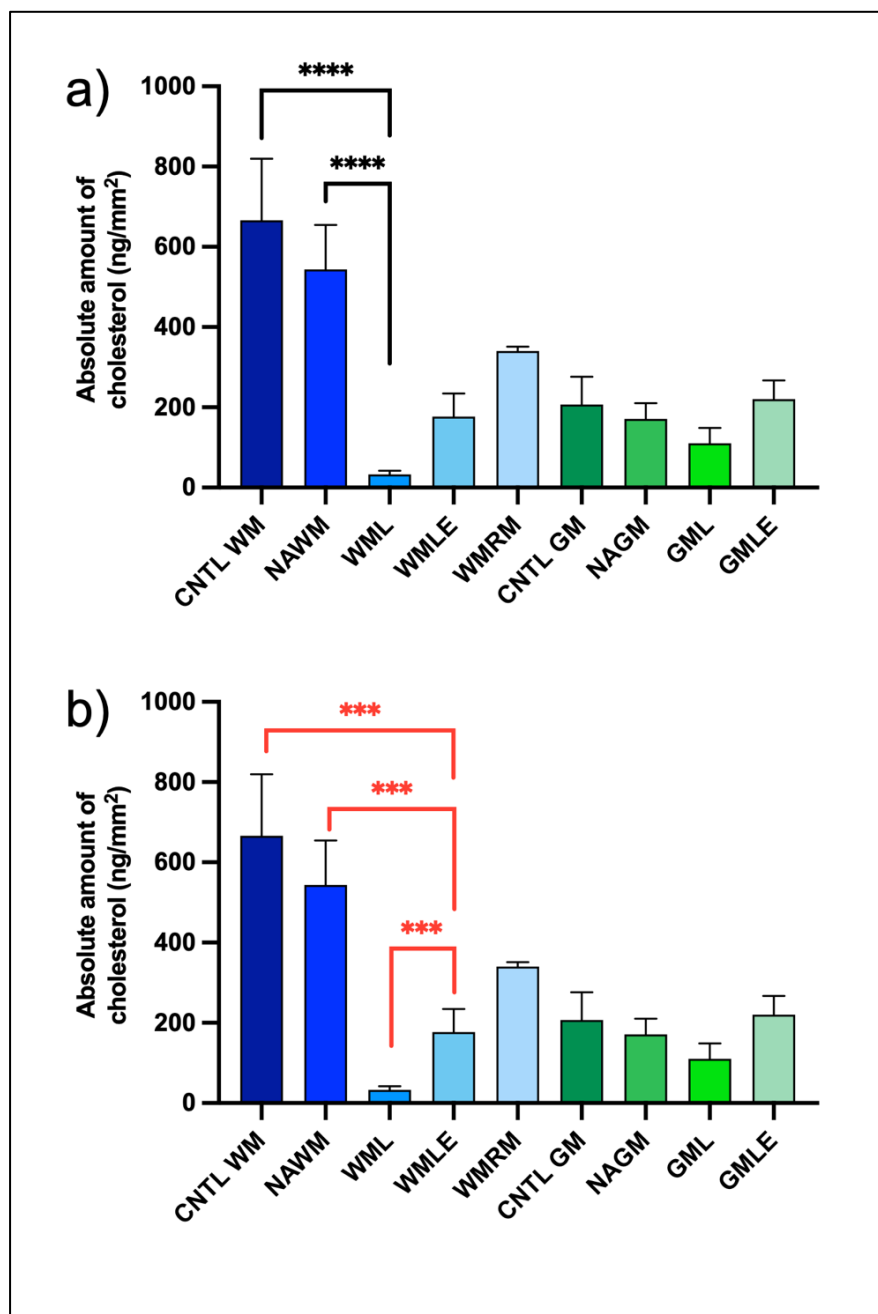


Figure 7.9. Quantifying cholesterol from regions of interest in human multiple sclerosis and control brain tissue. (a) For Kruskal-Wallis with Dunn's (black) there were significant differences observed between multiple sclerosis WML against CNTL WM and NAWM. (b) As part of an effort to further explore our pilot dataset, we conducted a series of uncorrected Mann-Whitney U-tests (red) to highlight those groups that were most different. (CNTL – control; WM – white matter; GM – grey matter; NA – normal-appearing; L – lesion centre; LE – lesion edge; RM – remyelinating).

There was a ~20% decrease in cholesterol in NAWM compared with CNTL WM, with the grey matter (GM) showing the same trend with a ~20% decrease in the

cholesterol present in the NAGM compared with the control GM, with no significance observed (Figure 7.9).

7.3.3. The visualisation of other lipids using Metaspace software

Although in this thesis we have concentrated on the capabilities of our MALDI method to visualise cholesterol, it can be applied to other lipid molecules. The data from the MALDI imaging file contains many other masses of interest. Here, we wanted to show the imaging of other lipid species on other tissue types as an observational study. Our specific interest within this thesis is with sterols, so to identify the other lipids we did not apply our derivatisation method, and used a slightly wider mass range on the mass spectrometer and inputted the RAW data into Metaspace, an online open-source imaging database that can identify and map various lipids within the datasets provided^{26,27}. The lipids listed using MetaSpace are only potential matches, with ITMSⁿ fragmentation needed to confirm these, however we felt this software was a potentially useful software for imaging.

The software analysed the dataset in an imzML format (MassTech converter used for conversion), and isolates masses of interest giving a list of possible molecules and a false discovery rate (FDR) for each to suggest the likelihood of that lipid being present in the sample, therefore the lower the FDR, the more likely it is present in the sample.

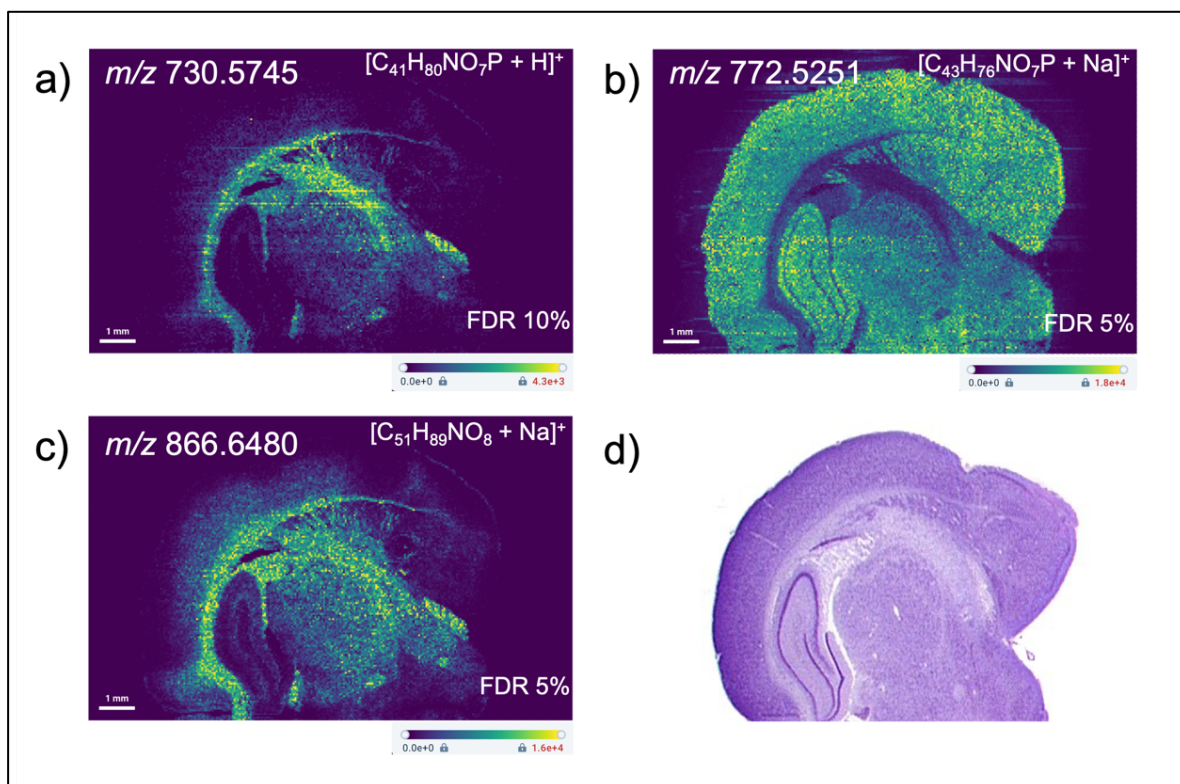


Figure 7.10. Identification of several masses using Metaspacer database software. The Metaspacer database identified a total of 33 masses, three of which are mapped above (a, b, c). The predicted molecular formula is given along with a list of possible structures/ lipids in order of likelihood. (d) A Nissl stained rat coronal brain section³¹. Masses are ± 3 ppm.

Metaspacer identified a total of 33 masses, all ± 3 ppm window (see Table 7.6) in the rat coronal brain tissue analysed with CHCA matrix, with each mass available to visualise across the tissue using the mapping option.

As well as mapping one mass of interest, it has the option to overlap and visualise two masses at the same time to look at how the two differ, or are similar, and which regions they are most abundant (see Figure 7.11).

The three masses discussed in Figure 7.10 are found in different regions of the brain, which is mirrored from the Nissl stained section shown in (d)³¹. For m/z 730.5745 ± 3 ppm and m/z 866.6480 ± 3 ppm, you can see they are almost exclusively found in the white matter tracts within the brain with 866 also seen in neuronal cells (see Figure 7.10c). This contrasts with the final mass m/z 772.5251 ± 3 ppm which is highly abundant in the grey matter and has previously been identified previously in rat brain^{32,33}. The difference is highlighted in Figure 7.11, which maps both m/z 772.5251 ± 3 ppm and m/z 866.6480 ± 3 ppm in conjunction, with slight overlap in the cortex.

The Metaspaces database gave a list of possible ions for all masses identified. For m/z 772.5251 \pm 3 ppm, there were 25 possible molecules identified, with the majority being either phosphatidylethanolamines (PE's) or phosphatidylcholines (PC's). For m/z 866.6480 \pm 3 ppm, there were a total of seven possible molecules identified at 5% FDR, five of which were identified as glucosylceramides (GlcCer's), and the other two as inositolphosphoryl-ceramides (IPC's). For confirmation of the lipids present within the brain, ion fragmentation can be carried out on the masses of interest and the unique fragmentation pattern compared to the molecules identified by Metaspaces. The use of Metaspaces in conjunction with our current cholesterol data for mouse and human tissue could add a vast amount of information on other lipid species present with MSⁿ confirmation and the correct internal standards, and hopefully shows it has the potential to be a useful and insightful tool for MALDI imaging lipidomics.

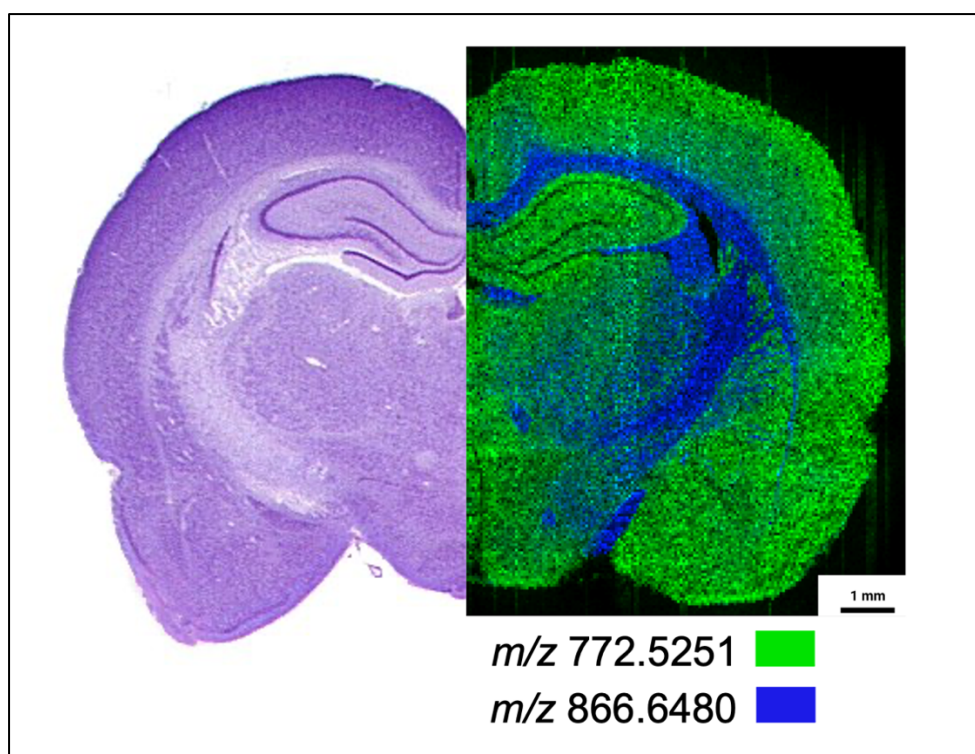


Figure 7.11. Dual mapping of two lipids of interest to explore the abundance across tissue. There are two m/z 's of interest that are mapped, m/z 772.5251 \pm 3 ppm (green) and m/z 866.6480 \pm 3 ppm (blue), where m/z 772 seems to be exclusively within the grey matter, with m/z 866 in the white matter tracts and neurons. This is compared to a Nissl-stained section of rat coronal brain tissue (left)³¹.

Relative amounts of cholesterol (ng/mm ²) for Q150 ^{-/-} control mouse model								
	Corpus callosum	Cerebellar WM	Hippocampus	Pons	Medulla oblongata	Cortex	Cerebellar GM	Caudate putamen
Slide 12 mb1	1155.6	1617.6	602.4	1032.0	980.4	699.6	556.8	614.4
Slide 12 mb2	577.2	765.6	306.0	735.6	651.6	306.0	262.8	423.6
Slide 12 mb3	681.6	849.6	342.0	728.4	674.4	402.0	300.0	472.8
Slide 12 mb4	502.8	650.4	267.6	592.8	556.8	270.0	214.8	387.6
Slide 12 mb5	564.0	775.2	303.6	673.2	673.2	276.0	331.2	424.8
Slide 12 mb6	632.4	831.6	331.2	686.4	652.8	285.6	289.2	499.2
Slide 14 mb1	597.6	807.6	292.8	705.6	709.2	309.6	237.6	453.6
Slide 14 mb2	544.8	734.4	276.0	655.2	638.4	280.8	244.8	384.0
Slide 14 mb3	601.2	720.0	291.6	639.6	736.8	292.8	250.8	416.4
Slide 14 mb4	592.8	765.6	291.6	666.0	718.8	276.0	279.6	424.8
Slide 14 mb5	610.8	800.4	303.6	673.2	760.8	310.8	300.0	430.8
Slide 14 mb6	604.8	813.6	309.6	727.2	762.0	298.8	268.8	439.2
Slide 16 mb1	679.2	800.4	284.4	759.6	805.2	308.4	280.8	447.6
Slide 16 mb2	577.2	724.8	259.2	636.0	735.6	256.8	235.2	373.2
Slide 16 mb3	620.4	704.4	270.0	663.6	705.6	270.0	243.6	405.6
Slide 16 mb4	591.6	632.4	255.6	654.0	702.0	247.2	232.8	376.8
Slide 16 mb5	585.6	693.6	264.0	643.2	722.4	272.4	241.2	393.6
Slide 16 mb6	586.8	649.2	256.8	618.0	711.6	254.4	230.4	385.2
Av	628.1	796.5	306.0	693.9	716.5	312.1	277.8	430.7
SD	138.1	214.9	78.0	95.0	86.2	102.6	76.0	57.3
CV	22.0	27.0	25.5	13.7	12.0	32.9	27.3	13.3

Table 7.2. Full dataset of quantified cholesterol from Q150^{-/-} control mouse brain tissue. Data is shown from all sections analysed from one mouse brain, quantifying eight regions of interest. Dataset highlighted in orange excluded from analysis due to identified outlier. Av – average value; SD – standard deviation; CV – coefficient of variation.

Relative amounts of cholesterol (ng/mm ²) for Q150 ⁺ disease mouse model								
	Corpus callosum	Cerebellar WM	Hippocampus	Pons	Medulla oblongata	Cortex	Cerebellar GM	Caudate putamen
Slide 6 mb1	502.8	699.6	260.4	554.4	598.8	228.0	212.4	409.2
Slide 6 mb2	597.6	733.2	297.6	591.6	628.8	258.0	224.4	380.4
Slide 6 mb3	546.0	657.6	256.2	585.6	537.6	224.4	219.6	394.8
Slide 6 mb4	594.0	732.0	278.4	679.2	588.0	249.6	304.8	435.6
Slide 6 mb5	756.0	864.0	367.2	790.8	679.2	351.6	321.6	494.4
Slide 6 mb6	565.2	609.6	267.6	601.2	495.6	260.4	208.8	376.8
Slide 7 mb1	628.8	877.2	302.4	740.4	572.4	285.6	243.6	466.8
Slide 7 mb2	692.4	822.0	312.0	718.8	568.8	295.2	236.4	464.4
Slide 7 mb3	858.0	1161.6	364.8	866.4	756.0	357.6	386.4	568.8
Slide 7 mb4	802.8	967.2	318.0	697.2	574.8	314.4	246.0	517.2
Slide 7 mb5	583.2	764.4	266.4	626.4	532.8	208.8	248.4	430.8
Slide 7 mb6	865.2	990.0	384.0	673.2	648.0	366.0	348.0	462.0
Slide 8 mb1	615.6	768.0	268.8	522.0	484.8	250.8	220.8	396.0
Slide 8 mb2	418.8	523.2	202.8	406.8	391.2	194.4	193.2	312.0
Slide 8 mb3	440.4	541.2	207.6	430.8	394.8	196.8	187.2	308.4
Slide 8 mb4	441.6	528.0	212.4	436.8	380.4	190.8	177.6	306.0
Slide 8 mb5	440.4	482.4	207.6	439.2	356.4	196.8	175.2	307.2
Slide 8 mb6	433.2	458.4	211.2	428.4	351.6	202.8	180.0	310.8
Av	599.0	732.2	277.0	599.4	530.0	257.3	240.8	407.9
SD	146.0	193.4	57.3	137.0	117.7	59.1	61.1	79.4
CV	24.4	26.4	20.7	22.9	22.2	23.0	25.4	19.5

Table 7.3. Full dataset of quantified cholesterol from Q150⁺ disease mouse brain tissue. Data is shown from all sections analysed from one mouse brain, quantifying eight regions of interest. Av – average value; SD – standard deviation; CV – coefficient of variation.

	Relative amounts of cholesterol (ng/mm ²) for control cases	
	White matter (WM)	Grey matter (GM)
NP13/011 s6	598.8	180.0
NP13/011 s7	586.8	172.8
NP13/011 s8	495.6	163.3
NP13/012 s1	592.8	145.2
NP13/012 s2	543.6	138.0
NP13/012 s3	685.2	177.6
NP13/128 s1	706.8	270.0
NP13/128 s2	789.2	290.0
NP13/128 s3	998.4	326.4
Av	666.36	207.02
SD	153.24	69.26
CV	23.00	33.46

Table 7.4. Full dataset of quantified cholesterol from control human brain tissue. Data is shown from grey and white matter across three cases, with three technical replicates of each. Av – average value; SD – standard deviation; CV – coefficient of variation.

Relative amounts of cholesterol (ng/mm ²) for multiple sclerosis cases							
	NAWM*	WML	WMLE	WMRM	NAGM	GML	GMLE
MS423 s24	568.6	46.0	-	-	264.4	163.2	-
MS423 s25	544.0	38.8	-	-	160.0	130.8	-
MS423 s26	549.6	36.0	-	-	170.4	139.2	-
MS473 s25	409.8	22.8	134.4	-	-	49.2	166.8
MS473 s26	544.2	26.2	214.8	-	-	46.8	240.0
MS473 s27	616.2	26.4	256.8	-	-	62.4	254.4
MS510 s1	634.8	-	-	328.8	140.4	124.8	-
MS510 s2	730.8	-	-	248.0	184.8	130.8	-
MS510 s3	667.8	-	-	345.6	169.2	116.4	-
MS513 s1	351.6	23.6*	102.0	-	128.4	94.8	-
MS513 s2	448.2	36.8*	148.8	-	168.0	120.0	-
MS513 s3	458.4	42.4*	204.0	-	156.0	144.0	-
Av	543.67	33.24	176.80	340.80	166.09	110.20	220.40
SD	111.13	8.61	57.90	10.46	42.31	38.44	46.97
CV	20.44	25.91	32.75	3.07	25.47	34.88	21.31

Table 7.5. Full dataset of quantified cholesterol from human multiple sclerosis brain tissue. Data is shown from different regions of interest

in the grey and white matter across four cases, with three technical replicates of each. * - average value of two or more regions;
NAWM – normal appearing white matter; WML – white matter lesion; WMLE – white matter lesion edge; WMRM – white matter remyelination; NAGM – normal appearing grey matter; GML – grey matter lesion; GMLE – grey matter lesion edge. Av – average value; SD – standard deviation; CV – coefficient of variation.

Annotations	m/z (± 3 ppm)	MSM	Max intensity	FDR (%)
[C ₄₀ H ₈₀ NO ₈ P + H] ⁺	734.5694	0.969	76150.7	5%
[C ₄₄ H ₈₆ NO ₈ P + H] ⁺	788.6163	0.931	30911.9	5%
[C ₄₃ H ₇₆ NO ₇ P + Na] ⁺	772.5251	0.911	36273.3	5%
[C ₄₇ H ₈₂ NO ₇ P + Na] ⁺	826.5721	0.892	17180.9	5%
[C ₄₆ H ₉₂ NO ₁₁ P + H] ⁺	866.6480	0.875	30262.7	5%
[C ₄₁ H ₈₃ N ₂ O ₆ P + H] ⁺	731.6061	0.868	20242.4	5%
[C ₅₁ H ₈₉ NO ₈ + Na] ⁺	866.6480	0.858	30262.7	5%
[C ₄₂ H ₈₄ NO ₈ P + H] ⁺	762.6007	0.857	12489.9	5%
[C ₄₄ H ₈₆ NO ₈ P + K] ⁺	826.5722	0.823	17180.9	5%
[C ₄₀ H ₈₀ NO ₈ P + K] ⁺	772.5253	0.820	36273.3	5%
[C ₄₈ H ₉₃ NO ₉ + K] ⁺	866.6482	0.813	30262.7	5%
[C ₄₅ H ₈₀ NO ₇ P + Na] ⁺	800.5564	0.811	6688.9	5%
[C ₄₄ H ₈₈ NO ₁₁ P + H] ⁺	838.6167	0.808	16531.7	5%
[C ₄₀ H ₆₇ O ₇ P + Na] ⁺	713.4516	0.803	11343.2	5%
[C ₄₄ H ₈₀ NO ₈ P + H] ⁺	782.5694	0.784	34157.3	5%
[C ₄₉ H ₈₅ NO ₈ + Na] ⁺	838.6167	0.783	16531.7	5%
[C ₄₈ H ₉₃ NO ₉ + H] ⁺	828.6923	0.780	6313.5	5%
[C ₄₂ H ₈₄ NO ₇ P + H] ⁺	746.6058	0.778	5389.4	5%
[C ₄₂ H ₈₂ NO ₈ P + H] ⁺	760.5850	0.771	114937.0	5%
[C ₄₅ H ₇₄ NO ₇ P + H] ⁺	772.5275	0.765	40909.2	5%
[C ₄₁ H ₈₀ NO ₇ P + H] ⁺	730.5745	0.748	7058.0	10%
[C ₄₁ H ₈₀ NO ₈ P + H] ⁺	746.5694	0.732	8720.4	10%
[C ₄₆ H ₉₀ NO ₁₀ P + H] ⁺	848.6375	0.729	16042.1	10%
[C ₄₁ H ₇₈ NO ₇ P + H] ⁺	728.5588	0.726	7396.3	10%
[C ₄₆ H ₉₀ NO ₁₁ P + H] ⁺	864.6324	0.720	17950.4	10%
[C ₄₈ H ₉₁ NO ₈ + H] ⁺	810.6817	0.715	7746.4	10%
[C ₃₉ H ₇₆ NO ₇ P + H] ⁺	702.5432	0.710	4740.1	10%
[C ₄₂ H ₈₁ NO ₃ + H] ⁺	648.6289	0.703	3408.5	10%
[C ₄₆ H ₈₄ NO ₈ P + H] ⁺	810.6007	0.702	14215.6	10%
[C ₄₆ H ₈₉ NO ₉ + H] ⁺	800.6610	0.692	3225.8	10%
[C ₅₀ H ₉₁ NO ₉ + H] ⁺	850.6766	0.687	4127.9	10%
[C ₄₅ H ₇₈ NO ₈ P + H] ⁺	792.5537	0.675	12039.0	10%
[C ₃₉ H ₇₇ NO ₄ + H] ⁺	624.5925	0.667	3417.1	10%

Table 7.6. All masses identified in Metaspace from MALDI-MS data from a coronal rat brain section. The table above shows all masses identified using the Metaspace database (total 33) from the coronal rat brain section with CHCA matrix, stating the m/z to 4 d.p ± 3 ppm, the metabolite-signal score (MSM), maximum intensity and organised based on their false discovery rate (FDR) percentage.

7.4. Discussion

During this chapter we have highlighted the potential of our optimised MALDI imaging method and how it can provide insight into cholesterol biology in various diseases, to expand on the knowledge of quantities found in specific brain structures and in areas of pathological interest. Here we have focused on quantifying cholesterol at sites of neurodegeneration, demyelination, remyelination and inflammation. This method could be equally applied to any tissue section, such as cancer biopsies or diseased liver, for example. We also briefly explored the wider, more general use of MALDI imaging in lipidomics, identifying a range of masses using a recently developed open-source online database aimed specifically for mass spectrometry imaging called Metaspace^{26,27}.

The first disease addressed in the proof of principle study was Huntington's disease, and although the work completed had a limited sample number for disease and control (n=1 for each group), the data extracted allowed for the relative quantification of cholesterol in many brain structures and provided visualisation and quantification of cholesterol across the brain in general. Before analysis, we centred around the importance of the striatum/ caudate putamen as a brain structure and its links with cholesterol and HD based from previous literature^{18,34}, however during the course of data analysis, the realisation that there were other key brain regions which were not originally identified as being important structures became apparent.

From our limited results, the striatum/caudate putamen region from the mouse models did not show any clear difference between HD and control, and generally all other brain regions showing a decrease in cholesterol in HD brain structures compared with control. There were two brain structures that did display a marked change between the two groupings, the pons and medulla oblongata, which, alongside the midbrain, comprise the brainstem. This observed change could be due to axon (and myelin) loss from the neuronal loss in the brain, direct neurodegenerative change affecting the brainstem and/or by the inhibition of SREBP activation in the presence of the mutant huntingtin (mHtt) via binding to the SREBP2 and sequestering it³⁵, which in turn would suppress the expression of several key enzymes for cholesterol synthesis, including HMG CoA reductase, 7DHC reductase and CYP51²⁰ to subsequently decrease cholesterol which agrees with published data from the Cattaneo group²⁰⁻²². Although this observation, that requires verifying, is

the first of its kind in terms of cholesterol, brainstem changes are noted in HD. In 2014, Rüb *et al* presented evidence of neurodegeneration of select brainstem nuclei in the pons and medulla oblongata, with a number of previous studies long suggesting and supporting this finding^{19,36–38}. Most interestingly, the study showed that this degeneration of brainstem nuclei did not correlate to the pathology found in the striatum, suggesting an independent mechanism causing the loss of neurons in the brainstem separate from the striatal and cortical pathology¹⁹, which may suggest our results reflect the neurodegeneration observed in this brain structure without observing any change in the striatum. It should be emphasised that these results are based on a limited sample size (n=1 for both HD and control), with more mouse brains, matched for gender, and possibly different mouse models, needed to confirm these results.

Unlike the HD data, the multiple sclerosis data was centred around the different pathologies witnessed in the human multiple sclerosis brain. From the four cases we analysed, it is truly apparent that although each one shows similar hallmarks including demyelinated lesions and inflammation to some degree, the pathologies are completely unique to each individual and their disease course.

Cholesterol is implicated in all these pathological hallmarks, either directly or indirectly but there were also differences identified within the same groupings. We observed around a 70% decrease in quantified cholesterol in the control grey matter and NAGM compared with control white matter and NAWM, respectively. We also observed around a 20% decrease in cholesterol in the normal appearing grey and white matter compared with its control counterparts, which reflects the reduced axon and myelin density found in progressive multiple sclerosis disease from focal demyelination but also retrograde loss of axons, neurons and subsequently myelin^{39,40}.

The demyelination observed within white matter lesions showed significantly less cholesterol compared with the NAWM and CNTL WM due to the loss of myelin of which cholesterol is a major component. This trend was also seen within the grey matter, with less cholesterol in grey matter lesions compared with NAGM and control GM, however the difference in cholesterol between these pathologies was much smaller, possibly due to the various cholesterol rich cell types found within the grey matter (neuronal cell bodies but also different astrocyte subtypes – the glial cells most involved in the synthesis and transport of cholesterol within the brain)^{41,42}.

The inflammation on the white matter lesion edge with activated microglia/macrophage cells (shown magnified in Figure 7.6; MS473 row 2, column 3 – page 201) shows significantly increased cholesterol compared to the demyelinated lesion centre, but significantly less compared with normal appearing and control white matter tissue. This was also seen in the grey matter, where cholesterol was increased in the inflammatory lesion edge, with increased cholesterol even compared with control and normal appearing grey matter. This finding likely reflects the large amount of cholesterol-rich myelin ingested by the phagocytic macrophages and microglia that define this region⁴³.

Finally, white matter remyelination showed decreased amounts of cholesterol compared to both normal appearing white matter in multiple sclerosis and control white matter, but more in comparison to both the white matter lesion and lesion edge. This finding could be of interest considering this mechanism of repair is a natural response to demyelination, where it represents a potential therapeutic target to improve the lives of people with multiple sclerosis⁴⁴. Previous literature researching remyelination has shown important links with cholesterol, with its availability a rate-limiting factor for myelin production in oligodendrocytes, which is why during remyelination cholesterol synthesis genes appear to be upregulated in oligodendrocyte lineage cells (OLC's)⁴⁵.

This suggests that the myelin that was produced to repair the lesion was lacking in cholesterol and therefore a different composition to 'normal' myelin within the brain. Data from 2005 used squalene-synthase knockout mouse models, an enzyme which is key to cholesterol production, and revealed a decreased rate of myelin production which in addition had an irregular composition⁴⁶.

The possibility that other lipids could also be compromised in normal appearing or repair myelin in conjunction with cholesterol could be explored in the future by using the general lipidomic feature of MALDI mentioned in the final part of this study. For example, sphingolipids, specifically ceramides, have been implicated in oligodendrocyte damage and acute demyelination^{47–50}. Our MALDI analysis could explore this pathological feature of multiple sclerosis to further characterise the composition of this newly formed repaired myelin.

Other lipids of interest in both HD and multiple sclerosis are oxysterols, which we have reported on in a previous chapter for multiple sclerosis. 24S-HC is a key oxysterol in neurodegenerative disease and is strongly linked with the loss of neurons

as the enzyme used for its synthesis (CYP46A1) is almost exclusively expressed in neurons⁵¹. The ability to image oxysterols using this MALDI method is unlikely, mainly due to separation techniques needed to distinguish various oxysterols of interest. Another method that could be used is liquid extraction surface analysis, or LESA⁵², which following cholesterol imaging of nearby sections by MALDI, could be used to quantify levels of 24S-HC and other precursors and metabolites of cholesterol in specific pathological regions of interest.

7.5. References

1. Björkhem, I. Crossing the barrier: Oxysterols as cholesterol transporters and metabolic modulators in the brain. *J. Intern. Med.* **260**, 493–508 (2006).
2. Testa, G. *et al.* Changes in brain oxysterols at different stages of Alzheimer's disease: Their involvement in neuroinflammation. *Redox Biol.* **10**, 24–33 (2016).
3. Paul, R. *et al.* Accumulation of Cholesterol and Homocysteine in the Nigrostriatal Pathway of Brain Contributes to the Dopaminergic Neurodegeneration in Mice. *Neuroscience* **388**, 347–356 (2018).
4. Björkhem, I. *et al.* Oxysterols and Parkinson's disease: Evidence that levels of 24S-hydroxycholesterol in cerebrospinal fluid correlates with the duration of the disease. *Neurosci. Lett.* **555**, 102–105 (2013).
5. Theofilopoulos, S. *et al.* Cholestenoic acids regulate motor neuron survival via liver X receptors. *J. Clin. Invest.* **124**, 4829–4842 (2014).
6. Lassmann, H., Brück, W. & Lucchinetti, C. F. The immunopathology of multiple sclerosis: An overview. in *Brain Pathology* vol. 17 210–218 (2007).
7. Goldenberg, M. M. Multiple sclerosis review. *P T* **37**, 175–84 (2012).
8. Morell, P. & Quarles, R. H. Characteristic Composition of Myelin. in *Basic Neurochemistry: Molecular, Cellular and Medical Aspects* (eds. Siegel, G. J., Agranoff, B. W., Albers, R. W., Fisher, S. K. & Uhler, M. D.) 81–82 (Lippincott-Raven, 1999).
9. Howell, O. W. *et al.* Activated microglia mediate axoglial disruption that contributes to axonal injury in multiple sclerosis. *J. Neuropathol. Exp. Neurol.* **69**, 1017–1033 (2010).
10. Rinaldi, F. *et al.* Cortical lesions and cognitive impairment in multiple sclerosis. *Neurol. Sci.* **31**, (2010).
11. Magliozzi, R. *et al.* Meningeal B-cell follicles in secondary progressive multiple sclerosis associate with early onset of disease and severe cortical pathology. *Brain* **130**, 1089–1104 (2007).
12. Lucchinetti, C. *et al.* Heterogeneity of multiple sclerosis lesions: Implications for the pathogenesis of demyelination. *Ann. Neurol.* **47**, 707–717 (2000).
13. Haider, L. *et al.* The topography of demyelination and neurodegeneration in the multiple sclerosis brain. *Brain* **139**, 807–815 (2016).
14. Kutzelnigg, A. *et al.* Cortical demyelination and diffuse white matter injury in multiple sclerosis. *Brain* **128**, 2705–2712 (2005).
15. Frischer, J. M. *et al.* The relation between inflammation and neurodegeneration in multiple sclerosis brains. *Brain* **132**, 1175–1189 (2009).
16. Ross, C. A. & Tabrizi, S. J. Huntington's disease: from molecular pathogenesis to clinical treatment. *Lancet Neurol.* **10**, 83–98 (2011).
17. Tabrizi, S. J. *et al.* Targeting Huntingtin Expression in Patients with Huntington's Disease. *N. Engl. J. Med.* **380**, 2307–2316 (2019).
18. Boussicault, L. *et al.* CYP46A1, the rate-limiting enzyme for cholesterol degradation, is neuroprotective in Huntington's disease. *Brain* **139**, 953–970 (2016).
19. Rüb, U. *et al.* Huntington's Disease (HD): Degeneration of Select Nuclei, Widespread Occurrence of Neuronal Nuclear and Axonal Inclusions in the Brainstem. *Brain Pathol.* **24**, 247–260 (2014).
20. Valenza, M. Dysfunction of the Cholesterol Biosynthetic Pathway in Huntington's Disease. *J. Neurosci.* **25**, 9932–9939 (2005).

21. Valenza, M. *et al.* Disruption of astrocyte-neuron cholesterol cross talk affects neuronal function in Huntington's disease. *Cell Death Differ.* **22**, 690–702 (2015).
22. Valenza, M. & Cattaneo, E. Emerging roles for cholesterol in Huntington's disease. *Trends Neurosci.* **34**, 474–486 (2011).
23. Woodman, B. *et al.* The HdhQ150/Q150 knock-in mouse model of HD and the R6/2 exon 1 model develop comparable and widespread molecular phenotypes. *Brain Res. Bull.* **72**, 83–97 (2007).
24. Valenza, M. *et al.* Progressive dysfunction of the cholesterol biosynthesis pathway in the R6/2 mouse model of Huntington's disease. *Neurobiol. Dis.* **28**, 133–142 (2007).
25. Zuccato, C. *et al.* Loss of Huntingtin-Mediated BDNF Gene Transcription in Huntington's Disease. *Science (80-.).* **293**, 493–498 (2001).
26. Palmer, A. *et al.* FDR-controlled metabolite annotation for high-resolution imaging mass spectrometry. *Nat. Methods* **14**, 57–60 (2017).
27. Alexandrov, T. *et al.* METASPACE: A community-populated knowledge base of spatial metabolomes in health and disease. *bioRxiv* **15**, (2019).
28. Angelini, R. *et al.* Visualizing Cholesterol in the Brain by On-Tissue Derivatization and Quantitative Mass Spectrometry Imaging. *Anal. Chem.* **93**, 4932–4943 (2021).
29. Trapp, B. D. & Herrup, K. Neurons and Neuroglia. in *Youmans and Winn Neurological Surgery* 369 (Elsevier, 2017).
30. Frischer, J. M. *et al.* Clinical and pathological insights into the dynamic nature of the white matter multiple sclerosis plaque. *Ann. Neurol.* **78**, 710–721 (2015).
31. Fiala, J. & Spacek, J. Hippocampus of the Rat. *SynapseWeb University of Texas Austin* <https://synapseweb.clm.utexas.edu/hippocampus-rat>.
32. Zemski Berry, K. A. *et al.* MALDI Imaging of Lipid Biochemistry in Tissues by Mass Spectrometry. *Chem. Rev.* **111**, 6491–6512 (2011).
33. Jackson, S. N., Wang, H.-Y. J. & Woods, A. S. In situ structural characterization of phosphatidylcholines in brain tissue using MALDI-MS/MS. *J. Am. Soc. Mass Spectrom.* **16**, 2052–2056 (2005).
34. Del Toro, D. *et al.* Altered cholesterol homeostasis contributes to enhanced excitotoxicity in Huntington's disease. *J. Neurochem.* **115**, 153–167 (2010).
35. Di Pardo, A. *et al.* Mutant huntingtin interacts with the sterol regulatory element-binding proteins and impairs their nuclear import. *Hum. Mol. Genet.* **29**, 418–431 (2020).
36. Leigh, R. J., Parhad, I. M., Clark, A. W., Buettner-Ennever, J. A. & Folstein, S. E. Brainstem findings in Huntington's disease. *J. Neurol. Sci.* **71**, 247–256 (1985).
37. Koeppen, A. H. The nucleus pontis centralis caudalis in Huntington's disease. *J. Neurol. Sci.* **91**, 129–141 (1989).
38. Rüb, U. *et al.* The human premotor oculomotor brainstem system - can it help to understand oculomotor symptoms in Huntington's disease? *Neuropathol. Appl. Neurobiol.* **35**, 4–15 (2009).
39. Ludwin, S. K. The Pathogenesis of Multiple Sclerosis. *J. Neuropathol. Exp. Neurol.* **65**, 305–318 (2006).
40. Lassmann, H. & van Horssen, J. Oxidative stress and its impact on neurons and glia in multiple sclerosis lesions. *Biochim. Biophys. Acta* **1862**, 506–510 (2015).

41. Li, J. *et al.* Astrocytes in Oligodendrocyte Lineage Development and White Matter Pathology. *Front. Cell. Neurosci.* **10**, (2016).
42. Dai, L. *et al.* Cholesterol Metabolism in Neurodegenerative Diseases: Molecular Mechanisms and Therapeutic Targets. *Mol. Neurobiol.* **58**, 2183–2201 (2021).
43. Greenspan, P., Yu, H., Mao, F. & Gutman, R. L. Cholesterol deposition in macrophages: foam cell formation mediated by cholesterol-enriched oxidized low density lipoprotein. *J. Lipid Res.* **38**, 101–109 (1997).
44. Franklin, R. J. M. & Ffrench-Constant, C. Regenerating CNS myelin — from mechanisms to experimental medicines. *Nat. Rev. Neurosci.* **18**, 753–769 (2017).
45. Voskuhl, R. R. *et al.* Gene expression in oligodendrocytes during remyelination reveals cholesterol homeostasis as a therapeutic target in multiple sclerosis. *Proc. Natl. Acad. Sci.* **116**, 10130–10139 (2019).
46. Saher, G. *et al.* High cholesterol level is essential for myelin membrane growth. *Nat. Neurosci.* **8**, 468–475 (2005).
47. Wheeler, D., Bandaru, V. V. R., Calabresi, P. A., Nath, A. & Haughey, N. J. A defect of sphingolipid metabolism modifies the properties of normal appearing white matter in multiple sclerosis. *Brain* **131**, 3092–3102 (2008).
48. Podbielska, M. *et al.* Cytokine-induced release of ceramide-enriched exosomes as a mediator of cell death signaling in an oligodendroglioma cell line. *J. Lipid Res.* **57**, 2028–2039 (2016).
49. Kim, S., Steelman, A. J., Zhang, Y., Kinney, H. C. & Li, J. Aberrant Upregulation of Astroglial Ceramide Potentiates Oligodendrocyte Injury. *Brain Pathol.* **22**, 41–57 (2012).
50. Kurz, J. *et al.* The relevance of ceramides and their synthesizing enzymes for multiple sclerosis. *Clin. Sci.* **132**, 1963–1976 (2018).
51. Leoni, V. *et al.* Changes in human plasma levels of the brain specific oxysterol 24S-hydroxycholesterol during progression of multiple sclerosis. *Neurosci. Lett.* **331**, 163–166 (2002).
52. Yutuc, E. *et al.* Localization of sterols and oxysterols in mouse brain reveals distinct spatial cholesterol metabolism. *Proc. Natl. Acad. Sci.* **117**, 5749–5760 (2020).

Chapter 8: General conclusions

8.1. Concluding findings

Throughout this thesis, sterols and their potential role in neurodegenerative diseases have been discussed. We were successfully able to analyse both fluid and tissue samples from a subset of neurological conditions including CTX, AD and multiple sclerosis, and successfully optimised a mass spectrometry imaging method for the visualisation and quantification of cholesterol across intact tissue section and applied that method to disease models, discovering significant differences in cholesterol within the human multiple sclerosis brain.

The CTX analysis in Chapter 3 gave us the ability to analyse all three biomaterials and meant we could investigate differences in both the periphery and within the brain itself. The results of the three different materials complimented each other, showing vast increases in the products of the 7α -hydroxylation pathway including 7α -HC, $7\alpha,12$ -diHC and cholestanol compared with control, and emphasised the compensatory mechanisms at play after the detrimental effects to the CYP27A1 enzyme and the subsequent restriction of the (25R)26-hydroxylation pathway.

For the other neurodegenerative diseases addressed in this thesis only the brain tissue was available to us for analysis, however this gave us the unique opportunity to look within the human brain tissue itself rather than analysing the periphery which has been previously reported in the literature¹⁻⁶. For the analysis in Chapter 4, using the AD/ MCI disease diagnosis did not reveal many trends within the data. However, splitting the cohort based on the ApoE genotyping did show significant and interesting changes in 24S,25-EC and (25R)26-HC, the latter of which showed large increases in Apoε2 and Apoε4 which have been linked to hyperlipoproteinemia type III or atherosclerosis^{7,8} and AD diagnosis, respectively⁹⁻¹¹.

In Chapter 5, again (25R)26-HC was identified as being increased in the multiple sclerosis cohort compared with control tissue. This sterol has been identified as a biomarker for blood brain barrier (BBB) disruption¹², which is a clinical feature of multiple sclerosis, AD and can be a cerebrovascular effect of atherosclerosis via hypertension over time^{13,14}. The high (25R)26-HC in brain tissue reflects the influx across the defective BBB and into the CNS.

24S-HC also showed decreased levels in multiple sclerosis compared with control tissue, with the 24S-HC/(25R)26-HC ratio significantly different between multiple sclerosis and control groupings, and highlights the neuronal loss seen within

established multiple sclerosis. The cohort from this study was progressive, which is characterised by extensive cortical and white matter demyelination, widespread inflammation, and considerable neuronal and axonal loss. Levels of 24S-HC have long been associated as a biomarker of neurodegeneration^{12,15}, with our work also supporting this notion.

In Chapters 4 and 5, we also discovered the presence of both 25-HCO and (25R)26-HCO in human brain tissue. These analytes were quantified in the AD, MCI, multiple sclerosis and control human brain tissue at low levels, and with previous literature identifying (25R)26-HCO in placenta and citing the enzyme HSD3B1 responsible for its formation¹⁶ with the enzyme present in the brain¹⁷, future work could be done to look at whether this same enzyme is responsible for the formation of 25-HCO.

Although homogenisation was the primary methodology utilised throughout this work, the tissue destruction during the process meant that optimising an MS imaging method was a key aim for this thesis. Our interest was in cholesterol due to the abundance found within the brain, with the main objectives to both visualise and quantify cholesterol across intact tissue sections which was successfully achieved in Chapter 6. The definitive reason for the development of this MSI method was to apply it to disease tissues, which is something explored in Chapter 7. Several cases from the multiple sclerosis tissue cohort used in Chapter 5 for homogenisation were also analysed for MALDI-MSI, which allowed us to understand and visualise for the first time the significant loss of cholesterol in lesioned areas in the multiple sclerosis brain. In addition, it also explored the levels of cholesterol in inflammatory regions of interest and looked at the loss of cholesterol from the myelin structure, providing a quantitative value for myelin/ axonal loss in the normal appearing tissue, which builds upon the information offered by standard immunohistochemical staining techniques. This was also the case in the HD mouse brain tissue, and highlighted cholesterol differences in areas previously thought to be unaffected in terms of cholesterol, including the pons and medulla. This analysis highlights the need for this cholesterol imaging method, showing significant changes in cholesterol within the brain. The application to not just these diseases but also others including cancer, Alzheimer's, motor neurons and Parkinson's could shed light on region-specific cholesterol differences in the brain and beyond.

Finally, our preliminary data for the application of our method for other lipid species paves the way for future work to characterise additional lipids in the brain, with the possibility for identification using ion-trap fragmentation and quantifying the levels too with the use of a suitable isotope-labelled standard. This could help build a clearer picture for diseases such as multiple sclerosis, where these specific lipid species are quantitatively unknown and could be key to understanding the mechanisms at play and aid in targeting potential therapeutics to alleviate certain pathologies.

8.2. Limitations of this work

Although this work provided a large amount of data, it did have some limitations which centred mainly around the samples for analysis.

Generally, across all chapters the sample sizes were limited with small n numbers for many of the groupings, for example the sample size in Chapter 3 for CTX was n=4 for plasma and CSF and n=1 for brain tissue which is mainly due to CTX being a rare disease and therefore few samples are available, with control samples only n=1. Another example is within the imaging of multiple sclerosis brain tissue in Chapter 7 there was only one case identified with a specified pathological hallmark (remyelinating tissue). These examples did affect the ability to carry out statistical analysis which was lacking in certain chapters of this thesis. To overcome this limitation, more samples need to be analysed to reinforce our current findings. Another limitation centred around the acquisition and condition of some of the brain tissue samples analysed. For the CTX brain tissue used in Chapter 3, storage was subpar and results in the tissue becoming porous. This meant the analysis was unreliable so to combat this limitation we normalised all data by cholesterol. For the multiple sclerosis homogenate brain tissue used in Chapter 5, the acquisition of the tissue was not optimal by using cryostat shavings instead of a piece of tissue and meant the weight of the tissue was unreliable. Again, to overcome this we normalised all data by cholesterol, although we were unable to confirm whether cholesterol was different in multiple sclerosis tissue compared to control due to the inability to accurately weigh the tissue. Therefore, we could not comment on any changes we observed in cholesterol content as it may have been due to increased tissue mass

rather than a true biochemical difference. The assumption of unchanged cholesterol was admittedly a flaw for the results reported in Chapter 5.

For an ideal brain tissue study, the set up would be the methodology seen in Chapter 4 (Alzheimer's), where a piece of tissue is extracted for the same region of interest across all brains and pre-weighed. We are aware this is rare and slightly unrealistic but having a set method for sample acquisition could reduce the concern over data variation.

The final limitation identified was the lack of certain demographics for some of the cases analysed. For example, within Chapter 4, two samples from the cohort were not provided with any identification and subsequent demographic information, and therefore had to be excluded from all analysis. There would also ideally have been a better sex-match between the control and disease samples, for example Chapter 4 where the cohort was predominantly male, with the females within the cohort mainly being control samples.

Additional information that could have split the cohorts further could also have been of use e.g. therapies, Braak staging etc, however this was less a limitation and more a preference for analysis.

8.3. Future directions

This work has highlighted the importance of oxysterols in neurodegenerative diseases, and therefore our fluid and tissue homogenisation methodology could be applied to other diseases including Parkinson's and motor neuron disease (MND) to analyse the peripheral and in situ oxysterol profiles within these diseases. Enzymatic work could also be carried out to further understand the pathways that produce 25-HCO.

The imaging method developed and optimised during this work also has potential to be applied to other disease tissue. Our MALDI-MSI method has focused on cholesterol in multiple sclerosis and Huntington's disease tissue, however there is opportunity to analyse other diseases including Alzheimer's disease, motor neuron disease and other non-neurological diseases such as cancer. There is also opportunity to expand our research for further lipid profiling within these disease tissues as mentioned previously. This includes further positive mode MS analysis, to look for lipids such as galactosyl-ceramides which are abundant in the white matter of the

brain, and also utilising negative ion mode to analyse other myelin lipids including sulfatides¹⁸.

Our focus within this work was cholesterol for imaging, however our homogenisation methodology has highlighted the differences of oxysterols within these tissues. Although MALDI-MSI would not be feasible for oxysterol analysis due to the need for chromatographic separation, other established methodology could be applied to analyse these molecules on intact tissue and within pathological regions of interest. Liquid extraction for surface analysis (LESA) is a novel technique that combines micro extraction with LC-MS¹⁹ to characterize the localisation of cholesterol precursors and metabolites across tissue sections. This could allow us to quantify oxysterols in specific pathological regions, for example the lesion edge of demyelinated lesions in multiple sclerosis brain tissue which are laden with active microglia/macrophage cells.

8.4. References

1. Crick, P. J. *et al.* Reduced Plasma Levels of 25-Hydroxycholesterol and Increased Cerebrospinal Fluid Levels of Bile Acid Precursors in Multiple Sclerosis Patients. *Mol. Neurobiol.* **54**, 8009–8020 (2017).
2. Griffiths, W. J. *et al.* Concentrations of bile acid precursors in cerebrospinal fluid of Alzheimer's disease patients. *Free Radic. Biol. Med.* **134**, 42–52 (2019).
3. Hughes, T. M. *et al.* Markers of Cholesterol Metabolism in the Brain Show Stronger Associations with Cerebrovascular Disease than Alzheimer's Disease. *J. Alzheimer's Dis.* **30**, 53–61 (2012).
4. Leoni, V. *et al.* Changes in human plasma levels of the brain specific oxysterol 24S-hydroxycholesterol during progression of multiple sclerosis. *Neurosci. Lett.* **331**, 163–166 (2002).
5. Teunissen, C. . *et al.* Decreased levels of the brain specific 24S-hydroxycholesterol and cholesterol precursors in serum of multiple sclerosis patients. *Neurosci. Lett.* **347**, 159–162 (2003).
6. Novakova, L. *et al.* Reduced cerebrospinal fluid concentrations of oxysterols in response to natalizumab treatment of relapsing remitting multiple sclerosis. *J. Neurol. Sci.* **358**, 201–206 (2015).
7. Sullivan, P. M., Mezdour, H., Quarfordt, S. H. & Maeda, N. Type III hyperlipoproteinemia and spontaneous atherosclerosis in mice resulting from gene replacement of mouse Apoe with human Apoe*2. *J. Clin. Invest.* **102**, 130–135 (1998).
8. Huang, Y., Schwendner, S. W., Rall, S. C., Sanan, D. A. & Mahley, R. W. Apolipoprotein E2 transgenic rabbits. Modulation of the type III hyperlipoproteinemic phenotype by estrogen and occurrence of spontaneous atherosclerosis. *J. Biol. Chem.* **272**, 22685–22694 (1997).
9. Gerritsen, G. *et al.* ApoE2-associated hypertriglyceridemia is ameliorated by increased levels of apoA-V but unaffected by apoC-III deficiency. *J. Lipid Res.* **49**, 1048–1055 (2008).
10. Castellano, J. M. *et al.* Human apoE Isoforms Differentially Regulate Brain Amyloid- β Peptide Clearance. *Sci. Transl. Med.* **3**, (2011).
11. Guo, T. *et al.* Molecular and cellular mechanisms underlying the pathogenesis of Alzheimer's disease. *Mol. Neurodegener.* **15**, 1–37 (2020).
12. Leoni, V. & Caccia, C. Oxysterols as biomarkers in neurodegenerative diseases. *Chem. Phys. Lipids* **164**, 515–524 (2011).
13. Hussain, B., Fang, C. & Chang, J. Blood–Brain Barrier Breakdown: An Emerging Biomarker of Cognitive Impairment in Normal Aging and Dementia. *Front. Neurosci.* **15**, (2021).
14. Shabir, O., Berwick, J. & Francis, S. E. Neurovascular dysfunction in vascular dementia, Alzheimer's and atherosclerosis. *BMC Neurosci.* **19**, 62 (2018).

15. Heverin, M. *et al.* Changes in the levels of cerebral and extracerebral sterols in the brain of patients with Alzheimer's disease. *J. Lipid Res.* **45**, 186–193 (2004).
16. Dickson, A. *et al.* HSD3B1 is an Oxysterol 3 β -Hydroxysteroid Dehydrogenase in Human Placenta. *bioRxiv* 2022.04.01.486576 (2022) doi:10.1101/2022.04.01.486576.
17. Uhlén, M. *et al.* Tissue-based map of the human proteome. *Science* (80-.). **347**, (2015).
18. Zemski Berry, K. A. *et al.* MALDI Imaging of Lipid Biochemistry in Tissues by Mass Spectrometry. *Chem. Rev.* **111**, 6491–6512 (2011).
19. Yutuc, E. *et al.* Localization of sterols and oxysterols in mouse brain reveals distinct spatial cholesterol metabolism. *Proc. Natl. Acad. Sci.* **117**, 5749–5760 (2020).

Appendix

List of Publications

Bevan, R.J., Evans, R., Griffiths, L., *et al.* Meningeal inflammation and cortical demyelination in acute multiple sclerosis. *Ann. Neurol.* **84**, 829 - 842 (2018).

Griffiths, L. *et al.* Substantial subpial cortical demyelination in progressive multiple sclerosis: have we underestimated the extent of cortical pathology? *Neuroimmunol Neuroinflammation.* **7**, 51 - 67 (2020).

Angelini, R., Yutuc, E., Wyatt, M.F., Newton, J., Yusuf, F.A., Griffiths, L. *et al.* Visualising cholesterol in the brain by on-tissue derivatisation and quantitative mass spectrometry imaging. *Anal. Chem.* **93**, 4932 – 4943 (2021).

Yutuc, E., Dickson, A.L., Pacciarini, M., Griffiths, L. *et al.* Deep mining of oxysterols and cholestenoic acids in human plasma and cerebrospinal fluid: Quantification using isotope dilution mass spectrometry. *Anal. Chim. Acta.* **1154** (2021).

Hoflinger, P., Hauser, S., Yutuc, E., Hengel, H., Griffiths, L. *et al.* Metabolic profiling in serum, cerebrospinal fluid, and brain of patients with cerebrotendinous xanthomatosis. *J. Lipid. Res.* **62** (2021).

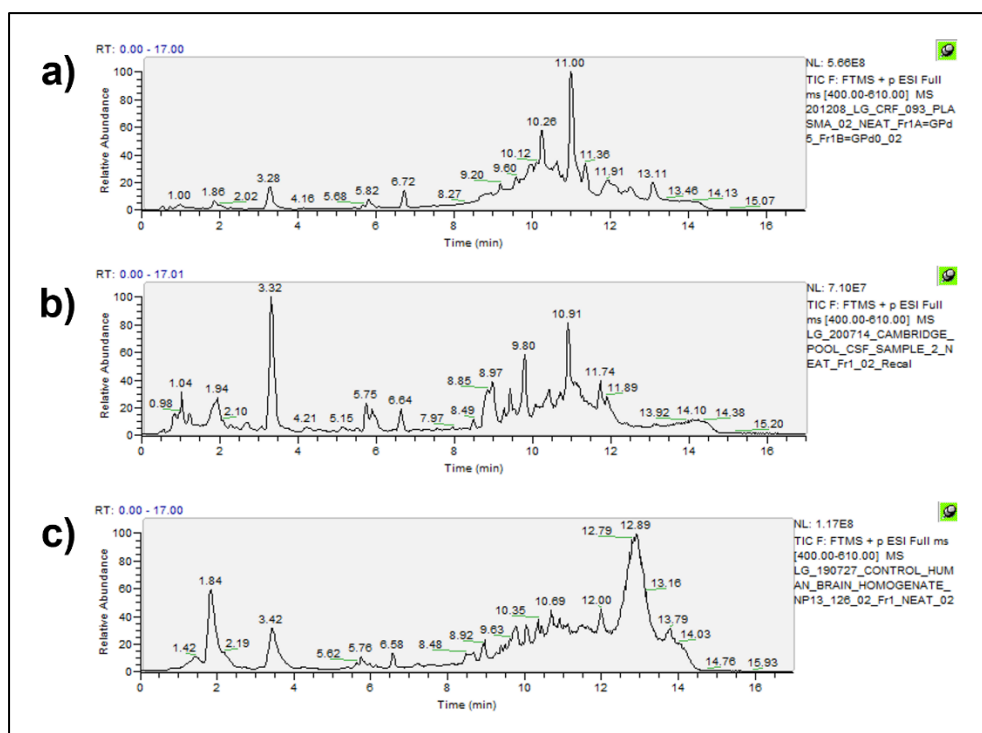


Figure 9.1. The TIC spectra from 17-minute run for (a) QC plasma, (b) pooled QC CSF, and (c) control brain tissue homogenate from Fraction 1.

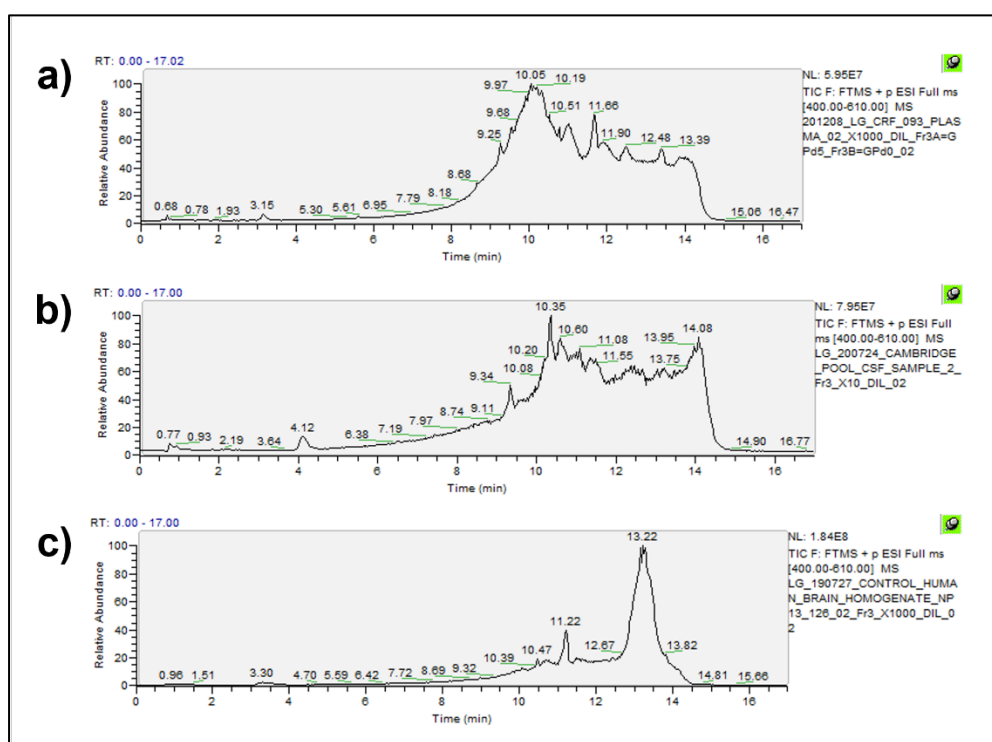
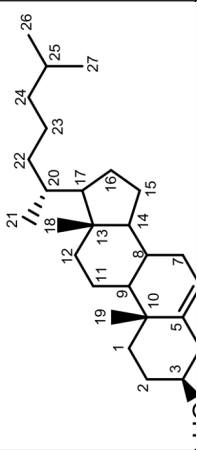
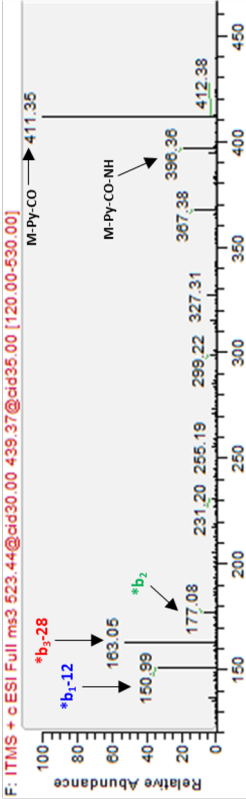
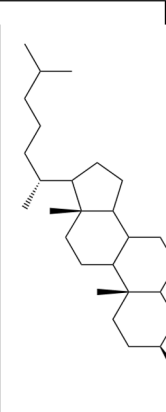
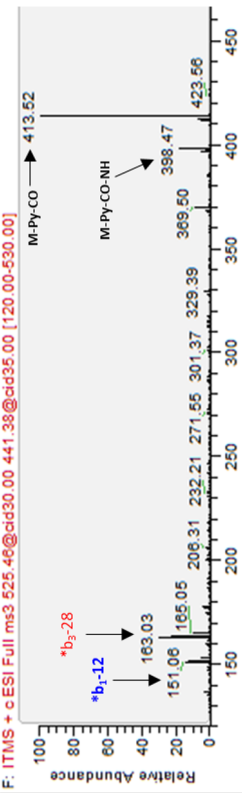
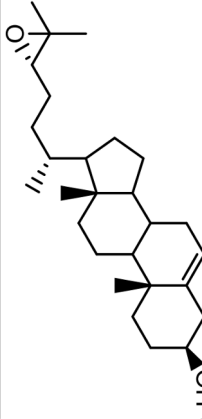
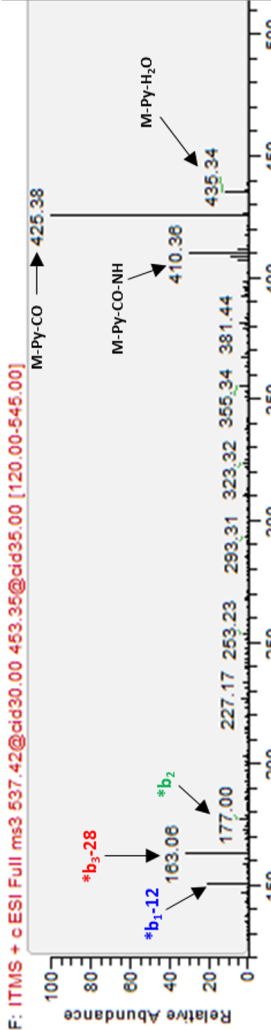
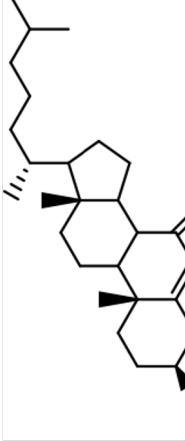
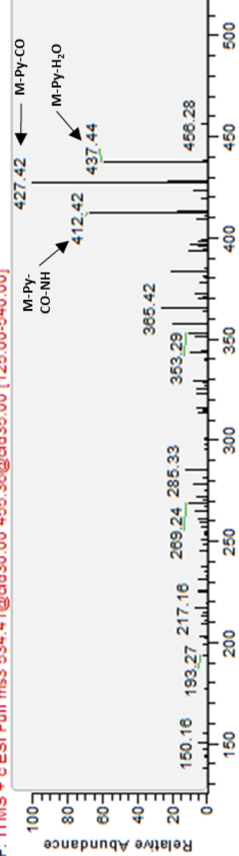
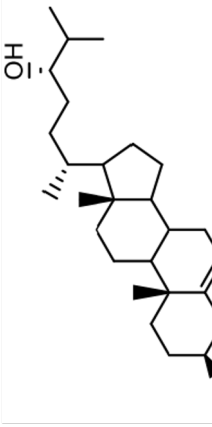
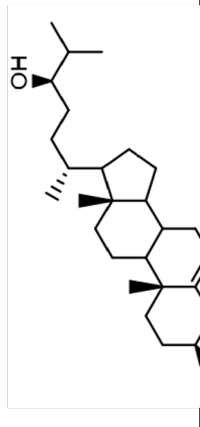
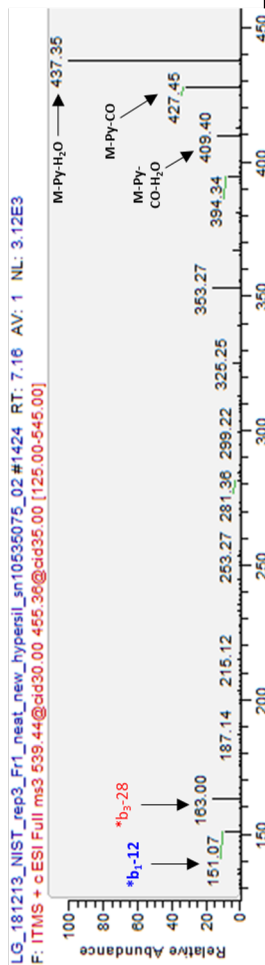


Figure 9.2. The TIC spectra from 17-minute run for (a) QC plasma, (b) pooled QC CSF, and (c) control brain tissue homogenate from Fraction 3.

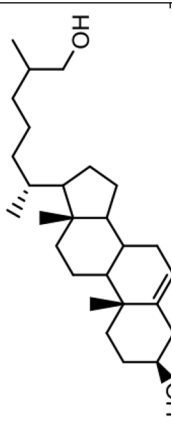
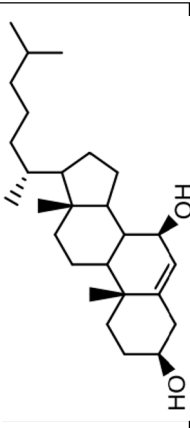
Sterol name	Abbreviation	Elemental composition	Originated structure mass (m/z)	$m/z \pm 5\text{ppm}$ (GpD5)	$m/z \pm 5\text{ppm}$ (GpD0)	Non (NE)/ enzymatic (E) formation	Structure
Cholest-5-en-3 β -ol	Cholesterol	C ₂₇ H ₄₆ O	386.3549	523.4414	518.4105	E	
<div>  <p>F: ITMS + c ESI Full ms3 523.44@dd30.00 439.37@dd35.00 [120.00-530.00]</p> </div>							
3 β -cholestanol	Cholestanol	C ₂₇ H ₄₈ O	388.3705	525.4575	-	E	
<div>  <p>F: ITMS + c ESI Full ms3 525.46@dd30.00 441.38@dd35.00 [120.00-530.00]</p> </div>							

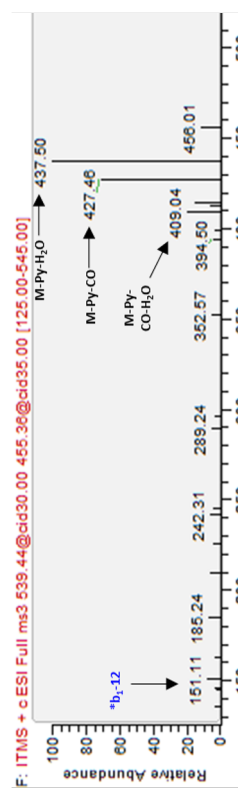
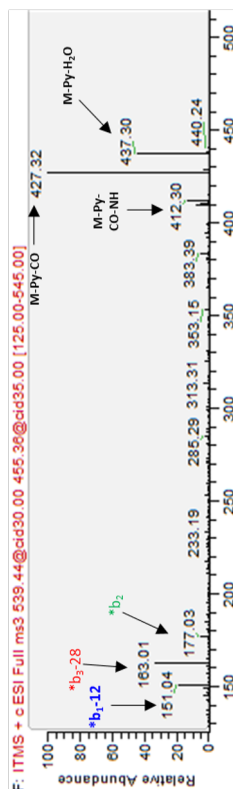
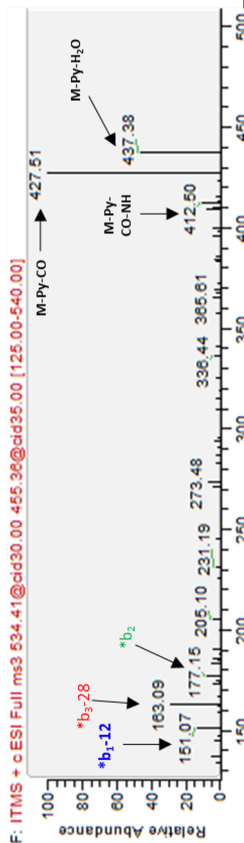
24S,25-Epoxycholest-5-ene-3 β -ol	24S,25-EC	C ₂₇ H ₄₄ O ₂	400.3341	537.4206	532.3898	E	
<p>F: ITMS + c ESI Full ms3 537.42@dd30.00 453.35@dd35.00 [120.00-545.00]</p> 							
3 β -Hydroxycholest-5-en-7-one	7-OC	C ₂₇ H ₄₄ O ₂	400.3341	-	534.4054	NE + E	
<p>F: ITMS + c ESI Full ms3 534.41@dd30.00 455.36@dd35.00 [125.00-540.00]</p> 							

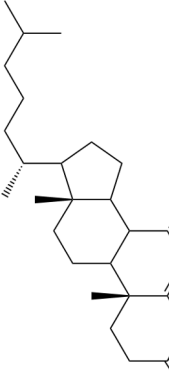
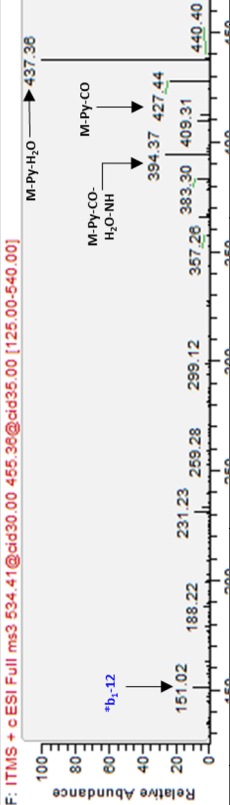
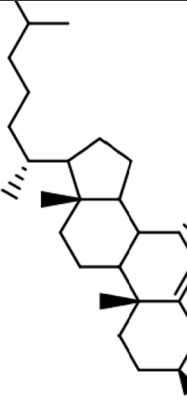
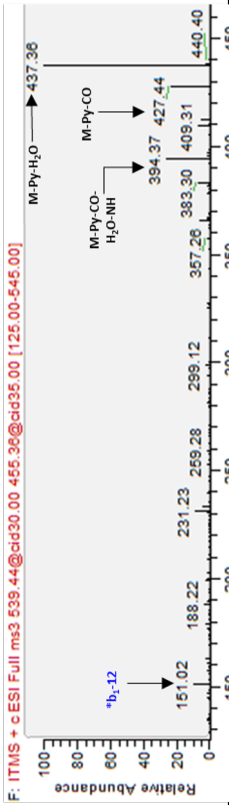
Cholest-5-ene-3 β ,24S-diol	24S-HC	C ₂₇ H ₄₆ O ₂	402.3498	539.4368	-	E	
Cholest-5-ene-3 β ,24R-diol	24R-HC	C ₂₇ H ₄₆ O ₂	402.3498	539.4368	-	E	

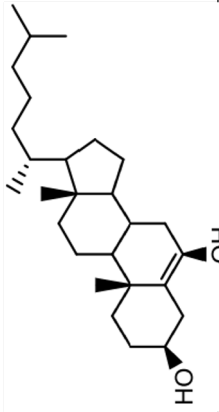
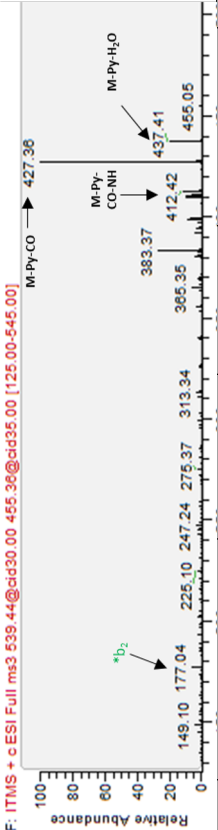
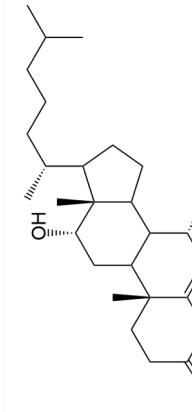
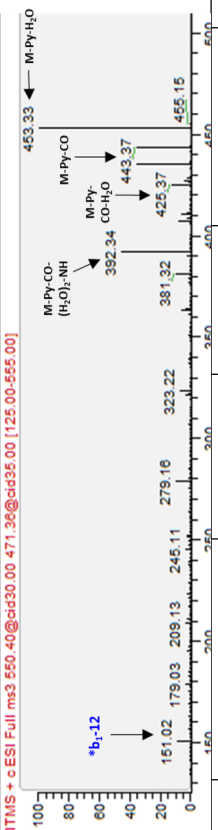
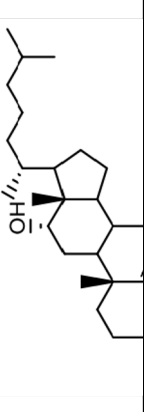


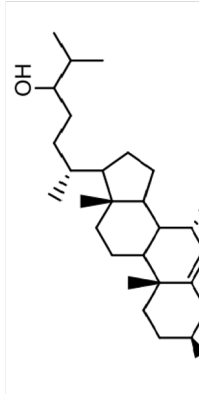
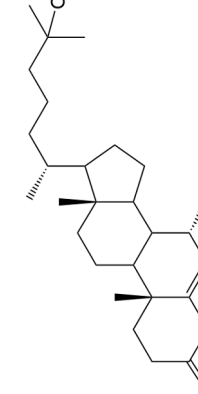
25-hydroxy-4-cholesten-3-one	25-HCO	C ₂₇ H ₄₄ O ₂	400.3341	-	534.4054	E	
Cholest-5-ene-3β,25-diol	25-HC	C ₂₇ H ₄₆ O ₂	402.3498	539.4368	-	NE + E	
(25R)26-hydroxy-4-cholesten-3-one	(25R)26-HCO	C ₂₇ H ₄₄ O ₂	400.3341	-	534.4054	E	

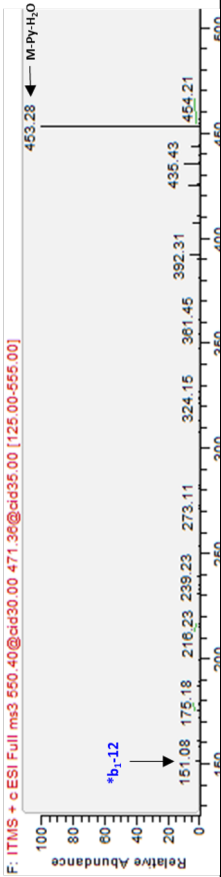
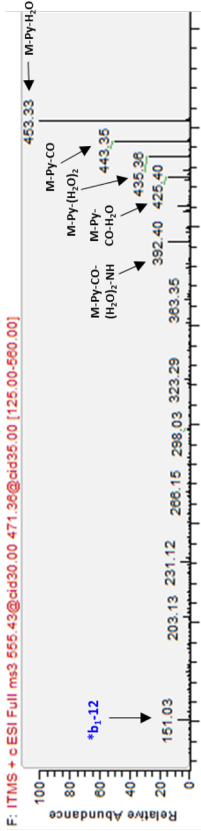
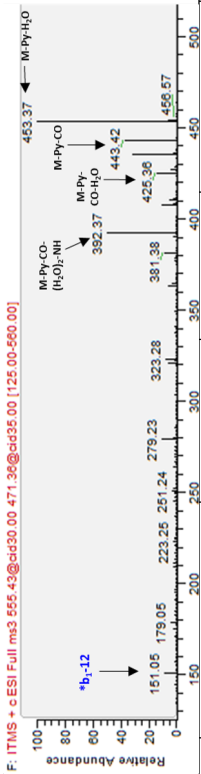
Cholest-5-ene-3 β -(25R)26-diol	(25R)26-HC	C ₂₇ H ₄₆ O ₂	402.3498	539.4368	-	E	
Cholest-5-ene-3 β ,7 β -diol	7 β -HC	C ₂₇ H ₄₆ O ₂	402.3498	539.4368	534.4054	NE + E	

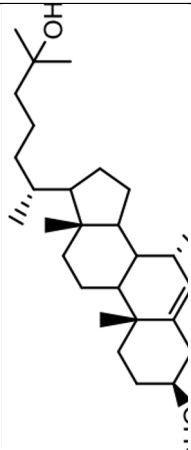
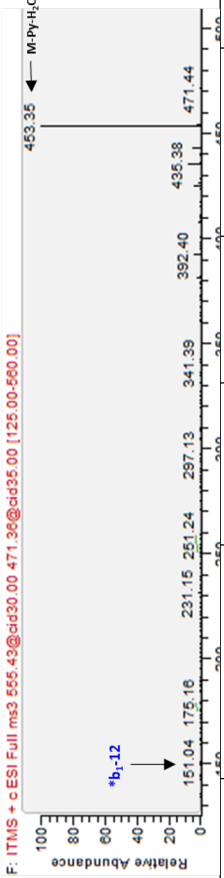
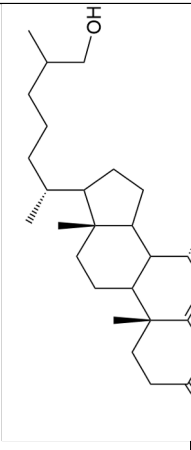
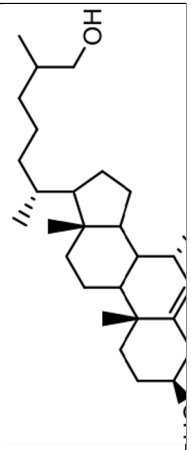
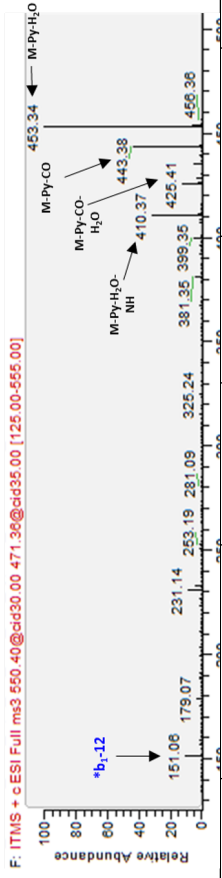


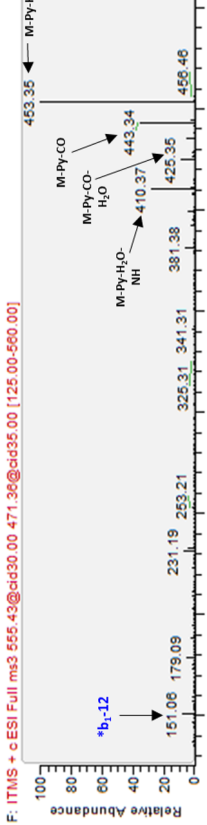
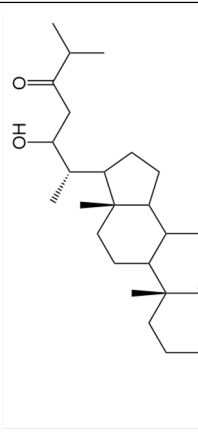
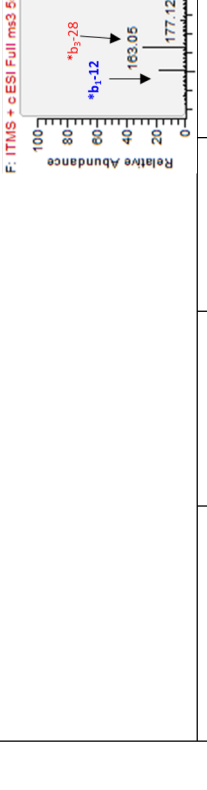
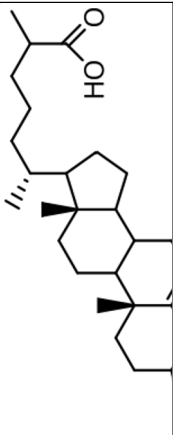
7 α -hydroxy-4-cholesten-3-one	7 α -HCO	C ₂₇ H ₄₄ O ₂	400.3341	-	534.4054	NE + E	
<p>F: ITMS + c ESI Full ms3 534.41@cd30.00 455.36@dd35.00 [125.00-540.00]</p> 							
Cholest-5-ene-3 β ,7 α -diol	7 α -HC	C ₂₇ H ₄₆ O ₂	402.3498	539.4368	-	NE + E	
<p>F: ITMS + c ESI Full ms3 539.44@cd30.00 455.36@dd35.00 [125.00-545.00]</p> 							

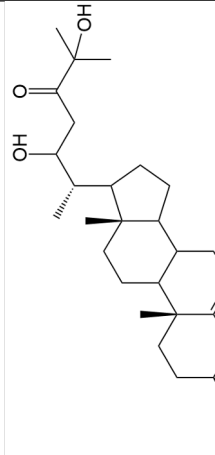
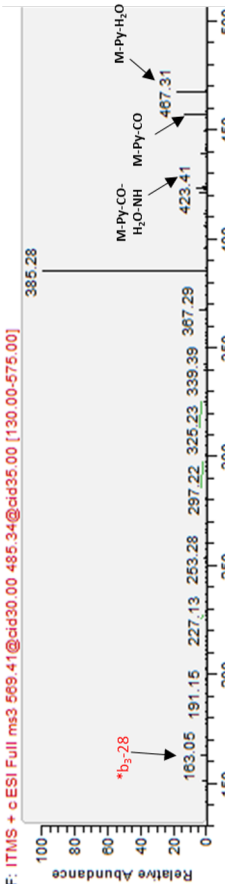
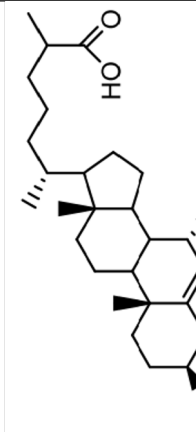
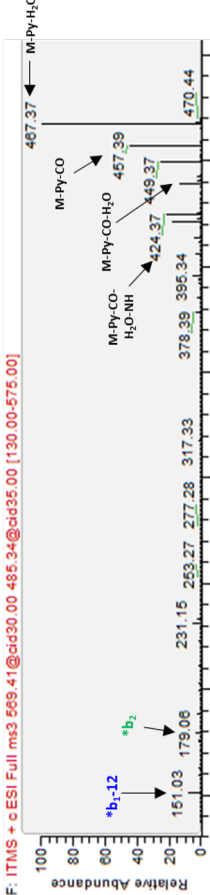
Cholest-5-ene-3 β ,6 β -diol	6 β -HC	C ₂₇ H ₄₆ O ₂	402.3498	539.4368	534.4054	NE + E	
<p>F: ITMS + c ESI Full ms3 539.44@dd30.00 455.36@dd35.00 [125.00-545.00]</p> 							
7 α ,12 α -Dihydroxycholest-4-en-3-one	7 α ,12-diHCO	C ₂₇ H ₄₄ O ₃	416.3290	-	550.4003	E	
<p>F: ITMS + c ESI Full ms3 550.40@dd30.00 471.36@dd35.00 [125.00-555.00]</p> 							
Cholest-5-ene-3 β ,7 α ,12-triol	7 α ,12-diHCO	C ₂₇ H ₄₆ O ₃	418.3447	555.4317	-	E	

Cholest-5-ene-3 β ,7 α ,24-triol	7 α ,24-diHC	C ₂₇ H ₄₆ O ₃	418.3447	555.4317	-	E	
7 α ,25-Dihydroxycholest-4-en-3-one-	7 α ,25-diHCO	C ₂₇ H ₄₄ O ₃	416.3290	-	550.4003	E	



Cholest-5-ene-3 β ,7 α ,25-triol	7 α ,25-diHC	C ₂₇ H ₄₆ O ₃	418.3447	555.4317	-	E	 
7 α , (25R)26-dihydroxycholest-4-en-3-one	7 α ,26-diHCO	C ₂₇ H ₄₄ O ₃	416.3290	-	550.4003	E	
Cholest-5-ene-3 β ,7 α , (25R)26-triol	7 α ,26-diHC	C ₂₇ H ₄₆ O ₃	418.3447	555.4317	-	E	 

<p>3β,22-Dihydroxycholest-5-en-24-one</p>	<p>-</p>	<p>C₂₇H₄₄O₃</p>	<p>416.3290</p>	<p>553.4161</p>	<p>E</p>
 <p>F: ITMS + c ESI Full ms3 553.42@dd30.00 471.38@dd35.00 [125.00-560.00]</p>					
<p>3β-Hydroxycholest-5-en-(25R)26-oic acid</p>	<p>-</p>	<p>C₂₇H₄₄O₃</p>	<p>416.3290</p>	<p>553.4161</p>	<p>E</p>
 <p>F: ITMS + c ESI Full ms3 553.42@dd30.00 469.34@dd35.00 [125.00-560.00]</p>					

3β,22,25-Trihydroxycholest-5-en-24-one	-	432.3240	569.4110	-	E		
<p>F: ITMS + c ESI Full ms3 569.41@dd30.00 485.34@dd35.00 [130.00-575.00]</p> 							
3β,7α-Dihydroxycholest-5-en-(25R)26-oic acid	3β,7α-diHCA	C ₂₇ H ₄₄ O ₄	432.3240	569.4110	-	E	
<p>F: ITMS + c ESI Full ms3 569.41@dd30.00 485.34@dd35.00 [130.00-575.00]</p> 							

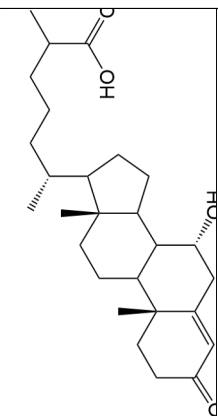
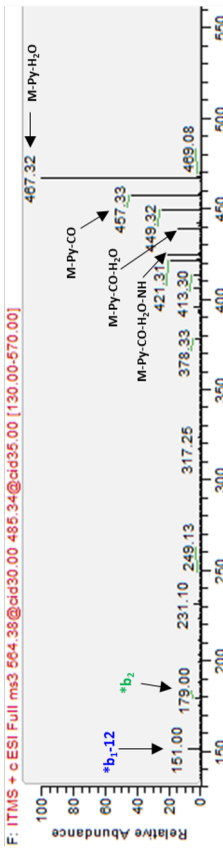
7 α -hydroxy-3-oxocholest-4-en-(25R)26-oic acid	7 α H,3O-CA	C ₂₇ H ₄₂ O ₄	432.3240	-	564.3796	E	
							

Table 9.1. A table of all oxysterols quantified. The structures of all oxysterols within this thesis, including name, abbreviation, elemental composition, type of synthesis (enzymatic/non-enzymatic), structure, exact mass before derivatisation and with derivatisation for GP-d5 and GP-d0, and the ion trap fragmentation (ITMS³) spectra. Please refer to Figure 2.5 on page 84 (section 2.2.9) for details on b₁-12, b₂ and b₃-28 structural fragments.

Test for normal distribution D'Agostino & Pearson test	24S,25-EC	24S-HC	24R-HC	(25R)26- HC	25-HCO	(25R)26- HCO	7β-HC	7-OC	7α-HC	6β-HC	3β-HCA
K2	3.321	9.761	1.682	2.441	14.87	74.42	0.2709	12.4	1.144	20.42	14.68
P value	0.19	0.0076	0.4312	0.295	0.0006	<0.0001	0.8733	0.002	0.5644	<0.0001	0.0006
Passed normality test (alpha=0.05)?	Yes	No	Yes	Yes	No	No	Yes	No	Yes	No	No
P value summary	ns	**	ns	ns	***	****	ns	**	ns	****	***
Number of values	38	38	38	38	38	38	38	38	38	38	38

Test for normal distribution D'Agostino & Pearson test	7α,25-diHC	7α,25-diHCO	7α,(25R)26- diHC	7α,(25R)26- diHCO	3β,7α-diHCA	7αH,3O-CA	Cholesterol
K2	2.438	5.656	49.49	25.12	15.61	5.954	8
P value	0.2955	0.0591	<0.0001	<0.0001	0.0004	0.051	0.0183
Passed normality test (alpha=0.05)?	Yes	Yes	No	No	No	Yes	No
P value summary	ns	ns	****	****	***	ns	*
Number of values	38	38	38	38	38	38	38

Table 9.2. Full statistical normality test results from Alzheimer's disease brain diagnosis grouping. P value significance levels were: * P < 0.05, ** P < 0.005, *** P < 0.0005, **** P < 0.0001.

Test for normal distribution D'Agostino & Pearson test	24S,25-EC	24S-HC	24R-HC	(25R)26- HC	25-HCO	(25R)26- HCO	7 β -HC	7-OC	7 α -HC	6 β -HC	3 β -HCA
K2	9.256	6.024	7.59	3.476	39.36	87.01	12.04	5.205	7.619	17.89	11.61
P value	0.0098	0.0492	0.0225	0.1759	<0.0001	<0.0001	0.0024	0.0741	0.0222	0.0001	0.003
Passed normality test (alpha=0.05)?	No	No	No	Yes	No	No	No	Yes	No	No	No
P value summary	**	*	*	ns	****	****	**	ns	*	***	**
Number of values	45	45	45	45	45	45	45	45	45	45	45

Test for normal distribution D'Agostino & Pearson test	7 α ,25-diHC	7 α ,25-diHCO	7 α ,25R)26- diHC	7 α ,25R)26- diHCO	3 β ,7 α -diHCA	7 α H,3O-CA	Cholesterol
K2	3.013	26.27	49.72	34.91	15.93	7.851	1.322
P value	0.2217	<0.0001	<0.0001	<0.0001	0.0003	0.0197	0.5163
Passed normality test (alpha=0.05)?	Yes	No	No	No	No	No	Yes
P value summary	ns	****	****	****	***	*	ns
Number of values	45	45	45	45	45	45	45

Table 9.3. Full statistical normality test results from Alzheimer's disease ApoE status grouping. P value significance levels were: * P < 0.05, ** P < 0.005, ***

P < 0.0005, **** P < 0.0001.

Test for normal distribution D'Agostino & Pearson test	24S,25- EC	24S-HC	24R-HC	25-HC	(25R)26- HC	25-HCO	(25R)26- HCO	7 β -HC	7-OC	7 α -HC	6 β -HC
K2	0.7431	1.305	40.27	1.87	37.02	28.15	17.96	40.01	34.74	39.55	7.616
P value	0.6897	0.5208	<0.0001	0.3925	<0.0001	<0.0001	0.0001	<0.0001	<0.0001	<0.0001	0.0222
Passed normality test (alpha=0.05)?	Yes	Yes	No	Yes	No	No	No	No	No	No	No
P value summary	ns	ns	****	ns	****	****	***	****	****	****	*
Number of values	18	18	18	18	18	18	18	18	18	18	18

Test for normal distribution D'Agostino & Pearson test	3 β -HCA	7 α ,25-diHC	7 α ,25-diHCO	7 α , (25R)26- diHC	7 α , (25R)26- diHCO	3 β ,7 α -diHCA	7 α H,3O-CA
K2	29.83	13.05	12.75	9.262	10.73	16.25	18.78
P value	<0.0001	0.0015	0.0017	0.0097	0.0047	0.0003	<0.0001
Passed normality test (alpha=0.05)?	No	No	No	No	No	No	No
P value summary	****	**	**	**	**	***	****
Number of values	18	18	18	18	18	18	18

Table 9.4. Full statistical normality test results from human multiple sclerosis and control homogenate cohort. P value significance levels were: * P < 0.05, ** P < 0.005, *** P < 0.0005, **** P < 0.0001.

Table 9.5. Bartlett's test results from one-way ANOVA test from multiple sclerosis homogenate tissue and corresponding controls.

Bartlett's test	
Bartlett's statistic (corrected)	1749
P value	< 0.0001
P value summary	****
Are SDs significantly different (P < 0.05)?	Yes

Table 9.6. Full statistical normality test results from the Q150+ and control mouse brain imaging data. P value significance levels were: * P < 0.05, ** P < 0.005, *** P < 0.0005, **** P < 0.0001.

	Control	HD/Q150
Anderson-Darling test		
A2*	0.5058	0.3665
P value	0.1387	0.3365
Passed normality test (alpha=0.05)?	Yes	Yes
P value summary	ns	ns

D'Agostino & Pearson test		
K2	4.221	1.696
P value	0.1212	0.4282
Passed normality test (alpha=0.05)?	Yes	Yes
P value summary	ns	ns

Shapiro-Wilk test		
W	0.8581	0.9048
P value	0.115	0.3186
Passed normality test (alpha=0.05)?	Yes	Yes
P value summary	ns	ns

Kolmogorov-Smirnov test		
KS distance	0.2201	0.206
P value	>0.1000	>0.1000
Passed normality test (alpha=0.05)?	Yes	Yes
P value summary	ns	ns

	CNTL WM	NAWM	WML	WMLE	WMRM	CNTL GM	NAGM	GML	GMLE
Anderson-Darling test									
A2*	0.4651	0.1815	0.3983	N too small	N too small	0.7001	0.7915	0.5977	N too small
P value	0.1898	0.8905	0.2875			0.0435	0.0244	0.0928	
Passed normality test (alpha=0.05)?	Yes	Yes	Yes			No	No	Yes	
P value summary	ns	ns	ns			*	*	ns	
D'Agostino & Pearson test									
K2	5.484	0.1285	2.217	N too small	N too small	1.927	12.66	1.541	N too small
P value	0.0645	0.9378	0.33			0.3816	0.0018	0.4628	
Passed normality test (alpha=0.05)?	Yes	Yes	Yes			Yes	No	Yes	
P value summary	ns	ns	ns			ns	**	ns	
Shapiro-Wilk test									
W	0.8869	0.9789	0.907	0.9619	0.8421	0.8415	0.8018	0.8929	0.8694
P value	0.1854	0.9789	0.2955	0.8343	0.2196	0.0601	0.0214	0.1283	0.2939
Passed normality test (alpha=0.05)?	Yes	Yes	Yes	Yes	Yes	Yes	No	Yes	Yes
P value summary	ns	ns	ns	ns	ns	ns	*	ns	ns
Kolmogorov-Smirnov test									
KS distance	0.2259	0.1679	0.231	0.1857	N too small	0.3185	0.2869	0.2307	N too small
P value	>0.1000	>0.1000	>0.1000	>0.1000		0.009	0.0314	0.0772	
Passed normality test (alpha=0.05)?	Yes	Yes	Yes	Yes		No	No	Yes	
P value summary	ns	ns	ns	ns		**	*	ns	

Table 9.7. Full statistical normality test results from the multiple sclerosis and control human brain imaging data. P value significance levels were: * P < 0.05, ** P < 0.005, *** P < 0.0005, **** P < 0.0001.